THERMAL SHOCK RESISTANCE PARAMETERS

FOR THE INDUSTRIAL LINING PROBLEM

By

FREDERICK JOSEPH BRADLEY

B.A.Sc., The University of British Columbia, 1981

A THESIS SUBMITTED IN PARTIAL FULFILLMENT OF

THE REQUIREMENTS FOR THE DEGREE OF

DOCTOR OF PHILOSOPHY

in

THE FACULTY OF GRADUATE STUDIES

Department of Metallurgical Engineering

We accept this thesis as conforming

to the required standard

THE UNIVERSITY OF BRITISH COLUMBIA

October, 1985

In presenting this thesis in partial fulfilment of the requirements for an advanced degree at the University of British Columbia, I agree that the Library shall make it freely available for reference and study. I further agree that permission for extensive copying of this thesis for scholarly purposes may be granted by the head of my department or by his or her representatives. It is understood that copying or publication of this thesis for financial gain shall not be allowed without my written permission.

Department of METALLURGY

The University of British Columbia
1956 Main Mall
Vancouver, Canada
V6T 1Y3

Date October 15, 1985

Abstract

A two-dimensional constant heating rate thermoelastic model has been used to develop design and selection criteria for refractory components of linings of high-temperature furnaces and process vessels. The criteria are in the form of resistance to fracture initiation and resistance to damage parameters which account for the influence of thermal and mechanical properties, geometry, and temperature range, while distinguishing between the heating and cooling cases. The resistance to fracture initiation parameter ϕ_s is the maximum rate at which a shape can be heated or cooled through a specified temperature range without causing fracture. The damage resistance parameter R_d is expressed as the ratio of surface energy per unit area to the elastic strain energy available for crack propagation. Both parameters can be quickly estimated for arbitrary conditions with the aid of tabulated solutions for the maximum principal tensile stress and total strain energy

Thermoelastic analyses were used to interpret published results of a variety of thermal shock experiments. Thermal conditions associated with water quenching, radiative furnace heating, gas burners, and controlled heating were simulated using appropriate analytical solutions. Finite element analysis was used to compute maximum principal tensile stresses and elastic strain energy. A simple procedure was developed to invert the stress solution and thereby determine the instant of fracture. Good agreement between thermoelastic predictions and published experimental results with regard to strength retained versus thermal shock relationships, location of fracture, and safe heating rates provided justification for a thermoelastic approach to the thermal shock.

TABLE OF CONTENTS

Page

Page

Page

Page

LIST OF TABLES

Chapter 2

LIST OF FIGURES

Chapter 4

Chapter 5

LIST OF SYMBOLS

α	coefficient of thermal expansion	$°C^{-1}$
a	thermal diffusivity	m^2/s
A	area	m^2
A_c	area of crack propagation	
β^*	Biot modulus	
b	radius of a sphere	M
c	crack length	M
c_p	specific heat	J/kg°C
ε_s	critical shear strain at fracture	
ε_t	critical tensile strain at fracture	
E	elastic modulus	GPa
ϕ	heating or cooling rate	°C/s
ϕ_s	safe heating or cooling rate	°C/s
f	bending force	
F	Weibull disribution function	
γ	surface energy per unit area	J/m^2
γ^*	dimensionless thermal load	
h	heat transfer coefficient	J/sm^2
k	thermal conductivity	J/sm°C

K	kinetic energy	J
K_{IC}	critical stress intensity factor	$MPam^{1/2}$
ℓ	length	m
m	Weibull modulus	
N	crack density	
ν	Poisson's ratio	
ρ	density	kg/m^3
R	resistance to fracture initiation parameter for instantaneous change in surface temperature case	
R'	resistance to fracture initiation parameter for constant heat transfer coefficient case	
R''	resistance to fracture initiation parameter for constant heating rate case	
R'''	resistance to damage parameter which neglects surface energy term	
R''''	resistance to damage parameter which accounts for surface energy term	
R_d	thermoelastic damage resistance parameter	
R_i	resistance to fracture initiation parameter for constant heating rate case	
R_{st}	resistance to fracture initiation parameter associated with unified theory	
S_a	strength after thermal shock	MPa

S_t	strength before thermal shock	MPa
S	spalling tendency, shape factor	
σ	stress	MPa
σ_f	fracture strength	MPa
σ_M	maximum principal	MPa
σ^*	dimensionless stress	
θ^*	Fourier modulus	
t	time	s
T_a	initial temperature	°K,°C
T_∞	ambient temperature	°K,°C
T_s	surface temperature	
ΔT	temperature difference	°K,°C
T	temperature	°K,°C
T''	second derivative of temperature with respect to space	$°Cm^{-2}$
T^*	dimensionless temperature	
τ	shear stress	MPa
U	strain energy	J
U^*	dimensionless strain energy	
U_o	strain energy density	MPa

subscripts

c	critical
eff	effective
f	fracture, final
g	Griffith
min	minimum
nbt	notched beam technique
s	shear
t	tensile
wof	work of fracture method
x	space coordinate
y	space coordinate
z	space coordinate

superscripts

c	center line
E	edge
*	dimensionless parameter

Acknowledgements

The author is deeply grateful to all those who helped throughout the course of my stay in the Department of Metallurgy. I would particularly like to thank Prof. A. Mitchell and Prof. A.C.D. Chaklader for the freedom to express myself and my wife Eva for the constant support and encouragement. The financial assistance provided by NSERC and Noranda is gratefully acknowledged.

Chapter 1

INTRODUCTION

1.1 Introduction

Thermal stress fracture of refractory structural components of high-temperature process vessels and industrial furnaces is a widespread industrial problem. While the principal origin of thermal stress may vary from process to process, a common feature of all processes is that the lining undergoes at least one thermal cycle in which the hot face of the lining is heated from ambient to operating temperature and cooled back again. During these stages thermal stresses develop due to nonlinear temperature distribution.

If heating or cooling is too rapid the transient temperature fields will produce a stress of sufficient magnitude to cause fracture which, in turn, will enhance refractory wear. Unlike the relatively constant rates associated with the other major wear mechanism, corrosion-erosion, thermal shock failure can cause a sudden catastrophic loss of brickwork of sufficient magnitude to halt production. In addition to being a significant operating cost, excessive refractory consumption involves higher labour, inventory, and capital costs.

On the other hand, if heating or cooling occurs over a prolonged period, the furnace or vessel is unavailable for production. Also, heat losses are higher and, consequently, energy costs increase. The industrial lining problem is thus concerned with heating or cooling a refractory component through a specified temperature range as rapidly as possible without causing fracture.

As a final point, a limiting factor to the use of higher operating temperature, often desirable from the standpoint of product recovery and process throughput, is lining material performance. In general, higher operating temperatures enhance corrosion-erosion rates and increase the likelihood of thermal stress fracture. One solution to the corrosion-erosion problem is the use of fully-dense lining components which, unfortunately, have extremely poor thermal shock resistance. It is clear that much motivation exists for the study of the thermal shock fracture behaviour of brittle materials.

1.2 Scope

The principal origins of thermal stress in industrial linings are nonlinear temperature distributions, boundary restraint, and in-service alteration of the lining components. Rather than considering the refractory wear problem of a particular industrial process, a more generalized approach is taken in the present work. To accomplish this a number of simplifying assumptions are made. The principal supposition is that the thermoelastic case of a homogeneous, traction-free, rectangular shape in which thermal stresses develop because of nonlinear temperature distributions yields results of relevance to the industrial lining problem.

The two major types of linings are monolithic and bricked. In the case of the latter type, refractory mortar can be used to cement adjacent bricks together or, alternatively, bricks are simply set in place. This work is applicable to industrial processes which have bricked linings in which the components are set in place.

The bricks in a newly-lined wall are in a traction-free state. The occurrence of boundary restraint is dependent on the method of installation which varies from plant to plant and process to process. If adequate thermal expansion allowance is not provided, stress relief in the form of localized chipping at the corners of the hot face will occur, thus returning the component to a traction-free state. During the cooling cycle the components are in a traction-free state as the hot face of each brick is contracting. Thus the assumption of traction-free boundaries appears reasonable.

Another source of thermal stress is the inhomogeneity which can result from in-service alteration and densification of the hot face region caused by penetration and/or chemical attack. The net effect is essentially the formation of a composite material. It is usually postulated that fracture is caused by stresses which develop on thermal cycling due to the difference in thermal expansion of the altered and unaltered zones. This problem is not considered in the present work. It is assumed that material properties are uniform throughout the body.

While recognizing that thermal shock failure in a particular process may be due to several interacting causes, this work is concerned solely with the thermal stress fracture of traction-free bodies due to one-dimensional nonlinear temperature distributions. The traction-free assumption is reasonable as it is likely that the expansion of the bricks can be accommodated by lateral movements, so stresses on the sides should be small. One-dimensional heat flow is a valid assumption as lining components are generally heated or cooled on one face only, usually referred to as the hot face. Thus, because of adjacent bricks, the temperature will be uniform in planes parallel to the hot face. In this work refractory components are modelled as two-dimensional rectangular shapes. Unless otherwise stated, the hot face corresponds to the width of the shape and heat flow is along the length.

1.3 Thermal Shock Behaviour of Brittle Materials

Refractory products are multi-phased materials containing an irregular, unpredictable flaw distribution consisting of both pores and microcracks. Flaws can influence thermal shock behaviour in two ways, through the statistical nature of strength and by influencing thermal and mechanical properties. Strength retained versus thermal shock relationships are generally interpreted in terms of the Hasselman unified theory of fracture initiation and crack propagation which treats flaws explicitly.

Typical thermal shock fracture behaviour is shown in Figure 1.1. On increasing the severity of thermal shock no change in strength occurs until a critical value of thermal shock is reached, at which point fracture initiation occurs and one of the three following types of behaviour occurs : (I) strength decreases gradually with increasing thermal shock, (II) strength drops abruptly at the critical value to some lower value (point B) and then decreases gradually with increasing thermal shock, or (III) strength drops abruptly to zero (point C) as a result of component separation.

A major portion of the present work is devoted to justifying a thermoelastic interpretation of thermal shock fracture behaviour. A thermoelastic model accounts for the influence of flaws implicitly through the magnitude of thermal and mechanical properties. Both the

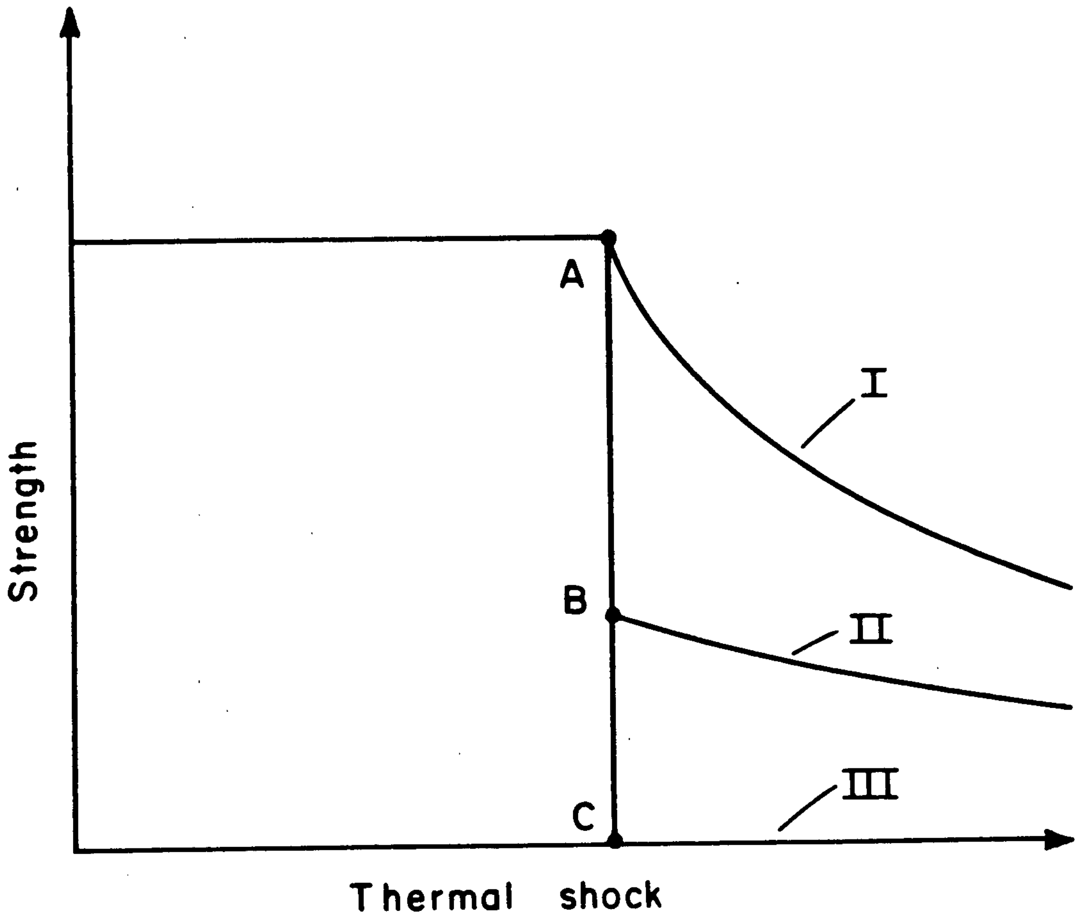

Figure 1.1 Typical strength retained versus thermal shock relationships.

Hasselman and thermoelastic interpretations of a wide variety of experimental results involving such diverse thermal conditions as water quenching and furnace heating are discussed.

1.4 Summary

This work considers the problem of thermal shock failure of refractory components on a general level. The overall goal is the development of theoretical design and selection criteria. With this in mind, the scale of the problem is reduced in such a way as to retain the essential industrial features, while permitting a general mathematical treatment. A two-dimensional thermoelastic traction-free model is used to simulate the thermal shock behaviour of lining components during heating and cooling stages.

This work is concerned primarily with two themes:

(i) the justification of the use of thermoelastic analysis for the interpretation of observed strength loss - thermal shock behaviour, and

(ii) the development of theoretical design and selection criteria in the form of resistance to fracture initiation and resistance to damage parameters which are applicable to the industrial lining problem.

A review of the literature is presented in Chapter 2 and a statement of the problem is made in Chapter 3. Alternative theoretical interpretations of thermal shock strength loss relationships are presented and discussed in Chapter 4. A suitable two-dimensional thermoelastic model for the industrial lining problem is described in Chapter 5 and used as the basis for the development of resistance to fracture initiation and resistance to damage parameters. A summary of findings and recommendations for future work are given in Chapter 6.

Appendix I contains a summary of the assumptions and pertinent thermoelastic equations, as well as some background information concerning the nature of the thermal stress fields that arise. Appendix II a description of the finite element numerical method used for the computation of stresses and strain energy. All details related to the thermoelastic formulation, numerical computations, and nature of the thermal stress field are to be found in these appendices. The remaining appendices contain numerical results and dimensional analyses.

Chapter 2

LITERATURE REVIEW

2.1 Introduction

Many approaches have been taken in the study of thermal shock behaviour of refractory materials. The term thermal shock is commonly applied to both the fracture initiation and damage aspects of the problem; the former being concerned with the determination of combinations of factors - material properties, geometry, thermal environment, etc. - which will just cause fracture and the latter with the influence of the same parameters on the extent of crack propagation. The objective in both cases is usually the development of criteria for the selection of materials for high temperature processes.

Thermoelastic analysis and the Hasselman treatment, two of the more popular approaches, are discussed in detail in sections 2.2 and 2.3, respectively. Other theoretical approaches and some of the implications of the flaw-dependence of strength are discussed in Section 2.4. Section 2.5 describes several of the more common thermal shock tests and discusses the relative merits of each. A summary is presented in Section 2.6

2.2 Thermoelastic Approach to Fracture Initiation

The first step of the thermoelastic approach is the computation of thermal stresses. Materials are usually assumed to be homogeneous and isotropic, linearly elastic, and to possess temperature-independent properties. Due to the relative complexity of multi-dimensional problems, one-dimensional geometries such as the infinite slab case have been considered most frequently. With the advances in computer technology and numerical methods in the past decade, more attention has been directed toward the multi-dimensional problem.

Thermal shock is usually modelled using an analytical solution for the temperature profiles which typically involves one of the three following thermal boundary conditions: (i) instantaneous change in surface temperature, (ii) constant convective heat transfer coefficient, and (iii) constant heating or cooling rate. The fracture criterion most often selected is that based on the maximum principal tensile stress. Once the thermal conditions and fracture criterion have been decided, the objective is to obtain a general solution for the critical member of the stress field as a function of thermal boundary condition and other relevant parameters.

With such a relationship it is possible to make inferences about thermal shock fracture behaviour which can be useful for design purposes. The underlying idea is that the variation of maximum principal tensile stress with an independent parameter, such as width, would reflect the influence of that parameter on fracture behaviour. For example, the implication of an increase in maximum principal tensile stress with width is that a reduction in width improves thermal shock resistance.

Due to the complexity of the problem, most thermoelastic analyses stop at this point. However, a general solution of the thermal stress problem is only the beginning of the fracture problem. A comprehensive thermoelastic treatment requires that the stress solution be put in an inverted form which gives all of the combinations of independent parameters that satisfy the fracture criterion.

Results from earlier work for the one-dimensional models are presented in Sections 2.2.1 and 2.2.2. The multi-dimensional problem is considered in Section 2.2.3. Finally, the validity of some of the assumptions with regard to refractory products is discussed in Section 2.2.4

2.2.1 Early Work

Norton (1925)[1-3] considered failure on rapid heating to be due entirely to shear stresses. Based on an analysis that assumed that the stress in a material subjected to a sudden temperature change is proportional to the temperature gradient at any point, he suggested that spalling tendency S (where spalling is fracture due to thermal stress) should be given by

$$S = \frac{\alpha}{\sqrt{a}\ \varepsilon_s} \qquad (2.1)$$

where α is the coefficient of thermal expansion, a is the thermal diffusivity, and ε_s is the critical shear strain at fracture.

Preston (1926)[4-5] thought that spalling under both quenching (rapid cooling) and the rapid heating conditions postulated by Norton was due to tensile rather than shear stresses. He showed that Norton's analysis was clearly incorrect, but failed to provide an alternative theoretical analysis. He simply stated that the stress distribution at fracture was similar to that found along the center line of an infinite slab through which heat flows only in the thickness direction (see Appendix I).

Neither Norton nor Preston clearly stated the geometry or thermal conditions associated with the 'typical' spalls under discussion. It was at times not clear whether the heating or cooling case was being considered. The effect of geometry, accounted for in the Norton derivation, albeit erroneously, was discounted by Preston who stated that the omission of a size dependence was one reason for his preference of the Winkelmann and Schott (1894)[6] formula,

$$S = \frac{\alpha}{\sqrt{a}\ \varepsilon_t} \tag{2.2}$$

where ε_t is the critical tensile strain at fracture.

The confusion and misunderstanding that arose in early work reflects the complexity of the subject. The nature and magnitude of the thermal stress field, and hence thermal stress fracture behaviour, is dependent on thermal and stress boundary conditions, geometry, and heating and cooling, as well as material properties. It is to the credit of the early investigations that they established a pattern of research, with regard to the theoretical derivation of parameters and experimental correlations, that has been followed to the present.

2.2.2 One-Dimensional Models

Kingery (1955)[7] presented the resistance to fracture initiation parameters that are most often referred to. He used the dimensionless form of the analytical solution for the case of the infinite slab symmetrically heated or cooled with a constant heat transfer coefficient (h) to derive the parameters R and R', where

$$R = \frac{\sigma_f (1-\nu)}{E\alpha} \tag{2.3}$$

and

$$R' = \frac{\sigma_f (1-\nu)\, k}{E\alpha} \tag{2.4}$$

and σ_f is the fracture strength, ν is Poisson's ratio, E is the elastic modulus, and k is the thermal conductivity. The parameter R is applicable for the case of instantaneous change in surface temperature (infinite h) and R' for that of relatively low Biot modulus ($\beta<2$).

Using a similar method the resistance parameter R", given by

$$R'' = \frac{\sigma_f (1-\nu)\, a}{E\alpha}, \tag{2.5}$$

was developed for the constant heating or cooling rate case. The parameters indicate that high resistance to fracture initiation is associated with combinations of high fracture strength, thermal conductivity, and thermal diffusivity, and low elastic modulus, Poisson's ratio, and coefficient of thermal expansion.

The infinite slab case is only valid for those geometries in which the width is at least twice the length. The geometry of basic oxygen furnace (BOF) bricks is such that the dimension in the direction of heat flow is far greater than the width. The observation of spall cracks parallel to the hot face suggested to Kienow[8] that the $(\sigma_y^c)_M$ (see Appendix I) component was responsible for the fracture behaviour. He used a simple one-dimensional spring model to obtain a quantitative estimate of σ_y. By considering a shape with constant temperature gradient over depth h from the hot face and constant temperature over the remainder of the length, he derived the following expression which relates fracture strength to the second derivative of the temperature field at the point of fracture,

$$\sigma_f = E\alpha \left(\frac{d^2T}{dy^2}\right)_{y=h} \left(\frac{w^2}{16 + \frac{3w^3}{h^3}}\right) \tag{2.6}$$

where $\left(\frac{d^2T}{dy^2}\right)_{y=h}$ is the critical value of the second derivative of temperature with respect to y at the point of fracture at y=h. Kienow described a graphical procedure for the determination of the two unknowns in (2.6), $(\frac{d^2T}{dy^2})_{y=h}$ and h, which have been used by several investigators[9-11] to calculate safe heat up rates and to investigate the effect of gunning on crack formation in BOF refractories.

2.2.3 Multi-dimensional Analysis

Clements (1959)[12] noted the limitations of one-dimensional models and discussed the characteristic features of the two-dimensional stress field associated with a traction-free rectangular shape heated from one end. The limitation of the infinite slab analysis is that it yields the center line σ_x distribution only. Such geometries (width greater than twice the length) possess significant σ_y and τ_{xy} fields, that arise due to an end effect, which are located in regions remote from the center line near the outside edges. By St. Venant's principle the end effect is assumed to not influence the σ_x center line distribution.

For narrow geometries (width much less than length), the end effect is felt throughout the body with the consequence that the σ_y and τ_{xy} fields dominate over the whole shape. For rectangular shapes in which the width is comparable to the length, the thermal stress field is a complex two-dimensional one consisting of overlapping σ_x, σ_y, and τ_{xy} fields. While both analytical and numerical methods are available for the solution of multi-dimensional problems, discussion is limited to numerical methods as they offer much greater flexibility and analytical solutions (when available) usually require computer evaluation as the final step.

Guilliat and Chandler (1977)[13], using a three-dimensional technique based on minimum complementary energy, and Chandler (1981)[14] in a separate study concerned with rectangular shapes, reported on the influence of geometry on the thermal stress field of shapes heated from one end. They found that the effect of increasing a square hot face cross-section of the block relative to its length and of increasing the aspect ratio (w/ℓ) of a rectangular shape is to cause a transition in dominant tensile stress from that acting perpendicular to the hot face (σ_y) to that acting parallel to the hot face (σ_x). The points of transition, where $(\sigma_x^c)_M = (\sigma_y^c)_M$, occur at aspect ratios of 1.4 and 1.0 for the block and rectangle cases, respectively.

Kumagai et al (1980)[15] used a three-dimensional finite element technique and Sweeney and Cross (1982)[16-17] a two-dimensional finite difference technique which incorporated viscoelastic effects in a non-linear single integral stress-strain law to examine the effect of geometry and restraint. With regard to geometry, their results are in general agreement with those of Guilliat and Chandler.

In one of the most comprehensive works to date, Chang et al (1983)[18] employed finite element analysis to compute the thermal stresses in BOF-type components in which the length is much greater than the width. They considered a wide range of variables and, on the basis of the influence of these variables on the magnitude of the peak σ_y component, made design recommendations. No results were presented for the peak σ_x component which, unfortunately, was the dominant maximum principal tensile stress in many of the cases considered. This work is considered in greater detail in Chapter 5.

In summary, a variety of numerical methods have been used for the computation of multi-dimensional thermal stress fields of two- and three-dimensional bodies heated from one end. The major finding is that the component which is the maximum principal tensile stress is dependent on geometry. This is significant with regard to fracture behaviour as the σ_x component tends to propagate cracks in a direction perpendicular to the hot face while the σ_y component tends to cause cracking in a direction parallel to the hot face. No general solution for the maximum principal tensile stress of any multi-dimensional problem applicable to the industrial lining problem could be found.

2.2.4 Thermoelastic Assumptions and Refractory Products

The principal thermoelastic assumptions in the stress analysis of refractories are temperature-independent properties, linear elastic stress-strain behaviour to brittle failure, and that the components behave as if they were flaw-free. The first two aspects are considered in this section while discussion of the latter takes place in Section 2.4.

The thermal and elastic properties of some refractory products are notably temperature-dependent while those of others are not. At the extremes, the thermal conductivity of alumina and magnesia refractories can decrease by factors of approximately two and three on going from room temperature to 1200°C, and that of insulating silica brick can increase by a factor of three over the same range. Most other products are much less temperature-dependent[19-21].

Elastic modulus can vary widely with temperature depending on type and quality. The elastic modulus of magnesia[22-23] and dolomite[24] refractories generally decreases gradually with temperature to about 60-90% of the room temperature value at 1000°C - 1200°C, while the elastic modulus is essentially temperature-insensitive for many alumina products[25]. On the other hand, the elastic modulus of magnesia-chrome ore refractories is relatively independent of temperature to about 800°C, but on further increase of temperature through the range of 800-1200°C the elastic modulus can increase by up to a factor of four times the room temperature value[26-30].

The stress-strain behaviour of most refractory materials is approximately linear up to temperatures of approximately 1000°C, the upper limit depending on the individual product[31-32]. At higher temperatures creep will occur to varying degrees and significant stress relaxation can result[33-34]. Finally, material properties can be significantly affected by thermal cycling which can cause extensive microcracking due to thermal expansion mismatch of constituent phases, phase changes, and/or chemical changes[35-37].

Spatially and temperature-dependent parameters distort the thermal stress field without altering the basic nature of the distribution[38-44]. The exact effect on both magnitude and location of the peak stress components is dependent on the nature and extent of the variation in properties. While some properties may vary by a factor of three or four over a range of temperature of 1200°C, the extent of variation of a given property will generally be much less as the maximum range of temperature across an in-service refractory component will normally be much less in order to avoid fracture. The use of average values of material properties evaluated at an intermediate temperature is expected to yield reasonable results.

2.3 Hasselman Approach

For those industrial applications in which the likelihood of fracture is high, Hasselman suggested that resistance to damage, rather than to fracture initiation, might be a better criterion for material selection. He went on to formulate several models and subsequently derived a number of resistance parameters. A common element in the Hasselman approach is that extent of crack propagation is related to elastic strain energy at the instant of fracture and surface energy per unit area.

The different methods of determining surface energy per unit area are described in Section 2.3.1. Section 2.3.2 briefly discusses the first attempt at the derivation of a damage resistance parameter. The unified theory of the thermal shock fracture initiation and crack propagation is presented in detail in Section 2.3.3 and the application to the theoretical analysis to the prediction of thermal shock-strength loss relationships is discussed in Section 2.3.4. Experimental confirmation of the Hasselman treatment is summarized in Section 2.3.5.

2.3.1 Surface Energy

Surface energy γ represents the energy required for the creation of unit area of crack surface. It is commonly determined by either the work of fracture (wof) or notched beam technique (nbt). The latter method, developed by Nakayama[46], is generally used for refractories.

Nakayama distinguished between catastrophic and stable behaviour in terms of relative U_{total} and U_{γ}, where U_{total} is the total elastic energy stored in the system - specimen plus testing apparatus - at the time of fracture and U_{γ} is the energy required for separation of the specimen. Catastrophic fracture corresponds to the case of $U_{total} > U_{\gamma}$, the excess energy being transformed, for example, to kinetic energy of the fragments. Stable fracture is said to occur when $U_{total} \leqslant U_{\gamma}$, in which case the external work is converted directly into surface energy with no excess energy.

The external work W is calculated from the load-time curve as

$$W = v \int_{o}^{t_c} f \, dt \tag{2.7}$$

where v is the speed of deflection, t_c is the time required for completion of fracture, and f is the bending force. The effective surface energy is then given by

$$\gamma_{wof} = \frac{W}{2A} \tag{2.8}$$

where A is the projected surface area of the fracture zone.

Figure 2.1 shows typical load-time curves for catastrophic, semi-catastrophic, and stable fracture behaviour. It is not possible to determine γ_{wof} of most brittle materials without modification of the specimen as otherwise fracture occurs catastrophically, the strain energy at fracture being the driving force for crack propagation. The strain energy at fracture is markedly reduced by introducing an artificial crack such as that shown in Figure 2.2. With a sufficient reduction of cross-section stable fracture is obtained.

In the notched beam technique a rectangular beam (see Figure 2.2) is loaded to failure in a bend test and a K_{IC} value is calculated using a standard formula. Fracture energy γ_{nbt} is then computed using

$$\gamma_{nbt} = \frac{K_{IC}\ (1-\nu^2)}{2\ E} \tag{2.9}$$

Larson et al[89] determined γ_{wof} and γ_{nbt} for a wide range of high-alumina refractories. From their results in Table I it appears that, on the whole, γ_{wof} is approximately one order of magnitude greater than γ_{nbt}.

During the fracture of heterogeneous brittle materials energy can be consumed in a number of different ways. For example, fracture in

TABLE I

Fracture Energies and Thermomechanical Properties of High-alumina Refractories (after reference 89)

Refractory No.	Al_2O_3 (%)	Modulus of rupture (psi)	Young's modulus (10^6 psi)	Coeff. of th. exp. (10^{-6} °C^{-1})	Fracture energy (10^3 ergs cm^{-2}) γ_{WOF}	γ_{NBT}	K_{Ic} (psi in.$^{1/2}$)	R'''' (cm)	R_{st} (°C cm$^{1/2}$)	MOR retained (%) ΔT = 800°C	ΔT = 1000°C
1	99	3600± 300*	17.0	9.3	90± 8*	8± 1*	1240± 100*	1.71	29.8	21.4	14.9
2	99	2060± 300	8.5	9.4	58± 11	6± 1	730± 50	1.70	33.5	19.4	13.0
3	90	3230± 500	12.2	7.5†	110± 17	11± 3	1230± 150	1.86	48.4	34.7	30.4
4	90	2830± 240	11.5	8.1†	103± 12	6± 1	860± 30	2.14	44.4	44.0	33.1
5	90	2470± 590	9.0	8.2†	99± 10	7± 1	870± 30	2.12	48.7	45.3	37.3
6	90	2760± 380	8.1	8.0	91± 8	15± 4	1160± 100	1.41	50.5	54.5	45.8
7	90	2020± 200	2.7	8.1	73± 10	14± 3	650± 70	0.70	77.2		
8	85	1980± 230	8.9	7.8†	94± 11	10± 4	990± 180	3.08	50.1	56.4	55.6
9	85	2940± 300	9.4	7.6	90± 10	13± 4	1190± 170	1.42	49.0	51.4	41.2
10	85	4400± 310	10.1	7.6	75± 8	24± 12	1610± 400	0.56	43.0	28.8	29.9
11	85	1793± 200	5.0	7.6	70± 6	5± 1	550± 70	1.59	59.4	49.1	48.3
12	85	2170± 180	7.5	7.4	70± 5	8± 2	810± 110	1.61	49.8		
13	85	1540± 90	9.0	7.3†	44± 5	8± 2	670± 90	2.43	36.5		
14	80	2010± 360	4.5	7.3	77± 9	11± 3	750± 90	1.24	68.2	58.5	59.5
15	80	1630± 180	4.9	7.3	54± 4	7± 2	630± 90	1.45	54.8	61.5	53.2
16	75	1031± 180	4.6	7.1	54± 8	5± 1	490± 50	3.40	58.2		
17	70		4.5	7.0	80± 9	11± 1	740± 30		72.9		
18	70		2.4	6.9	79± 8	11± 3	550± 80		100.9		
19	70	1650± 150	3.4	7.4†	70± 1	9± 1	600± 150	1.27	73.9	53.7	46.4
20	70	1590± 220	4.6	6.8	65± 2	9± 2	700± 70	1.73	66.8		
21	70	1020± 140	2.7	6.9	60± 6	5± 3	390	2.5	82.6	64.3	57.8
22	70	1500± 80	3.4	6.9	58± 7	16± 1	750± 140	1.26	71.8	66.4	54.2
23	70	4060± 390	11.0	6.9	57± 8	14± 2	1340± 110	0.56	39.9	29.4	27.9
24	70	3240± 150	11.6	6.2†	57± 8	13± 2	1290± 110	0.92	43.3	31.3	26.9
25	70	412± 70	3.7	6.8	40± 5	2± 1	310± 70	12.63	58.2		
26	60	1230± 60	4.1	6.5	64± 10	8± 1	620± 30	2.48	73.1	65.0	49.9
27	60	3320± 200	8.1	5.7†	63± 8	15± 3	1160± 140	0.67	58.9	38.7	32.7
28	60	2400± 200	5.8	6.2†	62± 8	10± 1	800± 50	0.90	63.5	42.8	43.7
29	60	1070± 150	3.9	6.5	61± 5	9± 2	640± 70	2.97	74.0	64.3	60.7
30	60	720± 140	2.0	6.5	61± 9	5± 2	330± 70	3.41	102.7	60.1	49.2
31	60	590± 200	2.4	6.6†	59± 10	4± 2	320± 80	5.81	90.4	46.4	49.3
32	60	1340± 180	3.4	6.5	57± 9	7± 1	510± 40	1.58	76.6	53.5	50.0
33	60	970± 100	2.4	6.5	56± 9	6± 1	420± 30	2.08	89.3	74.4	69.3
34	60	1470± 210	3.3	7.0†	46± 8	9± 2	580± 50	1.03	64.6	41.7	34.3
35	60	860± 170	2.1	6.5	34± 9	6± 1	360± 20	1.43	75.6	56.9	49.7
36	50	1530± 330	4.2	6.3	53± 7	1	230± 50	1.39	68.2	43.3	35.4
37	45	1380± 206	4.2	6.2	64± 14	6± 1	530± 40	2.05	76.2	54.2	46.5
38	45	330± 90	1.8	6.2	35± 4	2± 1	210± 40	8.23	85.3	70.2	56.3

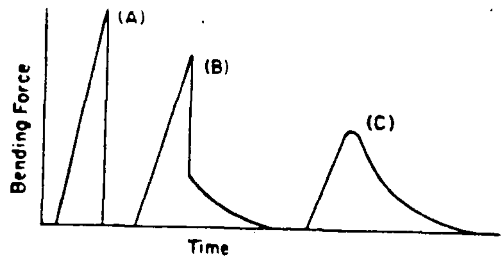

Figure 2.1 Typical load-time curves representing (A) catastrophic, (B) semi-stable, and (C) stable fracture (after reference 46)

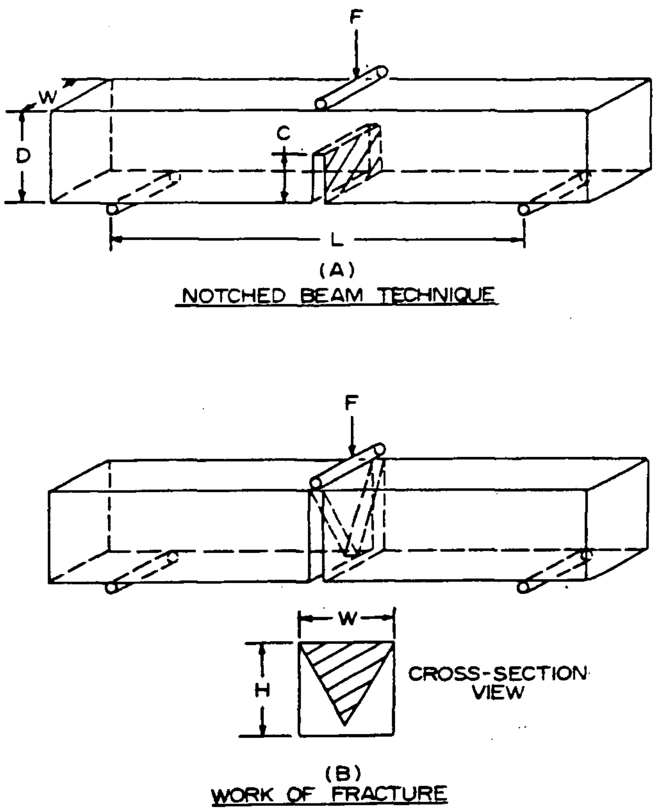

Figure 2.2 Typical specimens for (A) notched beam and (B) work of fracture surface energy determinations (after reference 23)

multiphase materials such as refractories is often part transgranular and part intergranular[23]. In general, the surface energy per unit area varies along the length of the fracture path. In the theoretical derivations which follow the variable γ refers to average surface energy per unit area. Unless otherwise stated, reported values were measured by the work of fracture method.

2.3.2 Early Work

In his first attempt at thermal shock damage analysis, Hasselman (1963)[45] considered the sphere subjected to thermal shock by heating and stated, without presentation of the elementary steps, that for such a case the total elastic strain energy at fracture U_f is given by

$$U_f = \frac{4\pi b^3 \sigma_f^2 (1-\nu)}{7 E} \tag{2.10}$$

where b is the radius and σ_f is the tensile fracture strength. Based on the premise that extent of crack propagation is directly proportional to the elastic strain energy stored at fracture and inversely proportional to the effective surface energy, he derived the thermal shock damage resistance parameters R''' and R'''', where

- 27 -

$$R''' = \frac{E}{\sigma_f^2\ (1-\nu)} \tag{2.11}$$

and

$$R'''' = \frac{E\ \gamma_{eff}}{\sigma_f^2(1-\nu)} \tag{2.12}$$

Nakayama and Ishizuka (1966)[47] tested a number of commerical refractories and, in support of the Hasselman treatment, found a correlation between R'''' and thermal shock damage as represented by the number of cycles to produce a given percentage weight loss. Clarke, Tattersall, and Tappin (1966)[48] derived a parameter which showed damage resistance to be proportional to γ and inversely proportional to elastic strain energy density in the region of fracture. However, no expression was given for strain energy density.

Davidge and Tappin (1967)[49] subjected a variety of ceramic materials to thermal shock via water quenching and found a direct correlation between the quenching temperature difference required to produce cracking and the Kingery R parameter. With regard to damage of alumina they reported that, scatter aside (see Figure 2.3), the fracture strength was constant up to a critical quenching temperature whereupon it abruptly fell to a much reduced value from which it decreased gradually with increasing quenching temperature difference.

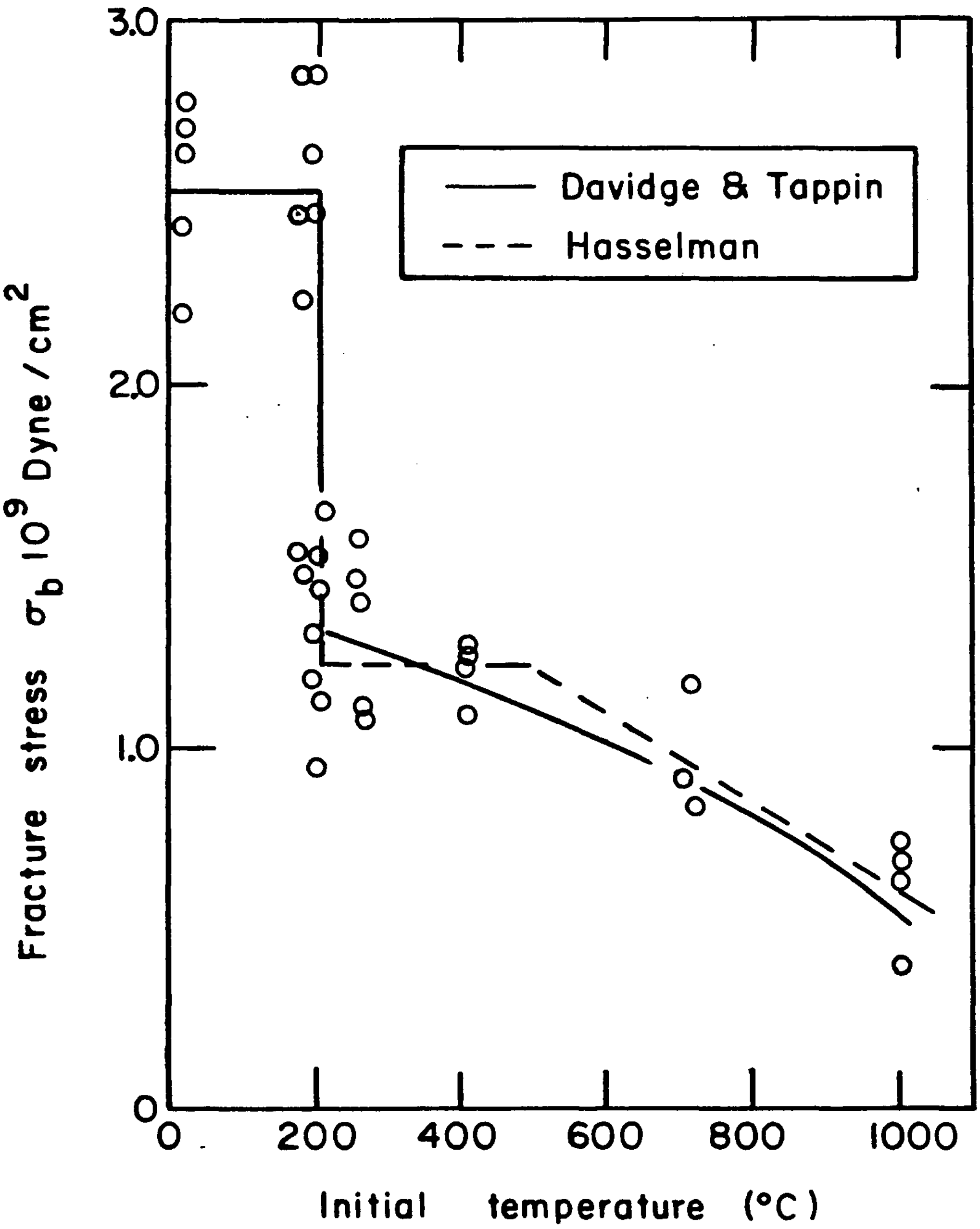

Figure 2.3 Fracture stresses of Al_2O_3 quenched from various temperatures into water at 20°C (after reference 49)

Ainsworth and Moore (1969)[50] also encountered significant scatter in the results of their study of the thermal shock behaviour of water-quenched Al_2O_3. Figure 2.4 shows the magnitude of scatter and the their interpretation of the overall trend of strength loss with increasing thermal shock.

2.3.3 Unified Theory

Hasselman (1969)[51] first developed a unified theory of thermal shock fracture initiation and crack propagation for the case of the fully-restrained, arbitrarily-shaped solid which is uniformly cooled through temperature difference (ΔT). Using the same approach (1971)[52], he then considered a uniaxially-restrained rectangular plate subjected to the same thermal conditions. The approach was adopted from the work of Berry (1960)[53-54] who was interested in the kinetic aspects of the Griffith criterion under both constant stress and constant deformation mechanical loading conditions.

The fundamental assumptions of both treatments are: (i) the sole driving force for crack propagation in thermally-shocked traction-free bodies is the elastic strain energy at fracture, (ii) fracture behaviour in the thermal loading traction-free case is analogous to the mechanical loading constant deformation case considered by Berry[54], (iii) the influence of flaws on fracture behaviour can be

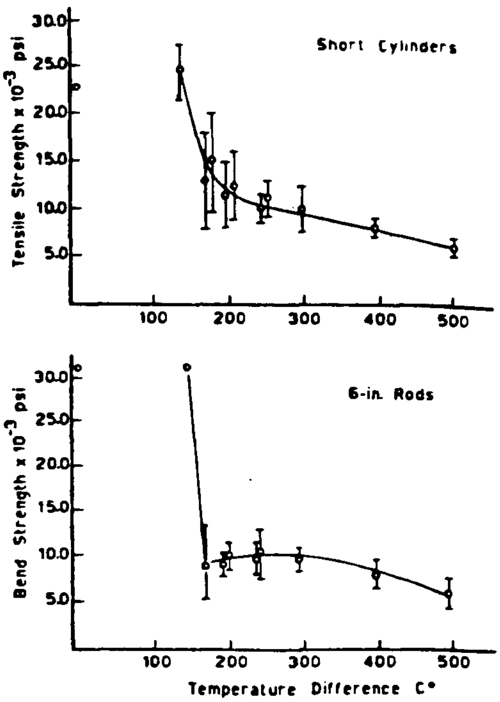

Figure 2.4 Strength behaviour as a function of thermal shock temperature difference (after reference 50)

accounted for by using the concept of effective Young's modulus, E_{eff}; (iv) the presence of a crack does not influence the stress field of neighbouring cracks, (v) the body possesses a uniform distribution of equal-sized cracks of crack density N where N is the number of cracks per unit volume, (vi) and crack propagation occurs by the simultaneous equal advancement of each crack.

The derivation consists of developing an expression for the total energy per unit volume - elastic strain energy plus surface energy - and then applying the Griffith criteria to arrive at an expression for the condition of crack instability. In the first case, rigidly constraining and uniformly cooling the body produces the uniform state of triaxial tensile stress[55] (in a homogeneous body) given by

$$\sigma = \frac{\alpha E \Delta T}{(1-2\nu)} . \tag{2.13}$$

The body is assumed to contain a uniform distribution N of penny-shaped cracks[56], with the effective elastic modulus being given by[57]

$$E_{eff} = E \left[1 + \frac{16 \ (1-\nu^2) \ Nc^3}{9 \ (1-2\nu)} \right]^{-1}, \tag{2.14}$$

where E is the elastic modulus of the crack-free material and c is the crack radius.

According to the concept of effective elastic modulus, the presence of flaws reduces the elastic modulus of the flaw-free material. The strain energy density U_o for the Hasselman flaw model, given by

$$U_o = \frac{3\sigma^2}{2E} \qquad (2.15)$$

for the flaw-free case, is obtained by replacing E in (2.13) and (2.15) with E_{eff} to yield

$$U_o = \frac{3\ (\alpha\Delta T)^2\ E}{2\ (1-2\nu)}\ [1 + \frac{16\ (1-\nu^2)\ Nc^3}{9\ (1-2\nu)}]^{-1} \qquad (2.16)$$

Total energy per unit volume is then given by

$$W_t = \frac{3\ (\alpha\Delta T)^2\ E}{2\ (1-2\nu)}\ [1 + \frac{16\ (1-\nu^2)\ Nc^3}{9\ (1-2\nu)}]^{-1} + 2\pi Nc^2\gamma \qquad (2.17)$$

and the Griffith criterion,

$$\frac{dW_t}{dc} = 0, \qquad (2.18)$$

applied to (2.17) to yield the following expression for crack instability:

$$\Delta T_c = \left[\frac{\pi \gamma \ (1-2\nu)^2}{2 E \ \alpha^2 \ (1-\nu^2) \ c}\right]^{\frac{1}{2}} \left[1 + \frac{16 \ (1-\nu^2) \ Nc^3}{9 \ (1-2\nu)}\right] \qquad (2.19)$$

where ΔT_c is the critical temperature difference associated with crack instability.

The Hasselman treatment of the flat plate case and the Berry analysis are completely analogous. Berry considered crack propagation in an infinite sheet of unit thickness which contains a central crack of initial length 2c and is subjected to mechanical loading conditions of constant stress and constant strain. He demonstrated that in order to produce crack growth the applied stress must be increased to a higher value (σ_c) than the theoretical value given by the Griffith criterion (σ_g), as at the lower critical value of σ_g both the initial velocity and initial acceleration are zero; and that the resulting kinetic crack behaviour is dependent on the difference between σ_c and σ_g.

Following Griffith[58], the stress-strain relationship of such a material is

$$\sigma = \frac{AE\varepsilon}{(A + 2\pi c^2)}, \qquad (2.20)$$

from which the effective elastic modulus is seen to be

$$E_{eff} = \frac{E}{(1 + \frac{2\pi c^2}{A})}, \tag{2.21}$$

where A represents the infinite area of the shape. Combining (2.20) with the Griffith expression

$$\sigma_g^2 = \frac{2E\gamma}{\pi c}, \tag{2.22}$$

by eliminating c yields

$$\varepsilon_g = \frac{\sigma_g}{E} + \frac{8E\gamma^2}{A\pi\sigma_g^3}, \tag{2.23}$$

where expression (2.23) defines the Griffith locus which is the combination of stresses and strains satisfying both the Griffith fracture criteria and the linear stress-strain law given in equation (2.20).

The shape of the Griffith locus is indicated by the solid line in Figure 2.5. While both σ_g and E_{eff} decrease continuously with increasing crack size, the ultimate strain (ε_g) passes through a minimum which occurs at a value of initial crack length given by

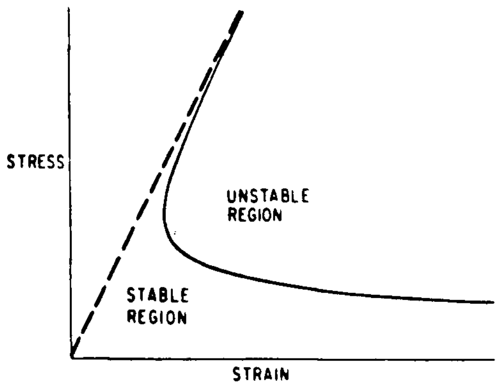

Figure 2.5 Griffith locus for fracture in tension (after reference 53).

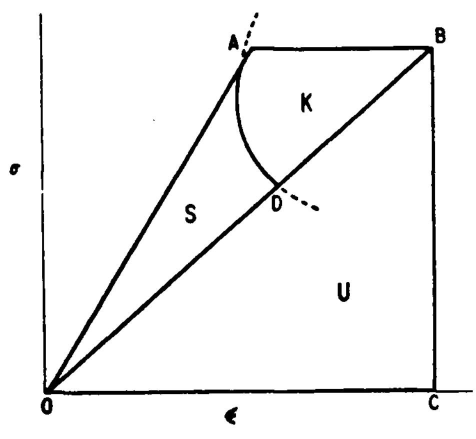

Figure 2.6 Distribution of energy in a tensile fracture process (after reference 53).

$$c_{min} = \left(\frac{A}{6\pi}\right)^{\frac{1}{2}} \tag{2.24}$$

The Griffith locus delineates the region of crack stability below the curve from the region of instability above.

Figure 2.6 is a qualitative representation of the energy balance for the tensile fracture process in which a sample is extended to fracture and the ultimate stress maintained constant as the crack increases in length. Line OA represents the stress-strain curve of the original sample. At a later arbitrary stage - point B - the work performed on the system is given by area OABC and the line OB represents the stress-strain curve for the sample with increased crack length. At this point the strain energy U of the system is given by area OBC; the part of the work expended as surface energy S by area OAD; and the kinetic energy K by the remaining area ABD. It is apparent that for this case catastrophic failure will always result as the kinetic energy of the system, at a minimum only at the instant of fracture initiation, increases with increasing crack length.

For the constant strain case, on the other hand, the mode of fracture behaviour is dependent on the relative sizes of initial crack length and c_{min}. For small initial crack length ($c < c_{min}$) the effective modulus is relatively high (as indicated by the steep slope of line OA in Figure 2.7 and the Griffith condition is satisfied (point A) on the part of the locus where the slope is positive. The various stages of crack growth under constant strain conditions can be traced along the line AG.

As crack length increases on moving through the region of instability (AC), the effective modulus decreases while the kinetic energy of the system increases. At point A the stress and initial crack length first satisfy the Griffith condition and K is zero. At point B the kinetic energy is given by area ABE, and the increase in surface energy associated with the increase in crack length by the area OAE. At point C, where the stress and crack length again satisfy the Griffith condition, the kinetic energy is at a maximum (AEC). Thus the crack continues to advance from C, with the surface energy increasing at the expense of both kinetic and strain energy, to point F where the crack stops and the kinetic energy is zero. At F the system possesses only strain energy (OFG) and surface energy (OAECD) and the crack is now subcritical. The crack reaches a point of instability when the stress reaches a value corresponding to that of point D.

For large cracks ($c > c_{min}$) the stress-strain curve is less steep and the Griffith criterion is satisfied on that part of the locus where the slope is negative (see Figure 2.8). Following the same reasoning, if the strain is held constant at a value of ultimate strain

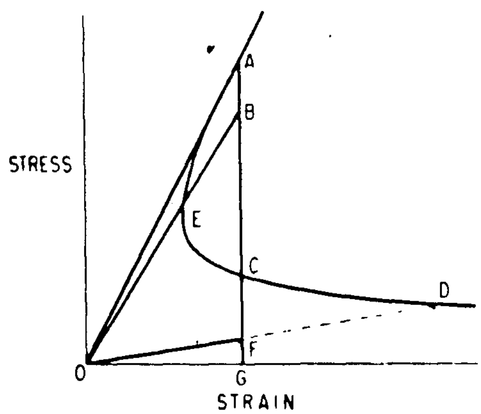

Figure 2.7 Behaviour of a small crack in a tensile sample (after reference 54).

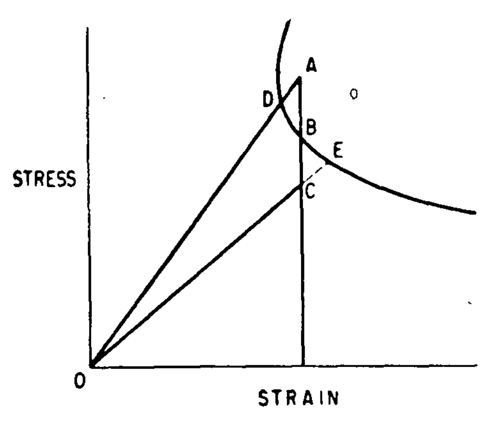

Figure 2.8 Behaviour of a large crack in a tensile specimen (after reference 54).

corresponding to that of point A, crack growth will proceed until the kinetic energy, which reaches a maximum (ADB) at point B where the Griffith criterion is satisfied, goes to zero at point C. Thus, for the large crack case, extent of crack propagation is primarily dependent on the amount by which the Griffith stress is exceeded.

The correspondence of the Berry constant deformation case with the Hasselman plate model - and some of the limitations of the latter - are at once apparent if the following manipulations of the Berry equations are made prior to discussing the plate model. Equations (2.20) and (2.22) can be combined with the elimination of σ to produce

$$\varepsilon_g = \left(\frac{2\gamma}{\pi E c}\right)^{\frac{1}{2}} \left(1 + \frac{2\pi c^2}{A}\right), \tag{2.25}$$

the Griffith locus in terms of critical strain and initial crack length. For short cracks $\left(\frac{2\pi c^2}{A} << 1\right)$, equation (2.25) reduces to

$$\varepsilon_g = \left(\frac{2\gamma}{\pi E c}\right)^{\frac{1}{2}} \tag{2.26}$$

and, for long cracks ($2\pi c^2 >> A$), it can be approximated with

$$\varepsilon_g = \left(\frac{8\pi\gamma c^3}{EA^2}\right)^{\frac{1}{2}} \qquad (2.27)$$

Berry determined the kinetic energy of the system at constant strain of arbitrary crack length c greater than initial length c_o to be

$$K = \frac{A^2E\varepsilon^2}{2}\left[\frac{1}{A + 2\pi c_o^2} - \frac{1}{A + 2\pi c^2}\right] - 4\gamma(c - c_o) \qquad (2.28)$$

An approximation for the final crack length c_f of the small crack case is obtained by setting K = 0 and assuming that $(A+2\pi c_o^2)^{-1} >> (A+2\pi c_f^2)^{-1}$ to give

$$4\gamma\ (c_f - c_o) = \frac{A^2\ E\ \varepsilon^2}{2}\ (A + 2\pi c_o^2)^{-1} \qquad (2.29)$$

Substituting equation (2.25) for ε and taking $2\pi c_o^2 << A$ yields

$$c_f = \frac{A}{4\pi c_o} \qquad (2.30)$$

The Hasselman flat plate thermal shock[52] model is now considered in some detail. As indicated in Figure 2.9 the physical model consists of a flat plate of crack density N cracks/unit area with all equal-sized cracks oriented perpendicular to the direction of

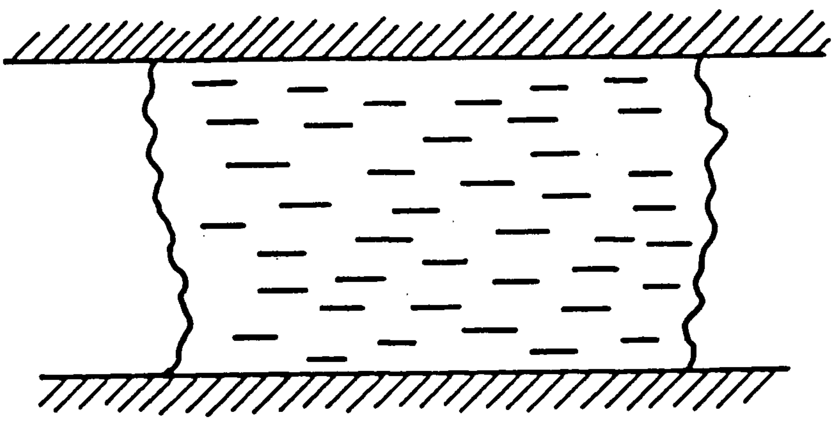

Figure 2.9 Mechanical model for analysis of thermal stress crack stability (after reference 52).

constraint. The plate is uniformly cooled through temperature difference (ΔT) to produce a state of uniaxial tensile stress of $E\alpha\Delta T$ and, for simplicity, the transverse strains are taken equal to zero. In addition to being more applicable to the industrial lining problem, this model is completely analogous to the Berry analysis.

Hasselman followed the same procedure as for the arbitrary three-dimensional shape model. For this case, the effective modulus is

$$E_{eff} = E\ (1 + 2\pi Nc^2)^{-1}, \qquad (2.31)$$

the total energy per unit volume is

$$W_t = \frac{\alpha^2(\Delta T)^2 E}{2\ (1+2\pi Nc^2)} + 4\gamma cN, \qquad (2.32)$$

and, following differentiation, the Griffith locus for crack instability for the thermal shock case is found to be

$$\Delta T_c = \left(\frac{2\gamma}{\pi\alpha^2 Ec}\right)^{1/2} (1 + 2\pi Nc^2) \qquad (2.33)$$

The form of the locus is indicated by the solid lines in Figure 2.10a, where loci for two crack densities ($N_1 > N_2$) are shown.

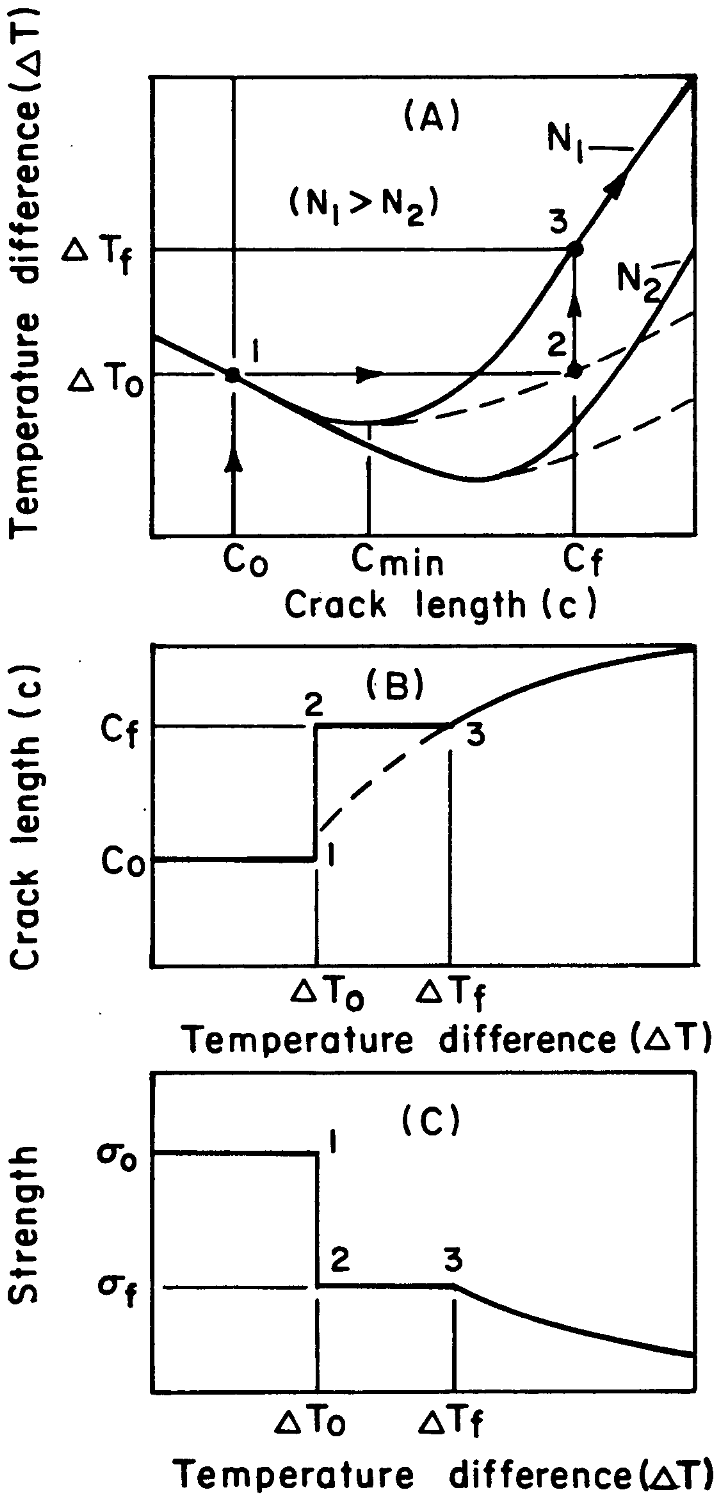

Figure 2.10 Thermal stress crack stability and catastrophic propagation behaviour for constrained plate with N cracks per unit area (after reference 88).

Hasselman argued that the critical temperature difference required to produce crack instability ΔT_c was only dependent on N for large cracks, since for small cracks the condition $2\pi Nc^2 \ll 1$ holds and equation (2.33) reduces to

$$\Delta T_c = \left(\frac{2\gamma}{\pi\alpha^2 Ec}\right)^{1/2} \tag{2.34}$$

For long cracks he assumed that the condition $2\pi Nc^2 \gg 1$ is valid and that ΔT_c could be approximated by

$$\Delta T_c = \left(\frac{8\pi\gamma N^2 c^3}{\alpha^2 E}\right)^{1/2} \tag{2.35}$$

The transition between long and short cracks occurs at the minimum in the instability curve which is given by

$$c_{min} = \left(\frac{1}{6\pi N}\right)^{1/2} \tag{2.36}$$

The final crack length c_f for the short crack length case ($c < c_{min}$) is approximated by

$$c_f = \frac{1}{4\pi Nc} \tag{2.37}$$

and indicated by the dotted lines in Figure 2.10a.

The unified theory was so-named because both resistance to fracture initiation and resistance to damage parameters could be derived using the same model. For a given crack density and initial crack size, it is clear from equation (33) that the magnitude of ΔT_c required to produce crack instability - the resistance to fracture initiation - is directly proportional to what Hasselman termed the "thermal stress crack stability parameter" R_{st} where

$$R_{st} = \left(\frac{\gamma}{\alpha^2 E}\right)^{1/2} \tag{2.38}$$

The thermal shock damage resistance parameter R'''' (minus the Poisson's ratio term) is obtained by substituting c as defined by the Griffith expression into equation (2.37) to produce

$$c_f = \frac{\sigma_f^2}{8E\gamma} , \tag{2.39}$$

where σ_f is the Griffith fracture strength. It is then argued that maximum thermal shock resistance corresponds to minimum c_f which occurs when $E\gamma/\sigma_f^2$ is a maximum. Thus the final crack length is directly proportional to the inverse of the damage resistance parameter,

$$c_f \propto (R'''')^{-1} \tag{2.40}$$

The correspondence of the Hasselman plate model and the Berry constant deformation case is demonstrated as follows. The thermal shock condition produces a constant strain of magnitude

$$\varepsilon = \alpha\Delta T. \tag{2.41}$$

Hasselman's equations can be obtained directly by replacing the terms ε and $1/A$ in Berry's expressions by the thermal strain $\alpha\Delta T$ and crack density N, respectively. The correspondence of the two treatments, not highlighted in the Hasselman papers, is extremely useful when evaluating the model predictions with regard to thermal shock-strength loss relationships and the significance of a term such as crack density N which has as its counterpart in the constant deformation analysis the inverse of an infinite area.

2.3.4 Thermal Shock-Strength Loss Predictions

Hasselman applied the unified theory to the interpretation of thermal shock experimental results of the type shown in Figures 2.3 and 2.4. Using the thermal shock form of the Griffith locus of crack instability as a starting point, he arrived at the theoretical prediction of thermal shock-strength loss behaviour shown in Figure 2.10c. The characteristic feature of the theoretically-predicted strength loss curve is the constant strength plateau.

According to the Hasselman rationale, the constant strength plateau is only observed for certain cases of initial crack size and crack density. With reference to Figure 2.10a consider a material of crack density N_1 and initial size c_o that is subjected to progressively severe thermal shock. The heavy solid lines indicate the locus of crack instability and the dotted lines show the approximation for the final crack length for the small-crack case. As ΔT is increased (moving up the vertical line at c_o in Figure 2.10a there is no change in crack length (Figure 2.10b) until the critical value ΔT_o at point 1 on the locus is reached. The initial crack length c_o is subcritical with respect to all temperature differences over the range $\Delta T < \Delta T_o$ and thus crack length (Figure 2.10b) and strength remain constant (Figure 2.10c) until ΔT_o is reached.

At T_o small-crack fracture behaviour occurs and the crack rapidly attains its final length c_f at point 2. The specimen is now subcritical with respect to ΔT_o. In fact crack propagation will not occur until the temperature difference reaches the value of ΔT_f at point 3. Thus, for a specimen with crack length c_f, increasing the thermal shock from ΔT_o to ΔT_f (moving up the vertical line at c_f in

Figure 2.10a from point 2 to 3) causes no change in crack length (Figure 2.10b) or strength (Figure 2.10c). For $\Delta T > \Delta T_f$ long-crack behaviour or quasi-static propagation occurs with the crack length increasing and strength decreasing gradually in the range $\Delta T > \Delta T_f$.

The sudden decrease in strength and the constant strength plateau are associated with small-crack ($c < c_{min}$) specimens only. This behaviour is commonly referred to as kinetic or catastrophic thermal shock fracture behaviour. As indicated for the Berry constant strain case, the plateau arises because - due to kinetic energy considerations - crack growth exceeds that associated with satisfaction of the Griffith condition, with the result that the extended crack becomes subcritical with respect to the thermal shock that produced it. Furthermore, it is clear from the nature of the curves in Figure 2.10a that the smaller the initial crack size - i.e. the stronger the material - the higher the thermal shock required for fracture initiation, but the greater the resulting crack extension, or strength loss.

On the other hand, for long-crack ($c > c_{min}$) specimens, strength decreases smoothly with increasing ΔT. Crack propagation occurs in a quasi-static or subcritical manner with growth being dependent on the magnitude of ΔT. The key factor with regard to mode of fracture is the size of the initial crack relative to c_{min}. According to equation (2.36) the minimum in the crack instability locus is dependent only on crack density N. For severe thermal environments Hasselman noted that materials with high densities of long cracks may be preferable to strong materials with short cracks.

2.3.5 Experimental Confirmation

The Hasselman theoretical treatment has motivated much experimental work. In addition to the strength loss-thermal shock experiments, where similar specimens are exposed to progressively severe thermal environments and then subjected to a strength test, investigations concerned with the assessment of relative thermal shock damage resistance of materials with different thermal and mechanical properties have been performed. In the latter case, numerous positive correlations between some indicator of damage (usually strength loss) and the Hasselman parameters, R'''' and R_{st}, have been accepted as additional corroboration of the Hasselman analysis.

For his first model[51] Hasselman used the results of Davidge and Tappin[49] as experimental support for the theoretically-predicted strength loss relationships. The solid line in Figure 2.3 indicates the Davidge and Tappin interpretation and the dotted line the Hasselman interpretation of the strength loss trend. The degree of scatter, which is characteristic of this type of experiment, unfortunately permits some licence in determining the trend. The majority of data points are concentrated about the point at which the initial strength decreases abruptly - the only obvious discontinuity in the trend - in order to satisfactorily delineate the critical temperature difference and extent of strength loss. Neither Davidge and Tappin[49] nor Ainsworth and Moore[50] indicated their suspicion as to the presence of another discontinuity in slope in the strength loss relationship.

Hasselman (1970)[60] offered the experimental results shown in Figure 2.11 in support of his hypothesis, and Gupta (1972)[61] provided the first independent experimental evidence (Figure 2.12). While these results seem to corroborate predicted behaviour, other experimental results are not as supportive, particularly with regard to the existence of the constant strength plateau. For example, other types of trends are seen in Figure 2.13 which gives results for the quenching of alumino silicate cylinders into silicone oil[62] and Figures 2.14 and 2.15 show results for the water quenching of silicon carbide specimens[63-64]. The trend in Figure 2.13 is due at least in part to the development of residual stresses during the thermal shock. Figure 2.15 is illustrative of the nature and magnitude of scatter generally associated with this type of experiment.

On the industrial side, those interested in the thermal shock performance of refractories have subjected various-sized specimens of

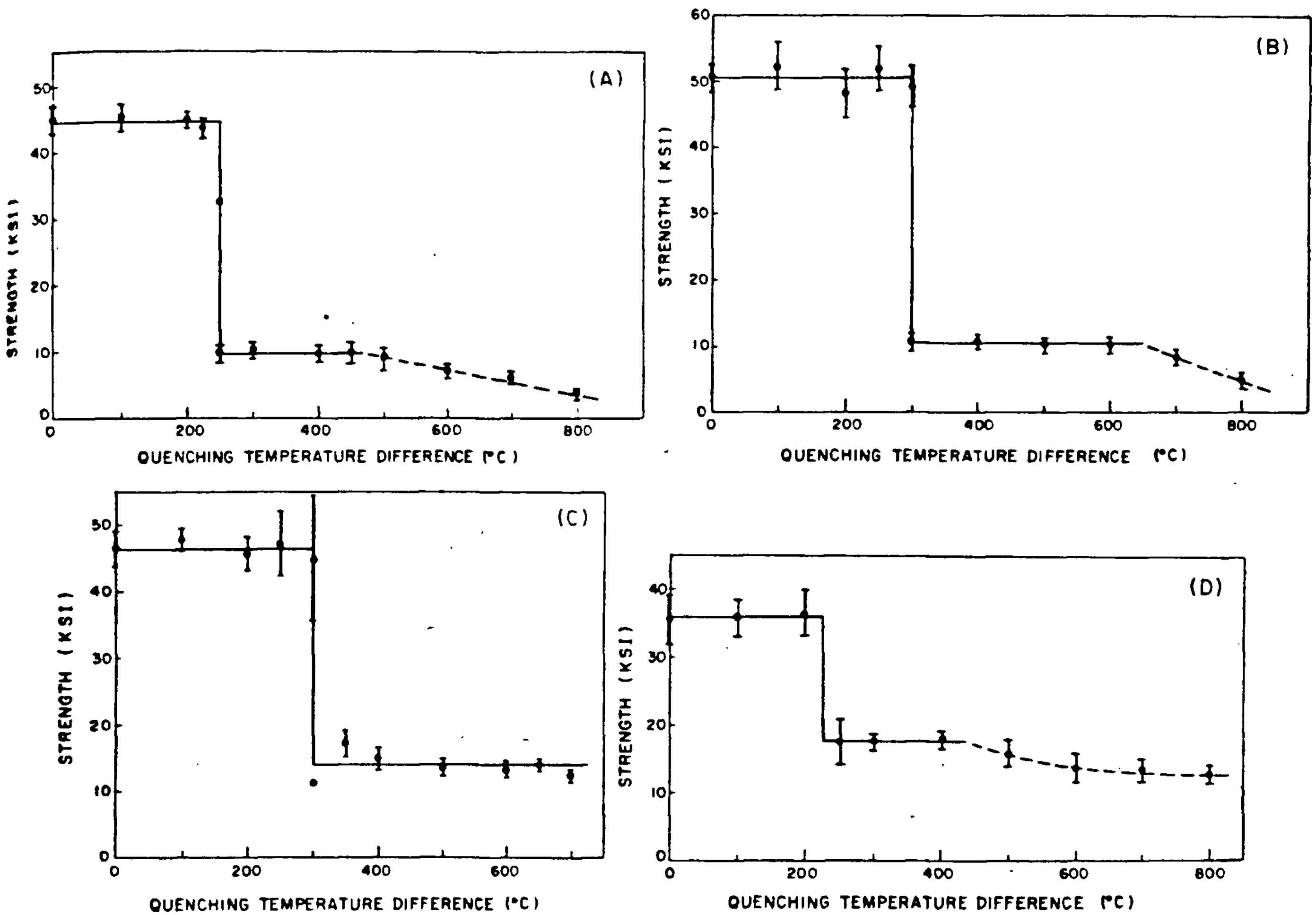

Figure 2.11 Strength as a function of quenching temperature difference for alumina rods (A) AD-94, 0.375 in. in diameter; (B) AD-94, 0.187 in. in diameter, (C) AD-94, 0.080 in. in diameter, and (D) AL-300, 0.195 in. in diameter. (Error bars denote standard deviation.) (After reference 60.)

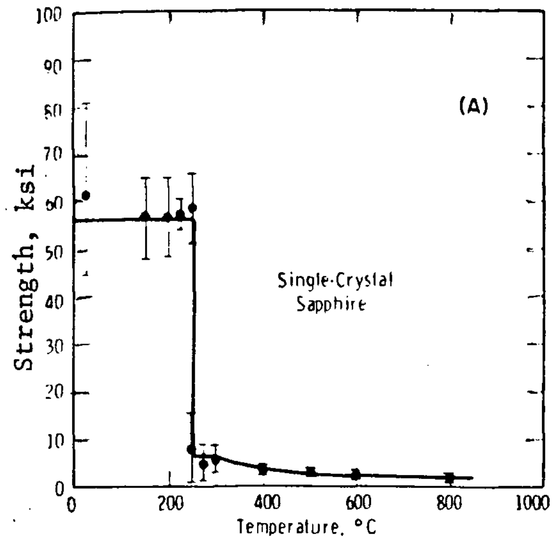

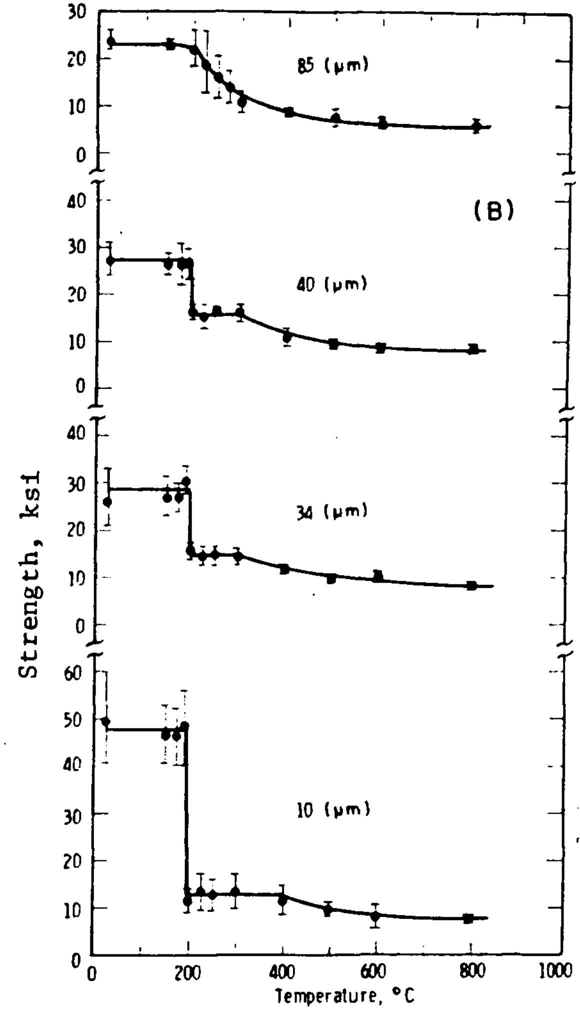

Figure 2.12 Room-temperature moduli of rupture of (A) sapphire and (B) polycrystalline Al_2O_3 as a function of quenching temperature (after reference 61).

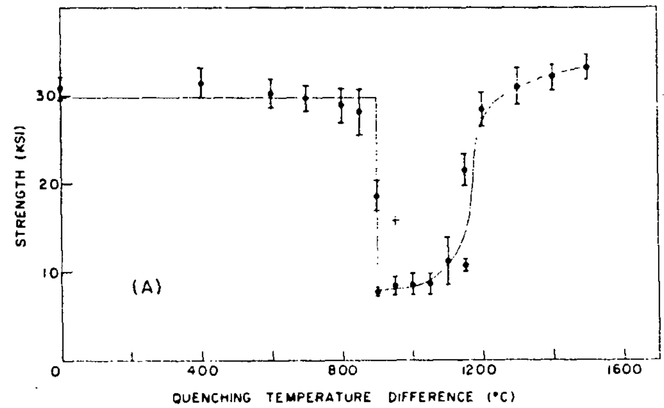

Figure 2.13 Room-temperature strength of alumino-silicate rods quenched in silicone oil (after reference 62)

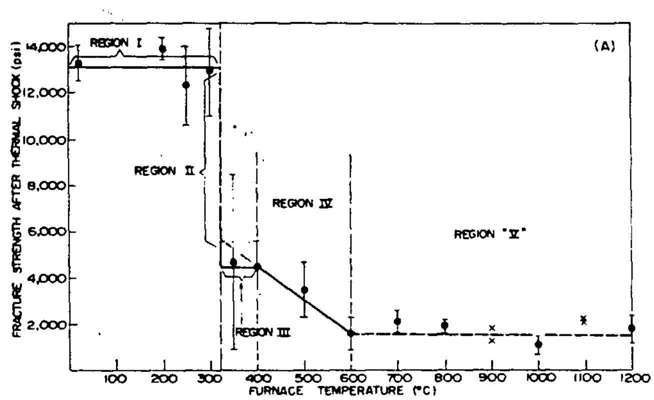

Figure 2.14 Changes in fracture strength with increasing severity of thermal shock for SiC (after reference 63)

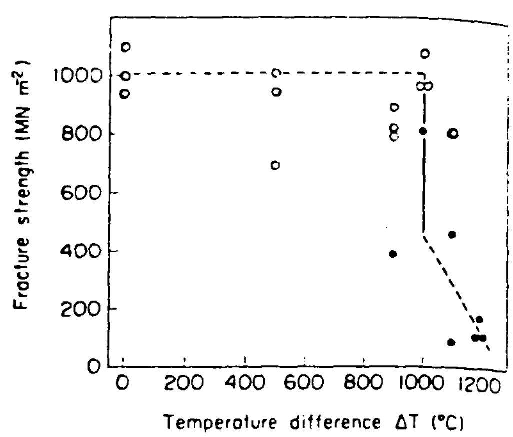

Figure 2.15 Fracture strength of the specimen after water quenching; o no cracks after quenching, • cracked after quenching (after reference 64)

different products to a variety of thermal environments and reported positive correlations of extent of damage - as indicated by weight loss, percentage strength or elastic modulus retained, and acoustic emission counts - with the parameters R'''' and R_{st} [65-71].

Hasselman[60] derived an expression for strength retained after thermal shock. Assuming that the temperature distribution at fracture is parabolic and that the elastic energy at fracture (W) of an infinite cylinder of radius b is

$$W = \frac{0.57\ S_t^2\ b^2}{E}, \tag{2.42}$$

where S_t is the strength before thermal shock, he went on to derive the following expression for strength after thermal shock (S_a):

$$S_a = \left(\frac{8\gamma_1\gamma_2^2 E^3 N_s}{S_t^2\ b}\right)^{1/4} \tag{2.43}$$

where γ_1 and γ_2 are the fracture surface energies per unit area corresponding to the thermal shock and strength testing environments, respectively, and N_s is the crack density. Experimental results for two rod sizes were in agreement with the predicted size dependence. Notable by their absence from (2.42) and (2.43) are the thermal properties of thermal conductivity, thermal diffusivity, and thermal expansion coefficient, terms naturally associated with a thermal shock problem.

Glenny and Royston (1958)[72], Gupta (1975)[73], and Becher et al (1980)[74] have also reported on the size effect observed on water quenching alumina specimens. As specimen size increases, both the temperature difference required to initiate fracture and the strength retained after fracture were found to decrease. While the influence of size on thermal profiles, stress fields, total strain energy at fracture, and flaw distribution has been cited in various studies, no quantitative analysis has been presented which accounts for the influence of geometry on thermal shock behaviour.

2.4 Flaws, Fracture Strength, and Failure Criterion

Stress intensity factor and Weibull statistical analysis are two other approaches to the thermal shock problem which have been employed to account for the flaw-dependence of fracture strength of brittle engineering materials. The former is based on the fact that the stress field in the region near an ideal crack is characterized by a stress singularity at the crack tip which decreases in proportion to the inverse square root of the distance from the crack. The stress intensity factor K is a measure of the singularity which is dependent on loading and specimen configuration. The onset of rapid fracture is taken to occur when K reaches a value of K_c, a material property termed critical stress intensity or fracture toughness.

This approach is most suitable for the fracture mechanics analysis of standard laboratory specimens of known crack geometry which are subjected to controlled loading. Evans[75-76] and Chandler[14] have discussed the application of this approach to simple thermal shock cases. The stress intensity factor analysis contains all of the assumptions of elastic analysis plus those associated with the size, shape, orientation, and location of the crack. It is unsuitable for the industrial lining problem as flaw distributions in refractory products are complex and unpredictable.

Unlike the other approaches in which the fracture criterion is explicitly stated - in terms of stress alone or a stress-flaw interaction - the Weibull approach[77] considers strength to be a statistical parameter. The general form of the Weibull distribution function is[78]

$$F = 1 - e^{-\int_V \left(\frac{\sigma-\sigma_u}{\sigma_o}\right)^m dV} \quad ; \quad \sigma > \sigma_u \qquad (2.44)$$

$$F = 0 \quad ; \quad \sigma \leqslant \sigma_u \qquad (2.45)$$

where F is the probability of failure of a component with stress field σ throughout the body, σ_u is a threshold stress which is usually taken to be zero, m is the Weibull modulus, and σ_o is a third material parameter. The derivation of this function is based on the weakest-link hypothesis which equates failure of a structure with that of the weakest member.

The Weibull theory highlights two points of relevance to the fracture behaviour of refractory products. The first is concerned with size effect prediction which, for the simple uniaxial tensile stress case, can be expressed quantitatively as

$$\frac{\sigma_1}{\sigma_2} = \left(\frac{V_2}{V_1} \right)^{1/m} \tag{2.46}$$

where σ_1 and σ_2 are mean fracture strengths of populations of specimens with volumes V_1 and V_2. The Weibull rationale for the size effect is that the probability is greater that a larger body contains a larger flaw than a smaller body given that the flaw distribution is the same in each.

Another consequence of the statistical treatment is that failure, while most likely to occur in regions of high stress, can occur at any point of non-zero stress. Failure will occur at some unknown point at which the stress-flaw interaction first reaches a critical value. It may be a point of high stress and innocuous flaw or of low stress and severe flaw or of some intermediate combination. Both of these points are significant in that the Weibull theory suggests that geometry, a fundamental design variable, plays a dual role in thermal shock fracture behaviour as it influences both the probability of finding a severe flaw and the nature and magnitude of the thermal stress field.

Stanley et al[79] summarize the most important assumptions of the Weibull analysis as follows:

(i) the material is isotropic and statistically homogeneous, i.e. the probability of finding a flaw of a given severity is the same throughout the volume the component,

(ii) once a crack has initiated it will propagate without further increase in load, resulting in fracture,

(iii) the contribution a flaw makes to the failure probability of a loaded component is independent of the position of the flaw in the body,

(iv) the three principal stresses at a general point contribute independently to the failure probability.

The validity of these assumptions is dependent on the nature of the particular problem being considered.

With regard to the industrial lining problem, assumption (i) is reasonable. While valid for applications like tensile and bend tests where fracture initiation is synonymous with failure, assumption (ii) is not as applicable in the case of thermal shock fracture of refractories; due to the crack arrest capability of such materials. The states of stress at surface and interior locations on heating and cooling for the one-dimensional rectangular beam and two-dimensional plane stress cases described in Appendix I and the three-dimensional case for conditions of traction-free boundaries and one-dimensional heat flow are summarized in Table II. While assumptions (iii) and (iv) are necessary from a computational standpoint the potential for peculiar fracture behaviour in individual cases exists due to the interaction of a complex multiaxial stress field with the random flaw distribution that is characteristic of a refractory product.

Two other aspects of importance to refractory materials are the relative values of tensile and compressive strength and the relative severity of surface flaws versus bulk or volume flaws. Kingery[7] states that since the compressive strength of ceramics is four to eight times the tensile strength, failure from compressive stresses is usually unimportant. In the Weibull computation the principal compressive stresses are usually discounted according to the ratio of compressive to

TABLE II

Stress States at Surface and Interior for Various Cases

Case	Heating		Cooling	
	Interior	Surface	Interior	Surface
3-dimensional	T-tension	B-compression	T-compression	B-tension
Plane Stress	B-tension	U-compression	B-compression	U-tension
1-dimensional (beam)	U-tension	U-compression	U-compression	U-tension

T - triaxial

B - biaxial

U - uniaxial

tensile strength. While surface and interior stresses should probably also be weighted, the influence of surface and volume flaws has not as yet been clearly established.

A statistical fracture criterion is inappropriate for use in a design problem such as the industrial lining problem where the number of independent parameters is large to begin with. In addition to highlighting the role of flaws in fracture behaviour, the main value of the Weibull analysis is in the statistical analysis of fracture strength data. The designer can then use the Weibull results and the desired probability of failure to determine an appropriate design strength for use in the thermoelastic analysis.

The maximum principal tensile stress fracture criterion - the most frequently encountered in thermal shock studies - is justified usually on the basis of mathematical convenience rather than appropriateness. The validity of multiaxial failure theories is generally demonstrated with experimental results obtained using thin-walled cylindrical tubes subjected simultaneously to internal pressure, uniaxial end load, and tension.

Experimental results for the biaxial stress state for a variety of materials are presented in Figure 2.16[80] where the horizontal and vertical axes represent the ratio of the biaxial principal stresses, σ_1

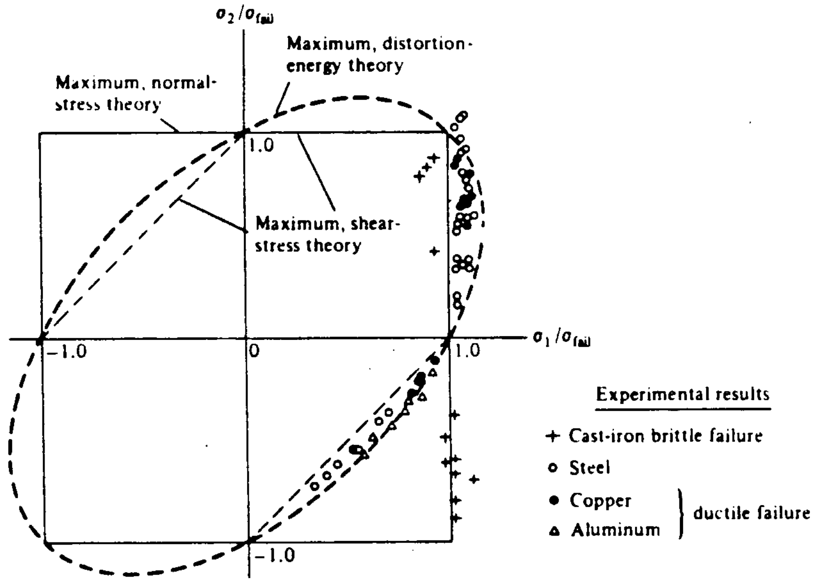

Figure 2.16 Experimental results for biaxial loading fracture tests (after reference 80)

and σ_2, to the uniaxial failure stress σ_{fail}. Figure 2.17 shows the stress state conditions and Figure 2.18 the results for similar experiments for alumina tubes[81]. The experimental evidence indicates that the maximum principal tensile stress fracture criterion appears to be reasonable for brittle materials subjected to general biaxial loading conditions.

2.5 Thermal Shock Testing

Thermal shock tests offer an alternative to the theoretical approach to the evaluation of thermal shock resistance. The standard thermal shock tests are the North American ASTM C38 Panel Spalling test, the British BS1902 Small Prism test, and the German DIN 51068 test. The Ribbon test[82] and the Modified Prism test[83] have been proposed as replacements for the ASTM C38 test. The main features and relative merits of each method are discussed.

The Panel Spalling test varies slightly depending on brick type but the essentials of the procedure are as follows. Test panels are constructed of full-size bricks, preheated to a specified temperature within 5-8 hours, maintained at that temperature for 24 hours, and then subjected to thermal cycling. For example, the procedure for super-duty fireclay brick calls for a preheat temperature of 1650°C and 12 spalling cycles of 20 minutes duration each. A thermal cycle consists of heating

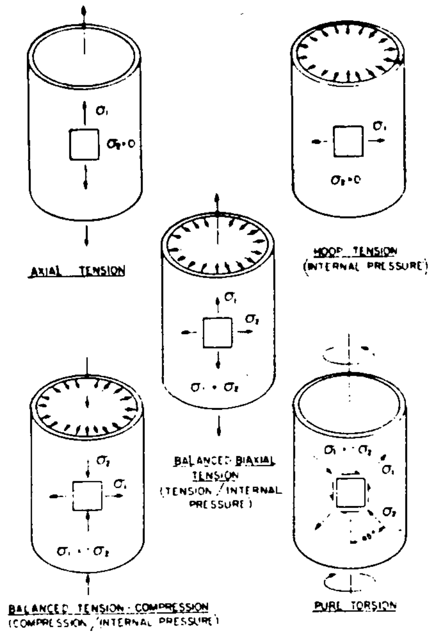

Figure 2.17 Stress state conditions examined for alumina tubes (after reference 81)

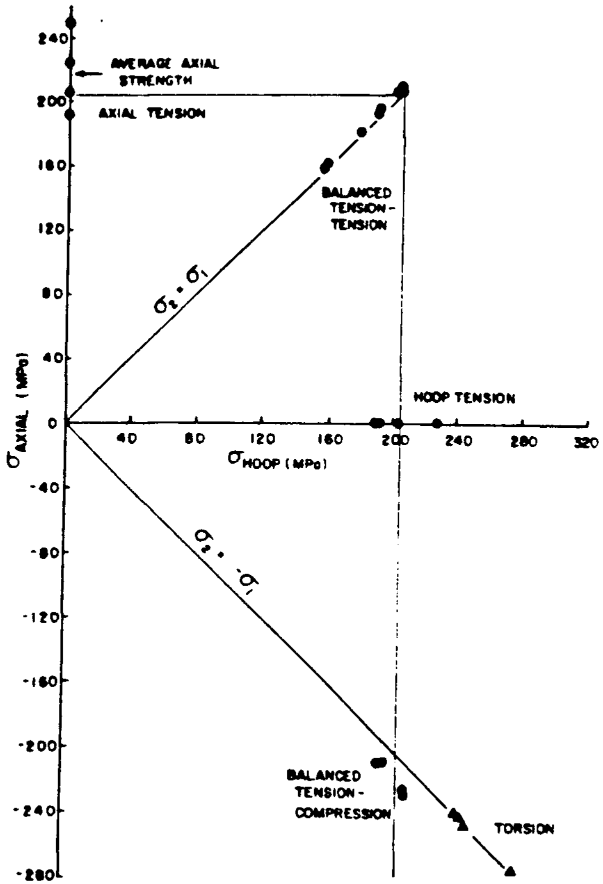

Figure 2.18 Results of multiaxial loading fracture tests for Al_2O_3 tubes (after reference 81)

the surface to 1400°C in 10 minutes and then cooling by air-water blast (8 min) and air blast (2 min). After cooling overnight the panel is dismantled. A trowel is use to dislodge broken pieces. Spalling behaviour is presented as percentage weight loss.

In the BS 1904 Small Prism test three specimens (2 in. square by 3 in.) are heated to test temperature in 30 minutes and then subjected to a number of 20 minute spalling cycles, 10 minutes of air cooling and 10 minutes of furnace heating. Towards the end of each cooling cycle the specimens are examined visually for cracks and loss of corners and then subjected to a mechanical loading via the rig shown in Figure 2.19. Test results consist of furnace temperature, number of cycles to failure, and the cycle at which cracks first appear.

The German DIN 51068 guidelines describe three types of tests. In one, cylindrical specimens are maintained at 950°C for 15 minutes, quenched into water and held for 3 minutes, and then dried at 110°C for 30 minutes. Spalling behaviour is determined as the number of cycles required to cause specimen separation or, alternatively, as gas permeability after a specified number of cycles.

In another a brick is inserted into the opening of a furnace set at 950°C in such a way that 1/3 of the brick projects into the furnace chamber and 1/3 of the brick is exposed to air. The brick is heated for

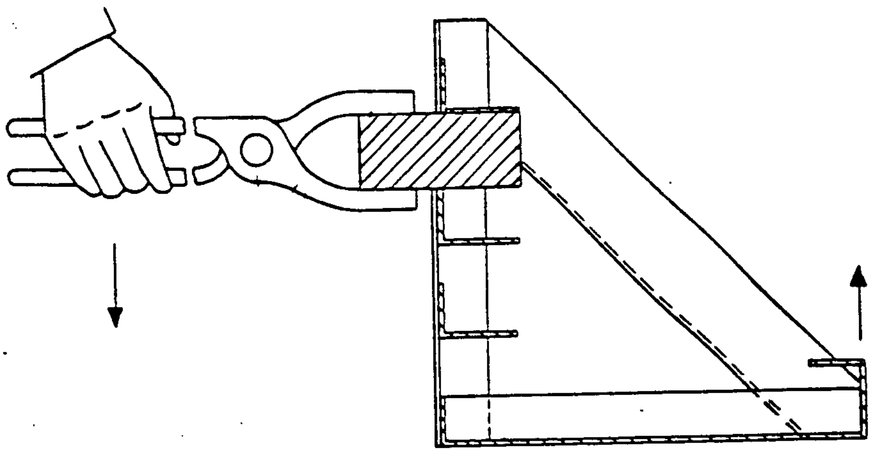

Figure 2.19 Test rig for spalling test (after reference 84)

50 minutes, quenched for 5 minutes in water, and air-cooled for 5 minutes. The test is complete when 50% of the hot end has spalled off, at which time the number of cycles corresponding to crack initiation, 25% loss, and 50% loss are recorded.

In the final test, samples (one-quarter of a brick) are preheated to 275°C prior to heating to 950°C in 45 minutes. After quenching by an air blast for 5 minutes, the specimen is subjected to a three-point bend test using a 3 kg load. The test is complete when the specimen fractures into two pieces or after 30 cycles.

In the Ribbon test specimens are heated on one face only by a fully-automated gas-fired line burner. One thermal cycle consists of 15 minutes of heating, during which time a hot face temperature of 1000°C is reached within 5 minutes and maintained for the duration of the heating stage, and 15 minutes of forced-air cooling. Test configuration permits variable specimen size. Thermal damage is assessed by noting the change in fracture strength or elastic modulus.

The Modified Prism Spalling test subjects the specimen to five thermal cycles, one cycle consisting of a 10 minute heating period in a furnace at 1200°C followed by 10 minutes of air cooling. From an initial specimen size of 6" x 1" x 1", a portion is used to measure the fracture strength and the remainder (2 1/2" x 1" x 1") is used as the test specimen. Thermal shock damage is expressed in terms of percentage strength loss.

The purpose of thermal shock testing is to provide a basis for material selection. In order that the basis be sound it is first necessary that test conditions simulate those of the industrial application, particularly with regard to (i) stress boundary condition, (ii) thermal environment (boundary condition, heating or cooling, temperature range), and (iii) geometry. These points are considered in turn.

The stress boundary conditions encountered during thermal shock testing - essentially traction-free - are industrially applicable for many processes. After experiencing thermal shock of sufficient magnitude to cause fracture, refractory specimens often will not separate cleanl y into fragments because of excellent crack arrest capability. Noting this, Clements[85] has suggested that much of the crack propagation in thermal shock tests attributed to thermal cycling may in fact be due to mechanical stresses as a result of scraping, bending, prying, dropping, steam generation during water quenching, or the lodging of dust or particles in existing cracks.

While the boundary conditions and temperature range on heating and cooling can vary widely from process to process or from processing stage to processing stage, a characteristic thermal feature is one-dimensional heat flow. Heat flow associated with the Prism and DIN tests is multi-dimensional and hence the nature of the thermal stress field causing fracture during these tests is expected to be different from that present in industrial linings.

A major limitation of all the thermal shock tests is that they employ thermal cycling to cause fracture. As the nature of the thermal stess field is different on heating from that on cooling, different fracture behaviour is expected during each stage. Also, depending on the process, more severe thermal loading is usually encountered during one stage than the other. It is quite conceivable that the results of a thermal shock test in which fracture is induced during the cooling stage may be used to select refractories for applications in which failure occurs primarily during the heating cycle.

As a final point the nature of the thermal stress field is also strongly dependent on geometry. Smaller specimens are generally used as a matter of convenience. The assumption is that the ranking of thermal shock resistance of a set of materials of one size will parallel that of another size of the same materials. While that may or may not be the case, the results of the thermal shock tests currently being used are not useful for design purposes or for optimizing thermal schedules of industrial process vessels.

Reproducibility is another important consideration. It is generally poor for the tests which utilize multi-dimensional thermal conditions and parameters such as weight loss and number of cycles to failure to characterize thermal damage. Furnace heating and air and water quenching, while easily accomplished in the laboratory, are difficult to characterize analytically and standardize experimentally.

Of the tests described, the Ribbon test has the greatest potential for simulating a variety of industrial conditions. Heat flow is one dimensional, thermal conditions are well-controlled, and specimen size is variable. Results in the form of percentage loss of strength or elastic modulus are relatively reproducible.

In summary, the philosophy behind thermal shock testing is to cause fracture and then to rank materials in terms of damage sustained. The implication of this approach is that fracture is unavoidable in the industrial application. While this strategy may be fine for comparative studies, it will not lead to the most efficient use of materials. Material optimization requires knowledge of the limits of a material. For the thermal shock application this means determining the most severe thermal condition which can be endured prior to fracture initiation.

2.6 Summary of the Literature

(1) Both theoretical and experimental studies indicate that thermal shock fracture behaviour of brittle, traction-free bodies is dependent on the combined effect of thermal and mechanical properties, geometry, and thermal boundary condition.

(2) The Kingery resistance to fracture initiation parameters, derived using dimensionless solutions for the maximum principal tensile stress of infinite slabs subjected to various thermal boundary conditions, account for the role of material properties only.

(3) The Kingery derivations neglect the transient aspect of the thermal shock problem with the result that the parameters R' and R" do not properly reflect the role of thermal conductivity and thermal diffusivity.

(4) The Kingery analysis does not account for the influence of geometry. It is limited to one-dimensional cases in which the width is at least twice the length.

(5) The Kienow analysis, in which a simple spring model is used to develop a procedure for determining safe heating rates, also does not account for the effect of geometry . The results of this derivation are limited to one-dimensional cases in which the width is much less than the length.

(6) More recent multi-dimensional thermoelastic analyses have indicated that the magnitude, location, and component of maximum principal tensile stress is strongly dependent on geometry. A major drawback of this approach is that conclusions and design recommendations are based on the results of a few select cases which may or may not

reflect general trends.

(7) In justification of such an approach in their study of the two-dimensional constant heating rate thermoelastic problem, Chang et al stated that the influence of the various parameters which affect the magnitude of thermal stress can not be readily expressed in dimensionless form as is common practice. As a consequence of not having a general solution at their disposal, Chang et al drew erroneous conclusions as to the effect of changes in thermal diffusivity and width on the maximum principal tensile stress.

(8) No general solution for either the maximum principal tensile stress or total strain energy of any multi-dimensional thermoelastic model of relevance to the industrial lining problem has been presented.

(9) Based on the premise that extent of crack propagation is directly proportional to strain energy at fracture and inversely proportional to surface energy per unit area, Hasselman used a thermoelastic sphere model to derive damage resistance parameters which indicate the role of material properties only. The derivation is based on an expression for total strain energy at fracture which can not be verified as the thermal boundary condition was not stated. It is also noteworthy that the strain energy expression contains neither of thermal expansion coefficient or thermal diffusivity, variables which are fundamental parameters of the thermal shock problem.

(10) The Hasselman unified theory of thermal shock behaviour is fundamentally unsound. In addition to the physical model of a restrained shape with a uniform distribution of equal-sized, non-interacting cracks being unrealistic, the analogy between the constant strain mechanical loading case of Berry and the traction-free thermal loading case is not valid as the nature of

the stress field at fracture is significantly different in each case. Furthermore, the analysis neglects the transient aspect of thermal stress development and thus does not account for the role of thermal diffusivity. Finally, the model in no way accounts for the observed effect of geometry on thermal shock behaviour.

(11) No theory of thermal shock fracture behaviour has been presented which satisfactorily explains experimental observations with regard to the influence of material properties, geometry, and thermal conditions on fracture initiation and extent of damage.

(12) Thermal shock resistance parameters useful for the design and selection of refractory structural components of linings of high-temperature industrial processes are not available in the literature.

Chapter 3

Statement of the Problem

In this work the thermal shock fracture behaviour of traction-free bodies is interpreted using thermoelastic analysis. The ultimate objective is the development of theoretical criteria which will assist in the design and selection of refractory components. The criteria are developed on the basis that a desirable operating strategy is to heat or cool a refractory lining component through a specified temperature range as rapidly as possible without causing fracture.

Two characteristic features of the thermoelastic models used for the analysis of previous experimental work and the development of theoretical criteria are one-dimensional heat flow and traction-free boundaries. The fundamental assumptions are that the material is homogeneous, isotropic, and possesses temperature-independent properties; displacements are small with respect to the geometry of the system; stress-strain behaviour is linear and elastic to fracture, and that the maximum principal tensile stress criterion is valid.

All of the cases considered are one-dimensional with respect to temperature and two-dimensional with respect to stress. The stress problem is a standard two-dimensional thermoelastic one in which the eight unknowns: the stresses ($\sigma_x, \sigma_y, \tau_{xy}$), the strains ($\varepsilon_x, \varepsilon_y, \gamma_{xy}$), and the displacements (u,v) satisfy two equilibrium equations (no body forces), three stress-strain relations, and three strain-displacement relations. The thermal stress field and total strain energy for particular cases are computed using a two-dimensional finite element model based on a displacement formulation with isoparametric 8-noded elements and Gauss quadrature numerical integration being used (see Appendix 1).

The remainder of this work consists of two sections. In Chapter 4 the thermoelastic approach to thermal shock fracture analysis is justified by theoretical analysis of previous experimental work. Constant heat transfer coefficient analytical temperature solutions are used to simulate the thermal shock conditions of experiments utilizing furnace radiative heating, water quenching, and flame heating. For this thermal boundary condition, the heat flux at the surface is directly proportional to a constant heat transfer coefficient (h) and the difference between ambient temperature and the surface temperature of the specimen (ΔT).

In Chapter 5 a two-dimensional constant heating rate model is used to develop both resistance to fracture initiation and resistance to damage parameters useful for the design and selection of refractory structural components for linings of high-temperature processes. For the constant heating rate thermal boundary condition case the hot face of the component increases linearly with time. Rectangular shapes are used to model both industrial lining components and specimens of the thermal shock experiments. In all cases heat flow is in the direction of the length and the width corresponds to the hot face.

A final important engineering consideration is the ease with which a parameter can be computed. Many of those involved in the design and selection of refractories and the establishment of thermal operating practice - from material scientists to refractory producers and material users - have neither the background in stress analysis nor the computer facilities required for complex evaluations. Therefore, another goal is to develop criteria which can be computed directly using tables.

To summarize, the two principal objectives of this work are:

1. To justify the use of thermoelastic analysis in thermal shock studies of brittle materials; and
2. To develop easily-computable theoretical resistance to fracture initiation and damage parameters.

Chapter 4

Strength Loss - Thermal Shock Relationships

4.1 Introduction

In this chapter the theoretical interpretation of strength loss-thermal shock relationships is considered. Three experimental investigations have been selected from the literature for detailed study. The cases, which have been chosen on the basis of relevance to the industrial lining problem, represent a range of refractories and thermal conditions. The theoretical interpretation of the experimental results is discussed from the standpoint of both the Hasselman and thermoelastic analysis approaches.

4.2 Previous Experimental Work

4.2.1 Introduction

The three studies which have been selected for detailed analysis are for convenience identified by principal author: (i) Nakayama, (ii) Larson, and (iii) Semler. The studies have been classified according to the nature of the thermal shock conditions. Both the Nakayama and

Larson investigations utilize symmetric heating or cooling conditions in which the hot and cold faces are subjected to identical thermal boundary conditions. The Semler study utilized non-symmetric conditions in which only one face is subjected to heating and cooling.

4.2.2 Symmetric Heating

4.2.2.1 Nakayama[86]

Noting that most thermal shock tests subject specimens to thermal cycling and also that there exist applications in which the fracture behaviour on heating only is of interest, Nakayama devised a single thermal shock by radiation heating test. Figure 4.1 illustrates the essential features of the thermal shock test. The procedure consisted of inserting the unit shown in Figure 4.1a, which consisted of two test specimens (2 x 2 x 7 cm) sandwiched between thermal insulation blocks, into an electric furnace preset at a specified temperature. After holding for approximately two minutes, the unit is slowly cooled to room temperature and the specimens are withdrawn and cut parallel to the heating surface (Figure 4.1b). The strength of each half is then measured using a three-point bend test (Figure 4.1c).

Six brands of commercial firebrick were tested. The brands were designated by letter and described as follows: (A) hard burned, dense

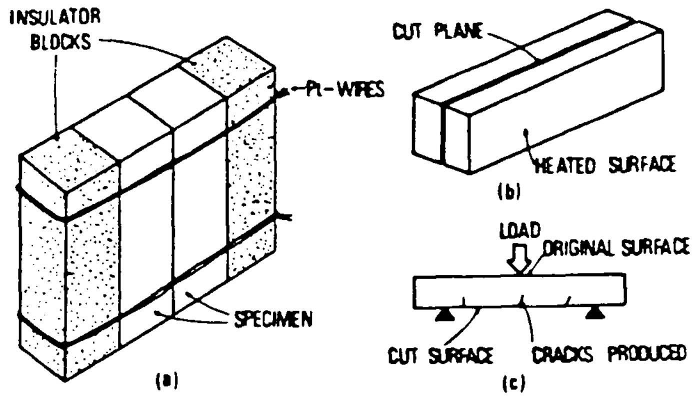

Figure 4.1 Schematic illustrations of (a) thermal shock specimen unit which is heated on both sides by radiation, (b) cutting direction in a specimen after thermal shock, and (c) strength measurement after cutting (after reference 86)

type aluminosilicate, (B) high alumina, clay bonded, (C) dense type aluminosilicate, (D) high alumina, spalling resistant, (E) high magnesia, direct bonded basic, and (F) chamotte fired to SK-34. Chamotte is a fireclay which contains a high percentage of grog. The physical properties are given in Table III. Three-point bend strength, elastic modulus by sonic wave velocity, and effective surface energy by the work of fracture method were measured at room temperature. Thermal expansion coefficients were determined over the range 25-500°C and thermal conductivity over the range 200-300°C.

The thermal shock test results for the six brands are given in Figure 4.2 in the form of curves of strength retained versus furnace radiation temperature. The critical radiation temperatures (T_{cr}) at which strength first decreases, the fraction of strength retained after thermal shock at the critical temperature (f_{sr}), and various thermal shock resistance parameters are given in Table IV. The parameters R'_{st} and critical stress intensity factor K_{IC} were computed using

$$R'_{st} = \left(\frac{k^2\gamma}{\alpha^2 E}\right)^{1/2} \qquad (4.1)$$

and

$$K_{IC} = (2E\gamma)^{1/2} \qquad (4.2)$$

In all cases but one, initial strength decreased abruptly at T_{cr} and

TABLE III

Properties of Refractories for Nakayama Study

Brick	σ_f (MPa)	E (GPa)	γ (J/m^2)	$\alpha \times 10^6$ ($°C^{-1}$)	k (J/sm°C)	$\sigma_f^* \times 10^3$ (ν=0.25)
A	25.8	74.2	40.1	15.5	2.9	0.261
B	20.0	55.7	48.6	3.5	1.3	0.269
C	14.2	31.9	44.7	15.5	1.3	0.334
D	16.0	47.6	39.1	3.5	1.3	0.252
E	22.0	91.3	49.6	12.6	9.2	0.181
F	4.8	10.4	41.2	8.5	1.0	0.346

TABLE IV

Summary of Results of the Nakayama Study

Brick	T_{cr} (°C)	f_{sr}	R' $(\frac{cal}{cm \cdot s})$	R'''' (cm)	R'_{st} $(\frac{cal}{cm^{1/2} \cdot s})$	K_{IC} $(Mpa \cdot m^{1/2})$
A	950	.13	.118	.59	.105	2.44
B	1050	.54	.230	.90	.253	2.33
C	850	.55	.065	.94	.072	1.69
D	1050	.65	.219	.96	.245	1.93
E	1100	.85	.315	1.25	.407	3.01
F	950	-	.102	2.48	.185	.93

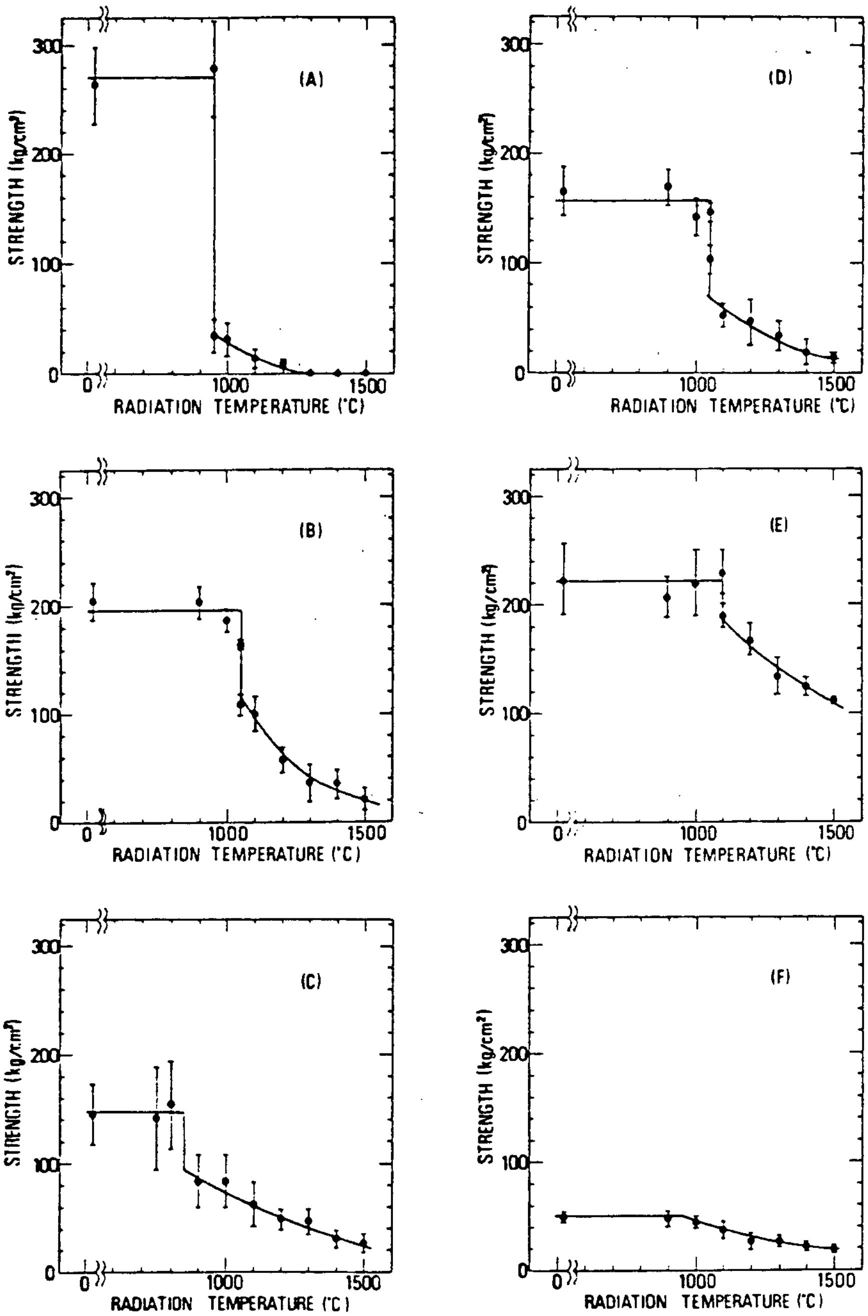

Figure 4.2 Strength variation of specimens subjected to radiation heating as a function radiation temperature. The capital letters shown in parenthesis correspond to the brands of firebrick (after reference 86)

then declined continuously with increasing radiation temperature. The strength of brick F fell gradually and continuously from the initial value with increasing furnace temperature above T_{cr}. In no case was a constant strength plateau observed as predicted by the Hasselman unified theory.

According to Nakayama the observed strength loss behaviour could be explained by the following sequence of events: the higher the radiation temperature, the greater the strain energy at fracture, the larger the resulting crack, and, consequently, the weaker the shocked specimen. In support of this hypothesis, Nakayama presented Figure 4.3 which shows the stress distributions (Figure 4.3a) and elastic energy stored in unit axial length (Figure 4.3b) as a function of radiation temperature for specimen A.

While the stress distributions (tension being negative in Figure 4.3) and the strain energy relationship are qualitatively correct, Nakayama did not supply sufficient data to reproduce the result. Furthermore, neither the type of numerical method used, nor the temperature field causing fracture, were stated. The sole comment with regard to the strain energy computation was that elastic energy at fracture was calculated by elementary elasticity theory.

Rather than follow up the idea that strength loss is dependent

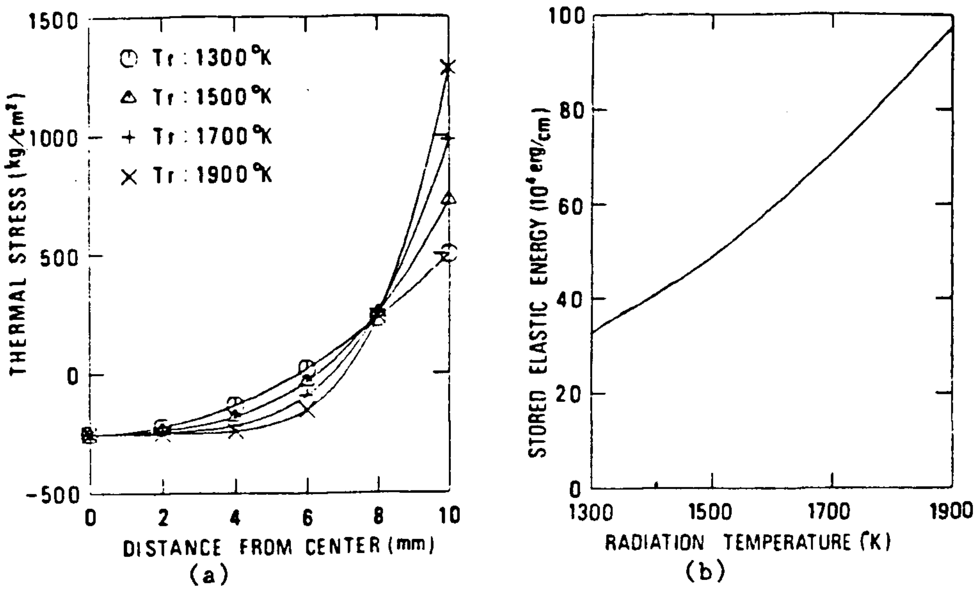

Figure 4.3 (a) Axial stress distributions in a specimen at fracture for various radiation temperatures, and (b) elastic energy stored in unit axial length as a function of radiation temperature (after reference 86)

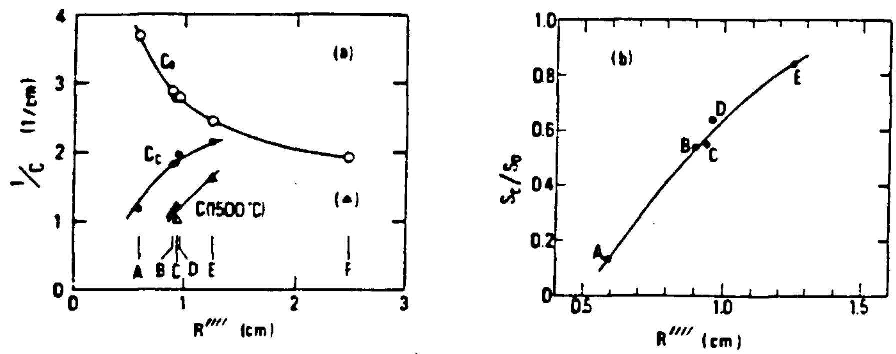

Figure 4.4 Comparison between test results and damage resistance parameter R''''. (a) Reciprocal crack length versus R'''', and (b) strength retained versus R'''' (after reference 86)

on strain energy stored at fracture by determining the time of fracture initiation and strain energy for each case, Nakayama interpreted the experimental findings in terms of the Hasselman theory. He implicitly assumed strain energy to be inversely related to R'''' and went on to rationalize the experimental results in the following manner. It was assumed that radiation heating produces only one crack in the central region of the specimen and that an estimate of the size of crack could be obtained by assuming that the crack-specimen configuration was similar to that of a rectangular bar with a plane crack of depth c on one edge.

The stress intensity factor formula[87] for this ideal case can be written as

$$K_{IC} = S_t \cdot c^{1/2} \cdot f \qquad (4.3)$$

where S_t is the three-point bend strength after thermal shock, c is the crack length, and f is a correction factor dependent on geometry. The size of the crack produced in each specimen on thermal shock is then obtained by substituting values of K_{IC} and S_t into (4.3).

Figure 4.4 shows a plot of reciprocal crack length versus R'''' for estimated crack length of the initial specimens c_o, after thermal shock at the critical radiation temperatured c_c, and after thermal shock

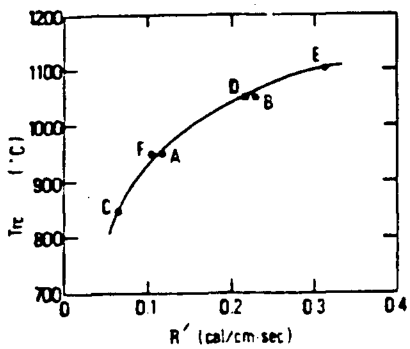

Figure 4.5 Critical radiation temperature T_{cr} versus R' (after reference 86)

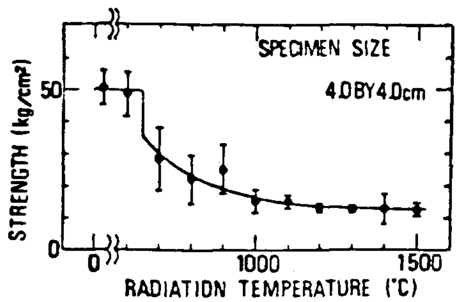

Figure 4.6 Discontinuous curve obtained with large specimens of F-brick (after reference 86)

at the maximum radiation temperature c(1500). The positive correlations of c_c and c(1500) versus R'''' are in agreement with the Hasselman prediction given by equation (2.36). Positive correlations between fraction of strength retained f_{sr} and R'''' (Figure 4.4) and critical radiation temperature T_{cr} and R' (Figure 4.5) were also found, but not between crack length and R'_{st}.

Nakayama also produced results which indicated that the nature of the strength loss-thermal shock relationship is size dependent. Figure 4.6 shows that a discontinuity exists in the strength loss curve of a 4 x 4 x 10 cm specimen of brick F which is not present in the curve of the 2 x 2 x 7 cm specimen in Figure 4.2. Furthermore, the critical radiation temperature is seen to decrease with the increase in specimen size. No analysis was provided to explain the effect of geometry on the strength loss behaviour.

4.2.2.2 Larson[88]

Larson and Hasselman[88] subjected a series of high-alumina refractories to the Nakayama radiant heating thermal shock test conditions. The relevant physical properties, thermal shock resistance parameters, and mode of fracture of each specimen are given in Table V. The after-shock strength (in psi) for the range of radiation temperatures considered is given in Table VI.

TABLE V

Properties and Thermal Shock Resistance Parameters for Larson and Hasselman Experiments

Code	$\%Al_2O_3$	σ_f (MPa)	E (GPa)	$\alpha \times 10^6$ ($°C^{-1}$)	γ_{wof} $\frac{J}{m^2}$	R_{st} ($°C \cdot cm^{1/2}$)	R'''' (cm)	Fracture Behaviour on Heating
2	99	14.2	58.6	9.4	58.2	33.5	1.70	Stable
6	90	19.0	55.8	8.0	91.1	50.5	1.41	Stable
8	85	13.7	61.4	7.8	93.8	50.1	3.08	Catastrophic
15	80	11.2	33.8	7.3	54.1	54.8	1.45	Stable
19	70	11.4	23.4	7.4	70.1	73.9	1.23	Stable
21	70	7.03	18.6	6.9	59.6	82.6	2.25	Stable
23	70	28.0	75.8	6.9	57.3	39.8	0.56	Catastrophic
27	60	22.9	55.8	5.7	62.9	58.9	0.67	Catastrophic
28	60	16.5	40.0	6.2	62.0	63.5	0.90	Catastrophic
31	60	4.07	16.5	6.6	58.9	90.3	5.81	Catastrophic
34	60	10.1	22.8	7.0	46.5	64.6	1.03	Catastrophic

TABLE VI

Strength of High-alumina Refractories After Thermal Shock by Heating (after reference 88)

Refractory Sample No. Code	*Temperature Difference (°C)*								
	0	800	900	1000	1100	1150	1200	1300	1400
2	1,720	1,860	1,690	1,820	1,710	—	1,390	1,150	640
6	2,890	—	—	2,710	2,710	2,500	2,390	2,330	1,720
8	1,850	1,790	1,950	2,075	1,800	—	1,150	1,150	830
15	1,620	1,530	1,580	1,400	1,310	—	1,320	1,200	800
19	1,650	1,510	1,630	1,560	1,680	1,500	1,220	1,110	870
21	950	740	810	750	690	—	550	420	—
23	4,020	—	4,060	4,520	—	—	1,230	910	380
27	1,840	—	—	1,880	1,590	—	1,840	800	830
28	2,350	2,240	2,040	2,030	2,150	1,360	1,230	1,220	1,310
31	500	530	480	470	310	—	315	320	—
34	1,580	1,190	1,270	1,040	540	—	540	480	—

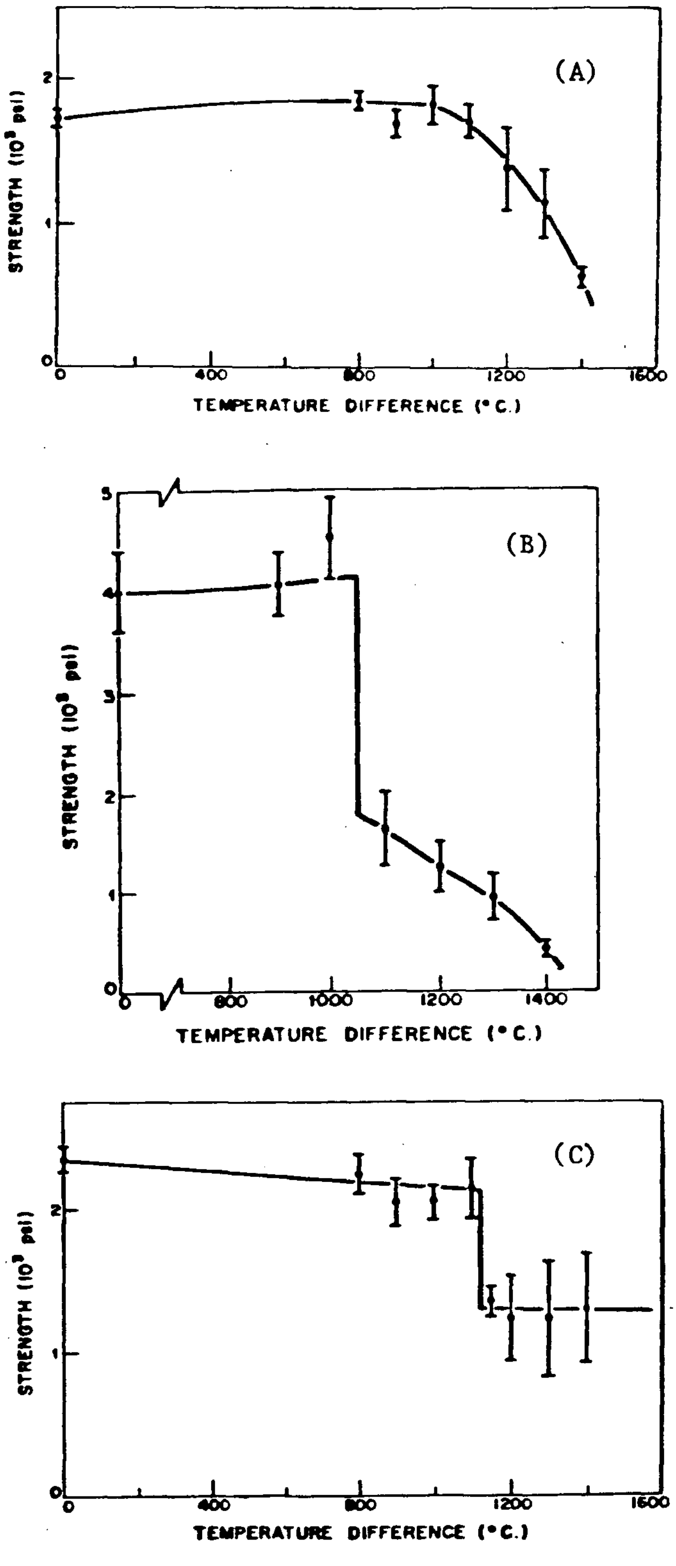

Figure 4.7 Strength behaviour of high-alumina refractory on heating. (A) specimen 15, (B) specimen 23, (C) specimen 28 (after reference 88)

Two modes of fracture behaviour were observed - stable and catastrophic. Typical stable crack propagation behaviour is illustrated in Figure 4.7A where the strength of specimen 15 is seen to decrease continuously from its initial value with increasing temperature difference above the critical value. Specimens 23 and 28 both exhibit catastrophic behaviour (Figure 4.7B and 4.7C) which is characterized by a discontinuous drop in strength at T_{cr}. For specimen 23 the strength decreases continuously with increasing radiation temperature above T_{cr}, while further increases in the radiation temperature cause no change in the strength of specimen 28.

The thermal shock fracture behaviour was interpreted in terms of the Hasselman unified theory which states that mode of crack propagation is dependent only on the relative size of the initial crack length c. For $c < c_{min}$, where c_{min} is a function of crack density only (see equation 2.36), crack propagation occurs in a catastrophic manner with the final crack length (and therefore strength loss) being directly proportional to the inverse of R'''' (see equation 2.40). For $c > c_{min}$, crack propagation occurs in a stable manner and strength loss is expected to be proportional to the difference $(\Delta T_f - \Delta T_c)$, where ΔT_f is the radiation temperature causing fracture and ΔT_c is the temperature difference associated with the stability locus. Thus stable crack propagation is interpreted in terms of R_{st} as this parameter is directly

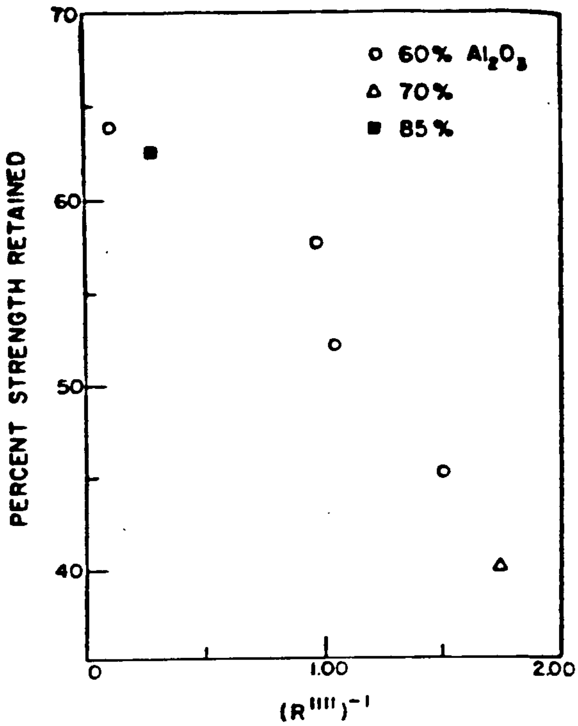

Figure 4.8 Percent strength retained by high-alumina refractories undergoing catastrophic fracture during thermal shock on heating as a function of the reciprocal of the thermal-stress resistance parameter R''' (after reference 88)

proportional to ΔT_c (see equations 2.33 and 2.38).

The investigators attempted to demonstrate the validity of the 'unified theory' interpretation of thermal shock fracture behaviour by first separating the results in Table VI according to fracture mode and then plotting a form of strength loss - either as a percent of initial strength or as a difference over a specified temperature range - against the appropriate thermal shock resistance parameter. For those specimens exhibiting catastrophic behaviour, the plot of percent strength retained after thermal shock at T_{cr} versus $(R'''')^{-1}$ yielded an inverse relationship (Figure 4.8) as did a plot of strength loss (psi) over the range 1200°C-1400°C versus R_{st} for the specimens which fractured in a stable manner (Figure 4.9).

While such excellent correlations appear to substantiate the theoretical analysis associated with the flaw model of thermal shock behaviour, the interpretation of the data raises several questions. First, the possibility of large error in the computation of percent strength loss at T_{cr} exists as the critical radiation temperatures are not at all well-defined. For example, consider specimen 23 in Table VI which has a strength of 4520 psi for 1000°C and 1230 psi for 1200°C. As no other intermediate values are given, not only is the percent strength loss in doubt but it is also unclear as to whether this specimen

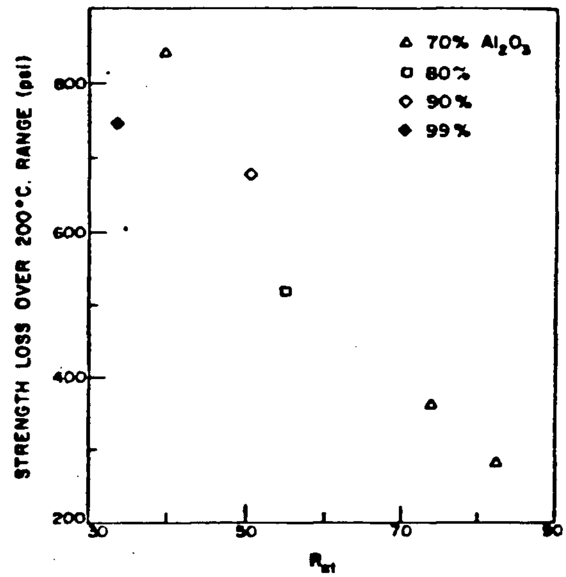

Figure 4.9 Strength loss of high-alumina refractories undergoing stable fracture during thermal shock on heating as a function of the thermal shock resistance parameter R_{st} (after reference 88)

exhibits catastrophic behaviour as is noted. Furthermore, the results for specimens 31 and 34, both of whose modes of failure are listed as catastrophic, do not rule out stable crack propagation.

With regard to the R_{st} correlation in Figure 4.9, the choice of temperature range for determining strength loss may or may not have been an arbitrary one, but no reason for the selection was stated. If, for example, the strength loss over the range 1000°C-1200°C is plotted against R_{st} the correlation is not so obvious. And finally, it is stated that 'in view of its clearcut fracture behaviour, the data for the high-alumina sample No. 23 were included in both these two criteria for strength loss'. The data point for specimen 23 is represented by the open triangle at the bottom of Figure 4.8 and at the top of Figure 4.9.

As indicated above, with no data points in the range 1000°C-1200°C, the fracture behaviour of this specimen is hardly 'clear-cut'. Furthermore, if the fracture behaviour is clear-cut the data point should - without ambiguity - fit in one correlation or the other, certainly not both. The fact that the point for specimen 23 fits smoothly into both correlations hardly strengthens the interpretation of the fracture behaviour in terms of catastrophic and stable modes of fracture.

4.2.3 Symmetric Cooling - Larson[88-89]

The spalling behaviour on cooling of the refractories listed in Table V was also investigated. The after-shock strengths are given in Table VII. The test consisted of quenching specimens of the same size as for the heating tests (0.75 x 0.75 x 4.5 in) which had been equilibrated at an elevated temperature into a water bath at room temperature. As with the heating test, after-shock strength was measured using a three-point bend test.

Typical behaviour is illustrated in Figure 4.10 which shows the strength loss-temperature difference for specimens 23 and 28, two specimens which fractured in the catastrophic mode on heating (Figure 4.7). A constant strength plateau, more pronounced in one case than the other, is apparent in both cases. For all refractories tested the mode of fracture on cooling was stable and strength loss correlated with R_{st} as indicated in Figure 4.11 which includes results for other specimens than those listed in Table VII. With regard to the R_{st} correlations for stable fracture on heating and cooling, it is not clear why the strength loss was represented as a difference for the heating case (Figure 4.9) and as a percentage for the cooling case (Figure 4.11).

The observation that some specimens fractured in a catastrophic

Table VII

Strength of High-alumina Refractories After Thermal Shock by Cooling (after reference 88)

Refractory Sample No. Code	*Temperature Difference (°C)*							
	0	200	300	400	600	800	1000	1180
2	2,060	1,590	1,050	720	510	400	270	320
6	2,760	2,620	2,550	2,250	1.880	1,500	1,260	1,200
8	1,980	1,900	1,870	1,830	1,190	1,120	1,100	1,110
15	1,630	1,650	1,630	1,450	1,210	1,020	870	760
19	1,650	1,560	1,200	1,120	1,180	880	760	660
21	1,020	1,140	1,010	940	740	660	590	440
23	4,060	3,890	3,140	2,740	1,770	1,190	1,130	800
27	3,320	2,450	2,020	1,820	1,420	1,280	1,080	900
28	2,090	1,450	1,460	1,530	1,080	1,030	1,050	800
31	590	440	570	440	370	280	290	250
34	1,470	1,480	1,240	900	720	610	510	360

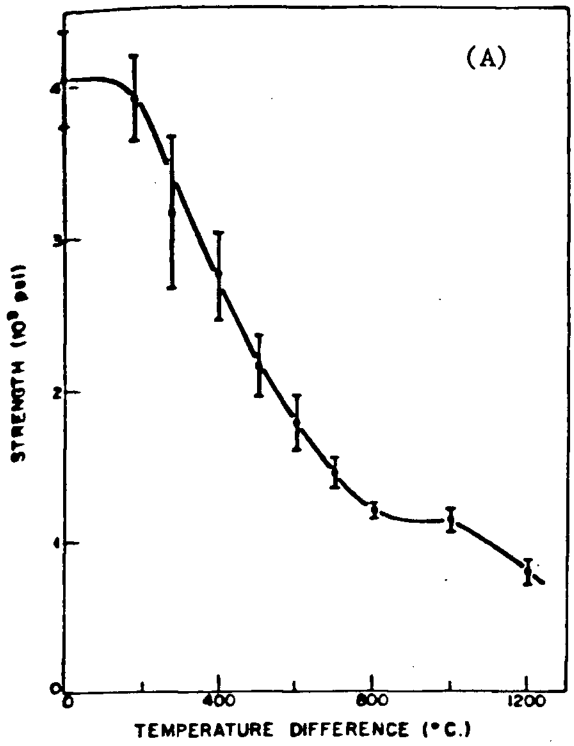

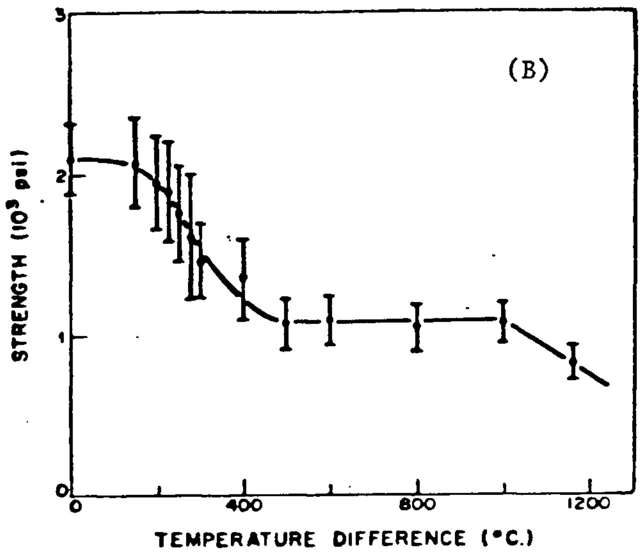

Figure 4.10 Strength behaviour of high-alumina refractories on cooling. (A) specimen 23, (B) specimen 28 (after reference 88)

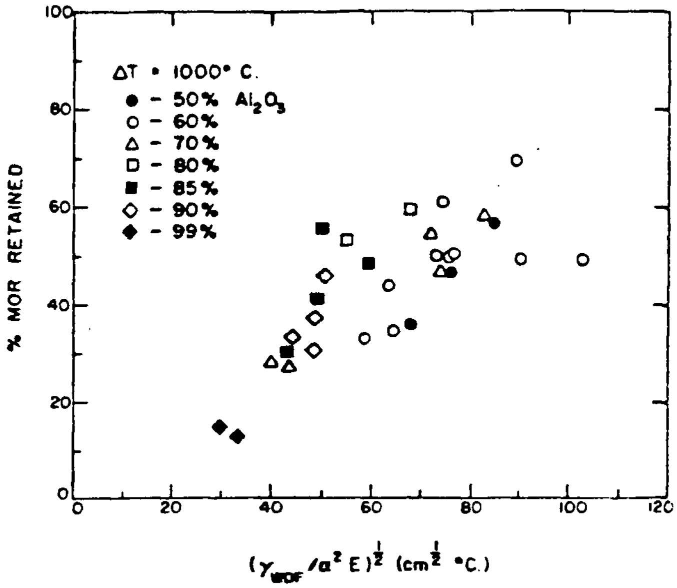

Figure 4.11 Retained strength of high-Al_2O_3 refractories quenched into water from 1000°C as a function of thermal stress resistance parameter R_{st} (after reference 89)

manner on heating and in a stable mode on cooling was rationalized in terms of crack density N. Specimen 23 was considered and it was noted that only 8 cracks were formed over the whole cross-section for the heating case which corresponded to $N \cong 0.4/cm^2$ which was calculated by substituting the appropriate values into equation (2.33). A higher crack density on cooling of $N = 16/cm^2$ was attributed to the introduction of flaws during surface preparation and also to subsequent flaw generation during the thermal shock.

Thus the rationale to explain the different fracture behaviour on heating and cooling of the same specimen is that the nature of thermal shock on cooling was such that it produced an increase in N of sufficient magnitude to reduce c_{min} enough to satisfy the stable fracture criteria (see equation 2.36). In the case of those specimens which fail in the stable mode on both heating and cooling, the initial crack density throughout the specimen must have been such that the condition of $c > c_{min}$ existed prior to quenching as, according to Larson et al, the transient behaviour of crack density is a surface phenomenon and that the crack density in the interior of the specimen remains relatively unaffected.

4.2.4 Nonsymmetric Heating - Semler[71,82]

Semler et al used the Ribbon test (see Section 2.5) to investigate the effect of sample size and thermal cycling on the thermal shock behaviour of a range of alumina refractories. The physical properties and damage resistance parameters are given in Table VIII. The dimensions of the three types of specimen - split, quarter, and bar - are shown in Figure 4.12. Figure 4.13 shows typical transient behaviour of the hot face temperature and of the cold face temperature for various hot face to cold face thicknesses. While Semler investigated the influence of both geometry and thermal cycling, only the effect of sample size is discussed as the influence of thermal cycling on fracture behaviour is considered beyond the scope of this work.

In the Ribbon test evaluation of thermal shock damage is non-destructive. Modulus of elasticity (MoE) measurements are made before and after the test cycle with thermal shock damage being expressed as % MoE retained. The applicability of the non-destructive technique was demonstrated by showing a direct correlation between after-shock MoE and modulus of rupture.

No apparent sample degradation was generally visible after thermal shock on heating, except on rare occasions when cracks oriented perpendicular to the hot face were observed. In the most extreme cases, several samples cracked in half. Thus, it is clear that methods based on separation of the specimen or the observation of external cracks,

TABLE VIII

Properties of the Alumina Refractories of the Semler Study
(after reference 71)

Al_2O_3 (wt%)	Bulk density, ϱ (g/cm^3)	Thermal expansion, α (°C^{-1} × 10^{-6})	Elastic modulus, E (MPa × 10^4)	Poisson's ratio, ν	Flexural strength, σ_f (MPa)	Work-of-fracture, γ_{wof} (J/m^2)	Calculated damage resistance parameters: R (°C)	R'''' (m × 10^{-3})	R_{st} (m$^{1/2}$·°C)
45	2.45	5.2	6.98	0.22	31.8 ± 1.7	22.5 ± 5.7	68	2.0	3.45
42	2.30	5.3	6.70	.16	34.1 ± 2.7	17.8 ± 1.5	81	1.2	3.08
59	2.50	5.9	4.61	.20	22.9 ± 0.8	34.0 ± 3.0	67	3.7	4.58
70	2.55	6.2	1.35	.15	9.8 ± 2.5	32.9 ± 12.8	100	5.4	7.96
70	2.58	5.7	1.05	.14	9.7 ± 1.4	70.0 ± 7.3	139	9.7	14.28
70	2.60	5.7	3.25	.14	17.3 ± 2.2	71.0 ± 18.1	80	9.0	8.18
72	2.60	6.6	2.41	.17	11.2 ± 1.3	58.0 ± 10.3	58	13.4	7.43
70	2.55	5.5	3.03	.14	13.9 ± 2.9	63.0 ± 25.5	72	11.5	8.28
72	2.60	6.8	3.03	.15	14.3 ± 1.2	48.0 ± 10.8	59	8.4	5.85
72	2.65	5.2	7.54	.18	27.4 ± 2.8	31.7 ± 4.3	57	3.9	3.94
85	2.90	7.1	9.30	.18	45.6 ± 1.5	56.0 ± 4.5	57	3.1	3.45
91	2.95	7.2	4.00	.16	20.0 ± 1.2	65.0 ± 8.0	58	7.7	5.59

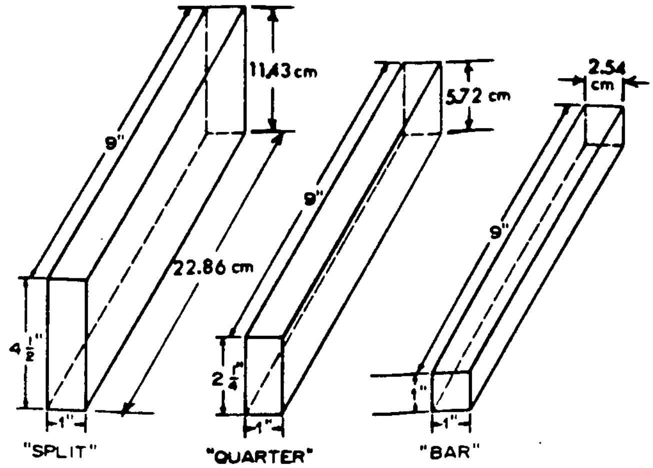

Figure 4.12 Dimensions of specimens of the Semler study (after reference 71)

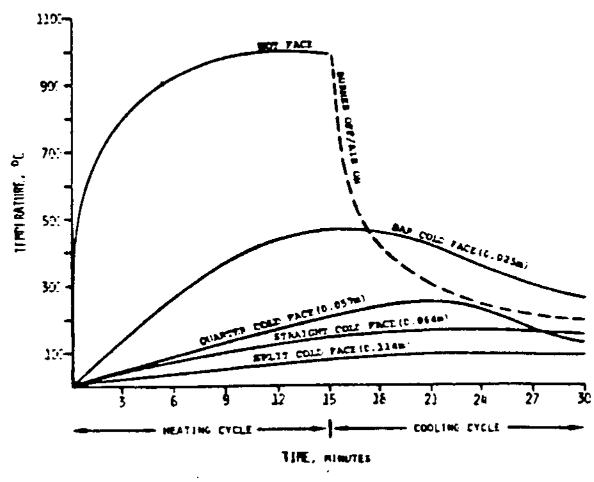

Figure 4.13 Representative measurements of hot face and cold face thermal history for different sized 90% alumina refractory samples during first cycle of the ribbon test. The hot face to cold face thickness is shown in parenthesis (after reference 82)

such as weight loss or cycles to failure which are used in the panel spalling and prism tests, would not be suitable for the evaluation of thermal damage in this type of heating study.

The results of the Semler study are presented in Figure 4.14 in the form of plots of percent modulus of elasticity retained versus R_{st} (Figure 4.14A) and R'''' (Figure 4.14B) for bars, quarters, and splits after one thermal shock cycle. Similar trends were observed for both parameters, with size having a pronounced effect on % MoR retained.

4.2.5 Summary

The thermal shock behaviour of refractory products has generally been interpreted in light of the Hasselman unified theory. The findings of the three cases selected for study can be summarized as follows:

(1) In support of the Hasselman approach, Nakayama reported a positive correlation between reciprocal of final crack length and the damage resistance parameter R'''' and also between fractional strength retained after shock at T_{cr} and R''''.

(2) In support of the Kingery analysis, Nakayama reported a positive correlation between critical radiation temperature T_{cr} and resistance to fracture initiation parameter R'.

(3) Nakayama observed both stable and catastrophic failure on heating but no constant strength plateau.

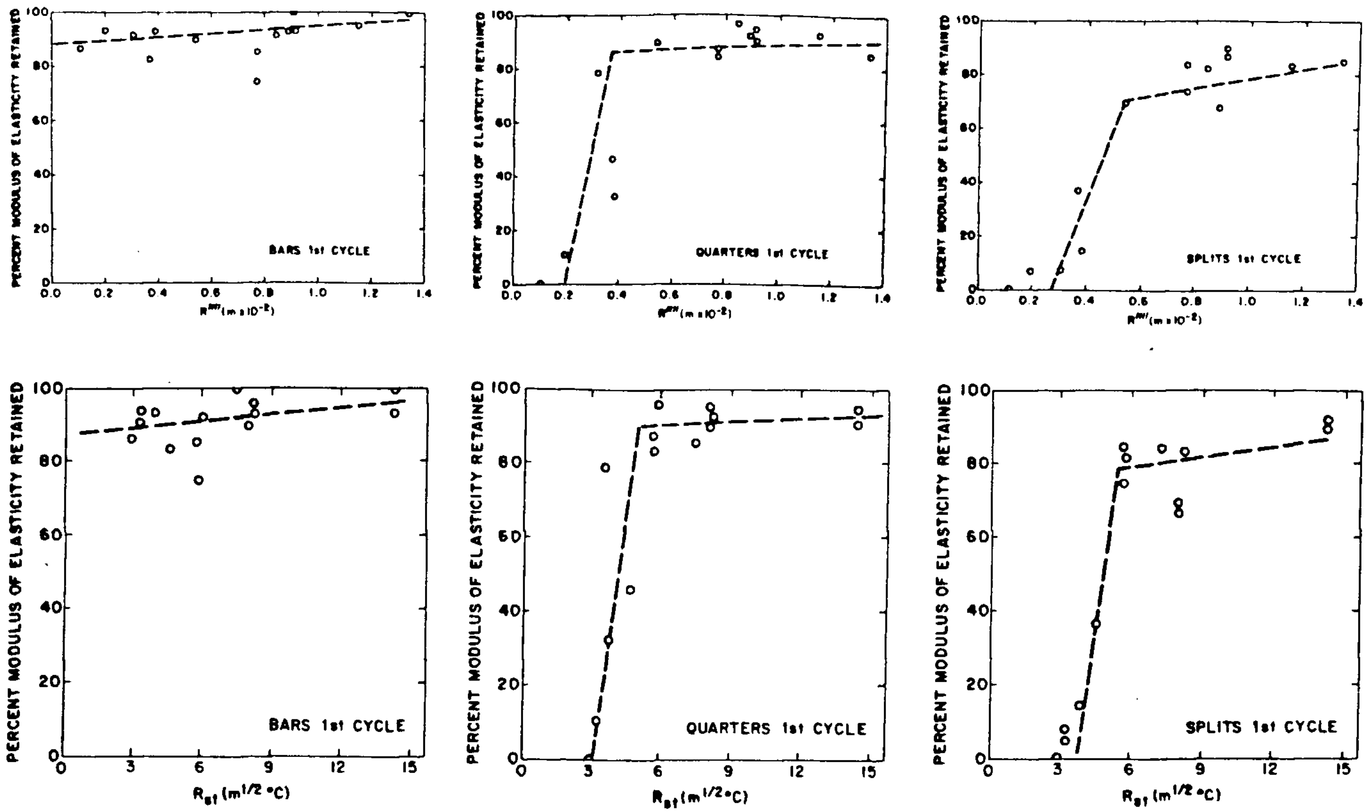

Figure 4.14 Damage trends versus R'''' and R_{st} values (after reference 71)

(4) Nakayama found the mode of fracture to be dependent on size.

(5) Larson observed both stable and catastrophic failure on heating but only stable behaviour on cooling.

(6) With regard to the heating case, Larson reported excellent correlations between percent strength retained and $(R'''')^{-1}$ for those specimens exhibiting catastrophic behaviour and also between strength loss over 1200-1400°C range versus R_{st} for those specimens which fractured in the stable mode.

(7) The behaviour of the specimens which fractured in a catastrophic manner on heating and a stable mode on cooling was explained in terms of a 'thermal shock dependent' crack density.

(8) Larson reported constant strength plateaus for both the heating and cooling cases.

(9) Semler found no significant difference in the trends of % MoR retained versus R'''' and % MoR retained versus R_{st}.

(10) Semler also observed strength loss to be strongly dependent on geometry.

4.3 Thermoelastic Analysis

4.3.1 Introduction

In this section the thermal shock experimental results of the Nakayama, Larson, and Semler studies are interpreted from a thermoelastic standpoint. Analytical solutions for the temperature field and simple expressions for approximating the thermal boundary conditions are used in conjunction with a tabulated solution for the maximum principal tensile stress to estimate the time of fracture initiation. The finite element numerical method (see Appendix II) is then applied to compute the thermal stress field and determine the location of fracture and total strain energy at fracture.

The specimens of the three studies all possess infinite slab geometry in which the dimension in the direction of heat flow ($\dot{q}$) is much less than the width w. The location of coordinate axes, direction of heat flow, and stress convention for the model of the symmetric heating and cooling cases are shown in Figure 4.15 and for the non-symmetric heating case in Figure I-1 in Appendix I. For the infinite slab case the maximum principal tensile stress is a component of the center line σ_x distribution. On heating it is located in the interior and on cooling at the surface.

The refractory specimens are modelled as ideal flaw-free,

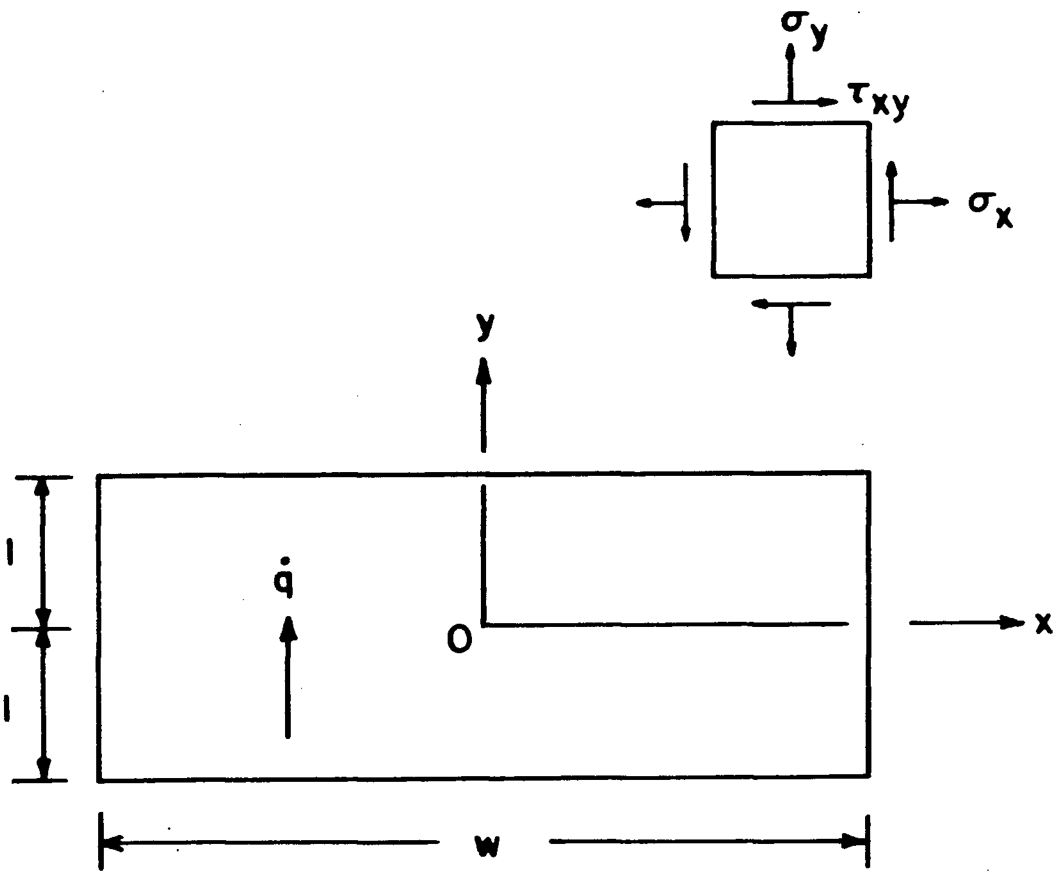

Figure 4.15 Location of axes, direction of heat flow, and stress convention for the infinite slab symmetric heating and cooling cases.

linearly elastic, brittle materials. Fracture is taken to occur when the maximum principal tensile stress reaches a specified value of fracture strength which, for this analaysis, is the reported room-temperature modulus of rupture value. The validity of these assumptions will be apparent in the comparison of thermoelastic predictions to be presented in a following section with the experimental observations of the studies discussed in the previous section.

The thermal conditions of the Nakayama, Larson, and Semler studies - radiation heating in an electric furnace, water quenching, and heating via the flame of a gas burner - are all relatively complex thermal processes. Due to the magnitude of the scatter in the strength loss-thermal shock results, sophisticated numerical analysis for the computation of the thermal fields is unwarranted. In each case constant heat transfer coefficient (h) analytical solutions are used to simulate the transient temperature profiles. The characteristic features of each thermal shock situation are incorporated by judicious selection of analytical solution.

The steps in the thermoelastic analysis of a thermal shock experiment can be summarized as follows: (i) simulate the thermal conditions, (ii) develop a general solution for the maximum principal tensile stress, (iii) invert the general solution to determine the instant at which the maximum principal tensile stress reaches a specified value of fracture strength, and (iv) use a numerical method to compute the thermal stress field and total strain energy at fracture.

In Section 4.3.2 the analytical temperature solutions and expressions for estimating the heat transfer coefficient for each case are given. In Sections 4.3.3 and 4.3.4 the solutions for the maximum principal tensile stress are discussed and the Kingery approach to thermoelastic analysis is briefly reviewed. In Section 4.3.5 the procedure for the analysis of fracture behaviour is described with reference to an example. In Section 4.3.6 the results of the thermoelastic analysis of the works of Nakayama, Larson and Semler are presented. In Section 4.3.7 the highlights of the thermoelastic approach to the analysis of thermal shock failure are summarized.

4.3.2 Modelling Thermal Conditions

4.3.2.1 Symmetric Heating

The transient temperature fields in the specimens subjected to the Nakayama radiant heating test are approximated by those of the ideal case[90] of the region $-\ell<y<\ell$ with zero initial temperature which is heated by radiation from a medium at T_∞. All thermophysical properties are temperature independent. The solution is

$$T = T_\infty \left(1 - \sum_{n=1}^{\infty} \left\{ \frac{2\,\beta^* \cos\left(\frac{\alpha_n y}{\ell}\right) \sec(\alpha_n)}{\beta^* (\beta^* + 1) + \alpha_n^2} \cdot e^{-\alpha_n^2 \theta^*} \right\}\right) \tag{4.4}$$

where the Biot modulus β^* and Fourier modulus θ^* are defined by

$$\beta^* = \frac{h\ell}{k}, \tag{4.5}$$

and

$$\theta^* = \frac{at}{\ell^2} \tag{4.6}$$

and α_n, n = 1, ... are the positive roots of

$$\alpha \tan \alpha - \beta^* = 0 \tag{4.7}$$

The constant radiative heat transfer coefficient h_r is calculated using

$$h_r = \sigma \left(\frac{T_\infty^4 - T_a^4}{T_\infty - T_a} \right) \tag{4.8}$$

where in this case σ is the Stefan-Boltzmann constant and T_a is the initial temperature of the specimen. Equation (4.8) assumes an emittance and shape factor of one. Figure 4.16 gives a plot of h_r versus T_∞ for $T_a = 20°C$.

4.3.2.2 Symmetric Cooling

The temperature profiles for the water quenching studies are approximated by using

$$T = T_i \left(\sum_{i=1}^{n} \frac{2\beta^* \cos\left(\frac{\alpha_n y}{\ell}\right) \sec(\alpha_n)}{\beta^* (\beta^* + 1) + \alpha_n^2} \cdot e^{-\alpha_n^2 \Theta^*} \right) \qquad (4.9)$$

which gives the profiles for the case of the region $-\ell<y<\ell$ with constant initial temperature T_i which is cooled by radiative and convective heat loss into a medium at zero temperature.[90]

As indicated in Figure 4.17[91], which shows typical heat flux versus temperature difference behaviour for a wire, tube, or horizontal surface in a pool of water, thermal phenomena associated with water quenching can be complex. Krieth[92] gives the following expression for average convective heat transfer coefficient h_b for heat transfer from horizontal surfaces within the film boiling regime,

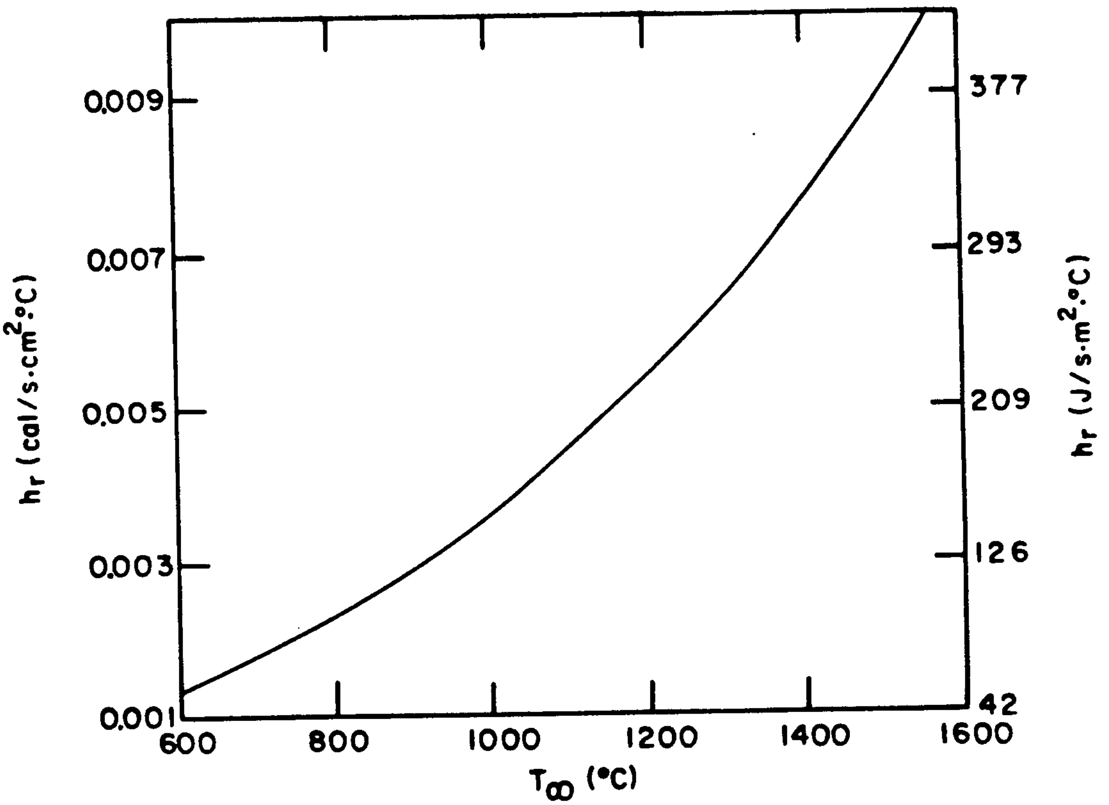

Figure 4.16 Estimate of heat transfer coefficient for the Nakayama radiative heating thermal shock test

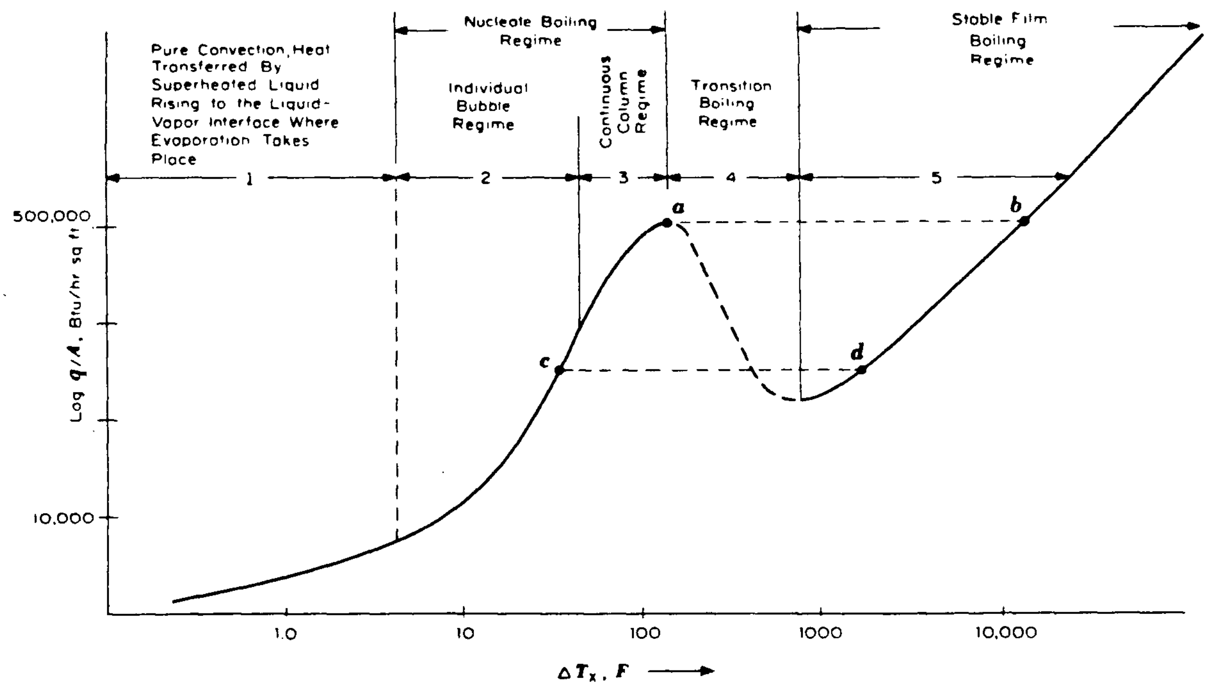

Figure 4.17 Typical boiling curves for a wire, tube or horizontal surface in a pool of water at atmospheric pressure (after reference 91)

$$h_b = 0.67 \frac{F}{\lambda_c^{1/4}} \tag{4.10}$$

where

$$F = \frac{\left[k_v^3 \rho_v(\rho_\ell - \rho_v) g h_{fg}\{1 + (0.34 C_v \Delta T_x / h_{fg})\}^2 \right]^{1/4}}{\mu_v \Delta T_x} \tag{4.11}$$

and

$$\lambda_c = 2\pi \left[\frac{g_c \sigma}{g (\rho_\ell - \rho_v)}\right] \tag{4.12}$$

Superimposed on h_b, which accounts only for heat transfer by conduction through the vapour film and by boiling convection from the surface of the film to the surrounding liquid, is heat transfer due to radiation. According to Kreith, the coefficient h_b for conduction and

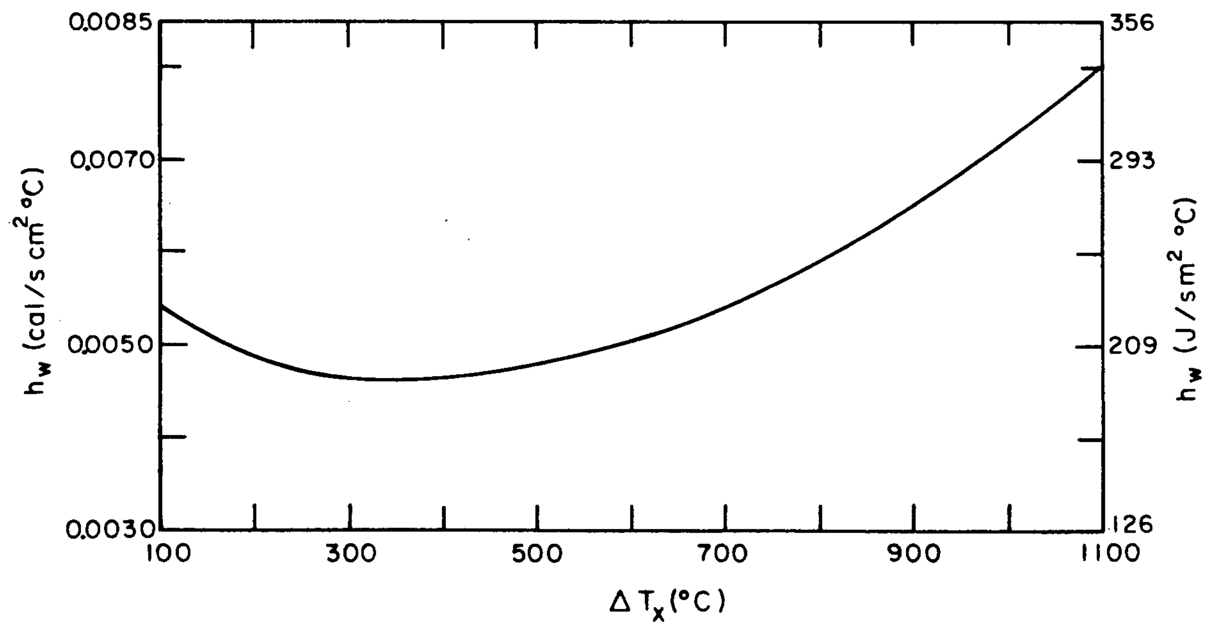

Figure 4.18 Estimate of heat transfer coefficient for the Larson water quenching thermal shock test

convection in the presence of appreciable radiation is less than in the absence of radiation. Thus the total surface heat transfer coefficient h_w for the water quench is estimated by

$$h_w = h_b \left(\frac{h_b}{h_w}\right)^{1/3} + h_r \tag{4.14}$$

where h_r is computed using equation (4.8).

The h_w versus ΔT_x plot in Figure 4.18 was constructed using the values given by Kreith for the film boiling case. This case was chosen to represent the thermal conditions of the water quench experiments because the results of Larson (see Table VII) indicate that fracture initiation did not occur until a ΔT of approximately 200-300°C. With respect to Figure 4.17 this temperature difference lies in the transition region near the beginning of the film boiling regime. As the mode of heat transfer is dependent on the nature of the surface as well as temperature difference, the boiling curve of Figure 4.17 may not apply for the refractory experiments. However, no better estimate of the heat transfer coefficient for this system could be found.

4.3.2.3 Non-symmetric Heating

The transient temperature profiles associated with the Ribbon test are simulated by transforming the coordinate system such that the

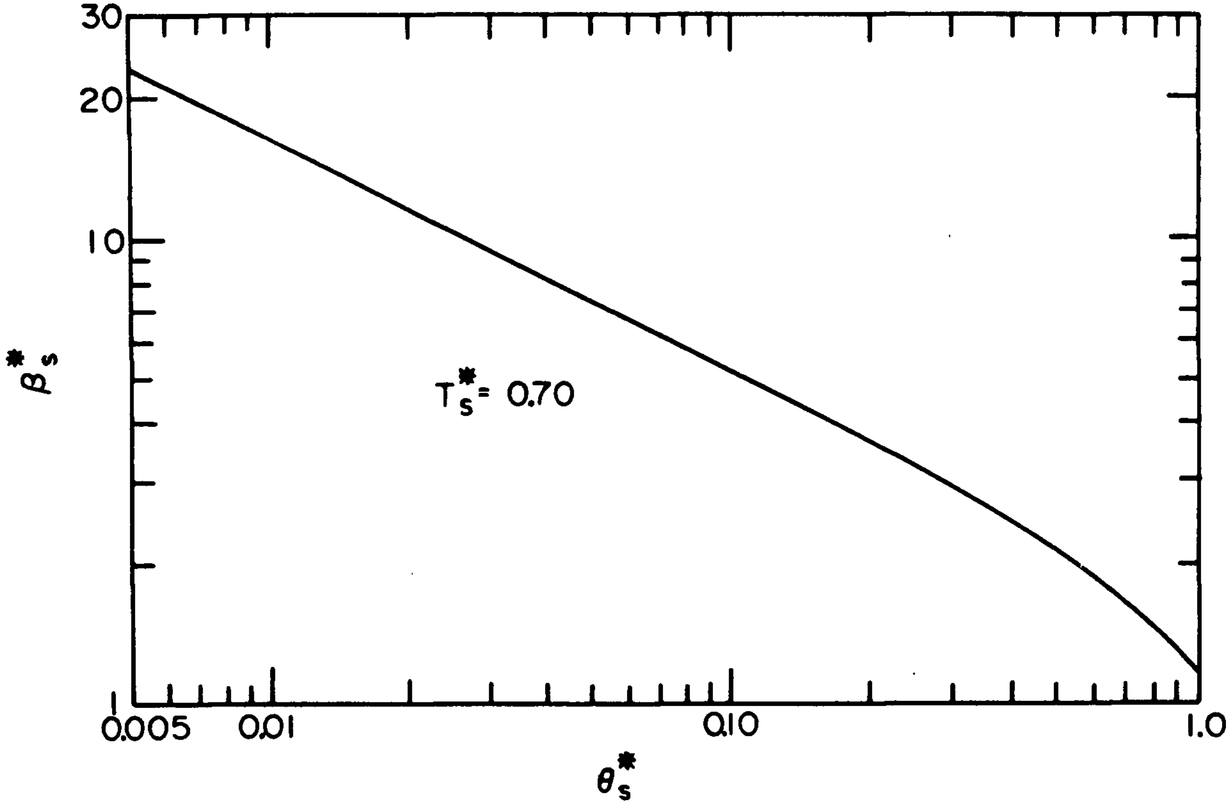

Figure 4.19 Combinations of Biot modulus which produce dimensionless surface temperature T_s^*=0.70 for the constant heat transfer coefficient heating case.

hot face is at $y=\ell$ and the insulated cold face at $y=0$ and using equation (4.4) over the range $0<y<\ell$. During the first five minutes of the test the temperature of the hot face is raised to 1000°C. This condition and the assumption of a flame temperature of T_∞ = 1430°C are used to estimate the constant heat transfer coefficient h_s for the heating phase of the Ribbon test.

Surface temperature T_s can be expressed in dimensionless form as

$$T_s^* = \frac{T_s}{T_\infty} . \qquad (4.15)$$

The combinations of β^* and θ^* which produce T_s^* = 0.70, which corresponds to T_s=1000°C and T_∞=1430°C, are presented in Figure 4.19.

An estimate of h_s for a particular test can be obtained quickly by substituting thermal diffusivity, length, and t = 300 s into (4.6) to get θ_s^*, using Figure 4.19 to obtain the corresponding β_s^*, and then substituting the appropriate values of thermal conductivity and length into

$$h_s = \frac{\beta_s^* k}{\ell} \qquad (4.16)$$

4.3.3 General Solution for Maximum Principal Tensile Stress

In addition to analytical expressions for modelling the thermal conditions, the other preliminary requirement for the thermoelastic analysis is a corresponding general solution for the maximum principal tensile stress σ_M. The σ_M dependence for the constant heat transfer coefficient infinite slab case can be expressed in functional form as

$$\sigma_M = f\,(t,\ E,\ \nu,\ \alpha,\ a,\ k,\ h,\ \Delta T,\ \ell) \tag{4.17}$$

where ΔT is the temperature difference between specimen and heating or cooling medium.

As indicated in Appendix III, the dimensionless form of equation (4.17) is

$$(\sigma_M^*)_h = f\,(\theta^*,\ \beta^*) \tag{4.18}$$

where β^* and θ^* are given by equations (4.5) and (4.6) and the constant h case dimensionless maximum principal tensile stress is defined by

$$(\sigma_M^*)_h = \frac{\sigma_M\,(1 - \nu)}{E\ \alpha\ \Delta T}\ . \tag{4.19}$$

The constant h case dimensionless fracture strength is obtained by substituting σ_f for σ_M in (4.19). In general, the subscripts f and h refer to values at fracture and those related to the constant heat transfer coefficient case.

The location of σ_M varies from case to case. For the symmetric heating and cooling cases it is invariant, as the σ_x distribution is symmetric, with σ_M being located at the midpoint of the center line on heating and at the outer surfaces on cooling. For the non-symmetric heating case the σ_x distribution is skewed toward the hot face during the initial stages of heating. With increasing time the location of σ_M moves away from the hot face and tends toward a limiting position at the midpoint.

Solutions for σ_M are usually presented in graphical form as indicated in Figure 4.20 which shows the transient behaviour of $(\sigma_M^*)_h$ for a range of Biot modulus for the case of the symmetrically cooled traction-free slab. Appendix IV contains a comprehensive set of tabulated values of $(\sigma_M^*)_h$ for this case, and for the symmetric and non-symmetric heating cases as well. The values were obtained by finite element analysis. Reproduction of the graphical results in Figure 4.20 was one means of verifying the finite element results.

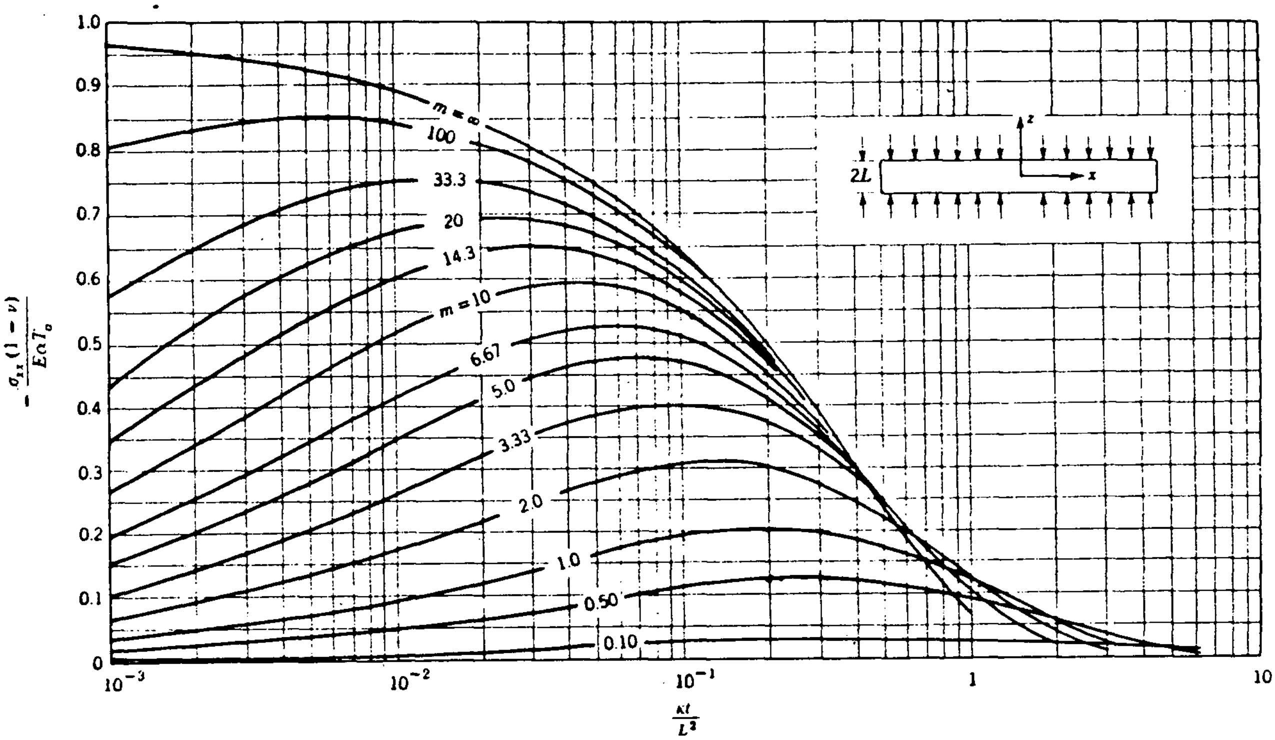

Figure 4.20 Thermal stresses at the surface of a free plate heated symetrically, through a boundary conductance h, on the faces z=±L. Initial temperature zero, ambient temperature T_a, Biot modulus m=hL/k. Note that the surface stress is compressive for heating ($T_a > 0$) and tensile for cooling ($T_a < 0$) (after reference 93)

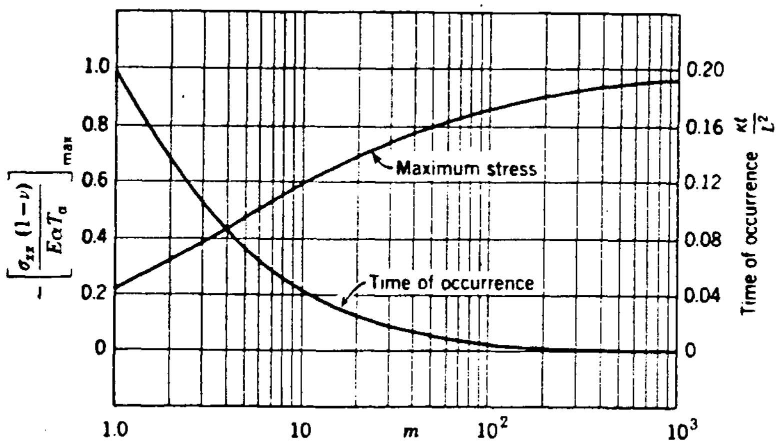

Figure 4.21 Maximum stress and time of occurrence for the problem of Figure 4.20. The maximum stress occurs on the surface (after reference 93)

The transient behaviour of $(\sigma_M^*)_h$ is typical for all three thermal cases. As indicated in Figure 4.20, for constant Biot modulus $(\sigma_M^*)_h$ rises with time to a peak value - $(\sigma_M^*)_{peak}$ - whereupon it falls to zero as the temperature distribution tends toward a uniform value. The time of occurrence decreases and the magnitude of the peak value increases with increasing Biot modulus - $(\sigma_M^*)_{peak} \to 1$ and $(\theta^*)_{peak} \to 0$ as $\beta^* \to \infty$ (see Figure 4.21). The limiting case of infinite heat transfer coefficient corresponds to the thermal boundary condition of instantaneous change in surface temperature.

4.3.4 Kingery Analysis

Kingery made use of two simple relationships involving $(\sigma_M^*)_{peak}$ for the symmetric cooling case to derive the resistance to fracture initiation parameters R and R'. For the case of instantaneous decrease in surface temperature of magnitude ΔT (infinite h), he manipulated the expression

$$(\sigma_M^*)_{peak} = 1 \tag{4.20}$$

to show that the temperature difference ΔT_f required to produce a stress equal to the fracture strength σ_f is given by

$$\Delta T_f = \frac{\sigma_f\ (1-\nu)}{E\alpha} \tag{4.21}$$

where ΔT_f is equivalent to the resistance to fracture initiation parameter R.

For the finite constant heat transfer coefficient case, Kingery expanded the simple relationship $(\sigma_M^*)_{peak}$ = (constant) β^* and again expressed the temperature difference required to produce the fracture strength in terms of the other parameters. This yielded

$$\Delta T_f \propto \frac{\sigma_f\ (1-\nu)\ k}{E\alpha} \cdot \frac{1}{\ell h} \tag{4.22}$$

which can be put in the general form of

$$\Delta T \propto R' \cdot S \cdot h^{-1} \tag{4.23}$$

where

$$R' = \frac{\sigma_f\ (1-\nu)\ k}{E\alpha} \tag{4.24}$$

and S is a shape factor.

The first point concerns the splitting of the terms of the thermal boundary condition and the use of only ΔT as a measure of resistance to thermal shock. The nature and magnitude of the thermal stress field is dependent on the nonlinear temperature distribution within the body which, in turn, is dependent on the rate of heat extraction or addition which is governed by two interrelated parameters, h and ΔT. It is clear from a preceding section that the h-ΔT relationship can be complex and highly nonlinear, particularly that associated with water quenching which has been the most popular type of experimental thermal shock environment.

Another point concerns the choice of the direct proportionality of $(\sigma_M^*)_{peak}$ and β^* upon which to base the R' analysis. Even a cursory examination of the curves in Figures 4.20 and 4.21 reveals that the solution for the maximum principal tensile stress is also relatively complex and highly nonlinear. A more thorough examination of the tabulated results in Appendix IV would indicate that the simple proportionality is valid only for small β^*. Thus the R and R' parameters apply to the cases of very large β^* and very small β^*, respectively. Many practical problems possess thermal conditions which are characterizable in terms of intermediate values of Biot modulus.

The final point concerns the implication of the Kingery analysis with regard to the transient aspect of the thermal shock problem. Consider the following example in which the material properties and thermal conditions are such that the transient behaviour of the maximum principal tensile stress is given by the curve $\beta^* = 5.0$ in Figure 4.20. Whether fracture occurs is dependent on the relative value of dimensionless fracture strength and the peak value on the $\beta^*=5.0$ curve. If $(\sigma_f^*)_h > (\sigma_M^*)_{peak}$, then σ_M never reaches σ_f and fracture does not occur. If $(\sigma_f^*)_h = (\sigma_M^*)_{peak}$, then the specimen is just on the verge of fracture. If $(\sigma_f^*)_h < (\sigma_M^*)_{peak}$, then fracture occurs - the smaller the magnitude of dimensionless fracture strength, the earlier the time of fracture.

The Kingery analysis is based on an expression which relates the maximum attainable or peak value of maximum principal tensile stress to the Biot modulus. Thus, implicit in any subsequent derivation is the under- standing that fracture initiation occurs at $(\sigma_M^*)_{peak}$. The peak value is only of interest in that it indicates which materials are susceptible to fracture for a particular value of Biot modulus. If the dimensionless fracture strength is less than the peak value, then the peak value is of academic interest only as fracture will have occurred prior to reaching the theoretically maximum attainable value. Thus the Kingery approach ignores the transient aspect of the thermal shock problem.

4.3.5 Procedure for the Analysis of Fracture Behaviour

Essentially, the thermoelastic analysis consists of the determination of the thermal stress and strain energy density fields at the instant of fracture initiation. The parameters of interest are the temperature field causing fracture, the time of fracture, the location and orientation of the stress component satisfying the fracture criterion, and the total strain energy available for the creation of fracture surface. The thermoelastic analysis is valid only to the instant of fracture, after which time the boundary conditions of the problem change and other methods must be used for any subsequent mathematical treatment.

The analysis consists of the following steps. Consider the case of a 2 x 2 x 7 cm specimen of refractory F subjected to radiant heating at $\Delta T = 950°C$. The data and results for this example are summarized in Table IX. The heat transfer coefficient is estimated using equation (4.8). The first step is to compute the dimensionless parameters which characterize the thermal shock problem which for the example case are $(\sigma_f^*)_h = 0.0429$ and $\beta_f^* = 1.3$. The next step is to find the corresponding Fourier modulus at fracture.

TABLE IX

Data and Results of Fracture Analysis
of 2x2x7 cm Refractory F of Nakayama Study

Data	Dimensionless Parameters	Results
σ_f = 4.85 MPa		
E = 10.4 GPa	$(\sigma_f^*)_h$ = 0.0429	t_f = 7.8 s
ν = 0.25		
α = 8.5 $(10^{-6})°C^{-1}$		
ΔT = 950°C		$(\sigma_f)_{FE}$ = 4.72 MPa
h = 135 $J/sm^2°C$		% Diff = −2.7%
ℓ = 1.0 cm	β_f^* = 1.3	
k = 1.0 J/sm°C		U_f = 0.237 J/cm
a = 0.005 cm^2/s	Θ_f^* = 0.039	A_c = 0.82 cm^2/cm^2
γ = 41.2 J/m^2		R_d = 1.22

The instant of fracture is determined by first finding all the combinations of variables which will just produce the specified fracture strength and then selecting the particular combination that satisfies the problem under consideration. In terms of dimensionless parameters, what is desired is the set of variables satisfying the general dependence given by

$$\theta_f^* = f\ (\beta_f^*, (\sigma_f^*)_h), \tag{4.25}$$

as then it would be a simple matter to determine the Fourier modulus at fracture for a particular case.

The set of variables satisfying equation (4.25) is found by using a graphical technique, which is illustrated in Figure 4.22, to invert the solution for the maximum principal tensile stress. The first step is to plot the portion of the $(\sigma_M^*)_h$ solution (Table IV-1 in Appendix IV) in the neighborhood of the characteristic dimensionless fracture strength and Biot modulus. The points of intersection of the $(\sigma_M^*)_h - \theta^*$ curves and the line $(\sigma_f^*)_h = 0.0429$ are then used to construct a locus of fracture initiation curve for the example case. Such a curve gives all the combinations of β_f^* and Θ_f^* which will produce a specified value of dimensionless fracture strength. The Fourier modulus at fracture is then obtained by interpolation and the time of fracture t_f

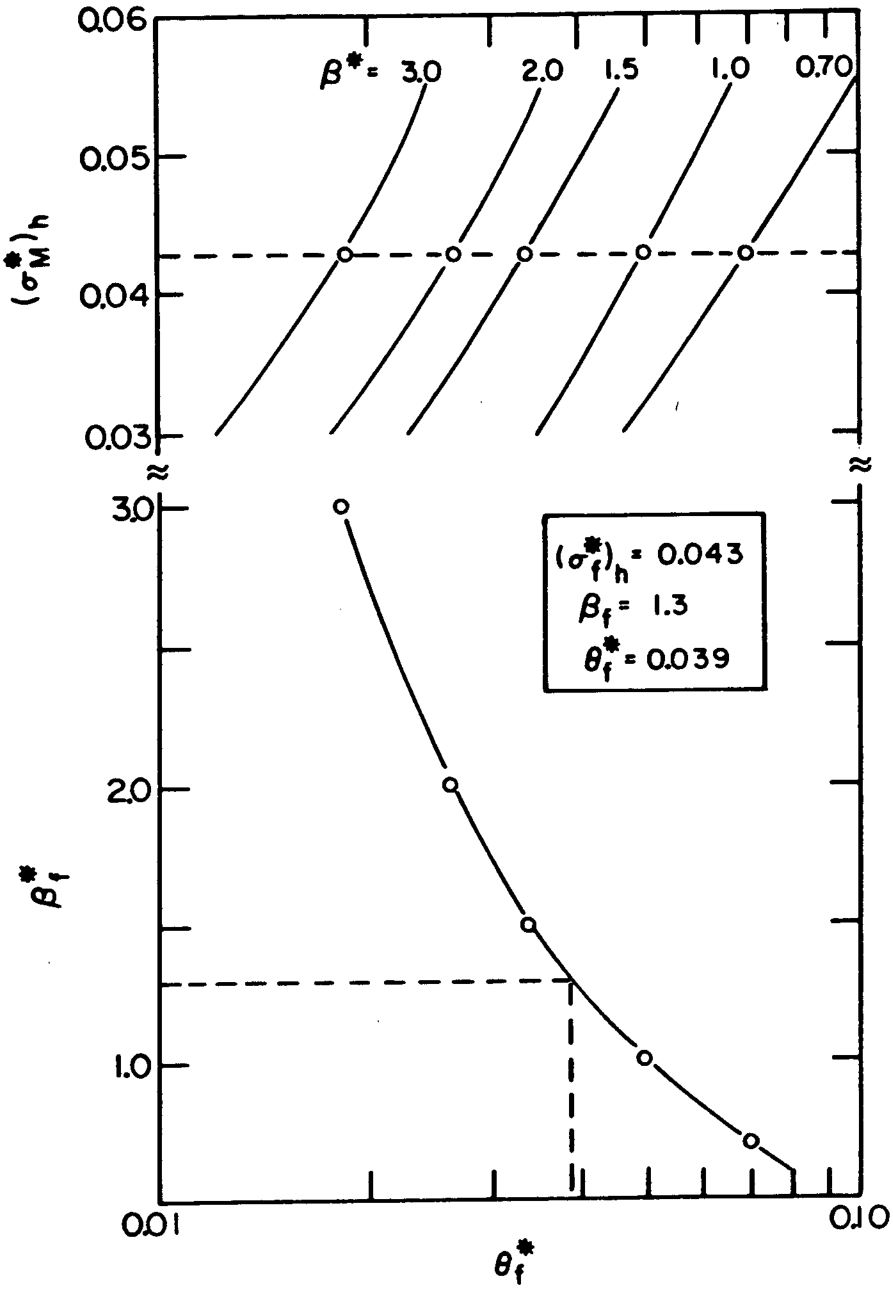

Figure 4.22 Illustration of the graphical procedure for determining Fourier modulus at fracture by inverting the solution for the dimensionless maximum principal tensile stress

is found using

$$t_f = \frac{\theta_f^* \ell^2}{a} \, . \qquad (4.26)$$

Once t_f has been determined, the temperature profile at fracture can be calculated using the appropriate analytical solution (equation 4.4 for the example case), and used with the finite element numerical method to compute the thermal stress and strain energy density U_o fields and total strain energy at the instant of fracture. Figure 4.23 shows the temperature profile, and centerline σ_x and U_o distributions at fracture for the example case. A check on the accuracy of the graphical procedure for determining time of fracture is the percent difference between the finite element computed value of fracture strength - $(\sigma_f)_{FE}$ - and the specified value, which in all cases was less than 5%.

The temperature profile in Figure 4.23 indicates that the thermal shock fracture, at least for the example case, is not a high temperature phenomenon. At the moment of fracture the thermal disturbance at the boundary had not fully penetrated the specimen. The hot face temperature (T_{hf}) reached a value of only 220°C. In general, fracture initiation is rapid in thermal shock experiments and there is little time available for the development of the thermal field. Thus

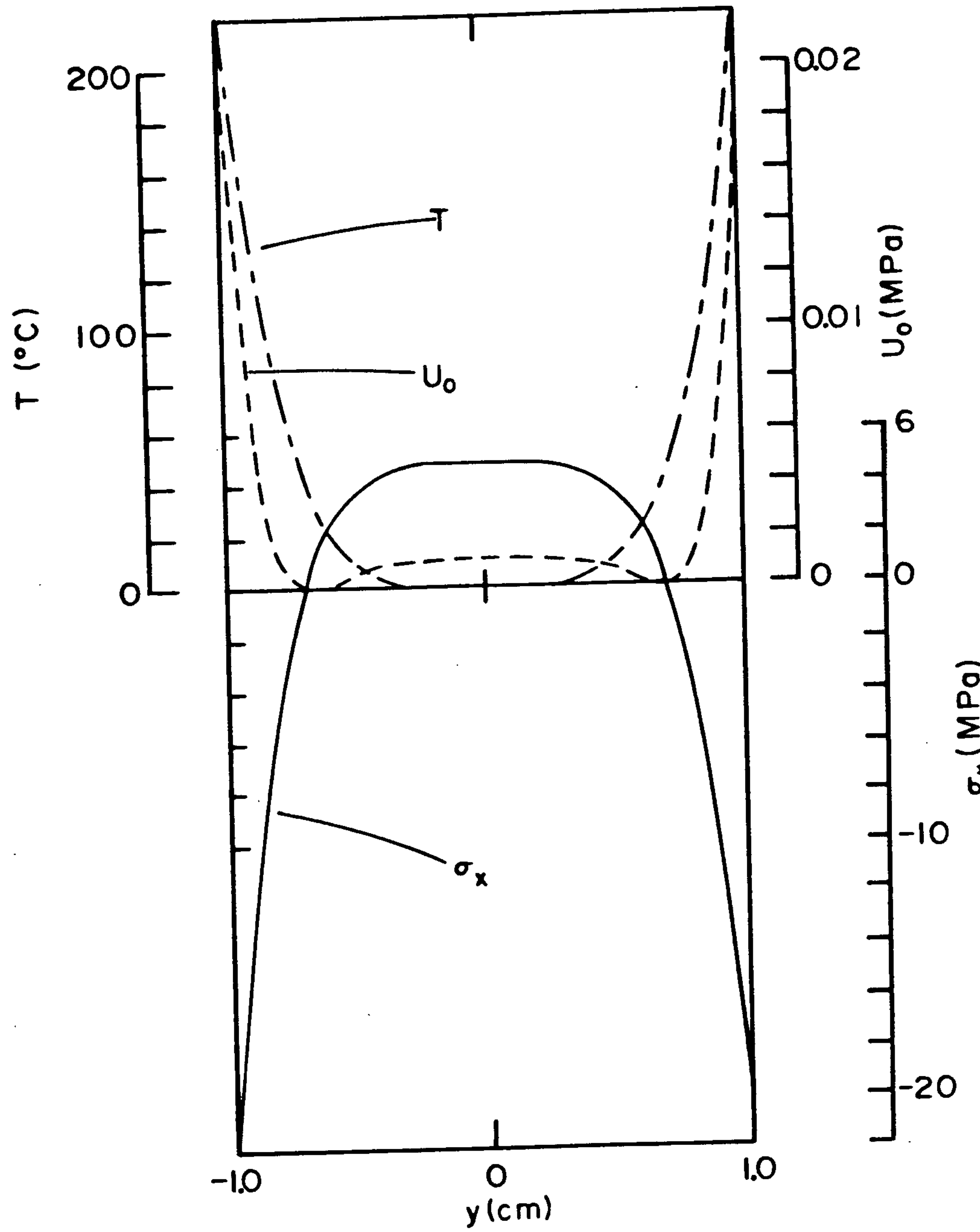

Figure 4.23 Temperature profile and center line stress and strain energy density fields at fracture for the example case of Table IX.

the influence of temperature-dependent properties on fracture behaviour is not expected to be significant for rapid heating or cooling thermal shock tests.

Three features of the σ_x stress distribution are worth noting. First, on heating the compressive stresses near the surface initially develop more rapidly than the tensile stresses in the central region. With time and penetration of the thermal field, the tensile stresses develop at a faster rate than the compressive stresses and hence the ratio of maximum compressive to maximum tensile stress declines with time. In general, for the thermal shock conditions considered in the following section, the magnitude of the surface stress is approximately three to five times greater than the maximum at the midpoint of the centerline at the instant of fracture.

Second, the tensile distribution in the central region is broad and flat, rather than sharp and pointed. Therefore it is quite likely that fracture initiation occurs at a point other than the midpoint of the center line and that, after sectioning along the mid-plane, specimen halves contain different size cracks. The expectation in these types of thermal shock experiments is that the average fracture strength reflects the actual size of the crack formed.

Third, crack propagation on heating is from the interior toward the surface, from a tensile region toward a compressive region. This is a characteristic feature of the traction-free thermal shock problem which undoubtedly is linked to the crack arrest capability of specimens. The shape of the centerline U_o distribution associated with the infinite slab heating case is also typical with minimums at the points of transition from tension to compression, maximums at the surface with a corresponding steep gradient in the compressive zones, and a broad, relatively uniform region of much-reduced magnitude in the central tensile zone.

The natural starting point for the derivation of a thermoelastic damage resistance parameter is the Hasselman[45] premise that the area over which a crack will propagate is directly proportional to the elastic energy stored at fracture and inversely proportional to surface energy per unit area. Total strain energy is computed by numerically integrating the two-dimensional strain energy density field over the area defined by the width and length of the specimen. This gives total strain energy in units of Joules/unit thickness. In all cases unit thickness was taken to be 1 cm.

In this work the Hasselman premise is modified slightly such that the area of crack propagation is taken to be directly proportional to the elastic energy available for the production of crack surface U_a, where U_a is that fraction of total strain energy U_f given by

$$U_a = \frac{U_f}{2w} \qquad (4.27)$$

Although somewhat arbitrary, the rationale for expression (4.27) is that the extent of crack propagation is dependent on the amount of elastic energy in the neighbourhood of the crack rather than in the total strain energy associated with the whole specimen. For the infinite slab case cracks are expected to propagate along the centerline. The factor (U_f/w) represents the average strain energy content of a 1 cm x 1 cm column of material running the length of the centerline.

From Figure 4.23 it is clear that along the center line part of the elastic energy is associated with the zones of compression at the two hot faces and the remainder with the tensile zone in the central region. It is assumed that only the portion of strain energy associated with the tensile region is consumed in the production of new crack surface and that this value is one-half of the average amount contained in the 1 cm x 1 cm column or ($U_f/2w$). While the fraction of strain energy associated with the compressive zones at the two hot faces and the tensile zone in the central region is expected to vary from case to case, the factor of one-half is considered reasonable as the shape of the stress and strain energy density fields in Figure 4.23 is typical.

The area of crack propagation A_c - to be thought of as a useful parameter rather than the actual measure of fracture surface - is thus given by

$$A_c = \frac{U_a}{\gamma} \tag{4.28}$$

The parameter A_c has the units of (area/area) which should be interpreted as the area of crack propagation equivalent to the consumption of the amount of available elastic strain energy stored in the 1 x 1 cm column of material running the length of the center line.

And finally, the thermoelastic damage resistance parameter is simply defined as the inverse of the area of crack propagation, i.e.

$$R_d = A_c^{-1}. \tag{4.29}$$

Theoretically, this single parameter reflects the influence of mechanical and thermal properties, geometry, and thermal boundary condition, while at the same time distinguishing between the heating and cooling cases.

4.3.6 Thermoelastic Analysis of Previous Work

4.3.6.1 Introduction

In this section thermoelastic analysis is applied to the experimental work of Nakayama, Larson, and Semler. The thermal models of section 4.3.2, the solutions for the maximum principal tensile stress contained in Appendix IV, and the procedure outlined in the last section are used to determine the time of fracture and total strain energy at fracture for each thermal shock experiment. The observed thermal shock behaviour of each study is interpreted in terms of the resistance to damage parameter R_d and a resistance to fracture initiation parameter R_i which will be derived in the following section.

Together, the Nakayama, Larson, and Semler studies consider all the pertinent parameters that have a bearing on the thermal shock behaviour of traction-free bodies: (i) thermal and mechanical properties, (ii) geometry, (iii) thermal boundary condition, and (iv) heating/cooling. The Nakayama results are considered in greatest detail as the study covers the broadest range of commercial refractories, highlights the influence of geometry, and the results appear to be the most consistent with regard to the determination of ΔT_{cr}. The Larson and Semler results are used to support a thermoelastic interpretation of the influence of heating and cooling and geometry on thermal shock fracture behaviour.

Thermal diffusivity and thermal conductivity are both fundamental properties required for the thermoelastic analysis. Without knowledge of each the temperature field causing fracture can not be determined. In no case were values of thermal diffusivity given, and in only one case - the Nakayama study - was thermal conductivity supplied. Estimates of the thermal conductivity were obtained from references [19-21]. For all cases the thermal diffusivity in cm^2/s was taken to be twice the value of k in cal/s cm°C, a reasonable estimate for most refractories which follows from typical values of bulk density and specific heat.

In all cases the plane strain two-dimensional formulation was used and total strain energy was calculated on the basis of an out-of-plane thickness of 1 cm. A value of $\nu=0.25$ was used when Poisson's ratio was not supplied. Results of the thermoelastic analysis of the Nakayama, Larson, and Semler thermal shock studies are contained in Appendices V, VI, and VII, respectively.

4.3.6.2 Nakayama

4.3.6.2.1 Resistance to Fracture Initiation

The results of the thermoelastic analysis of Nakayama's experiments are first considered from a fracture initiation standpoint. Due to the large number of variables, the initial requirement for the derivation of a resistance to fracture initiation parameter is an expression which relates the dimensionless parameters at fracture. Kingery used a simple proportionality between peak dimensionless maximum principal tensile stress and Biot modulus. A slightly more complicated expression which includes Fourier modulus and dimensionless fracture strength can be obtained by considering Figure 4.22 and noting the general trends of $(\sigma_f^*)_h$, β_f^*, and Θ_f^* when one variable is held fixed.

For fixed $(\sigma_f^*)_h$, it is apparent from the curve at the bottom of the figure that β_f^* is inversely proportional to θ_f^*. The net effect of increasing $(\sigma_f^*)_h$ is to push the β_f^*-θ_f^* curve up and to the right which, for constant β_f^*, leads to an increase in θ_f^*. These general trends among the dimensionless parameters at fracture initiation can be expressed mathematically as

$$\theta_f^* \propto \frac{(\sigma_f^*)_h}{\beta_f^*} \tag{4.30}$$

The plot of Fourier modulus versus the ratio of dimensionless fracture strength and Biot modulus for values at ΔT_{cr} (see Table X) in Figure 4.24 suggests that the direct porportionality of equation (4.29) holds with the restriction that - due to the nonlinearity of the stress solution - the range of the dimensionless parameters is not too great.

TABLE X

Data and Dimensionless Parameters for Fracture Initiation Analysis of Results for Critical Temperature Difference of Nakayama Study

Brick	$a \times 10^6$ $(\frac{m^2}{s})$	ΔT_{cr} (°C)	h_{cr} $(\frac{J}{sm^2 °C})$	$(\sigma_f^*)_h$	β^*_{cr}	θ^*_{cr}	$\frac{(\sigma_f^*)_h}{\beta^*_{cr}}$
A	1.4	950	135	0.0177	0.46	0.0425	0.0385
B	0.60	1050	170	0.0731	1.35	0.0730	0.0541
C	0.60	850	108	0.0254	0.86	0.0327	0.0295
D	0.60	1050	170	0.0686	1.35	0.0682	0.0508
E	4.4	1100	186	0.0131	0.20	0.0680	0.0655
F	0.50	950	135	0.0428	1.28	0.0390	0.0334
F'	0.50	650	65	0.0626	1.23	0.0650	0.0510

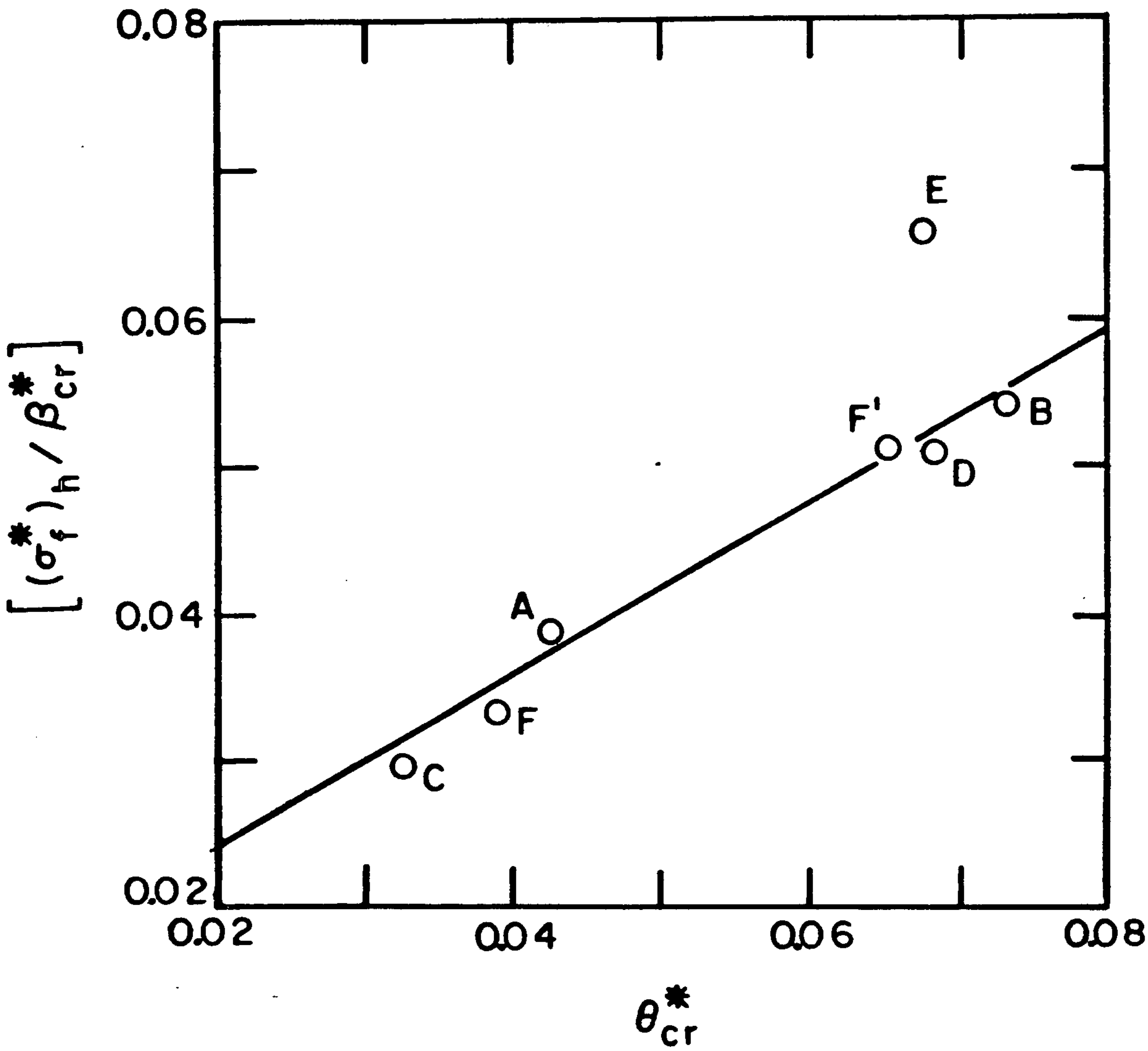

Figure 4.24 Plot of the ratio of dimensionless fracture strength to Biot modulus versus Fourier modulus at fracture for ΔT_{cr} of the Nakayama experiments.

The results for the two sizes of the F specimen, with the F' designation indicating the 10 x 4 cm size, fit into the general trend.

The dimensional from of equation (4.30) is

$$\frac{at_f}{\ell^2} \propto \frac{\sigma_f\ (1-\nu)}{E\ \alpha\ \Delta T_f} \cdot \frac{k}{h_f \ell} \tag{4.31}$$

which can be used to derive another resistance to fracture initiation parameter. Regardless of the way in which equation (4.31) is manipulated, it is clear that when the transient aspect of the thermal shock problem is accounted for the variable t_f must be present. A natural form is to have t_f as the dependent variable which, on rearranging equation (4.31) gives

$$t_f \propto R_i \tag{4.32}$$

where the resistance to fracture initiation parameter R_i is defined as

$$R_i = \frac{\sigma_f\ (1-\nu)\ k\ \ell}{E\ \alpha\ (h\Delta T)_f\ a} \tag{4.33}$$

In this derivation, resistance to fracture initiation is directly proportional to time of fracture - the only measurable parameter of a thermal shock experiment associated with fracture initiation and also to the temperature of the hot face at fracture.

The Kingery analysis and the previous derivation are similar in that they both begin with a dimensionless relationship. However, in disregarding the transient aspect of the problem, the Kingery approach over-emphasizes the role of material properties and, as will be shown shortly, incorrectly accounts for the influence of the thermal properties. Furthermore, while equating resistance to fracture initiation to temperature difference required to produce fracture might make sense from a laboratory experimental standpoint, it is not a suitable approach for the industrial problem where one means of preventing thermal shock fracture is by controlling the thermal conditions through the adjustment of both ΔT and h. The preheating of linings of many industrial processes is a typical example of this.

Two characteristic features of the thermal shock problem not accounted for by the Kingery analysis are the interdependence of material properties with other parameters and the time-dependence of fracture. In evaluating a group of refractories two parameters which might be of interest are time of fracture and temperature of hot face at fracture T_{hf}. Some thermoelastic results which pertain to the critical thermal condition of the Nakayama study are given in Table XI and plotted in Figure 4.25 where the t_f-R' points are indicated by circles, the t_f-R_i points by squares, and the T_{hf}-R_i points by triangles. The

TABLE XI

Time of Fracture and Resistance to Fracture Initiation Parameters

Brick	ΔT_{cr} (°C)	R' $(\frac{J}{m \cdot s})$	t_f (s)	R_i (s)	T_{hf} (°C)	R_d
A	950	49.4	3.00	2.72	93	0.56
B	1050	96.3	12.2	9.32	324	1.33
C	850	27.2	5.45	5.10	131	0.78
D	1050	91.7	11.4	8.74	315	1.32
E	1100	132	1.55	1.47	63	1.75
F	950	42.7	7.80	6.34	221	2.43
F'	650	42.7	52.0	38.5	179	1.88

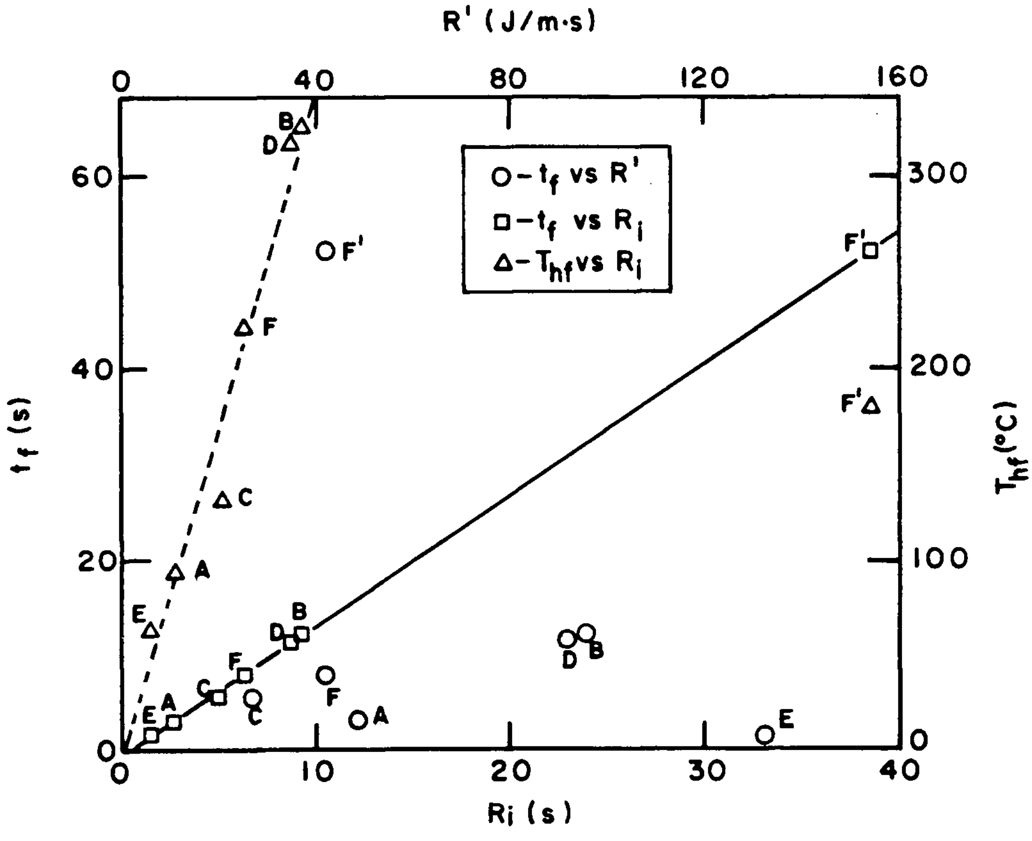

Figure 4.25 Time of fracture and temperature of hot face at fracture versus resistance to fracture initiation parameter for ΔT_{cr} of the Nakayama experiments.

correlation of R_i with the computed values of t_f and T_{hf} (indicated by the solid and dashed lines in Figure 4.25) suggests that the single parameter R_i reflects the interdependence of material properties, geometry, and thermal boundary conditions on thermal shock behaviour.

It is apparent from Figure 4.25 that there is no overall correlation between t_f and R'. However, if only those specimens having similar thermal conductivity are considered (C-F-D-B), time of fracture appears to vary directly with the Kingery parameter. The points lying outside this trend are either associated with materials of high thermal conductivity (E-A) or different geometry (F'). As the Kingery parameter does not account for geometry, discussion is restricted to the underlying reason for the location of points A and E.

That the points A and E do not follow the general trend of the t_f-R' plot reflects the fact that the Kingery analysis incorrectly accounts for the role of thermal properties. According to the Kingery derivation (equation 4.24) resistance to fracture initiation is directly proportional to thermal conductivity k while the thermoelastic analysis suggests that it is directly proportional to the ratio of thermal conductivity to thermal diffusivity (k/a) - regardless of how thermal shock resistance is expressed (see equation 4.31). The discrepancy arises because the Kingery derivation ignores the transient aspect of the problem.

This is a significant point as the range of variation is large in one case and relatively small in the other. Table XII gives typical thermal properties for a wide spectrum of refractories. With the exception of the rebonded fused grain (RFG) MgO-chrome ore and dolomite refractories (the data of which was obtained from manufacturers brochures), the values of bulk density (ρ_b) and thermal conductivity were obtained from [20] and specific heat from [21]. Typical compositions of many of the materials in Table XII are given in Table XIII. The final two columns in Table XII gives values of k and (k/a) which have been normalized with respect to the values of silica. It is apparent from these values that the range of variation of k is greater than an order of magnitude while that of (k/a) is only about a factor of two.

The location of points E and A of the t_f-R' plot in Figure 4.25 is directly attributable to the fact that the Kingery parameter gives far too much weight to the variable k. In neglecting the transient nature of the problem, thermal diffusivity - the fundamental thermal property - is ignored. Thermal conductivity is primarily associated with the special case of constant heat transfer coefficient boundary condition, while thermal diffusivity must be accounted for in all treatments of traction-free thermal shock problems in which the cause of stress is transient nonlinear temperature fields.

TABLE XII

Typical Thermal Properties of Various Refractories

Refractory	Mean Temp (°C)	$\rho_b \times 10^{-3}$ $(\frac{kg}{m^3})$	c_p $(\frac{J}{kg°C})$	k $(\frac{J}{sm°C})$	$a \times 10^6$ $(\frac{m^2}{s})$	$k/a \times 10^6$ $(\frac{J}{m^3°C})$	N_k	$N_{k/a}$
Silica	148	1.81	795	1.10	0.762	1.44	1.0	1.0
Fireclay	167	2.35	837	1.42	0.719	1.97	1.3	1.4
60% Alumina	179	2.37	837	1.36	0.683	1.99	1.2	1.4
90% Alumina	151	2.79	837	2.38	1.02	2.33	2.2	1.6
99% Alumina	125	2.90	837	5.28	2.18	2.42	4.8	1.7
Chrome	160	3.11	754	2.16	0.921	2.35	2.0	1.6
Chrome-MgO	160	3.01	837	1.67	0.665	2.51	1.5	1.7
Forsterite Type	160	2.63	837	1.80	0.820	2.20	1.6	1.5
MgO-Chrome (DB)	131	2.79	879	1.79	0.729	2.46	1.6	1.7
MgO-Chrome (RFG)	93	3.20	879	5.19	1.85	2.81	4.7	2.0
Magnesia	161	2.79	921	10.1	3.93	2.57	9.2	1.8
Dolomite	260	2.96	921	3.75	1.37	2.74	3.4	1.9
Clay-bonded SiC	162	2.66	712	18.4	9.72	1.89	16.7	1.3
Zircon	160	3.76	504	4.16	2.19	1.90	3.8	1.3

TABLE XIII

Typical Compositions of Various Refractories (after reference 20)

Type of Brick	Per Cent Silica (SiO_2)	Per Cent Alumina (Al_2O_3)	Per Cent Titania (TiO_2)	Per Cent Other Oxides
Fireclay				
Superduty	49-56	40-44	1.5-2.5	2.5-4.0
High-Duty	51-61	35-41	1.7-3.0	3-6
Medium-Duty	57-70	25-38	1.3-2.1	4-7
Low-Duty	60-70	22-33	1.0-2.0	5-8
Semi-Silica	72-80	18-26	1.0-1.5	1-3
High-Alumina				
50% Alumina Class	41-47	47.5-52.5	2.0-2.8	3-4
60% Alumina Class	31-37	57.5-62.5	2.0-3.3	3-4
70% Alumina Class	20-26	67.5-72.5	3.0-4.0	3-4
80% Alumina Class	11-15	77.5-82.5	3.0-4.0	3-4
90% Alumina Class	7.5-9.0	89-91	0.4-0.8	1-2
Mullite Class	18-34	60-78	0.5-3.1	1-3
Corundum Class	0.2-1.0	98.0-99.5	Trace	0.3-1.0

Type of Brick	Per Cent Silica (SiO_2)	Per Cent Alumina (Al_2O_3)	Per Cent Lime (CaO)	Per Cent Magnesia (MgO)	Per Cent Iron Oxide (Fe_2O_3)	Per Cent Chromic Oxide (Cr_2O_3)	Per Cent Other Oxides
Silica							
Superduty	95-97	0.15-0.35	2.5-3.5	......	0.3-2.2	......	0.02-0.10
Conventional	94-97	0.45-1.20	1.8-3.5	......	0.3-0.9	......	0.10-0.30
Basic							
Chrome	3-6	15-34	......	14-19	11-17	28-38	1-2
Forsterite	30-39	1-11	......	47-55	7-11	......	1-3
Magnesite	0.7-10.0	0.3-1.5	1.0-3.5	85-93	0.3-7.0	......	0.5-1.0
Magnesite, High-Periclase	0.5-5.0	0.2-1.0	0.5-1.5	92-98+	0.2-1.0	......	0.0-0.6
Magnesite, Spinel-Bonded	1.0-2.0	8.5-10.5	1.0-1.5	86-88	0.5-1.0	......	0.1-0.6
Magnesite-Chrome*	3.0-8.5	4.5-23.0	0.7-1.5	53-82	2.5-7.5	4.5-16.0	......
Chrome-Magnesite*	4-8	16-27	0.7-1.5	27-53	8-14	18-28	......

* Composition after heating and removal of all volatiles.

Figure 4.26, which shows a plot of time of fracture versus R_i for the radiation temperature differences of ΔT_{cr}, 1200°C, and 1500°C, indicates that the positive correlation holds for other thermal conditions than ΔT_{cr}. The linear relationship between t_f and ΔT_f shows that the effect of exceeding ΔT_{cr} is simply to cause fracture to occur at an earlier time. That is, as indicated by equation (4.31), the time of fracture is inversely related to the temperature difference causing fracture, an important dependence which is not apparent from the Kingery analysis.

As a final point, material E is the most thermal shock resistant according to R' while R_i suggests that the same material is the least thermal shock resistant. As noted above, this can be attributed to the fact that the time of fracture is inversely proportional to the temperature difference causing fracture. The important practical consideration is that the thermal shock resistance parameter used for the assessment of a group of refractories reflect the requirements of the industrial application. Depending on the particular problem, time to fracture, temperature of hot face at fracture, or the magnitude of the thermal boundary condition causing fracture may be the relevant parameter

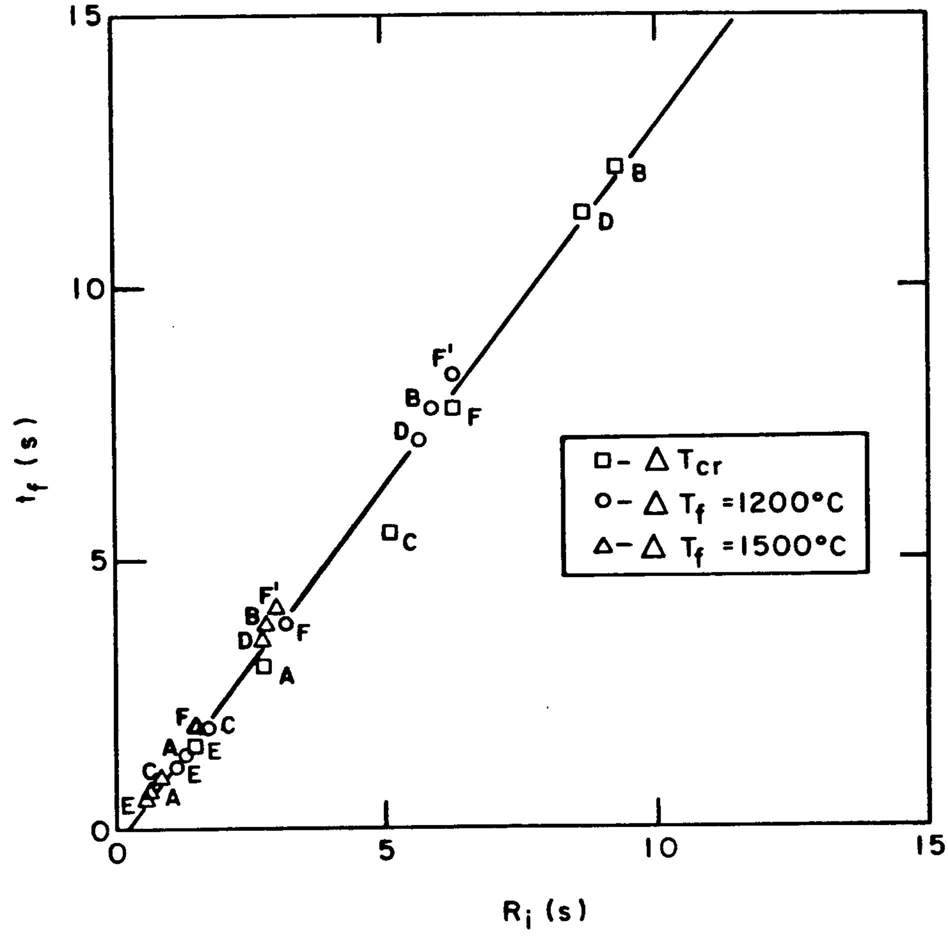

Figure 4.26 Time of fracture versus R_i for ΔT_{cr}, ΔT_f=1200°C, and ΔT_f=1500°C of the Nakayama experiments.

4.3.6.2.2 Resistance to Damage

A thermoelastic interpretation of thermal shock damage is now presented. Figure 4.27 shows a plot of percent strength loss at the critical radiation temperature versus the damage resistance parameter R_d. The inverse relationship is support for the basic premise that strength loss is proportional to the available strain energy at fracture U_a and inversely proportional to the surface energy γ. The scatter apparent in the plot is quite reasonable in light of the sources of error inherent in the strength measurements.

Figure 4.28 shows R_d-ΔT_f curves and the strength retained relationships for the two materials which experience the greatest and least damage on fracture at ΔT_{cr}, materials A and E. Figure 4.29 gives the R_d-ΔT_f curves for the two sizes of specimen F. As the surface energy term is constant for a given material the variation of R_d with ΔT reflects the variation of available strain energy at fracture.

The thermoelastically-predicted curves in Figure 4.28 reflect not only the general trend, but also the relative steepness of the strength retained curves for both materials. Thus the parallel trend of the R_d-ΔT_f curves and the corresponding experimental strength loss curves provides strong support for the fundamental assumption of the thermoelastic model that extent of crack propagation is proportional to available strain energy at fracture.

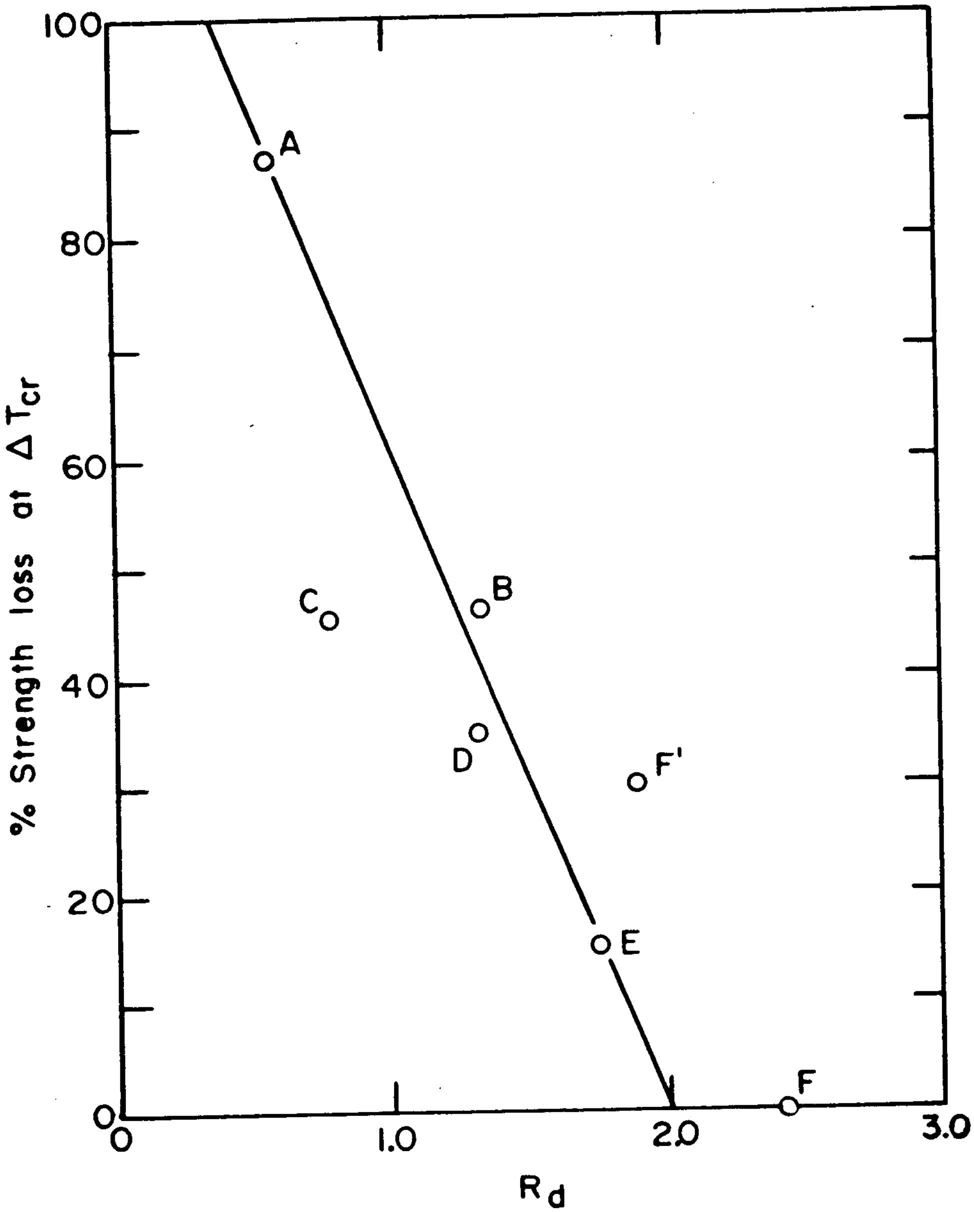

Figure 4.27 Strength loss at ΔT_{cr} versus damage resistance parameter R_d for the Nakayama study.

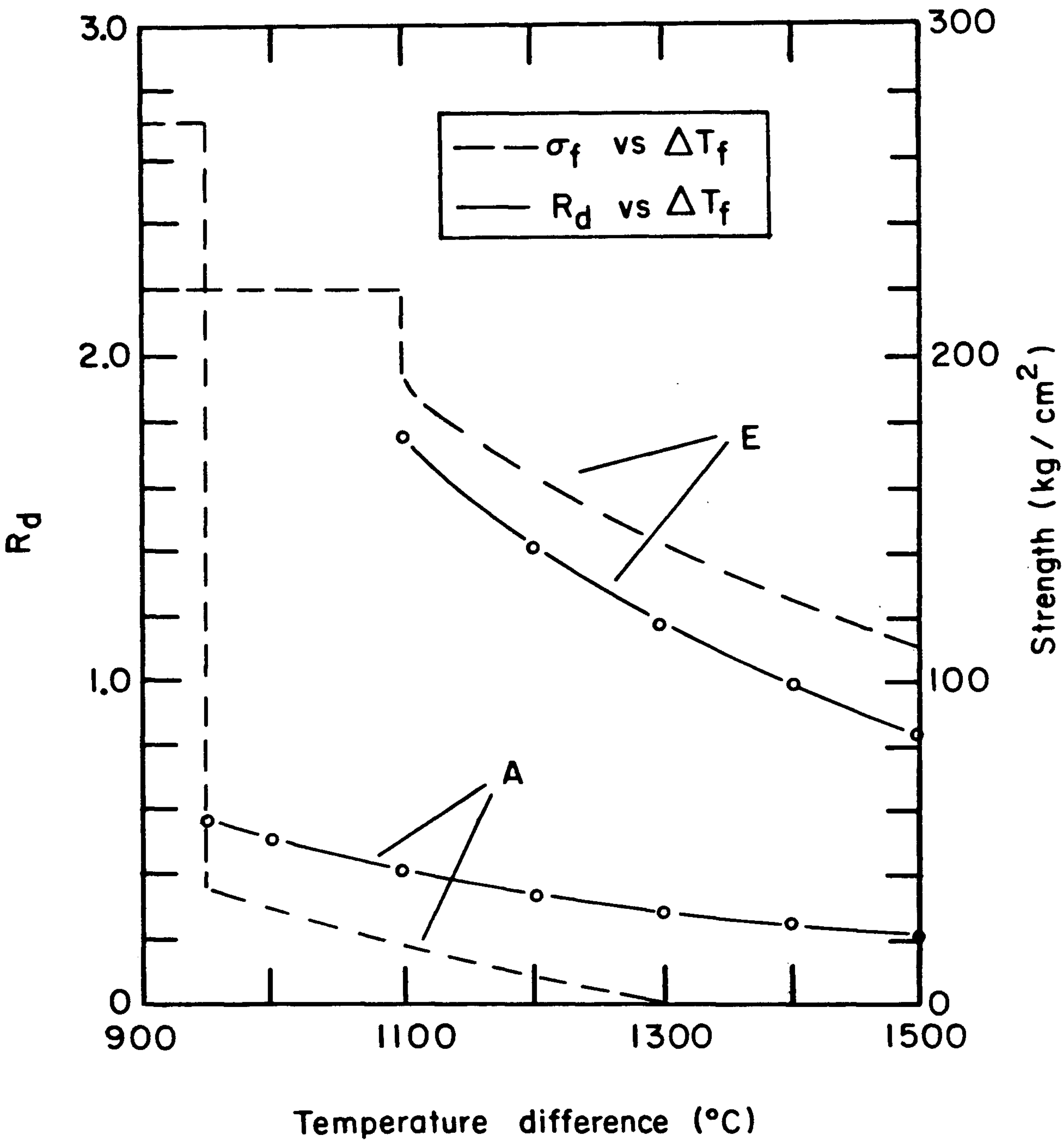

Figure 4.28 Strength retained and damage resistance parameter R_d versus radiation temperature difference for materials A and E of the Nakayama study.

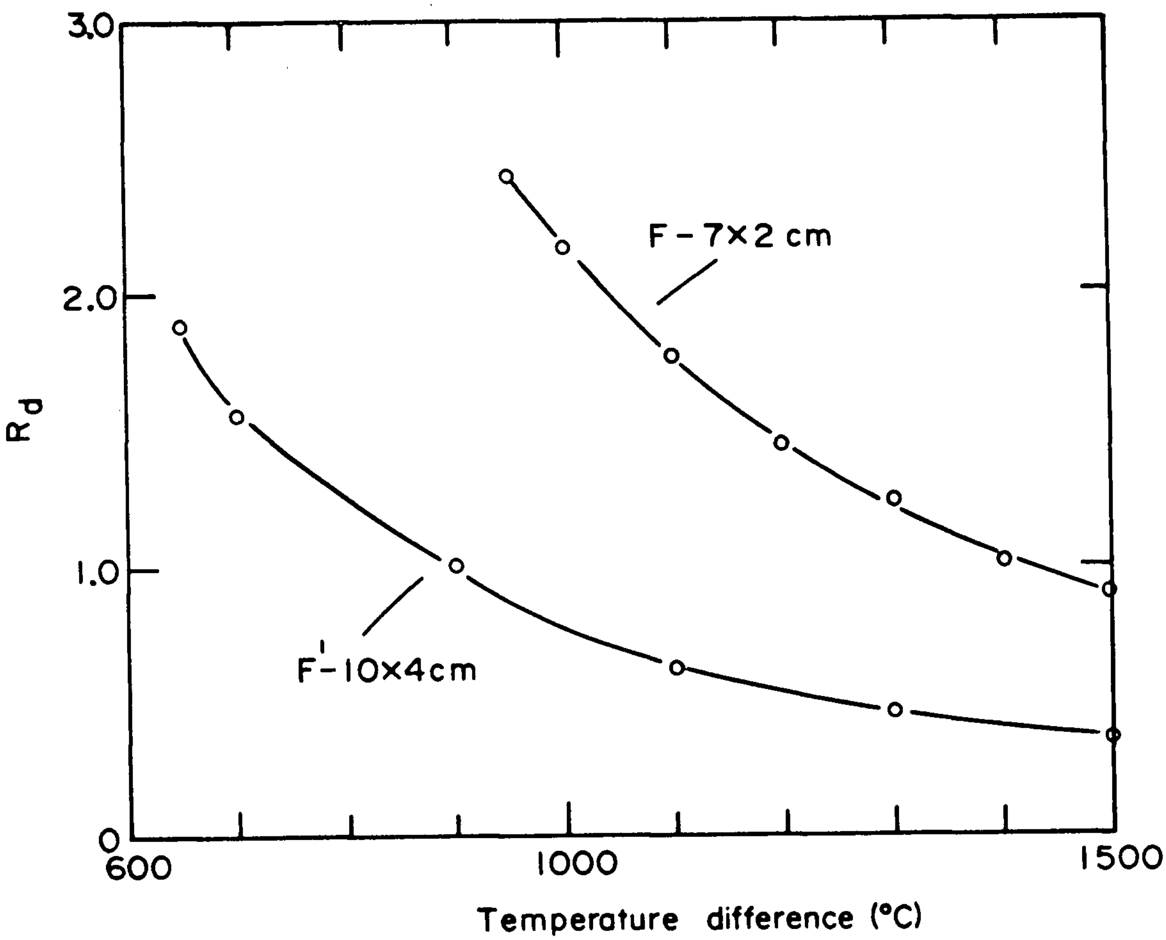

Figure 4.29 Thermal shock resistance parameter R_d versus radiation temperature difference for the two sizes of specimen F of the Nakayama study.

A key point is that R_d distinguishs between the thermal shock damage resistance of different sizes of a specimen as indicated by the relative positions of points F and F' in Figure 4.27 and the nature of the curves in Figure 4.29. This is important with regard to the design and selection of refractories for industrial linings, as components are often available in a variety of sizes and shapes, and represents a significant advantage in comparison to the Hasselman damage resistance parameters.

For materials in which elastic modulus plays a dominant role in determining fracture behaviour, the Kingery and Hasselman parameters indicate that resistance to fracture initiation and resistance to damage are inversely related. Nakayama produced correlations in support of both the Kingery initiation parameter R' and the Hasselman damage parameter R'''', but did not note any trend between the two. The thermoelastic model of thermal shock behaviour is ideal for the study of the interdependence of resistance to initiation and resistance to damage.

Figure 4.30 shows a plot of the R_i and R_d values of each specimen for the radiation temperature of 1200 °C. The material properties of each brick are given in Table III along with dimensionless

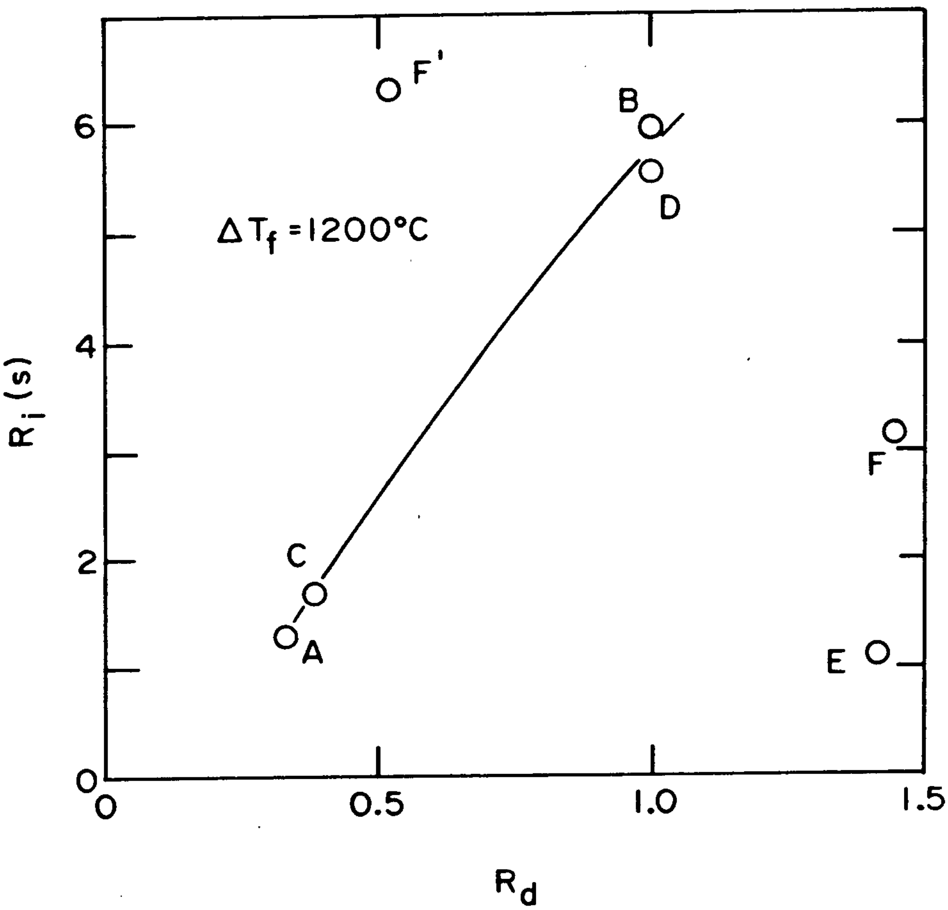

Figure 4.30 Resistance to fracture initiation R_i versus resistance to damage R_d for ΔT_f=1200°C of the Nakayama study

fracture strength σ_f^*, where

$$\sigma_f^* = \frac{\sigma_f\ (1-\nu)}{E}, \tag{4.34}$$

which is the relevant fracture initiation parameter associated with strength, rather than σ_f alone. As there is no wide variation in γ, the Nakayama results essentially reflect the effect of the thermoelastic variables.

While the role of material properties with regard to fracture initiation is apparent from equation (4.33), a simple expression relating material properties to damage resistance is not obtained easily due to the complexity of the strain energy computation. Thus the role of material properties with regard to damage resistance is evaluated by comparing the results of individual cases.

The influence of thermal expansion coefficient on combined resistance is evident from the location of the points of materials A, B, C, and D, which are connected by the solid line in Figure 4.30. The high values of R_i and R_d for the high-alumina specimens (B and D) can be attributed primarily to extremely low thermal expansion coefficient, as all other properties are of intermediate value. Even though there is some variation in the other properties, the poor resistance to both fracture initiation and damage of the dense aluminosilicates (A and C) is due mainly to high thermal expansion coefficient.

While the relative thermal shock resistance of A, B, C, and D can be explained in terms of α alone, that of materials E and F is due to a complex interaction of the mechanical and thermal properties. The larger R_1 value of F, three times that of E, follows in a straightforward manner from the values of σ_f^* and α, but the underlying reason for the eqivalent damage resistance of the two materials is not obvious as the materials possess extreme values of E, σ_f^*, k, and a. In the use of E and F difference in thermal expansion coefficient has only a marginal effect on the relative damage resistance as the smaller α of F is compensated for by the larger γ of material E.

Table XIV contains the pertinent data and results of selected cases based on refractories E and F. The temperature fields and stress distributions at fracture for cases E, E1, E2, and E3 are shown in Figure 4.31 and 4.32, respectively, and for case F in Figure 4.23. While no analytical expression exists which relates strain energy and temperature distribution at fracture, equation (4.35), which applies to the infinite slab geometry (see Appendix I)

$$U_0 = \frac{1}{2} \sigma_x \alpha \ (T_{ave} - T) \tag{4.35}$$

TABLE XIV

<u>Data and Results for the Analysis of Fracture Behaviour of Materials E and F Subjected to a Thermal Shock of ΔT=1200°C</u>

Case	k $(\frac{J}{sm°C})$	$a \times 10^6$ $(\frac{m^2}{s})$	σ_f (MPa)	E (GPa)	$\sigma_f^* \times 10^3$	t_f (s)	U_f (J/m²)	T_{hf} (°C)	R_i (s)	R_d
F	1.0	0.50	4.8	10.4	0.346	3.8	0.041	317	3.14	1.44
E	9.2	4.4	22.0	91.3	0.181	1.15	0.049	71	1.11	1.41
E1	1.0	0.50	22.0	91.3	0.181	1.24	0.203	200	1.11	0.34
E2	9.2	4.4	42.1	91.3	0.346	2.50	0.109	103	2.12	0.64
E3	9.2	4.4	22.0	47.7	0.346	2.50	0.057	103	2.12	1.23
F1	1.0	0.50	4.8	10.4	0.346	10.8	0.019	462	7.62	3.02

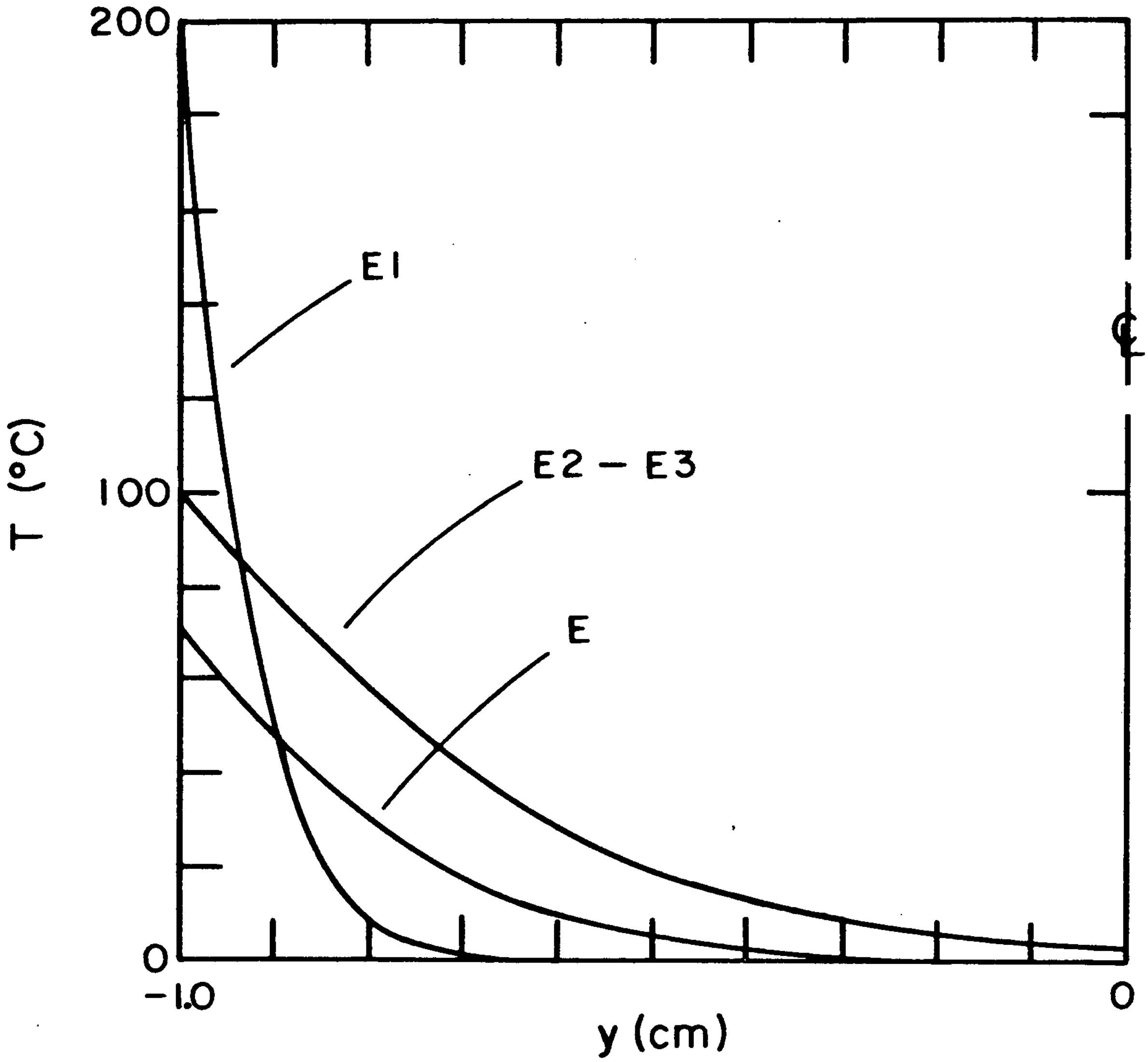

Figure 4.31 Temperature distributions at fracture for cases E, E1, E2, and E3 of Table XIV.

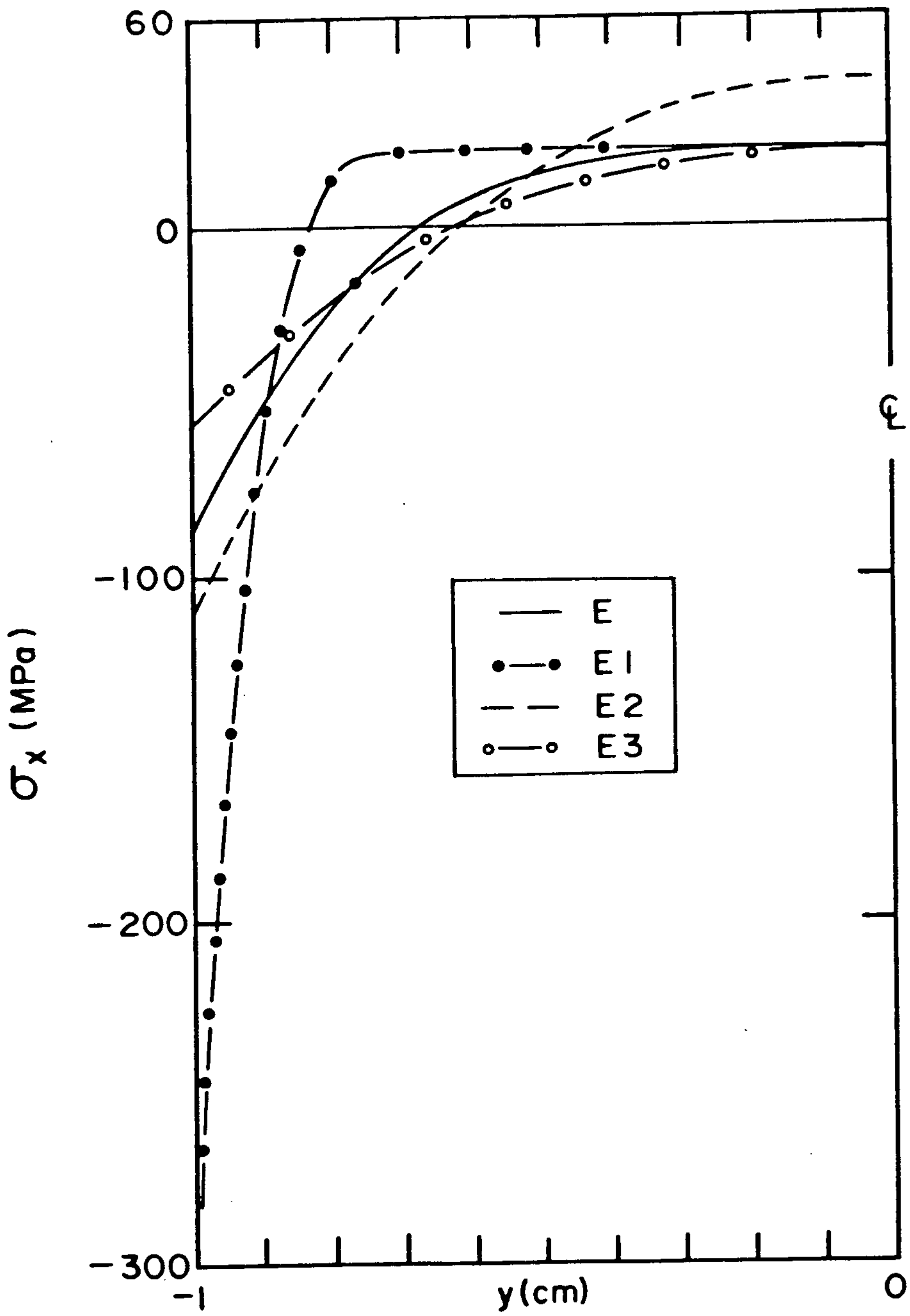

Figure 4.32 Stress distribution at fracture for cases E, E1, E2, and E3 of Table XIV.

is helpful for damage analysis as it relates the temperature and stress distribution to the strain energy density function which, when integrated over the the region of the slab, gives the total strain energy.

In case E1, the effect of a change in thermal conductivity is investigated by assigning the thermal properties of F to E. The results in Table XIV indicate that an order of magnitude decrease in k reduces R_d by a factor of four with negligible impact on R_i. From Figure 4.31 it is apparent that the reduction in k produces a much steeper temperature gradient and, from Figure 4.32, that correspondingly higher stresses and strains develop in the hot face region and, consequently, greater strain energy at fracture. This is due to the much-reduced rate of heat flow away from the boundary region due to the lower thermal properties of case E1. A potentially beneficial effect of the reduction in k apparent from cases E and E1 is a significant increase in hot face temperature at fracture.

Thus resistance to damage appears to be strongly dependent on the magnitude of thermal conductivity while the time of fracture or R_i is not. High values of R_d are associated with large values of thermal conductivity and thermal diffusivity. In neglecting the transient aspect of the problem the Hasselman derivation does not account for the influence of the thermal properties on damage.

In cases E2 and E3, first the fracture strength and then the elastic modulus of material E are changed such that σ_f^* of material E is identical to that of material F. A comparison of the results for cases E and E2 indicates that the effect of doubling σ_f is to essentially double R_i and halve R_d. The increase in U_f noted for case E2 is attributed primarily to the larger σ_x field at fracture rather than to steeper temperature gradients as in case E1. The thermoelastic analysis is in agreement with the Kingery and Hasselman treatments as to the effect of changes in fracture strength σ_f on resistance to fracture initiation and resistance to damage.

The results for cases E and E3 indicate that reducing the elastic modulus by a factor of two causes resistance to fracture initiation to double, in agreement with the Kingery parameter; but has little effect on resistance to damage. Although the time to fracture of case E3 is double that of case E, it is apparent from Figures 4.31 and 4.32 that there is little difference in the $(T_{ave}-T)$ or σ_x distributions of the E and E3 cases. Hence the total strain energy at fracture and the damage resistance of the two cases is similar.

This result is in opposition to the Hasselman treatment which, according to the R'''' parameter, suggests that damage resistance is directly proportional to elastic modulus. It again reflects the fact that the Hasselman model does not account for the transient nature of the thermal phenomena. To summarize, the results of cases E2 and E3 indicate that, if thermal shock resistance is to be influenced by an increase in σ_f^*, then a reduction in elastic modulus is preferable to an increase in fracture strength. With the former approach an increase in the time to fracture and all the benefits associated with a more-highly developed thermal field are obtained without the disadvantage of increased strain energy at fracture.

The final case F1, in which material F is assigned the low thermal expansion coefficient of materials B and D, is illustrative of the type of material which would offer the best combined resistance to thermal shock. In addition to low thermal expansion coefficient, the characteristic features of such a material are low elastic modulus and moderate fracture strength, and high values of the thermal properties.

4.3.6.3 Larson

In this section a thermoelastic interpretation of some of the experimental work of Larson et al[88] is presented. Fracture initiation analysis is not attempted as the critical temperature differences were not well delineated. A strength loss versus R_d correlation for the heating case is presented and strength loss behaviour of specimens which exhibit catastrophic failure on heating and stable fracture on cooling is explained in terms of strain energy at fracture.

Table XV contains data and results from both the Nakayama and Larson studies for the case of thermal shock on heating of ΔT_f=1200 °C. The specimens are ranked in order of decreasing strength loss which is plotted against the damage resistance parameter in Figure 4.33. Although considerable scatter is evident, particularly in comparison to the correlations in Figures 4.8 and 4.9, a general trend of decreasing percent strength loss with increasing R_d is discernible. Further support for the thermoelastic approach is the fact that results of independent investigators using the same thermal shock test, but specimens of a different size and type, can be presented in the same correlation.

While Larson found positive correlations between percent strength retained vs. $(R'''')^{-1}$ for catastrophic behaviour and strength loss over 200°C range (psi) vs. R_{st} for stable behaviour (Figures 4.8 and 4.9), it is clear that there are no trends within the general trend in Figure 4.33. Neither strength loss of specimens exhibiting catastrophic behaviour (squares) or stable fracture (circles) correlate with R_d. This indicates that the mode of fracture behaviour is not a characteristic feature of thermal shock behaviour in the thermoelastic

TABLE XV

Summary of Larson and Nakayama Results for Heating and ΔT=1200°C

Brick	k $(\frac{J}{sm°C})$	a x 10^6 $(\frac{m^2}{s})$	α x 10^6 $(°C^{-1})$	σ_f (MPa)	E (GPa)	γ (J/m^2)	R_d	$\%\sigma_{loss}$
A	2.9	1.4	15.5	25.8	74.2	40.1	0.33	96-C
C	1.3	0.60	15.5	14.2	31.9	44.7	0.38	65-C
23	1.7	0.80	6.9	28.0	75.8	57.3	0.52	69-C
F'	1.0	0.50	8.5	4.8	10.4	41.2	0.52	71-C
27	1.3	0.60	5.7	22.9	55.8	62.9	0.67	0-C
28	1.3	0.60	6.2	16.5	40.0	62.0	0.85	48-C
34	1.3	0.60	7.0	10.1	22.8	46.5	0.94	66-C
B	1.3	0.60	3.5	20.0	55.7	48.6	0.99	70-C
D	1.3	0.60	3.5	16.0	47.6	39.1	1.00	73-C
15	2.1	1.0	7.3	11.2	33.8	54.1	1.39	18-S
E	9.2	4.4	12.6	22.0	91.3	49.6	1.41	39-C
F	1.0	0.50	8.5	4.8	10.4	41.2	1.44	38-S
19	1.7	0.80	7.4	11.4	23.4	70.1	1.46	26-S
6	2.9	1.4	8.0	19.0	55.8	91.1	1.57	17-S
2	4.2	2.0	9.4	14.2	58.6	58.2	1.63	19-S
21	1.7	0.80	6.9	7.03	18.6	59.6	2.21	42-S
8	2.5	1.2	7.8	13.7	61.4	93.8	2.36	38-C
31	1.3	0.60	6.6	4.07	16.5	58.9	3.53	37-C

C - Catastrophic
S - Stable

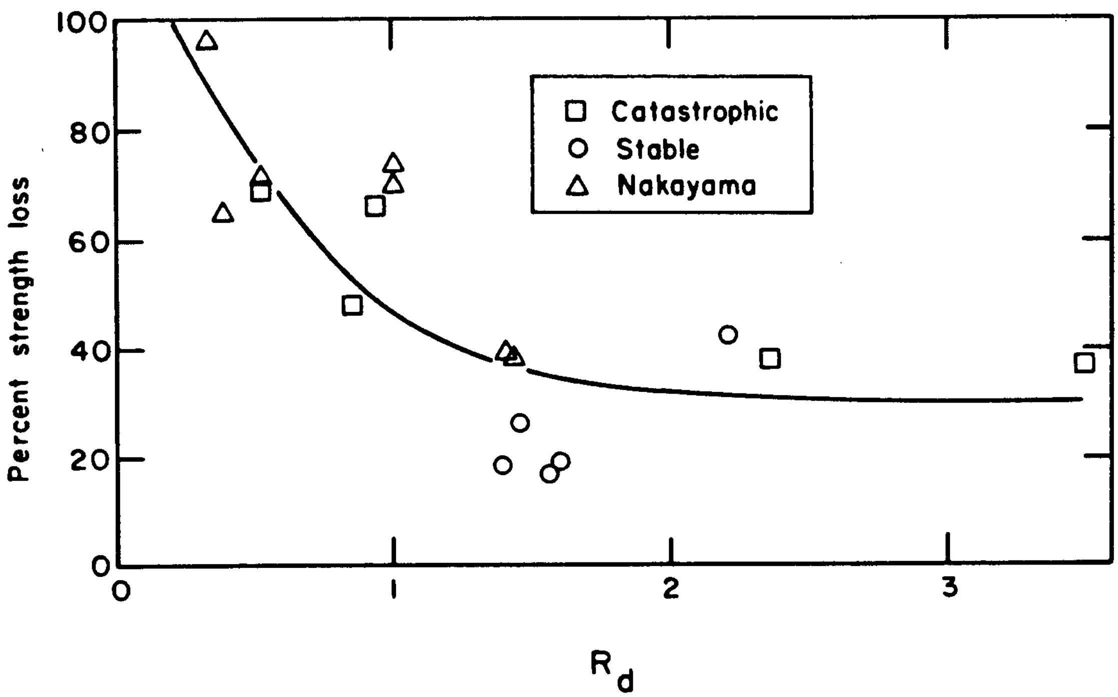

Figure 4.33 Strength loss versus thermal shock resistance parameter R_d. Results from both Nakayama and Larson studies for a thermal shock on heating of 1200°C.

analysis as it is in the Hasselman treatment. The most that can be said is that the relative location of the circles in Figure 4.33 indicates that percent strength loss of the stable specimens is generally smaller than for the catastrophic specimens.

The specimens which fractured in a stable manner and those which failed catastrophically with small strength loss (located in the bottom half of Table XV) possess at least one of low elastic modulus, low fracture strength, high values of thermal properties, or large surface energy per unit area. While the influence of thermal expansion coefficient is highlighted in the Nakayama study - low α being desirable - the effect of γ on strength loss is much more apparent in the Larson study. In general, the Larson and Nakayama studies are in agreement as to the role of material properties in thermal shock damage resistance.

Specimen 28 fractured in the catastrophic mode on heating and in a stable manner on cooling. This behaviour was attributed primarily to an increase in crack density during cooling which, in turn, reduced c_{min} sufficiently to satisfy the condition for stable propagation of $c > c_{min}$. Figures 4.34 and 4.35 show the strength retained and R_d versus ΔT_f curves for the heating and cooling cases.

The R_d versus ΔT_f curves for heating and cooling cases for specimen 28 do not correspond at all with the Larson experimental

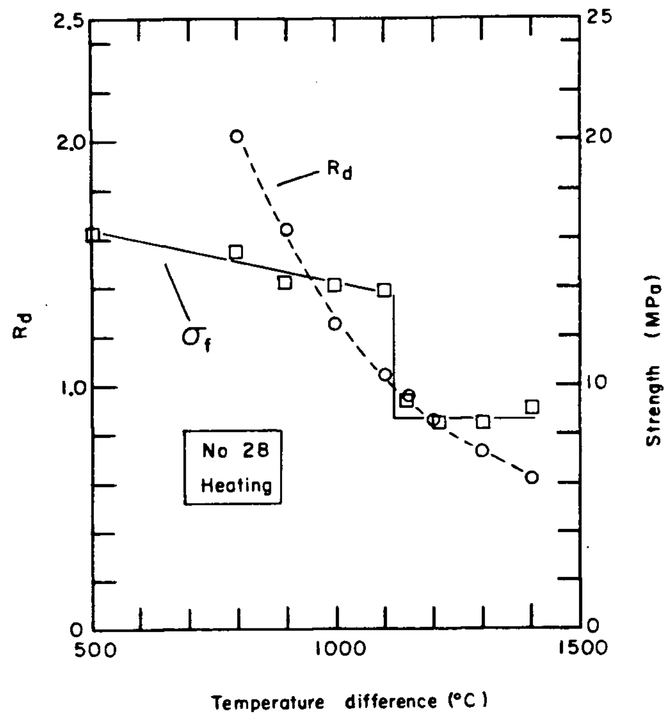

Figure 4.34 Strength retained and thermal shock resistance parameter R_d versus temperature difference for the heating case of specimen 28 of the Larson study.

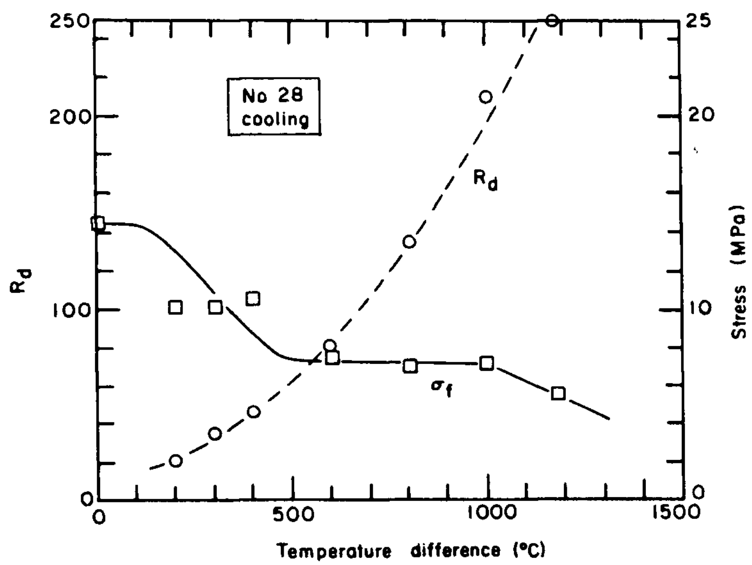

Figure 4.35 Strength retained and thermal shock resistance parameter R_d versus temperature difference for the cooling case for specimen 28 of the Larson study.

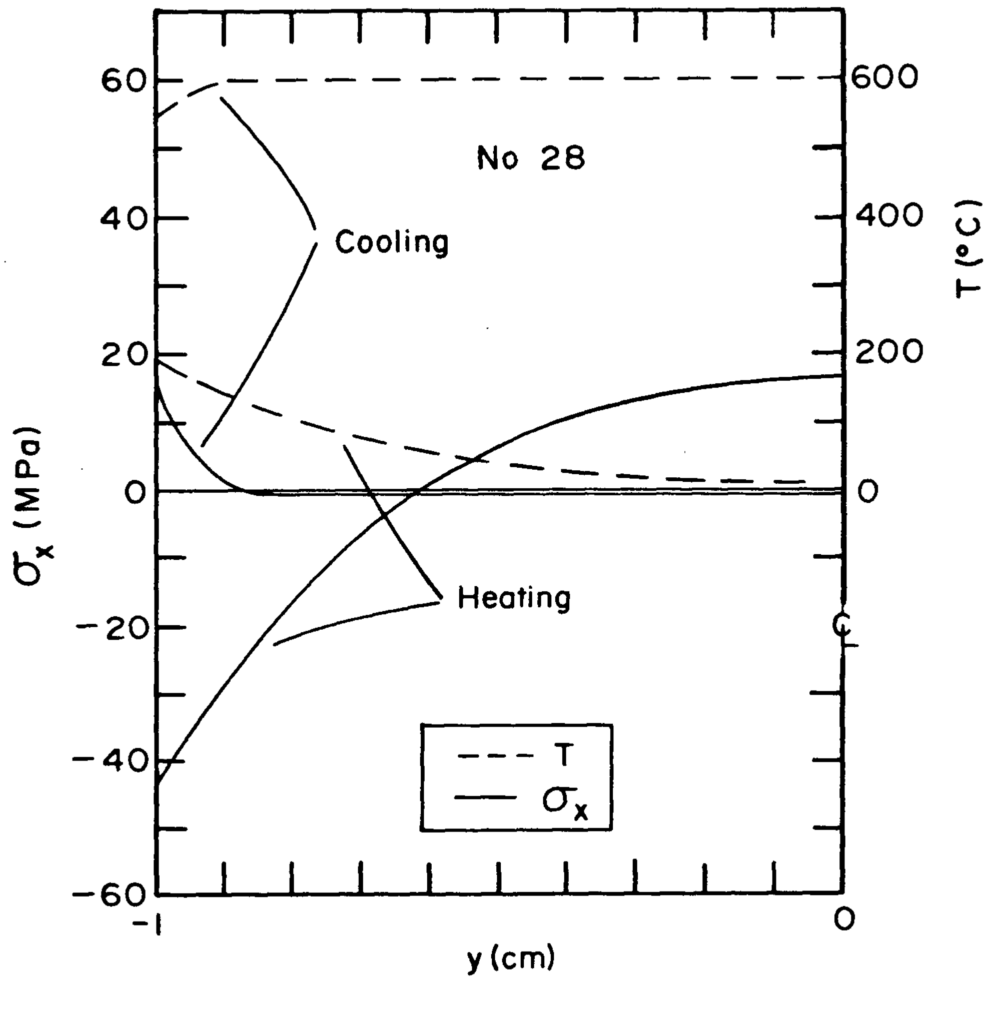

Figure 4.36 Stress and temperature distributions at fracture for the cooling (ΔT=600°C) and heating (ΔT=800°C) cases of specimen 28 of the Larson study.

findings. The smooth thermoelastically-predicted curves suggest no constant strength plateau and, moreover, indicate that the mode of fracture on heating is distinct from that on cooling. On heating the resistance to damage parameter decreases with increasing temperature difference in support of the underlying assumption that strength loss is related to the strain energy at fracture.

The opposing trend for cooling suggests that, at least for the case of severe thermal shock, fracture behaviour is unrelated to total strain energy at fracture since strain energy decreases - R_d increases - with increasing temperature difference and strength loss. Not only is strain energy at fracture for cooling approximately two orders of magnitude less than that for heating, but the trend suggests that strength loss tends to a maximum as strain energy at fracture tends to a minimum which, in the limit, is zero.

The observed trend of ΔR_d - ΔT_f on cooling makes sense from a thermoelastic point of view as the limiting case is an elementary ideal case which has been described by Goodier[55] as follows. A part or the whole of the surface of a free solid at temperature T_2 is suddenly cooled to T_1. Initially, before the temperature change has penetrated below the surface, biaxial tensile stress of magnitude $E\,\alpha\,(T_2-T_1)/(1-v)$ is developed in the surface layer only, wherever the cooling occurs. If the temperature difference is sufficient to induce a tensile stress equal to the strength then fracture occurs at time t=0.

While stress and strain energy density are defined at a point, strain energy - an integral quantity - is only defined with respect to a finite region. Thus the strain energy at fracture at t=0 is zero for the ideal cooling case described above since the thermal disturbance at the boundary has not had time to penetrate into the body. In general, for the traction-free case there exists a correspondence between the rate of development of strain energy and the rate at which the thermal disturbance at the boundary moves through the body.

This is illustrated in Figure 4.36 which shows the stress and temperature distributions at the instant of fracture for the cooling (ΔT_f=600°C) and heating (ΔT_f=800°C) cases for specimen 28. In the heating case considerable time ellapses (t_f=18.8 s) before the tensile stress in the interior of the specimen attains the fracture strength and, consequently, the thermal profile is reasonably well-developed with a hot face temperature of T_{hf}=188°C.

In contrast to the heating case, the fracture strength is attained almost instantaneously (t_f=0.43 s) at the surface of the cooled specimen. The thermal disturbance at the boundary has hardly altered the temperature profile of the body. The hot face temperature changes by only approximately 50°C and the depth of penetration of the temperature change is minimal. Consequently, for rapid cooling the strain energy at fracture is small and localized in the vicinity of the surface.

4.3.6.4 Semler

Semler subjected three sizes of high-alumina refractory specimens to the thermal shock conditions of the Ribbon test and presented the results as six separate correlations of R'''' and R_{st} versus percent elastic modulus retained (see Figure 4.14). Table XVI contains the estimates of the thermal properties and the %E retained and R_d values of each specimen for split (22.9 x 11.4 cm) quarter (22.9 x 5.7 cm), and bar (22.9 x 2.5 cm) geometries. The hot face in all three cases is 22.9 x 2.5 cm. The remainder of the material properties are listed in Table VIII. As no specimen designation is given there, the γ values have been reproduced in Table XVI as a means of matching up the data in the two tables. The %E retained values were estimated from the correlations in Figure 4.14.

As the thermoelastic model of thermal shock fracture accounts for the influence of geometry all of the results of the Semler study can be presented in a single plot of percent elastic modulus retained versus R_d. This has been done in Figure 4.37. In general, with other factors held fixed, the specimens with the smaller dimension in the direction of

TABLE XVI

Data and Results of Thermoelastic Analysis
of Semler Experiments

No.	k ($\frac{J}{sm°C}$)	a x 10^6 ($\frac{m^2}{s}$)	γ (J/m^2)	Splits		Quarters		Bars	
				%E Retain	R_d	%E Retain	R_d	%E Retain	R_d
S1	2.9	1.4	65.0	75	0.24	85	0.538	85	1.39
S2	2.5	1.2	56.0	8	0.090	79	0.204	92	0.528
S3	1.7	0.8	31.7	13	0.108	32	0.244	94	0.631
S4	1.7	0.8	48.0	82	0.242	96	0.534	93	1.40
S5	1.7	0.8	58.0	85	0.377	85	0.679	100	2.20
S6	1.7	0.8	63.0	83	0.38	92	0.813	95	2.05
S7	1.7	0.8	71.0	68	0.313	91	0.666	93	1.73
S8	1.7	0.8	70.0	90	0.445	90	0.866	100	*
S9	1.7	0.8	32.9	70	0.214	90	0.441	92	*
S10	1.3	0.6	34.0	37	0.106	46	0.237	82	0.592
S11	.84	0.4	17.8	0	0.037	0	0.082	87	0.208
S12	.84	0.4	22.5	7	0.052	11	0.113	95	0.306

* - fracture strength not reached

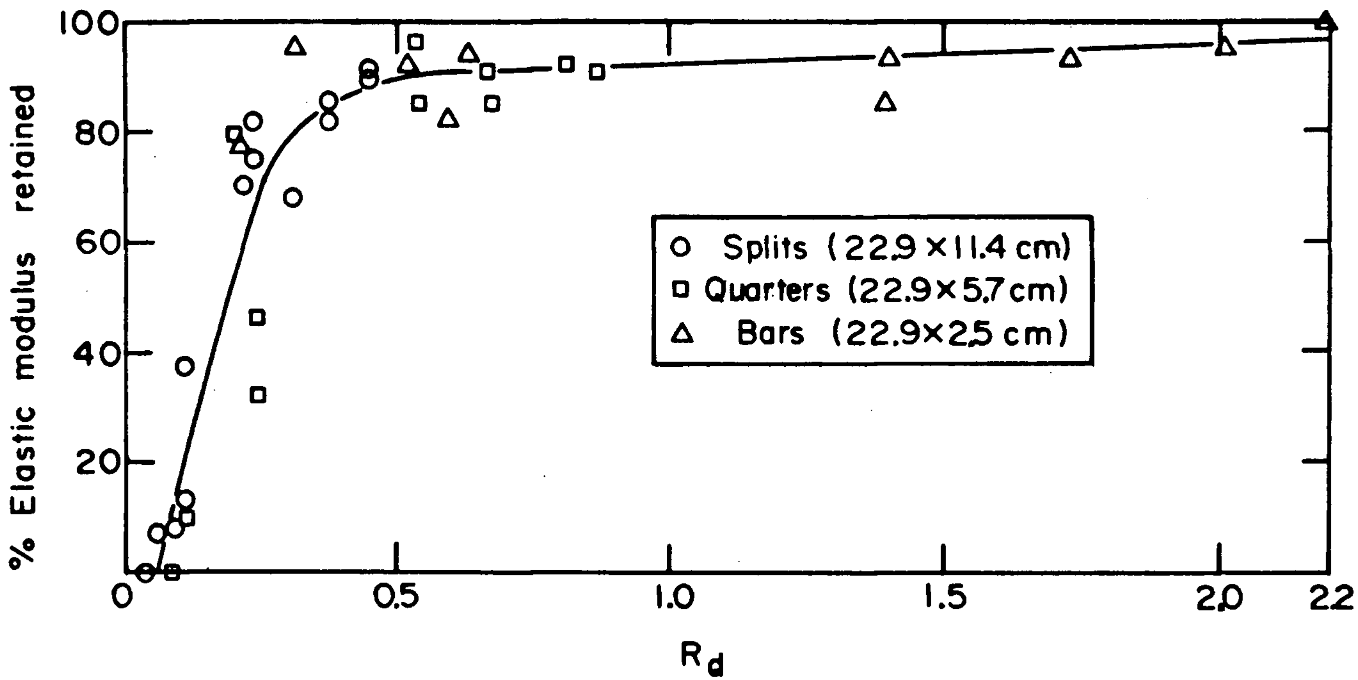

Figure 4.37 Percent elastic modulus retained versus resistance to damage parameter R_d for bar, quarter, and split geometry of the Semler study.

heat flow possess the greater resistance to thermal shock damage. The asymptotic relationship suggests that there exists a limiting dimension in the direction of heat flow at which a specimen becomes relatively insensitive to a particular thermal shock. The interdependence of geometry and material properties is reflected by the intermingling of circles, squares, and triangles.

The role of some of the material properties with regard to resistance to thermal shock damage is apparent from Table XVII which gives the ranking (from best to worst) in terms of R_d of the split specimens along with some pertinent data. It is apparent from the values of R'''' that the Hasselman parameter accounts for the relative damage resistance of a series of specimens of fixed size and similar thermal properties. The major limitation of the R'''' parameter is that it does not account for the interdependence of transient and geometric effects and thereby neglects the influence of thermal conductivity, thermal diffusivity, coefficient of thermal expansion, and size, all of which are important with regard to the industrial problem.

TABLE XVII

Material Properties, Damage Resistance Parameters, and %E Retained for Split Specimens of the Semler Study

Brick	k $(\frac{J}{sm°C})$	a x 10^6 $(\frac{m^2}{s})$	R'''' $(mx10^{-3})$	σ_f (MPa)	E (GPa)	γ (J/m^2)	R_d	%E Retain
S11	0.8	0.4	1.2	34.1	67.0	17.8	0.037	0
S12	0.8	0.4	2.0	31.8	69.8	22.5	0.052	7
S2	2.5	1.2	3.1	45.6	93.0	56.0	0.090	8
S10	1.3	0.6	3.7	22.9	46.1	34.0	0.106	37
S3	1.7	0.8	3.9	27.4	75.4	31.7	0.108	13
S9	1.7	0.8	5.4	9.8	13.5	32.9	0.214	70
S1	2.9	1.4	7.7	20.0	40.0	65.0	0.240	75
S4	1.7	0.8	8.4	14.3	30.3	48.0	0.242	82
S7	1.7	0.8	9.0	17.3	32.5	71.0	0.313	68
S5	1.7	0.8	13.4	11.2	24.1	58.0	0.377	85
S6	1.7	0.8	11.5	13.9	30.3	63.0	0.380	83
S8	1.7	0.8	9.7	9.7	10.5	70.0	0.445	90

4.3.7 Summary

(1) A thermoelastic model of the constant heat transfer coefficient thermal shock case has been used to derive both resistance to fracture initiation (R_i) and resistance to damage (R_d) parameters which account for the transient and geometric aspects of the problem as well as material properties.

(2) The validity of the fracture initiation parameter is suggested by correlations between the computed values of time of fracture and temperature of hot face at fracture of the Nakayama experiments and parameter R_i.

(3) As indicated by R_i, resistance to fracture initiation is directly proportional to fracture strength, the factor $(1-\nu)$, and the ratio of thermal conductivity to thermal diffusivity; and inversely related to elastic modulus, coefficient of thermal expansion, and the thermal boundary condition $(h,\Delta T)$.

(4) With regard to the Nakayama and Larson radiation heating thermal shock experiments, inverse relationships of percent strength loss and damage parameter R_d provide justification for the premise that extent of crack propagation is proportional to 'available' strain energy at fracture and inversely proportional to surface energy.

(5) Additional support for the thermoelastic approach is provided by the excellent agreement between the predicted shape of the strength retained-temperature difference curves, as reflected by the R_d-ΔT_f curves, and the experimental curves for specimens A,

E, F, and F' of the Nakayama study.

(6) Unlike the Hasselman model which predicts a constant strength plateau, the thermoelastic treatment suggests that strength decreases continuously over the range $\Delta T > \Delta T_{cr}$ for the heating case

(7) In contrast to the heating case, the thermoelastic analysis suggests that extent of crack propagation for the rapid cooling case is unrelated to the total strain energy at fracture which, for the limiting case of instantaneous change in surface temperature, is zero.

(8) Additional support for the thermoelastic approch is a correlation of the results of the Semler thermal shock study which utilized three geometries in the form of a single plot of percent elastic modulus retained versus damage parameter R_d.

(9) With regard to geometry, both the Nakayama and Semler investigations indicate that damage resistance is greatest in those specimens with the smaller dimension in the direction of heat flow; and the Semler results suggest that there is a limiting value of this dimension for which the specimen becomes insensitive to a particular thermal shock.

(10) The thermoelastic analysis indicates that resistance to thermal shock damage varies directly with thermal conductivity and inversely with coefficient of thermal expansion. The Semler results indicate that both the Hasselman R'''' and thermoelastic R_d parameters are in agreement with regard to the influence of elastic modulus, fracture strength, and surface energy on resistance to damage.

4.4 Discussion

Experimental observation of the constant strength plateau in the strength retained versus temperature difference curves is strong evidence in support of the Hasselman unified theory of thermal shock. While consistent with most experimental findings, the thermoelastic model predicts a continuous variation in strength with increasing temperature difference subsequent to fracture initiation at the critical condition. In this section some of the fundamental aspects of the two treatments are considered in an attempt to resolve this apparent discrepancy.

Fracture occurs in bodies subjected to thermal shock as a result of the internal stress reaching a critical value. The nature of the stress field is dependent on the thermal loading which is determined by the stress boundary conditions and the temperature field. As the thermal loading of the Hasselman and thermoelastic models is radically different, so are the stress fields at fracture in both cases.

In the Hasselman rectangular shape model thermal stress develops due to boundary restraint. The plate is uniformly and instantaneously cooled through temperature difference ΔT to produce a state of uniaxial tensile stress. The model is only applicable to the cooling case as uniformly heating the restrained plate produces a state of uniaxial compression which would tend to close the existing flaws rather than promote fracture. Thus application of the unified theory to the interpretation of strength loss relationships for the heating case, as has been done in the Larsen study, is questionable on this basis alone.

Furthermore, uniformly and instantaneously changing the temperature of a body would require infinite thermal conductivity and thus is thermodynamically impossible. The poor thermal shock resistance of many ceramic materials is in fact due to relatively low thermal conductivity. In all of the experimental studies considered in the previous section the specimens are essentially traction-free and thermal stresses develop due to temperature gradients which arise as a result of a finite rate of heat flow from the thermal disturbance at the boundary.

The Hasselman theory has most often been applied to the interpretation of fracture behaviour of specimens subjected to severe thermal shock conditions such as water quenching. In such cases it is assumed that fracture occurs instantaneously and thus the transient aspect of the problem can be neglected. A fundamental premise of the derivation for this rapid cooling case is that the sole driving force for crack propagation is the elastic strain energy stored within the body at fracture.

As noted in the previous section thermoelastic computations of the Larson water quenching studies suggest that strain energy at fracture decreases with increasing severity of thermal shock. As strength loss tends to increase with increasing quench temperature difference, this suggests another mechanism of fracture than the Hasselman suggestion of stored elastic strain energy. Paradoxically, in the one practical case to which the Hasselman theory seemingly applies there is, in the limit, no driving force for crack propagation.

Thermal shock fracture behaviour during rapid cooling appears to be more analogous to the fracture behaviour observed in the determination of surface energy by the work-of-fracture method than to the constant deformation mechanical model considered by Hasselman. In the work-of-fracture method the type of fracture - catastrophic, semistable or stable - is dependent on the size of the notch (see Figure 2.1). In developing an analogy, the counterpart to the notch for the thermal problem would be the cooling rate.

With slow cooling rates or small notches the catastrophic mode of fracture is observed as substantial elastic strain energy develops within the body prior to failure. At the other extreme of rapid cooling rates or large notches the stable mode of fracture is observed as little strain energy develops in the system prior to failure. For such a mode of fracture the work associated with the loading is converted directly to surface energy. In the case of catastrophic failure the rate of fracture is expected to be extremely rapid while the rate of crack propagation for the stable mode is expected to be dependent on the rate of loading.

In the Hasselman flaw model, the body consists of a uniform distribution of equal-sized non-interacting cracks and crack propagation occurs by the simultaneous equal advancement of each crack. This implies that total failure occurs with a sudden disintegration of the body into fragments. While crack patterns can in practice be quite complicated - depending on the nature of the thermal shock - simple crack patterns are usually obseved in bodies which are subjected to one-dimensional heat flow.

Figure 4.38 shows typical patterns of cracking in bricks of various sizes which have been heated in one direction. In general the orientation of the cracks can be related to the nature of the thermal stress field in the traction-free body at the instant of fracture. Thus, for the thermal conditions associated with the industrial lining problem, it is apparent that crack propagation occurs along discrete paths at particular locations in the body rather than by the equal

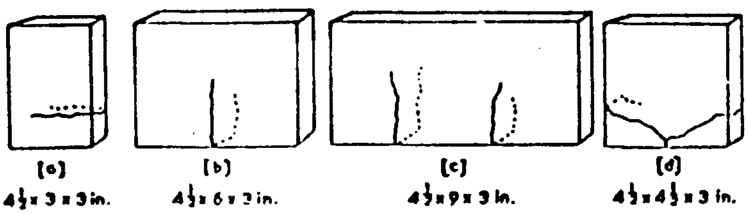

Figure 4.38 Typical patterns of cracking of various sizes (heated faces downwards) (after reference 12)

advancement of all flaws as proposed by the Hasselman model

According to the unified theory the plateau originates when the catastrophic or kinetic mode of fracture prevails. This mode dominates when the initial flaw size is less that a characteristic value c_{min} which is dependent only on crack density. Under such conditions, due to kinetic energy considerations, the crack formed in the specimen becomes subcritical with the result that a finite increase in ΔT is required to produce subsequent crack propagation and a further decrease in strength.

Another paradox of the Hasselman treatment is that experimental verification of the flaw model explanation of the constant strength plateau is impossible. The sequence of events required to produce the results shown in Figures 2.11 and 2.12 is outlined with reference to Figure 2.10. The experimental procedure consists of subjecting a series of specimens of presumably the same initial flaw distribution to water quenches of varying severity. For example, in a hypothetical experiment a single data point is obtained by subjecting a specimen of initial flaw size c_0 and strength σ_0 to a quench of temperature difference ΔT_0 and then measuring the strength of the quenched specimen in a three-point bend test.

It is apparent from Figure 2.10 that the after-quench strength

σ_f reflects the increase in crack length from c_0 to c_f. According to the Hasselman theory the quenched specimen with a crack length of c_f is subcritical with respect to all quenches of magnitude $\Delta T < \Delta T_f$. However, it is impossible to verify this prediction since the strength test is destructive and thus this specimen can not be subjected to another quench.

Experimental results of the type in Figure 2.11 and 2.12 simply reflect the effect of increasing magnitude of quenching temperature difference on strength retained of a series of specimens from the same population. Thus the smooth trends presented by Davidge and Tappin (Figure 2.3) and Ainsworth and Moore (Figure 2.4) which are characterized by significant scatter seem more reasonable than the strength retained curves presented in Figures 2.11 and 2.12 which are characterized by the well-defined discontinuity in slope associated with the constant strength plateau.

The effect of flaws is expected to be reflected in the scatter of strength retained values of specimens subjected to the same quench temperature difference. It is not obvious how the general trend of 'average' strength retained over the range of ΔT investigated can be influenced by flaws. Another possible explanation for the constant strength plateau, which is suggested by the shape of the h-ΔT curve in Figure 4.18, is that the rate of heat extraction remains constant over the range of ΔT covered by the plateau. However, the thermoelastic analysis of the Larson experiments suggests that this is unlikely.

Despite the fact that flaws are not accounted for in a direct manner, the thermoelastic model provides a better interpretation of observed thermal shock behaviour than the Hasselman flaw models. The key features of the thermoelastic approch are summarized with reference to Figure 4.39 which shows a schematic of the thermoelastic prediction of the strength retained curve as well as the general variation of maximum principal tensile stress, time of fracture and strain energy at fracture with increasing thermal shock. The error bars and cross-hatched regions indicate that strength retained after thermal shock is a statistical parameter. The thermoelastic prediction applies only to the trend of average strength retained.

In the thermoelastic model the body is considered traction-free and the development of stress is due solely to nonlinear temperature distributions. The influence of flaws is accounted for indirectly via the magnitude of material properties. Fracture is taken to occur at the instant and location at which the maximum principal tensile stress reaches a specified value of fracture strength. Extent of crack propagation is assumed to vary directly with the available strain energy and inversely with surface energy.

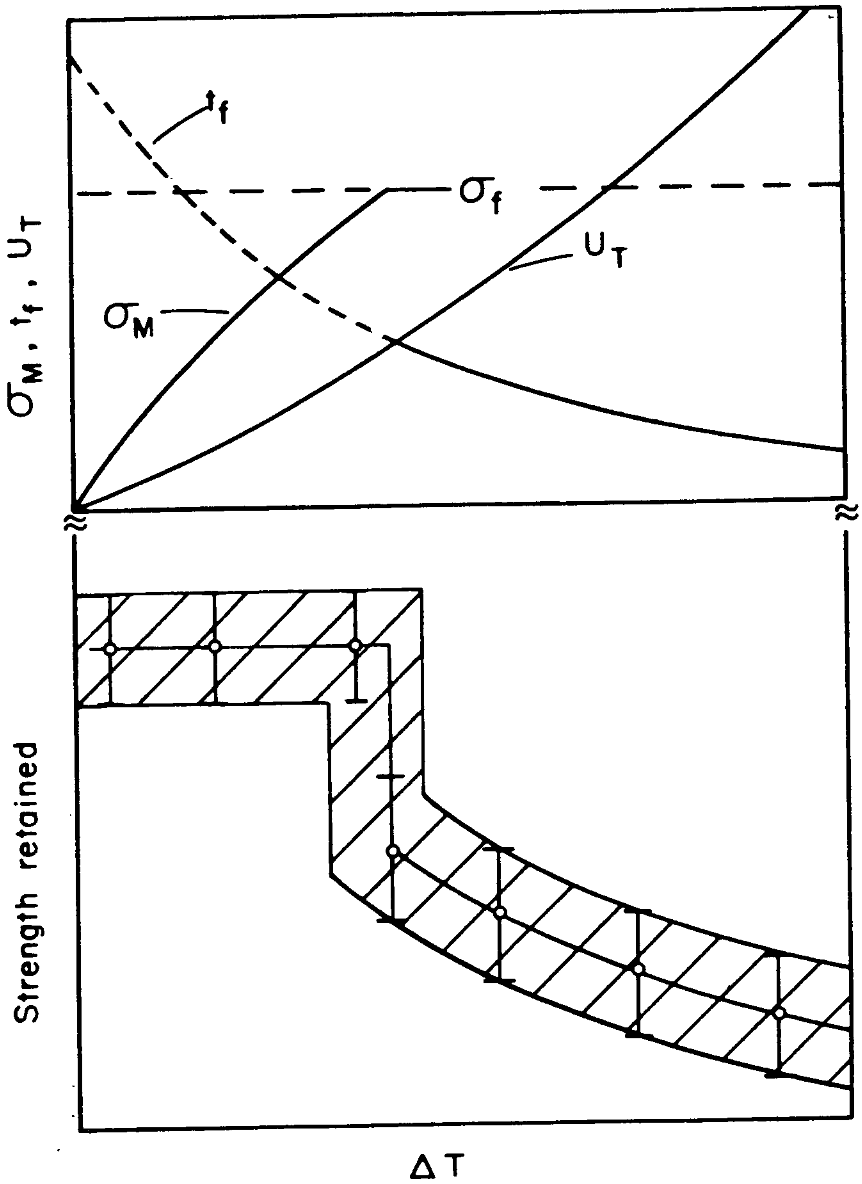

Figure 4.39 Thermoelastic interpretation of strength retained versus thermal shock behaviour for the heating case.

The thermoelastic model accounts for the shape of the strength retained curve as follows. The important relationships are sketched at the top of Figure 4.39 where it is seen that maximum principal tensile stress and total strain energy, increase and time of fracture decreases with increasing thermal shock. No change in strength is noted until a critical value of thermal shock is reached at which point σ_M attains the fracture strength. Further increases in the magnitude of thermal shock cause fracture to occur at an earlier time and with a greater content of strain energy. Thus, as strain energy increases continuously with increasing thermal shock for the heating cases considered, the thermoelastic model predicts a continuous decrease in strength.

In summary, the thermoelastic interpretation of thermal shock behaviour for the heating case is generally in line with published experimental results. The thermoelastic model suggests that the strength retained versus temperature difference relationship in the range above the critical value is continuous. It is possible that the curve may be relatively flat in this region for cases in which conditions are such that the strain energy at fracture does not vary appreciably with increasing severity of thermal shock. However, the thermoelastic treatment gives no indication of a discontinuity in slope in the strength retained versus temperature difference relationship at ΔT greater than the critical value for fracture initiation as does the Hasselman flaw model. Finally, the thermoelastic analysis indicates that fracture behaviour for the rapid cooling case is unrelated to total strain energy at fracture, a fundamental premise of the unified theory.

Chapter 5

THERMAL SHOCK RESISTANCE PARAMETERS FOR INDUSTRIAL APPLICATIONS

5.1 Introduction

A thermal problem of widespread industrial importance is the thermal stress fracture of refractory structural components of high temperature process vessels and industrial furnaces. While the principal origin of thermal stress may vary from process to process, a common feature of all processes is that the lining undergoes at least one thermal cycle in which the hot face of the lining is heated from ambient to operating temperature and cooled back again. During these stages thermal stresses develop due to nonlinear temperature distributions.

If heating or cooling is too rapid the transient temperature fields will produce stress of sufficient magnitude to cause fracture and thus enhance refractory wear. On the other hand, if heating or cooling occurs over a prolonged period, then energy costs increase, vessel or furnace availability decreases, and, in general, production efficiency falls. The industrial lining problem is thus concerned with safely heating or cooling through a specified temperature range as rapidly as possible.

This chapter is concerned with the development of theoretical fracture initiation and damage resistance parameters useful for the design and selection of refractory structural components for industrial linings. In section 5.2 an appropriate mathematical model for the industrial lining - the two-dimensional constant heating rate thermoelastic problem - is presented. In sections 5.3 and 5.4 general solutions for the maximum principal tensile stress and total strain energy are developed. A procedure for inverting the stress solution is described in section 5.5. The derivation and application of resistance to fracture initiation and resistance to damage parameters is discussed in sections 5.6 and 5.7

5.2 Industrial Lining Model

A two-dimensional thermoelastic mathematical model is used to simulate refractory components. The physical model is illustrated in Figure 5.1 where the half-shape of a rectangular component of arbitrary width (w) and length (ℓ) is shown. Heat flow ($\dot{q}$) is one-dimensional, from the hot face (y=0) to the cold face (y=ℓ). The boundaries between adjacent components (x = $\pm$ w/2) are insulated and traction-free. The ideal material is homogeneous, isotropic, and possesses temperature-independent properties. Displacements (u,v) are assumed

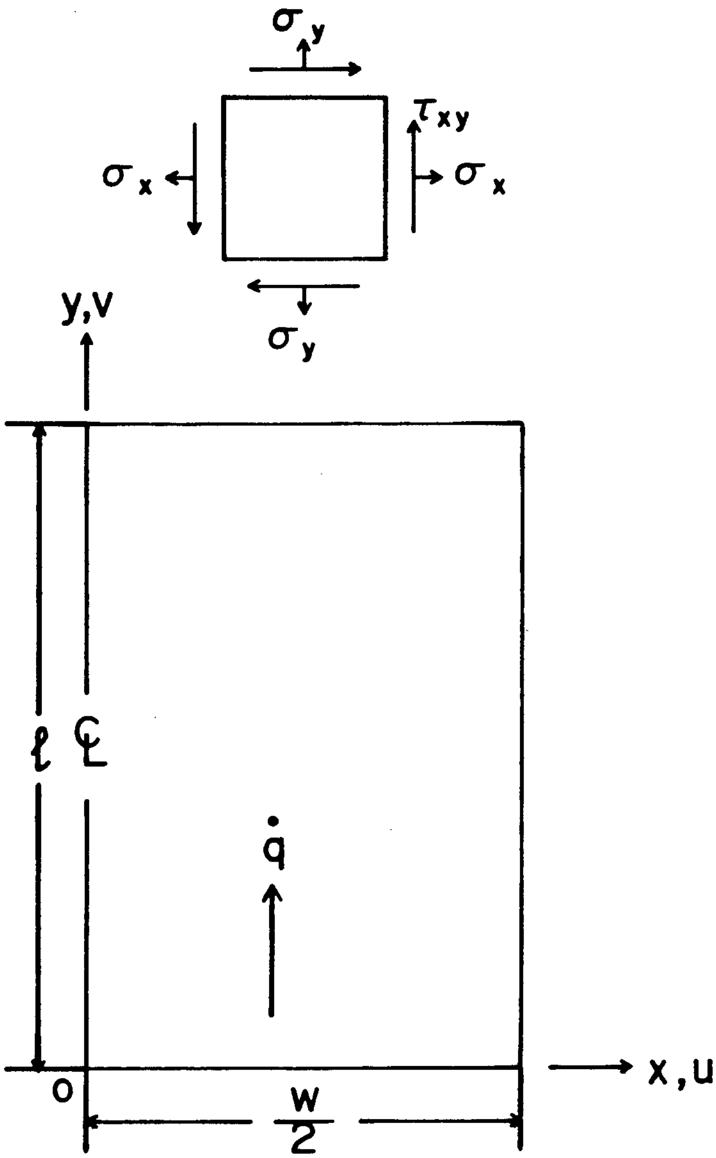

Figure 5.1 Geometry, orientation of axes, direction of heat flow, and stress convention of constant heating rate model.

small with respect to the component geometry. Stress-strain behaviour is linear and elastic to fracture. Fracture is taken to occur at the location and time at which the maximum principal tensile stress within the shape just reaches a specified value of fracture strength.

Industrial linings are often of composite construction, consisting of a working lining and safety or insulating lining. The modelling of heat flow in such structures can be difficult due to complex boundary conditions at the hot face and outer wall and indeterminate thermal resistances at the interfaces. Also, in most processes the nature of the refractory components change during operation as a result of refractory wear and in-service alteration of the hot face zone due to penetration or chemical attack.

For simplicity and generality the constant heating rate (ϕ) hot face boundary condition case is considered. The temperature profiles are computed using the analytical solution for a semi-infinite slab over the range $o<y<\ell$. The solution is

$$T = 4\ \phi t\ i^2\mathrm{erfc}\left(\frac{y}{2\sqrt{at}} \right) \tag{5.1}$$

where t is time, a is thermal diffusivity, and i^2erfc is a repeated integral of the error function. The hot face boundary condition and initial condition are

$$T(t) = \phi t, \ t>0 \tag{5.2}$$

$$T(y) = 0, \ 0<y<\ell, \ t=0 \tag{5.3}$$

The temperature solution is presented graphically in Figure 5.2 as curves of dimensionless temperture T^* versus Fourier modulus for various y^* where

$$T^* = \frac{T}{\phi t} \tag{5.4}$$

and

$$y^* = \frac{y}{\ell} \ . \tag{5.5}$$

Previous theoretical treatments of the constant heating rate problem have considered the case of the insulated cold face boundary for which the following analytical solution[94] applies

$$T = \phi t + \frac{\phi(y^2-\ell^2)}{2a} +$$

$$\frac{16\phi\ell^2}{a\pi^3} \sum_{n=0}^{\infty} \{\frac{(-1)^n}{(2n+1)^3} \cdot \cos[\frac{(2n+1)\pi y}{2\ell}] \cdot e^{-(\frac{a(2n+1)^2\pi^2 t}{4\ell^2})} \tag{5.6}$$

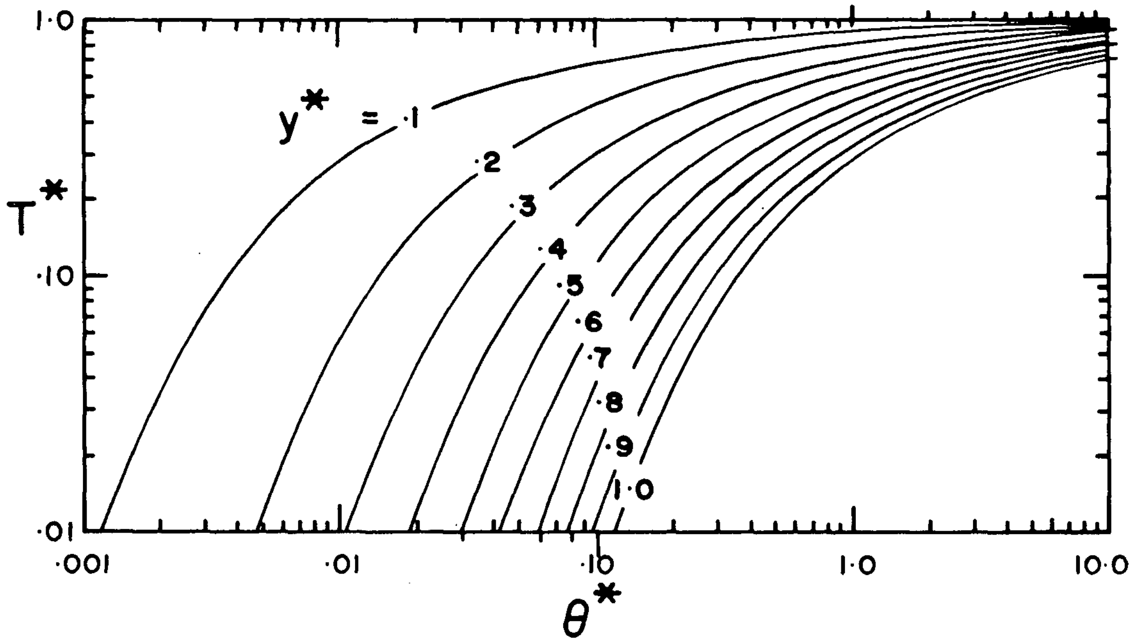

Figure 5.2 Temperature solution for the constant heating rate problem in the form of domensionless temperature versus Fourier modulus.

A practical consideration in choosing the semi-infinite slab solution is that the error function solution does not require the evaluation of an infinite series. For a given set of conditions, the temperature profile associated with a composite structure consisting of a safety and working lining of different thermal properties is expected to lie between those given by equations 5.1 and 5.6.

A significant advantage of the constant heating rate case over the constant heat transfer coefficient case is that the thermal boundary condition is expressed as a single parameter (ϕ) rather than several ($h, \Delta T$). This characteristic and the nature of the thermal stress solution enable the development of a general solution for the maximum principal tensile stress. A further point in favour of the constant heating rate case is that values of safe heating rates for various refractory shapes have been published.

5.3 Solution for the Maximum Principal Tensile stress

5.3.1 Introduction

The stress dependence of the two-dimensional constant heating rate problem can be expressed as

$$\sigma = f(x, y, t, \phi, a, E, \nu, \alpha, \ell, w) \tag{5.7}$$

The transient behaviour of thermal stress arises solely from that of temperature, each temperature distribution producing a unique stress field. The cooling problem is obtained by making ϕ negative and adding an initial temperature term to equation (5.1).

Since a basic premise is that fracture initiation is governed by the maximum principal tensile stress criterion, the only stress component of interest is the maximum principal tensile stress σ_M. What is required is a general solution for the following dependence

$$\sigma_M = f(t, \phi, a, E, \nu, \alpha, \ell, w) \tag{5.8}$$

The maximum principal tensile stress is always either a σ_x or σ_y component located along the center line or external boundary.

The characteristic features of the center line and edge distributions of the thermal stress field of a rectangular shape heated from one end are illustrated in Figure 5.3. The maximum tensile and compressive values of the σ_x distribution, designated $(\sigma_x^c)_M$ and (σ_x^0), are located along the center line (Figure 5.3A). With regard to the σ_y distribution, the maximum tensile value $(\sigma_y^c)_M$ is located along the

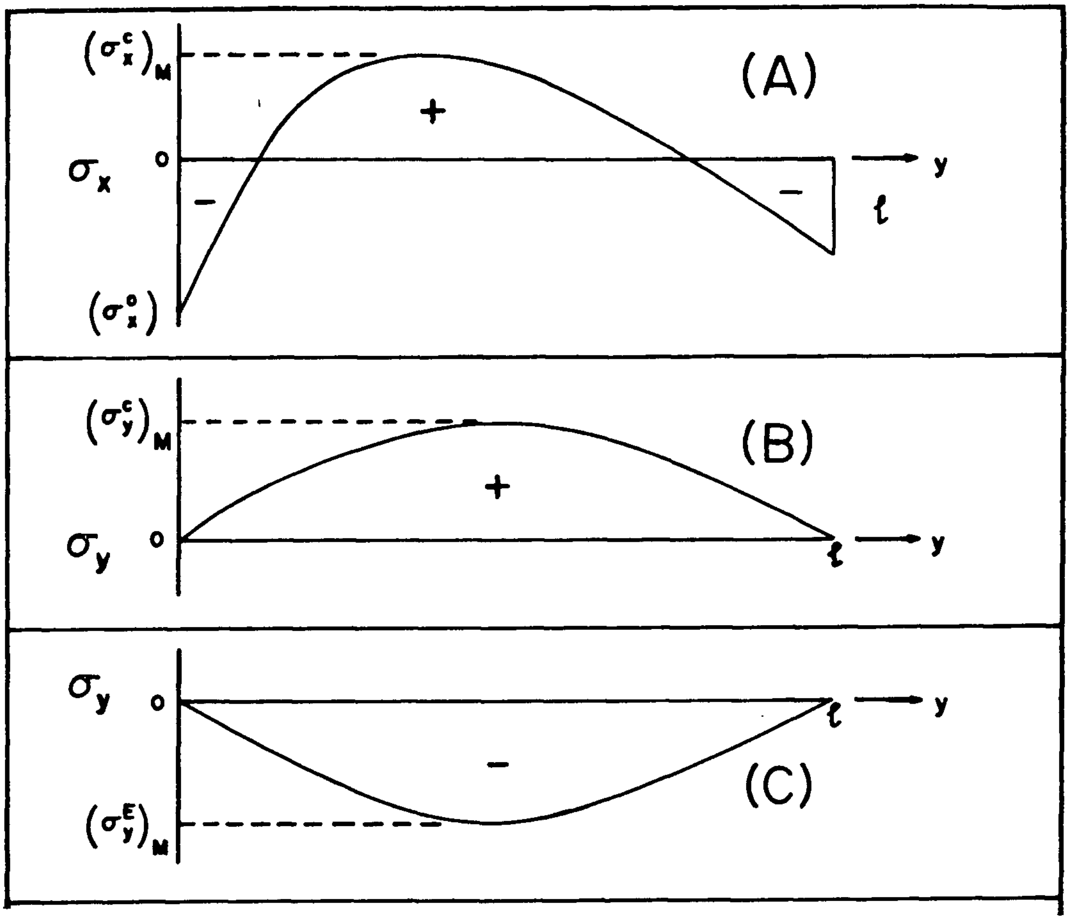

Figure 5.3 Typical stress distributions in rectangular shapes heated from one end. (A) center line σ_x distribution, (B) center line σ_y distribution, (C) outside edge σ_y distribution.

center line and the maximum compressive value, $(\sigma_y^E)_M$, along the sides (Figure 5.3C).

The effect of cooling at the same rate is simply to reverse the sign of the stresses. Since the stress components along the center line and external boundaries are also principal stresses, on heating the maximum principal tensile stress is the greater of $(\sigma_x^c)_M$ and $(\sigma_y^c)_M$ and, on cooling, it is the greater of σ_x^0 and $(\sigma_y^E)_M$. While the location of the σ_x^0 component is fixed at the midpoint of the hot face, that of the other peak components is variable and is dependent on conditions at the instant of fracture.

5.3.2 General Solution

The experimental results of multivariable fluid flow and heat and mass transfer problems which contain a large number of variables are often presented in the form of empirical equations involving dimensionless parameters. A similar approach is used here. Dimensional analysis is used to reduce the number of variables sufficiently to enable a tabulated solution. The results for selected cases, obtained by finite element analysis, are used as discrete data points to construct interpolation curves from which results for arbitrary cases can be quickly estimated.

The dimensional analysis of the stress dependence of the constant heating rate thermal stress problem contained in Appendix VIII indicates that the dimensionless form of equation (5.8) is

$$\sigma_M^* = f(\ \theta^*,\ r^*,\ \gamma^*) \tag{5.9}$$

where dimensionless maximum principal tensile stress σ_M^*, Fourier modulus θ^*, aspect ratio r^*, and dimensionless thermal load γ^* are given by

$$\sigma_M^* = \frac{\sigma_M\ (1-\nu)}{E} \tag{5.10}$$

$$\theta^* = \frac{at}{\ell^2} \tag{5.11}$$

$$r^* = \frac{w}{\ell} \tag{5.12}$$

and

$$\gamma^* = \frac{\phi\alpha\ell^2}{a} \tag{5.13}$$

In addition to reducing the number of independent variables, the grouping of variables into significant combinations which reflect transient, geometric, and thermal loading effects facilitates subsequent analysis.

While the number of variables has been reduced from nine to four, equation (5.9) still contains one too many independent parameters for a general tabulated or graphical representation. It is necessary to follow a two-step procedure to get the general solution. In the first step dimensionless thermal load is fixed and the reduced form of

$$\sigma^*_{0.01} = f(\theta^*, r^*) \tag{5.14}$$

is considered where $\sigma^*_{0.01}$ refers to σ^*_M for γ^*=0.01. Generalization for arbitrary dimensionless thermal load is accomplished in the second step with an appropriate σ^*_M-γ^* relationship.

The solution of equation (5.14) for a wide range of Fourier modulus and aspect ratio for both the heating and cooling cases is given in Tables XVIII and XIX. Some of the tabulated results are plotted in Figure 5.4 which shows the transient behaviour of the dimensionless maximum principal tensile stress on heating for several aspect ratio and γ^*=0.01. In general, the maximum principal tensile stress increases with increasing Fourier modulus to a limiting value at large θ^*.

A characteristic feature of the transient behaviour is a point

Table XVIII

Dimensionless Peak σ_x and σ_y Principal Tensile Stresses on Heating

θ^*	σ_M^*	r^*										
		.125	.25	.375	.50	.625	.75	.875	1.0	1.25	1.50	2.0
.001	x	.000862	.00128	.00144	.00136	.00127	.00117	.00108	.000993	.000878	.000812	.000758
	y	.000732	.000651	.000532	.000436	.000369	.000318	.000277	.000272	.000272	.000271	.000271
.002	x	.00112	.00226	.00274	.00285	.00276	.00267	.00255	.00241	.00221	.00208	.00196
	y	.00130	.00143	.00127	.00110	.000948	.000835	.000736	.000643	.000470	.000316	.000293
.004	x	.00128	.00330	.00467	.00553	.00564	.00570	.00561	.00550	.00525	.00507	.00490
	y	.00198	.00284	.00282	.00259	.00235	.00211	.00189	.00168	.00124	.000839	.000309
.010	x	.00137	.00462	.00785	.0103	.0120	.0132	.0139	.0142	.0148	.0150	.0152
	y	.00306	.00582	.00694	.00716	.00696	.00658	.00613	.00554	.00419	.00286	.00107
.040	x	.00144	.00545	.0116	.0184	.0250	.0314	.0372	.0427	.0518	.0581	.0639
	y	.00446	.0118	.0183	.0230	.0260	.0275	.0275	.0261	.0206	.0144	.00543
.100	x	.00145	.00569	.0124	.0213	.0317	.0433	.0559	.0693	.0936	.111	.128
	y	.00518	.0157	.0275	.0386	.0477	.0538	.0560	.0544	.0441	.0314	.0119
.400	x	.00146	.00581	.0130	.0229	.0365	.0557	.0810	.110	.163	.201	.237
	y	.00589	.0201	.0397	.0622	.0835	.0987	.106	.104	.0848	.0616	.0230
1.0	x	.00147	.00582	.0130	.0232	.0378	.0609	.0938	.131	.199	.247	.292
	y	.00620	.0221	.0456	.0743	.102	.122	.130	.128	.105	.0782	.0285
4.0	x	.00147	.00582	.0130	.0232	.0389	.0664	.107	.153	.234	.291	.345
	y	.00647	.0240	.0516	.0866	.120	.144	.154	.152	.125	.0880	.0338
10.0	x	.00147	.00582	.0130	.0232	.0393	.0686	.113	.161	.248	.308	.365
	y	.00659	.0248	.0541	.0914	.127	.152	.163	.161	.132	.0933	.0358

Table XIX

Dimensionless Peak σ_x and σ_y Principal Tensile Stresses on Cooling

θ^*	σ_M^*	r^* .125	.25	.375	.50	.625	.75	.875	1.0	1.25	1.50	2.0
.001	x	.00338	.00575	.00695	.00765	.00810	.00842	.00865	.00882	.00903	.00914	.00922
	y	.00240	.00296	.00296	.00297	.00298	.00294	.00288	.00262	.00254	.00241	.00207
.002	x	.00452	.00901	.0117	.0135	.0146	.0154	.0160	.0165	.0171	.0175	.0177
	y	.00368	.00517	.00566	.00570	.00578	.00581	.00580	.00573	.00539	.00523	.00490
.004	x	.00561	.0131	.0187	.0226	.0253	.0274	.0290	.0301	.0317	.0327	.0332
	y	.00489	.00850	.0102	.0108	.0112	.0112	.0112	.0112	.0112	.0111	.0108
.010	x	.00680	.0191	.0308	.0405	.0483	.0544	.0594	.0632	.0684	.0715	.0734
	y	.00709	.0150	.0203	.0237	.0254	.0265	.0270	.0275	.0279	.0279	.0280
.040	x	.00796	.0267	.0506	.0757	.100	.122	.142	.159	.184	.197	.208
	y	.00955	.0270	.0444	.0597	.0717	.0806	.0875	.0922	.0958	.0966	.0966
.100	x	.00841	.0300	.0609	.0971	.136	.175	.212	.246	.295	.324	.346
	y	.0108	.0340	.0621	.0907	.117	.140	.158	.171	.183	.186	.187
.400	x	.00880	.0331	.0710	.119	.177	.240	.304	.363	.454	.509	.551
	y	.0120	.0419	.0842	.135	.189	.239	.279	.307	.334	.340	.340
1.0	x	.00895	.0342	.0746	.129	.194	.268	.342	.416	.528	.596	.648
	y	.0126	.0454	.0946	.157	.226	.290	.341	.377	.410	.418	.418
4.0	x	.00907	.0352	.0779	.136	.209	.294	.382	.465	.597	.676	.737
	y	.0130	.0488	.105	.180	.264	.341	.402	.444	.484	.495	.495
10.0	x	.00912	.0356	.0792	.139	.215	.304	.396	.484	.622	.706	.771
	y	.0132	.0502	.110	.190	.279	.361	.425	.470	.513	.524	.524

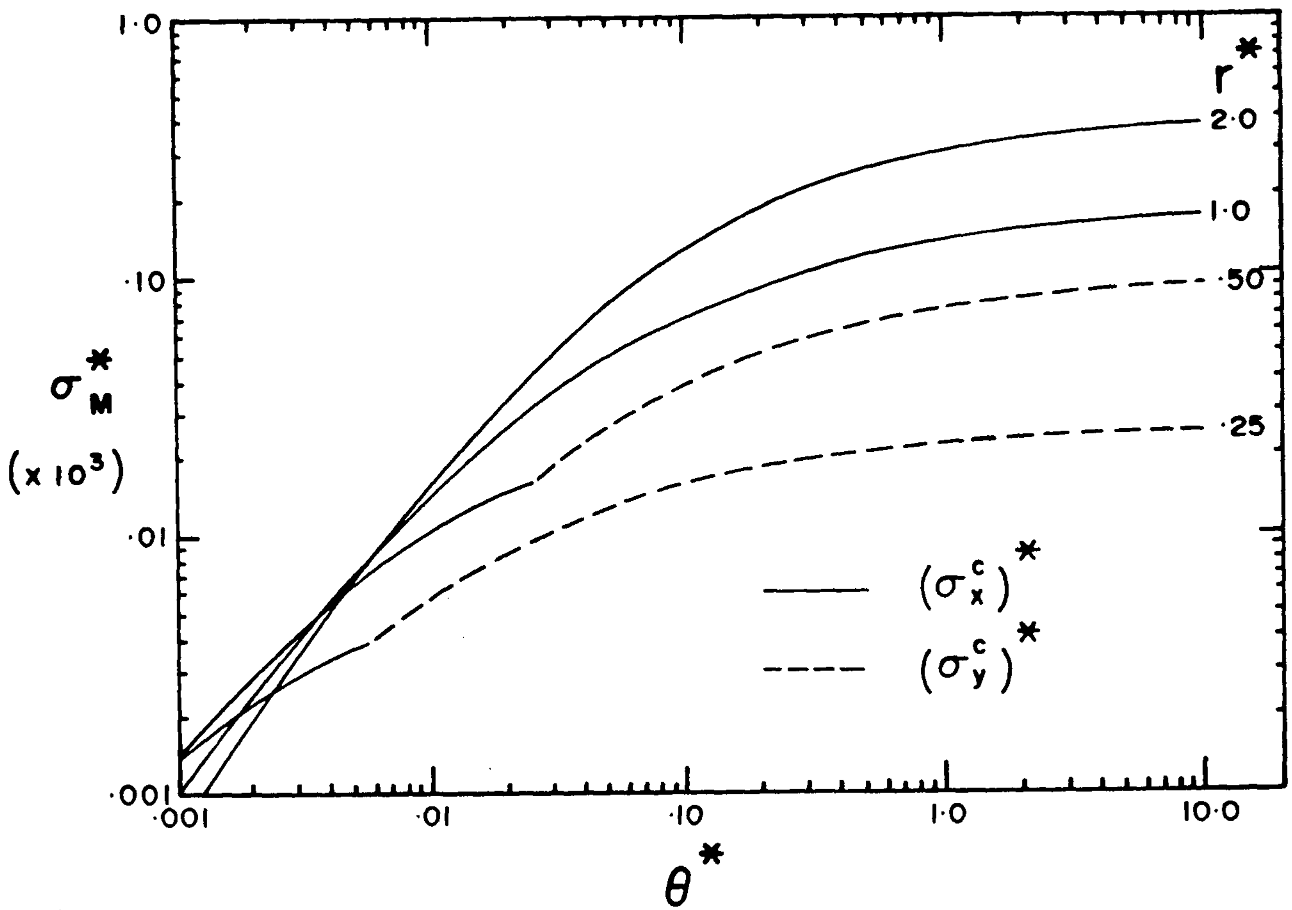

Figure 5.4 Dimensionless maximum principal tensile stress versus Fourier modulus for several aspect ratio and heating case.

of discontinuity in slope for cases of $r^* < 1.0$ at which a transition in maximum principal tensile stress component occurs. For the heating case the $(\sigma_x^c)_M$ component dominates during the early stages (the portion of the curve to the left of the discontinuity) and the $(\sigma_y^c)_M$ component during the latter stages. Similarly, the (σ_x^0) component dominates during the early portion of a cooling cycle before being exceeded at some later time by the $(\sigma_y^E)_M$ component.

A point of discontinuity in slope is also apparent in the solid line in Figure 5.5 which shows the variation of the peak values of the σ_x and σ_y center line distributions as a function of aspect ratio for conditions of heating, $\theta^*=0.10$, and $\gamma^*=0.05$. The peak σ_y component is greater in the range $r^* < r^*_{cr}$, while the σ_x component dominates in the range of aspect ratio greater than the critical value.

The significance of the infinite slab geometry - width greater than twice the length - is apparent from Figure 5.5 where the maximum principal tensile stress is seen to be independent of aspect ratio in the range $r^* > 2.0$. For such geometries one-dimensional treatments which consider the σ_x component only are clearly justified. The decline in magnitude of the peak σ_y component with increasing aspect ratio reflects the fact that the σ_y distribution is associated with a localized edge

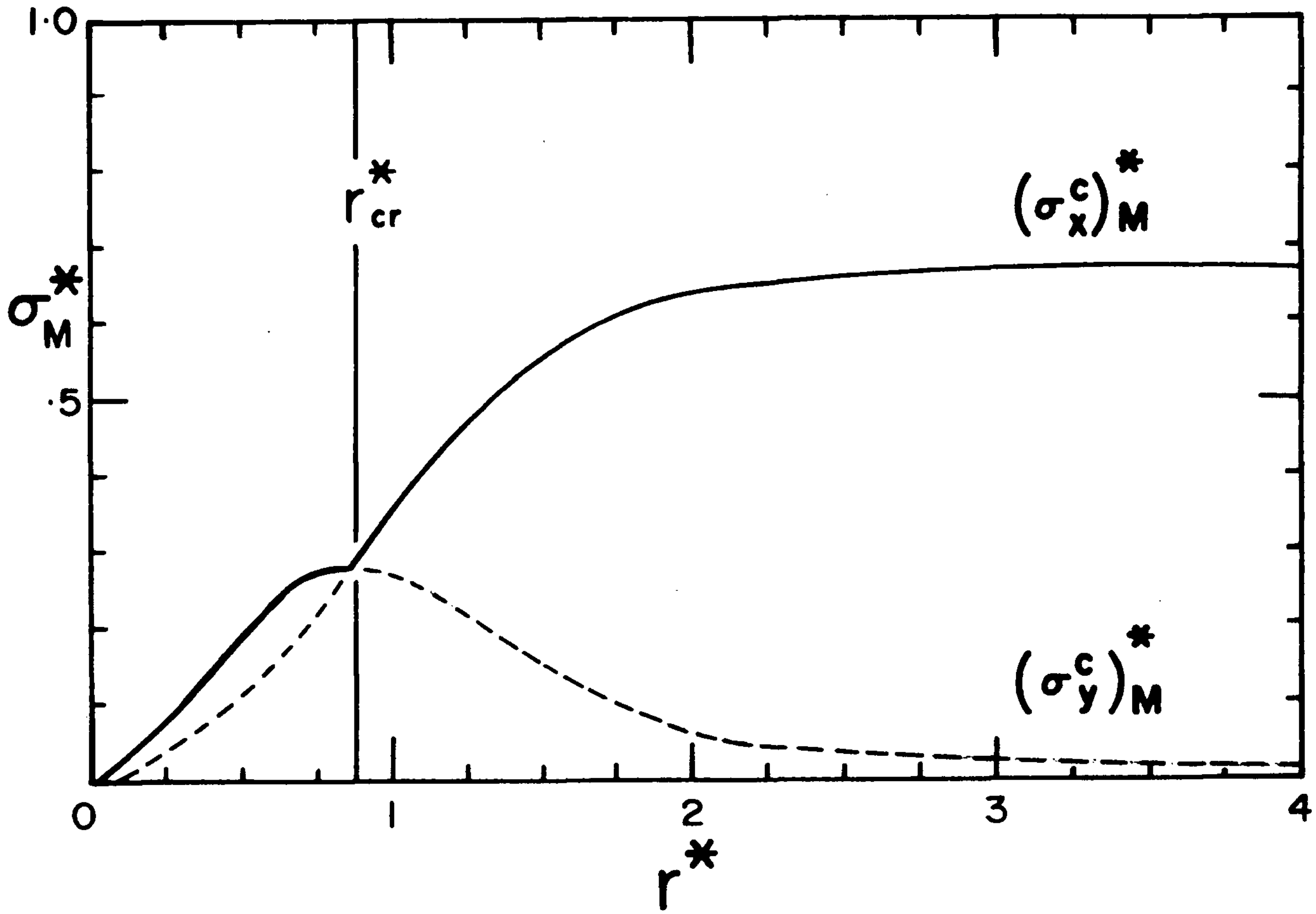

Figure 5.5 Dimensionless peak σ_x and σ_y principal tensile stresses on heating versus aspect ratio (θ^*=0.10 and γ^*=0.05).

effect.

The values of the peak σ_x and σ_y components in Tables XVIII and XIX for $\gamma^*=0.01$ can be used to obtain the maximum principal tensile stress for arbitrary conditions by taking advantage of a unique property of the constant heating rate problem. It turns out that dimensionless stress is directly proportional to dimensionless thermal load for conditions of fixed Fourier modulus and aspect ratio. Thus σ_M^* for arbitrary γ^* can be computed using

$$\sigma_M^* = \sigma_{0.01}^* \left(\frac{\gamma^*}{0.01} \right) \tag{5.15}$$

where $\sigma_{0.01}^*$ can be estimated from interpolation curves such as those in Figure 5.4. Equation 5.15 follows from the nature of the second derivative of temperature, the use of a linear constitutive law, and the stipulation of fixed aspect ratio.

The dimensionless form of the solution can be used to obtain both the plane strain and plane stress result, the former type of two-dimensional analysis usually being applied to long prismatic bodies and the latter to thin bodies. When evaluating σ_M substitution of a nonzero value of Poisson's ratio into equation 5.10 gives the plane strain value while setting ν to zero yields the plane stress value.

5.3.3 Discussion

No comprehensive treatment of the two-dimensional constant heating rate thermoelastic problem has been presented in the literature. Previous work has not accounted for the influence of transient and geometric effects on fracture initiation behaviour in a completely satisfactory manner. In this section the Kingery[7] derivation of a constant heating rate resistance to initiation parameter and the results of Chang et al[18] for selected two-dimensional cases are examined in some detail in order to clarify the role of the individual variables, particularly those associated with the Fourier modulus and aspect ratio.

The Chang study was primarily concerned with the thermal shock behaviour of BOF bricks and, consequently, interest was focused on geometries of small aspect ratio in which the length (the dimension in the direction of heat flow) is much greater than the width. As fracture in components of this type usually occurs in a direction parallel to the hot face, conclusions and design recommendations were based on the variation of the peak σ_y component only, even though it was noted that for shorter times and/or higher heating rates the σ_x component can exceed the σ_y component.

The results of the Chang investigation concerning the influence of heating rate, time, thermal diffusivity, width, and length on the magnitude of the peak σ_y component, which are given in Figures 5.6 - 5.9, are summarized as follows:

(i) for moderate heating rates the maximum tensile component occurred along the center line parallel to the component length in accordance with the fracture mode observed in practice, ie. the σ_y component,

(ii) for high heating rates the maximum tensile component can occur parallel to the face being heated, ie. the σ_x component,

(iii) the magnitude of stress is proportional to heating rate and an inverse function of thermal diffusivity (see Figures 5.6 and 5.8),

(iv) the location of fracture is anticipated to be a function of heating rate because with increasing heating rate the position for any prescribed value of stress such as the tensile fracture strength moves toward the face being heated (see Figure 5.6),

(v) the location of fracture is also expected to be a function of time as the peak stress increases and moves away from the hot

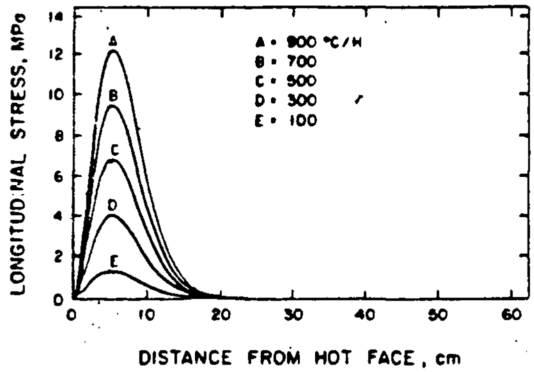

Figure 5.6 Longitudinal stress distribution along the center line for a range of heating rates using values of a=12.9x10^{-3} cm^2/s, w=10 cm, ℓ=60 cm at t=1000 s. (after reference 18)

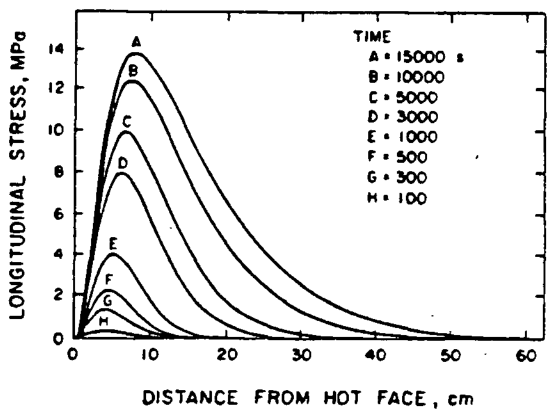

Figure 5.7 Longitudinal stress distribution along the center line for a range of times using values of a=12.9x10^{-3} cm^2/s, ϕ=300 °C/h, w=10 cm, and ℓ=60 cm. (after reference 18)

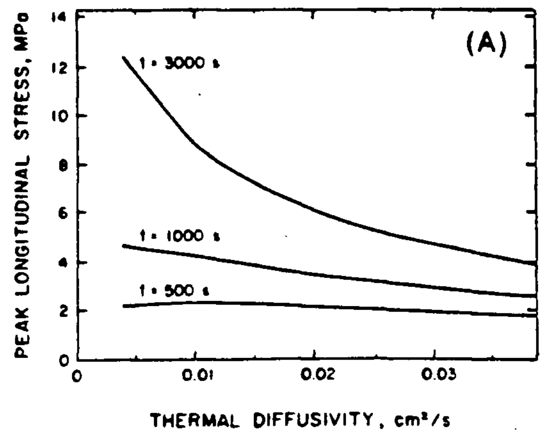

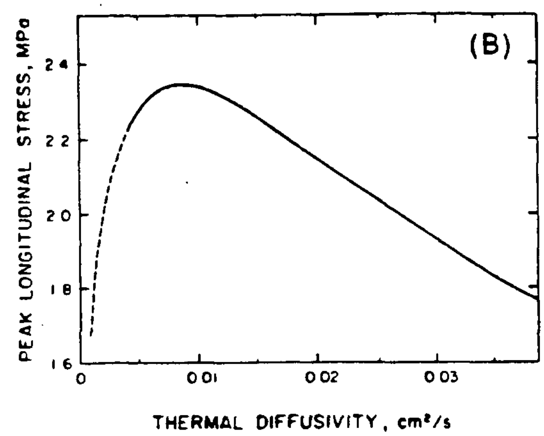

Figure 5.8 Peak longitudinal stress as a function of thermal diffusivity and values of ϕ=300 °C/h, w=10 cm,and ℓ=60 cm: (A) range of values of time and (B) expanded scale for t=500 s. (after reference 18)

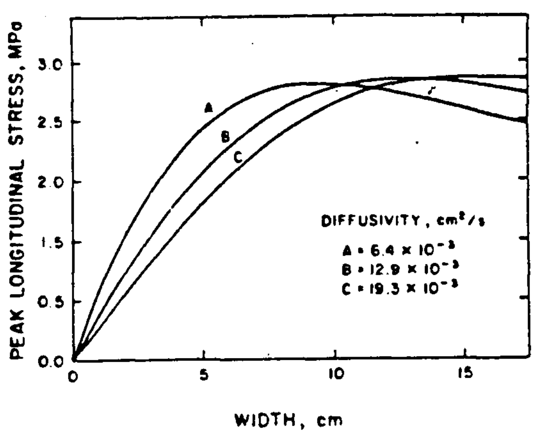

Figure 5.9 Peak longitudinal stress as a function of segment width for three values of thermal diffusivity with ℓ=60 cm and ϕ=300 °C/h at t=500 s.(after reference 18)

face with increasing time (see Figure 5.7),

(vi) a maximum was observed at an intermediate value of thermal diffusivity for the case t=500 s (see Figure 5.8),

(vii) maximum values of stress were encountered for intermediate values of width (see Figure 5.9)

(viii) the magnitude of the peak σ_y component is independent of length for the range $40<\ell<80$ cm.

The observation of maximum values of the peak σ_y component for intermediate values of width led Chang et al to suggest that the incidence of thermal stress failure might be reduced by either reductions or increases in the values of width commonly used in practice. The solid line in Figure 5.10 represents the dimensionless form of the Chang results for case A in Figure 5.9, while the dashed line shows the variation of the peak σ_x stress for the same case.

As the σ_x component dominates at larger aspect ratio, such a design recommendation is clearly misleading. If the variations of the peak values of both components are considered, the general conclusion must be that for these conditions the maximum principal tensile stress increases with increasing width with a transition in component of

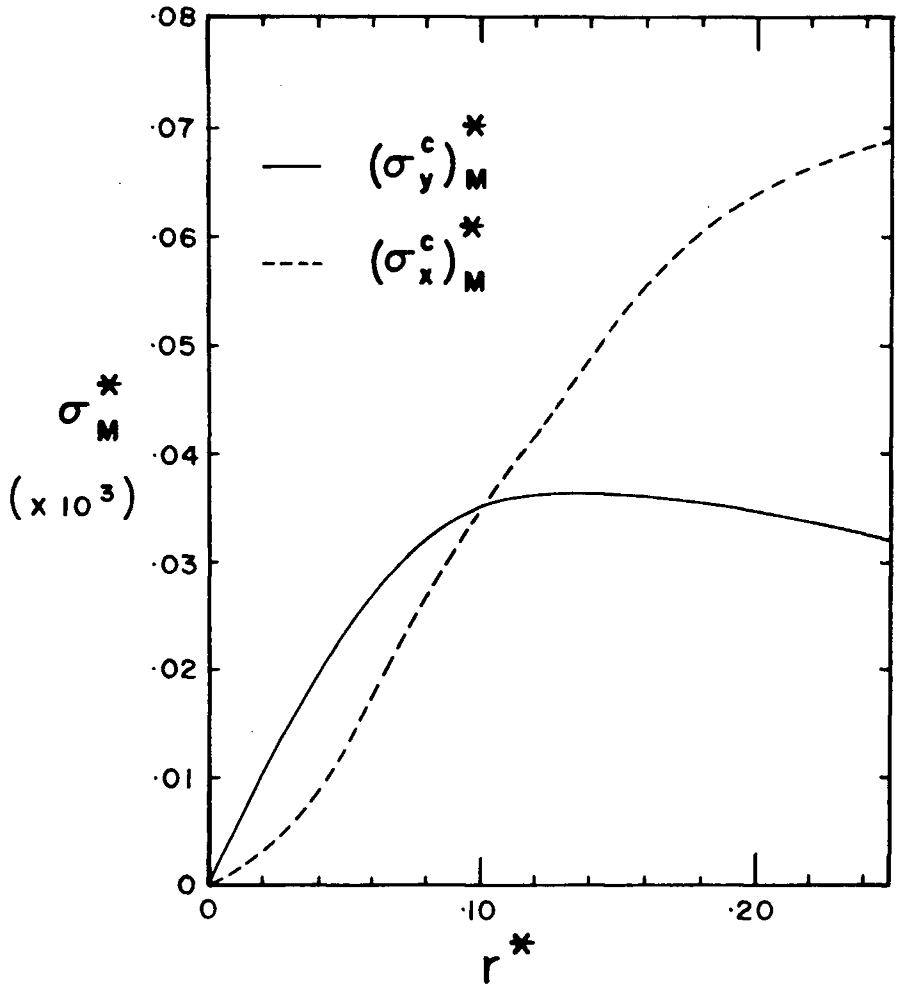

Figure 5.10 Dimensionless peak σ_x and σ_y principal tensile stresses on heating versus aspect ratio for the conditions of cas A of Figure 5.9 of the Chang study

maximum principal tensile stress occurring at an intermediate value of width. Furthermore, the values of heating rate and time used to produce the results in Figure 5.9 combine to give a hot face temperature of approximately 50°C which is unreasonable for an industrial lining application.

It is also necessary to determine the magnitude of both σ_x and σ_y peak stresses when assessing the influence of thermal diffusivity on maximum principal tensile stress. The Chang results of Figure 5.8B have been reproduced in dimensionless form as the solid line in Figure 5.11. The dashed line again indicates the variation of the peak σ_x value. While a maximum exists in the peak σ_y curve, the general trend is one of decreasing maximum principal tensile stress with increasing thermal diffusivity with a transition in component occurring at an intermediate value of thermal diffusivity.

The curves in Figures 5.4, 5.5, 5.10, and 5.11 indicate that the orientation of the maximum pricipal tensile stress is dependent on Fourier modulus and aspect ratio. The consequences of this with regard to fracture are illustrated in Figure 5.12 which shows the relative location and orientation of the possibilities for maximum principal tensile stress. The σ_x component tends to propagate cracks in a direction perpendicular to the hot face and the σ_y component tends to cause cracking in a direction parallel to the hot face.

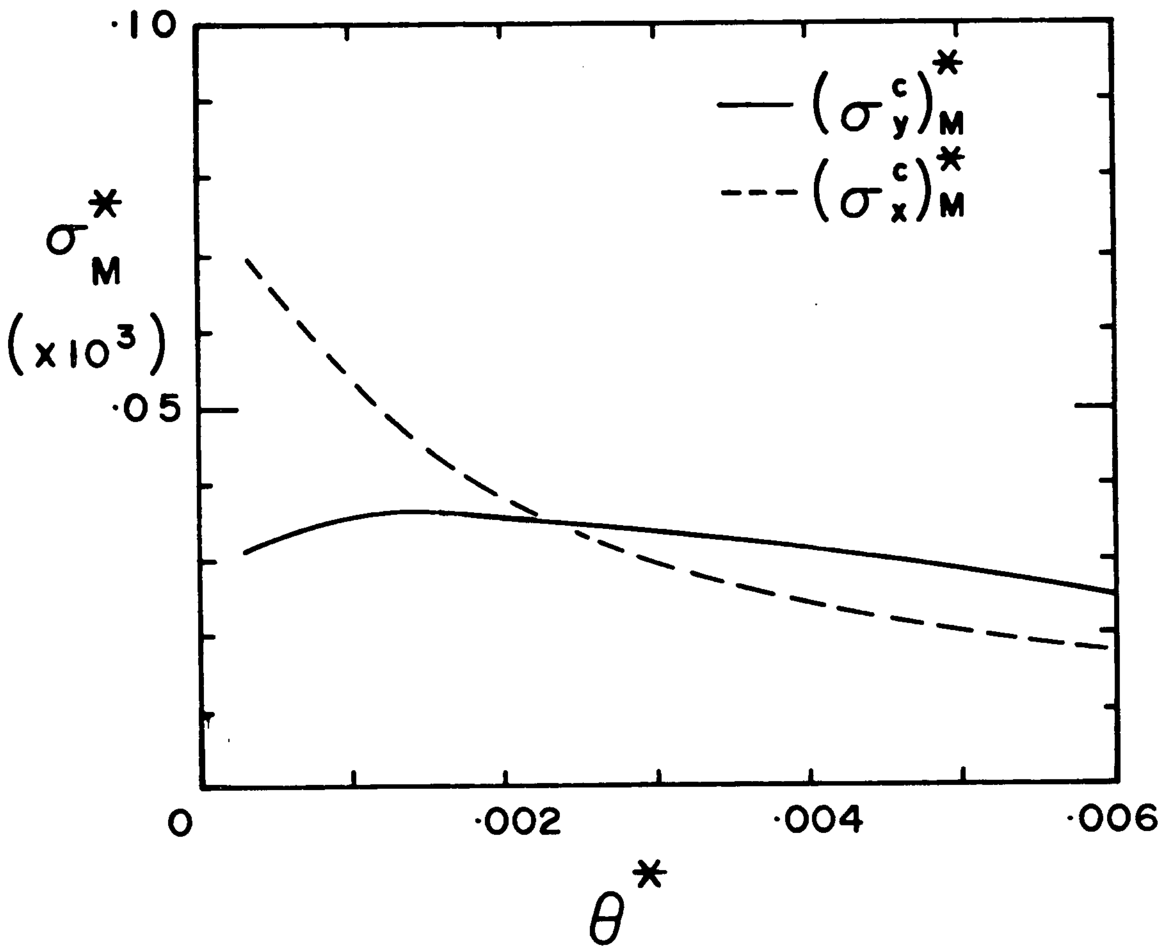

Figure 5.11 Dimensionless peak σ_x and σ_y principal tensile stresses on heating versus Fourier modulus for the conditions of Figure 5.8B of the Chang study.

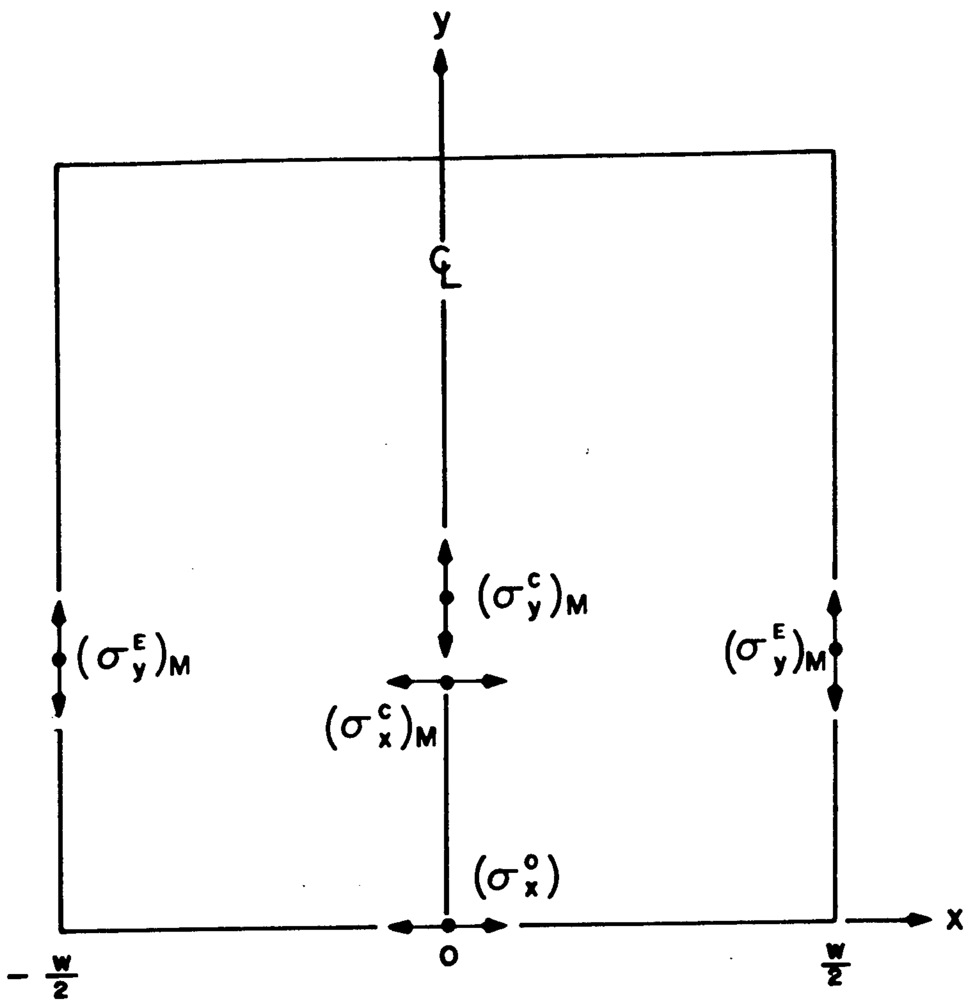

Figure 5.12 Relative orientation and location of the peak principal tensile stresses on heating and cooling.

The component which is the maximum principal tensile for a particular set of conditions can be determined from Figure 5.13 which shows plots of the critical combinations of Fourier modulus and aspect ratio for which the peak σ_x and σ_y values are equal for the heating case (solid line) and the cooling case (dashed line). The σ_x component is dominant for all combinations of Fourier modulus and aspect ratio above the curve and the σ_y component for all combinations below the curve.

Kingery based the derivation of a resistance to fracture initiation parameter for the case of an infinite slab heated at a constant rate ϕ on the following expressions for the maximum principal tensile stress:

$$\sigma_M = \frac{E\alpha}{1-\nu} \cdot \frac{\phi \ell^2}{3a} \quad \text{(surface)} \qquad (5.16)$$

$$\sigma_M = \frac{E\alpha}{1-\nu} \cdot \frac{\phi \ell^2}{6a} \quad \text{(center)} \qquad (5.17)$$

Equations 5.16 and 5.17 are obtained by substituting the non-transient portion of the analytical solution given by equation 5.6 into

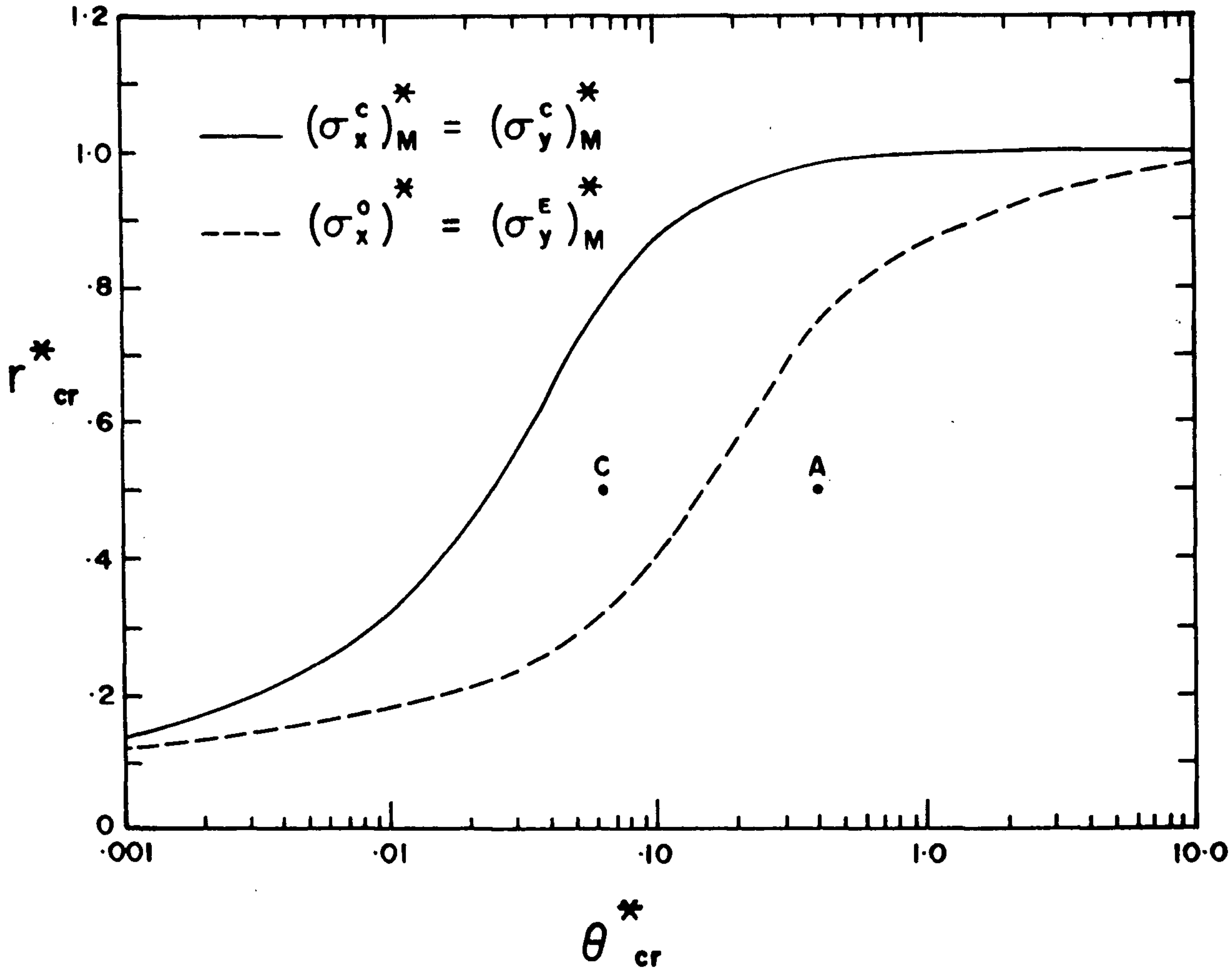

Figure 5.13 Combinations of Fourier modulus and aspect ratio for which the peak σ_x and σ_y principal stresses on heating and cooling are equal.

$$\sigma = \frac{E\alpha}{1-\nu} \left\{ -T + \frac{1}{2h} \int_{-h}^{+h} T dy + \frac{3y}{2h^3} \int_{-h}^{+h} T y dy \right\} \qquad (5.18)$$

which gives the through thickness stress distribution of an infinite slab of half-thickness h.

The maximum rate of temperature change without fracture ϕ_{max} is thus

$$\phi_{max} = \frac{\sigma_f \, (1-\nu) \, a}{E \, \alpha} \cdot S = R'' \cdot S \qquad (5.19)$$

where S is a size factor and R" is the resistance to fracture initiation parameter for the constant heating rate problem. Alternatively, R" can be derived directly from the proportionality of σ^* and γ^* which in expanded form is

$$\frac{\sigma_M \, (1-\nu)}{E} \propto \frac{\phi \alpha \ell^2}{a} . \qquad (5.20)$$

In any case, as noted previously, a major advantage of the constant heating rate case over the constant convective heat transfer coefficient case apparent from equation 5.19 is that the resistance to thermal shock parameter is directly related to the boundary condition.

The Kingery parameter correctly suggests that resistance to fracture initiation for the constant heating rate case is proportional to fracture strength, the factor $(1-\nu)$, and thermal diffusivity; and inversely related to elastic modulus and coefficient of thermal expansion. However, in neglecting the transient aspect of the problem, the model over-simplifies the influence of thermal diffusivity. Furthermore, the R" parameter is not useful for assessing geometric effects.

The maximum in the peak stress variation in Figure 5.8B is associated with the complex role of thermal diffusivity in relation to the nature and magnitude of the thermal loading. As constant and linear temperature fields produce no stress in traction-free rectangular shapes, thermal loading is related to the second derivative of temperature with respect to space T", which is

$$T'' = \frac{\phi}{a} \operatorname{erfc} \left[\frac{y}{2 \sqrt{(at)}} \right] \tag{5.21}$$

where erfc is the complement of the error function. The complex influence of thermal diffusivity can be attributed to the fact that the variable appears in both the transient and non-transient parts of the expression for T"; hence the appearance of the combinations of (ϕ/a) in γ^* and (at) in θ^*.

The effect of length on σ_M is particularly difficult to sort out as this variable is present in all three independent dimensionless parameters. An interesting finding of Chang et al from the design standpoint was that the magnitude of the peak tensile stress is independent of length for $40<\ell<80$ cm for values of time, width, and heating rate considered. In support of this finding is Figure 5.14, a plot of σ_M^* versus θ^* which highlights the influence of the variables contained in the Fourier modulus.

In each case the curves labelled A, B, and C are obtained by varying the respective parameter while holding all other variables fixed. The starting case (Table XX) is indicated by the large dot at the intersection of the curves. Curves A and B reflect the fact that, for the example case, σ_M increases with time and decreases with thermal diffusivity over the ranges of $40<t<40000$ s and $0.001<a<0.01$ cm^2/s.

Curve C is additional support for the finding of Chang et al that the maximum principal tensile stress is essentially independent of length over a wide range of conditions. This behaviour can be attributed to compensating thermal loading and geometric effects. An increase in length tends to: (i) increase γ^* which tends to increase σ_M, (ii) decrease θ^* which tends to reduce σ_M, and (iii) decrease r^* which tends to reduce σ_M.

Table XX

Data for curves in Figures 5.14 and 5.17

Heating Rate (ϕ_f)	1.5 °C/min
Time (t)	4000 s
Thermal Expansion Coefficient (α)	10×10^{-6} °C^{-1}
Thermal Diffusivity (a)	0.01 cm^2s^{-1}
Elastic Modulus (E)	60 GPa
Poisson's Ratio (ν)	0.20
Width (w)	10 cm
Length (ℓ)	20 cm

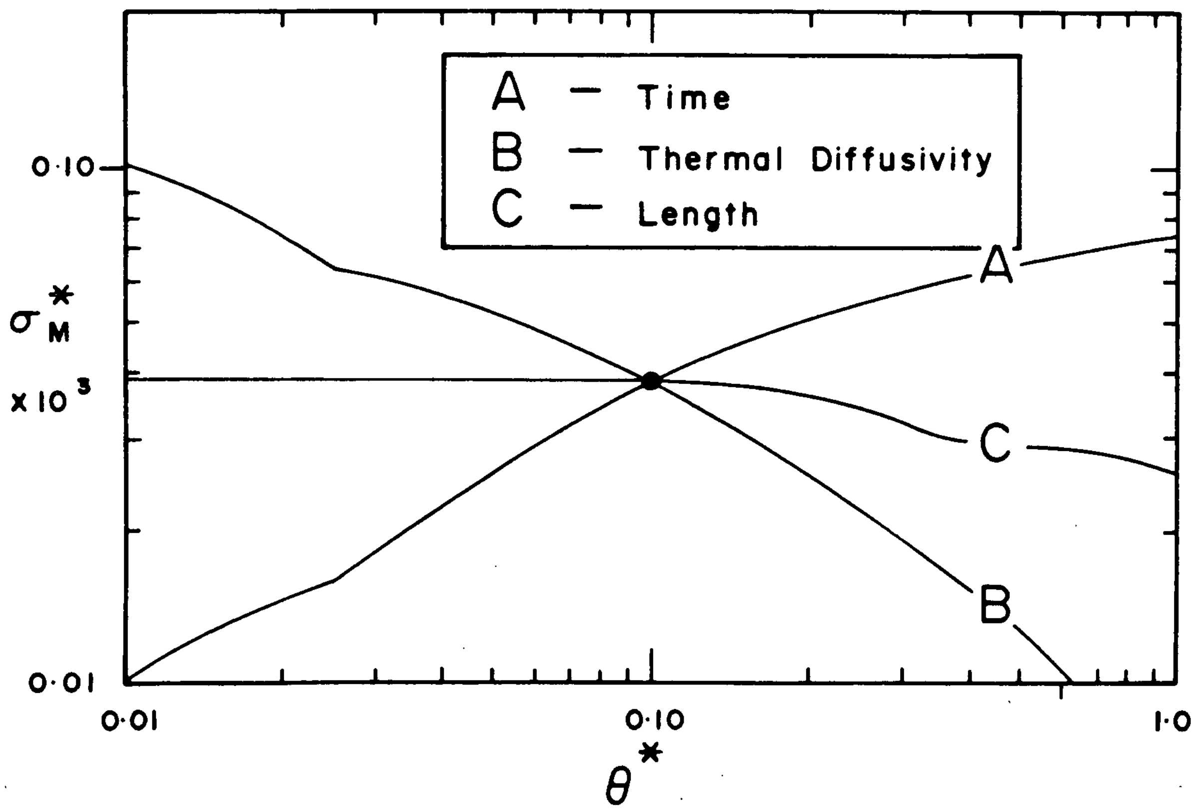

Figure 5.14 Dimensionless maximum principal tensile stress versus Fourier modulus. Curves are constructed by varying time (A), thermal diffusivity (B), and length (C) in turn while holding all other variables fixed at the values in Table XX.

5.3.4 Summary

The finite element method and dimensional analysis have been used to develop a convenient tabulated form of the general solution for the maximum principal tensile stress of a traction-free rectangular shape subjected to a constant heating or cooling rate. The solution is the basis for the development of a theoretical resistance to fracture initiation parameter which accounts for the influence of geometry and temperature range, as well as thermal and mechanical properties.

5.4 Solution for Total Strain Energy

The Hasselman relationships involving total strain energy (equations 2.10, 2.16, and 2.32) are not applicable to the industrial lining problem and, in any case, lack transient and geometric terms. No general solutions, or indeed any results for individual cases, for the total strain energy of traction-free rectangular shapes subjected to any thermal boundary condition could be found in the literature. In this section a solution for the total strain energy of the two-dimensional constant heating rate thermoelastic problem is presented.

The strain energy dependence for the two-dimensional constant heating rate problem is

$$U = f(\ t,\ \phi,\ a,\ E,\ \alpha,\ \nu,\ \ell,\ w\ ) \tag{5.22}$$

where U is the total strain energy per unit thickness. Dimensional analysis, outlined in Appendix IX, can be used to reduce the number of variables from nine to four. The dimensionless form of equation (5.22) is

$$U^* = f(\ \theta^*, \gamma^*, r^*), \tag{5.23}$$

which indicates that the dimensionless total strain energy U^*,

$$U^* = \frac{U(1-\nu)}{E\ell^2(1+\nu)} \tag{5.24}$$

is dependent on Fourier modulus, dimensionless thermal load, and aspect ratio.

As with the solution for maximum principal tensile stress, a two-step procedure is used to obtain U^* for arbitrary conditions. A property of the constant heating rate problem is that dimensionless total strain energy is directly proportional to the square of dimensionless thermal load for conditions of fixed Fourier modulus and aspect ratio. This relationship follows from the fact that strain energy is dependent on the product of stress and strain, both of which are directly proportional to heating rate and thermal expansion coefficient. Thus the general solution of equation 5.23 for arbitrary γ^* is given by

$$U^* = U^*_{0.01} \left(\frac{\gamma^*}{0.01} \right)^2 \tag{5.25}$$

where $U^*_{0.01}$, the dimensionless total strain energy for the condition of $\gamma^*=0.01$, is obtained from interpolation curves which are constructed using the results in Table XXI. The total strain energy is then found using

$$U = U^* \; E \; \ell^2 \, \frac{(1+\nu)}{(1-\nu)} \; . \tag{5.26}$$

The dimensional analysis and the numerical results are used to highlight the influence of the individual variables on total strain energy. Since the dimensionless strain energy is independent of elastic properties (see equation 5.23), the role of these variables is apparent from equation 5.26 which indicates the total strain energy is directly proportional to elastic modulus and the factor $(1+\nu)/(1-\nu)$. While the U-E direct proportionality holds when all other variables are fixed, the Hasselman premise that strain energy at fracture is inversely proportional to elastic modulus is valid. This point is considered in greater detail in section 5.7.

Table XXI

Dimensionless Total Strain Energy for Various Aspect Ratio and Fourier Modulus ($\gamma^*=0.01$)

θ^*	r^*					
	0.125	0.25	0.375	0.50	0.625	0.75
0.001	$0.500(10^{-7})$	$0.309(10^{-6})$	$0.724(10^{-6})$	$0.123(10^{-5})$	$0.180(10^{-5})$	$0.240(10^{-6})$
0.002	$0.127(10^{-6})$	$0.105(10^{-5})$	$0.280(10^{-5})$	$0.513(10^{-5})$	$0.786(10^{-5})$	$0.109(10^{-4})$
0.004	$0.283(10^{-6})$	$0.311(10^{-5})$	$0.973(10^{-5})$	$0.196(10^{-4})$	$0.319(10^{-4})$	$0.460(10^{-4})$
0.010	$0.682(10^{-6})$	$0.105(10^{-4})$	$0.412(10^{-4})$	$0.962(10^{-4})$	$0.174(10^{-3})$	$0.270(10^{-3})$
0.040	$0.197(10^{-5})$	$0.434(10^{-4})$	$0.228(10^{-3})$	$0.674(10^{-3})$	$0.146(10^{-2})$	$0.262(10^{-2})$
0.100	$0.355(10^{-5})$	$0.899(10^{-4})$	$0.540(10^{-3})$	$0.179(10^{-2})$	$0.430(10^{-2})$	$0.835(10^{-2})$
0.400	$0.751(10^{-5})$	$0.210(10^{-3})$	$0.138(10^{-2})$	$0.498(10^{-2})$	$0.127(10^{-1})$	$0.259(10^{-1})$
1.0	$0.106(10^{-4})$	$0.301(10^{-3})$	$0.202(10^{-2})$	$0.736(10^{-2})$	$0.190(10^{-1})$	$0.390(10^{-1})$
4.0	$0.144(10^{-4})$	$0.412(10^{-3})$	$0.277(10^{-2})$	$0.102(10^{-1})$	$0.264(10^{-1})$	$0.543(10^{-1})$
10.0	$0.160(10^{-4})$	$0.460(10^{-3})$	$0.310(10^{-2})$	$0.114(10^{-1})$	$0.296(10^{-1})$	$0.608(10^{-1})$

Table XXI (continued)

Dimensionless Total Strain Energy for Various Aspect Ratio and Fourier Modulus (γ^*=0.01)

θ^*	r^*					
	0.875	1.0	1.25	1.5	2.0	4.0
0.001	0.303(10^{-5})	0.369(10^{-5})	0.502(10^{-5})	0.638(10^{-5})	0.909(10^{-5})	0.207(10^{-4})
0.002	0.141(10^{-4})	0.174(10^{-4})	0.243(10^{-4})	0.314(10^{-4})	0.455(10^{-4})	0.103(10^{-3})
0.004	0.615(10^{-4})	0.781(10^{-4})	0.113(10^{-3})	0.148(10^{-3})	0.219(10^{-3})	0.503(10^{-3})
0.010	0.270(10^{-3})	0.383(10^{-3})	0.506(10^{-3})	0.105(10^{-2})	0.160(10^{-2})	0.381(10^{-2})
0.040	0.413(10^{-2})	0.592(10^{-2})	0.997(10^{-2})	0.143(10^{-1})	0.230(10^{-1})	0.576(10^{-1})
0.100	0.139(10^{-1})	0.208(10^{-1})	0.367(10^{-1})	0.538(10^{-1})	0.884(10^{-1})	0.226
0.400	0.447(10^{-1})	0.681(10^{-1})	0.123	0.183	0.304	0.784
1.0	0.676(10^{-1})	0.103	0.188	0.280	0.464	1.20
4.0	0.942(10^{-1})	0.144	0.262	0.390	0.649	1.68
10.0	0.106	0.162	0.294	0.438	0.728	1.88

A theoretical interpretation of the influence of coefficient of thermal expansion on thermal shock damage is possible with the aid of equation 5.25 which indicates that total strain energy is proportional to the square of the thermal expansion coefficient. This relationship alone explains the impact of α noted in the Nakayama study and accounts for the relative damage resistance of specimens A, B, C, and D (see Figure 4.30).

The time-dependence of total strain energy is revealed in Figure 5.15 which shows the variation of U^* with Fourier modulus for various aspect ratio. The shape of the curves reflects the rate of development of the stress and strain fields with regard to both magnitude and extent of penetration into the body; the rate being governed by the velocity at which the thermal disturbance at the boundary propagates through the body. As with the magnitude of stress, the strain energy tends to a limiting value at large Fourier modulus.

The influence of width on total strain energy is apparent from Figure 5.16 which highlights the variation of U^* with aspect ratio for various Fourier modulus. With all other variables held fixed, the curves reflect the effect of increasing width. As strain energy is computed as the integral of a density function over a space, the role of

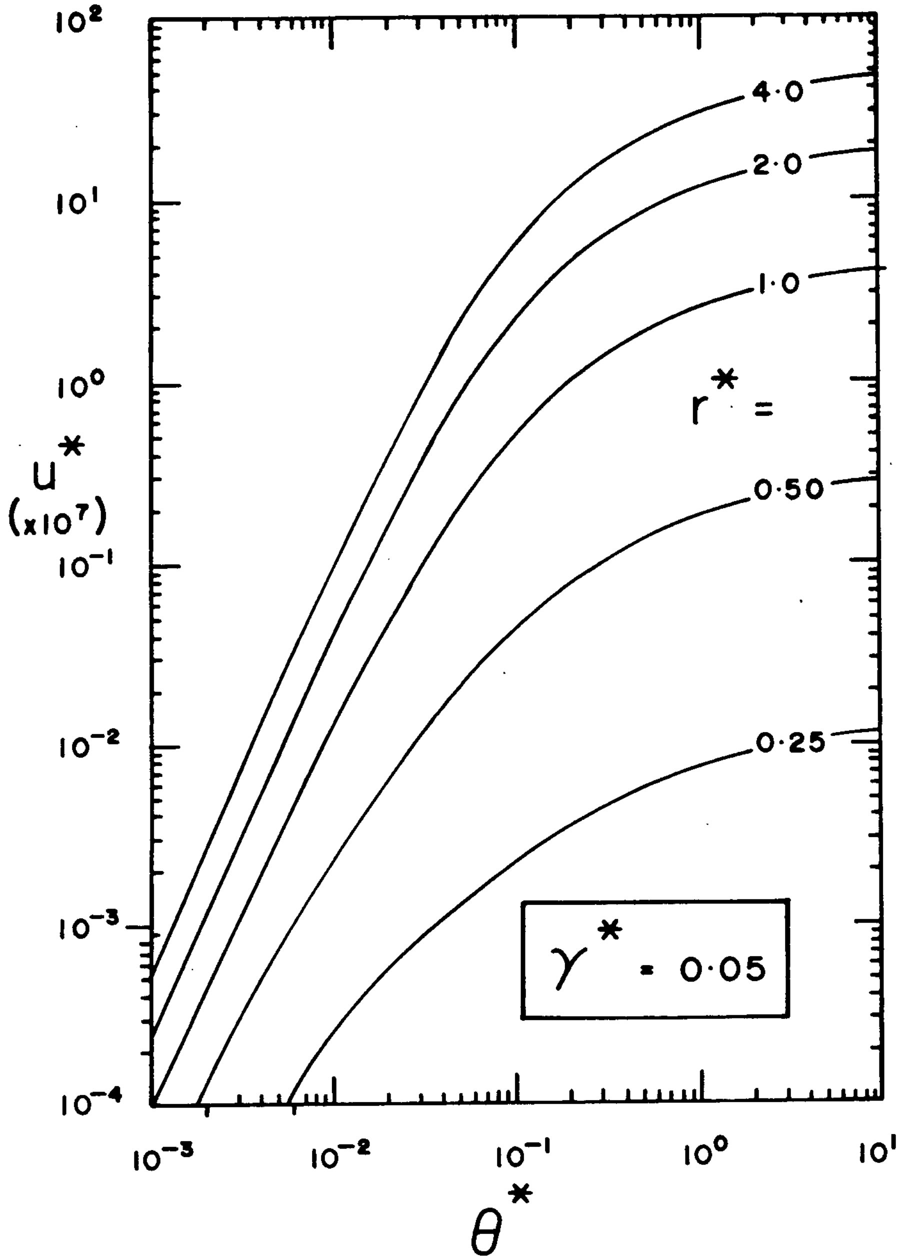

Figure 5.15 Dimensionless total strain energy versus Fourier modulus for various aspect ratio. (γ^*=0.05).

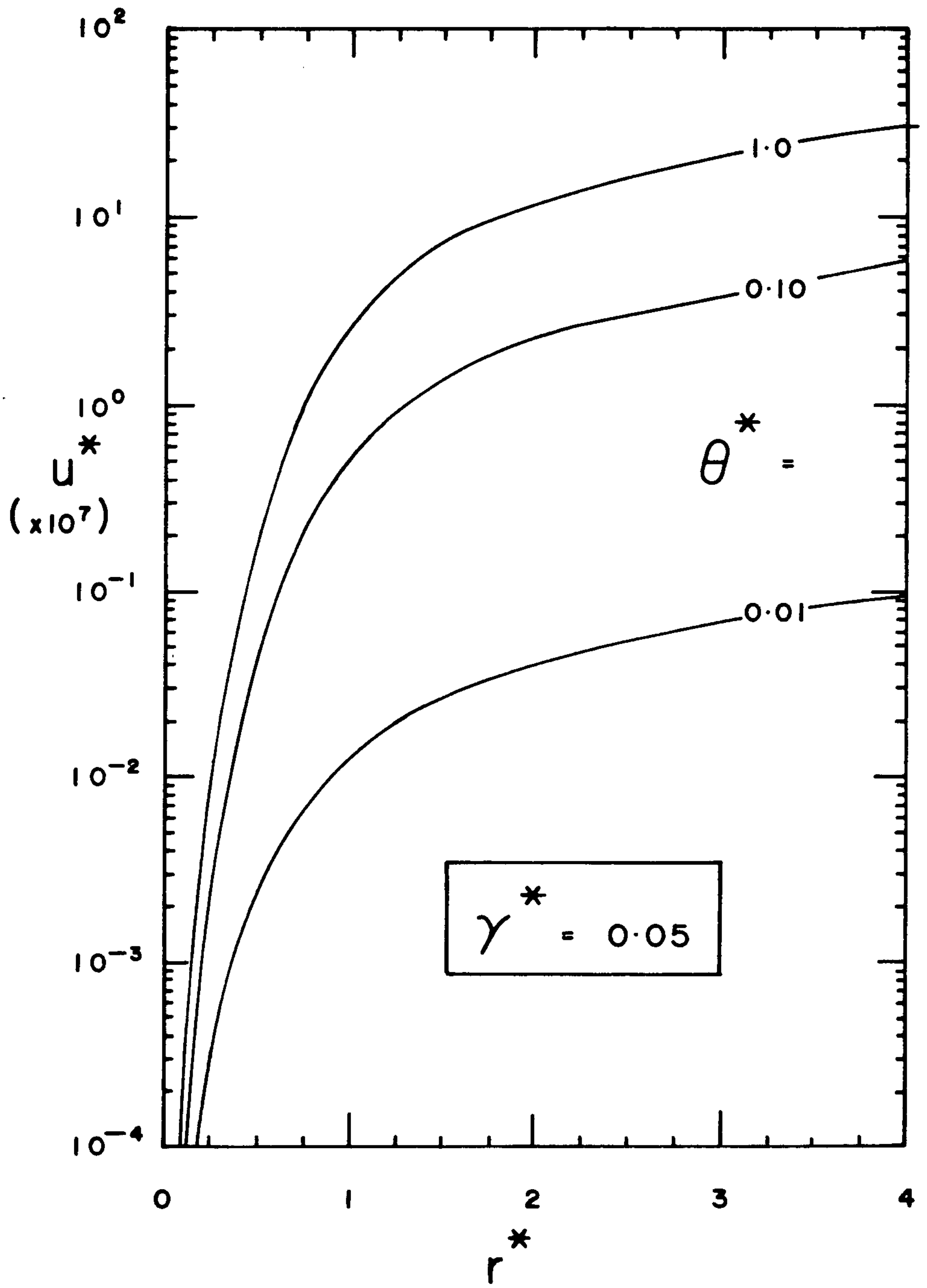

Figure 5.16 Dimensionless total strain energy versus aspect ratio for various Fourier modulus. (γ^*=0.05)

width is two-fold. The rapid increase in U with increasing w over the range $r^* < 1.0$ is due primarily to the influence of width on the nature and magnitude of the stress and strain fields, while the less rapid increase in U over the range $r^* > 2.0$ is due mainly to an increase in size.

The effect of changes in thermal diffusivity and length on total strain energy is not as easily ascertained as these variables are contained in several dimensionless parameters. The $U^*-\theta^*$ curves of Figure 5.17 reflect the influence of time (curve A), thermal diffusivity (curve B), and length (curve C) on dimensionless strain energy. The curves were constructed using the example case of Table XX as the starting point and and varying each parameter in turn while holding all others fixed. Thus the range of Fourier modulus corresponds to the following ranges of time, thermal diffusivity, and length: $400 < t < 40000$ s, $0.001 < a < 0.10$ cm^2/s, and $6.32 < \ell < 63.2$ cm.

From equation 5.26 it is apparent that the variation of U^* reflects the influence of time and thermal diffusivity on U. Thus curves A and B indicate that the total strain energy varies directly with time and inversely with thermal diffusivity over the applicable ranges. While curve C gives the variation of U^* with length, it is also noted from equation 5.26 that the total strain energy is related to the product of dimensionless strain energy and length squared. The plot of

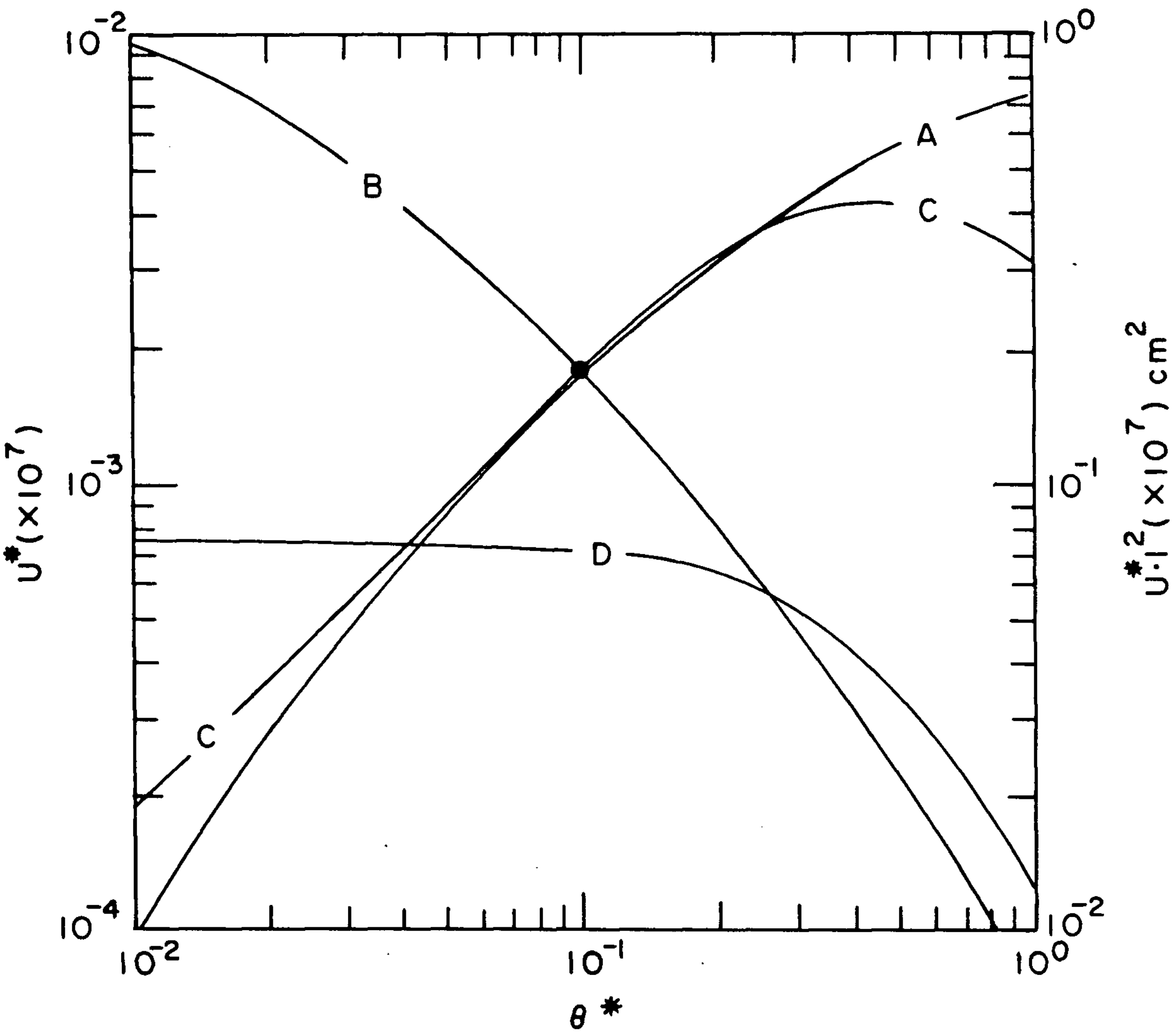

Figure 5.17 Dimensionless total strain energy versus Fourier modulus. Curves constructed by varying time (A), thermal diffusivity (B), and length (C) in turn while holding all other variables fixed at the values of Table XX. Curve (D) is the product of total dimensionless strain energy and length squared versus Fourier modulus.

$(U^* \ell^2)$ versus Fourier modulus (curve D) suggests that total strain energy is independent of length over the range $20<\ell<63.2$ cm, but that further decreases in length over the range $6.32<\ell<20$ cm cause a corresponding decrease in strain energy.

To summarize, the finite element method and dimensional analysis have been used to develop a convenient tabulated form of solution for the total strain energy of the two-dimensional constant heating rate problem. Total strain energy was found to be proportional to elastic modulus, the factor $(1+\nu)/(1-\nu)$, and the square of the heating rate and the coefficient of thermal expansion; and to increase in a highly nonlinear way with increasing time and width; and, for a selected range, to vary inversely with thermal diffusivity and directly with length. The influence of length is particularly complex as total strain energy appears to be independent of length for certain conditions.

5.5 The Thermal Shock Fracture Problem

5.5.1 Locus of Fracture Initiation

It is important to distinguish between the thermal stress problem and the thermal shock fracture problem. While the latter is usually concerned with assessing the influence of the individual variables on the magnitude of the maximum principal tensile stress σ_M, the former involves the determination of the sets of variables which will just produce a maximum principal tensile stress equal to a specified value of fracture strength. In the thermoelastic approach, the thermal shock fracture problem can be regarded as an inverse thermal stress problem.

A convenient mathematical form of the inverse problem is

$$t_f = f(\ \phi_f,\ a,\ \alpha,\ \sigma_f,\ E,\ \nu,\ \ell,\ w\ ) \tag{5.27}$$

where the subscript f denotes values at fracture. In this inverted form time of fracture is the dependent variable, whereas stress - in the form of fracture strength - is an independent parameter.

The dimensionless form of the inverse problem can be expressed mathematically as

$$\theta_f^* = f(\ \gamma_f^*,\ \sigma_f^*,\ r^*) \tag{5.28}$$

where

$$\theta_f^* = \frac{a\ t_f}{\ell^2} \tag{5.29}$$

$$\gamma_f^* = \frac{\phi_f \alpha\, \ell^2}{a} \tag{5.30}$$

and

$$\sigma_f^* = \frac{\sigma_f(1-\nu)}{E}\,. \tag{5.31}$$

Solution curves satisfying equation (5.28), in the form of $\gamma_f^*-\theta_f^*$ plots for specified σ_f^* and r^*, can be constructed from discrete data points which are computed by using the tabulated values of $\sigma_{0.01}^*$ in conjunction with the following relationship,

$$\gamma_f^* = 0.01 \left(\frac{\sigma_f^*}{\sigma_{0.01}^*} \right)\,. \tag{5.32}$$

Expression (5.32) is another consequence of the direct proportionality of dimensionless stress and dimensionless thermal load for conditions of fixed Fourier modulus and aspect ratio.

A $\gamma_f^*-\theta_f^*$ curve is essentially a locus of fracture initiation conditions for shapes with specified combinations of mechanical properties and geometry. The curve in Figure 5.18, which gives all the combinations of heating rates and fracture times for the example case in

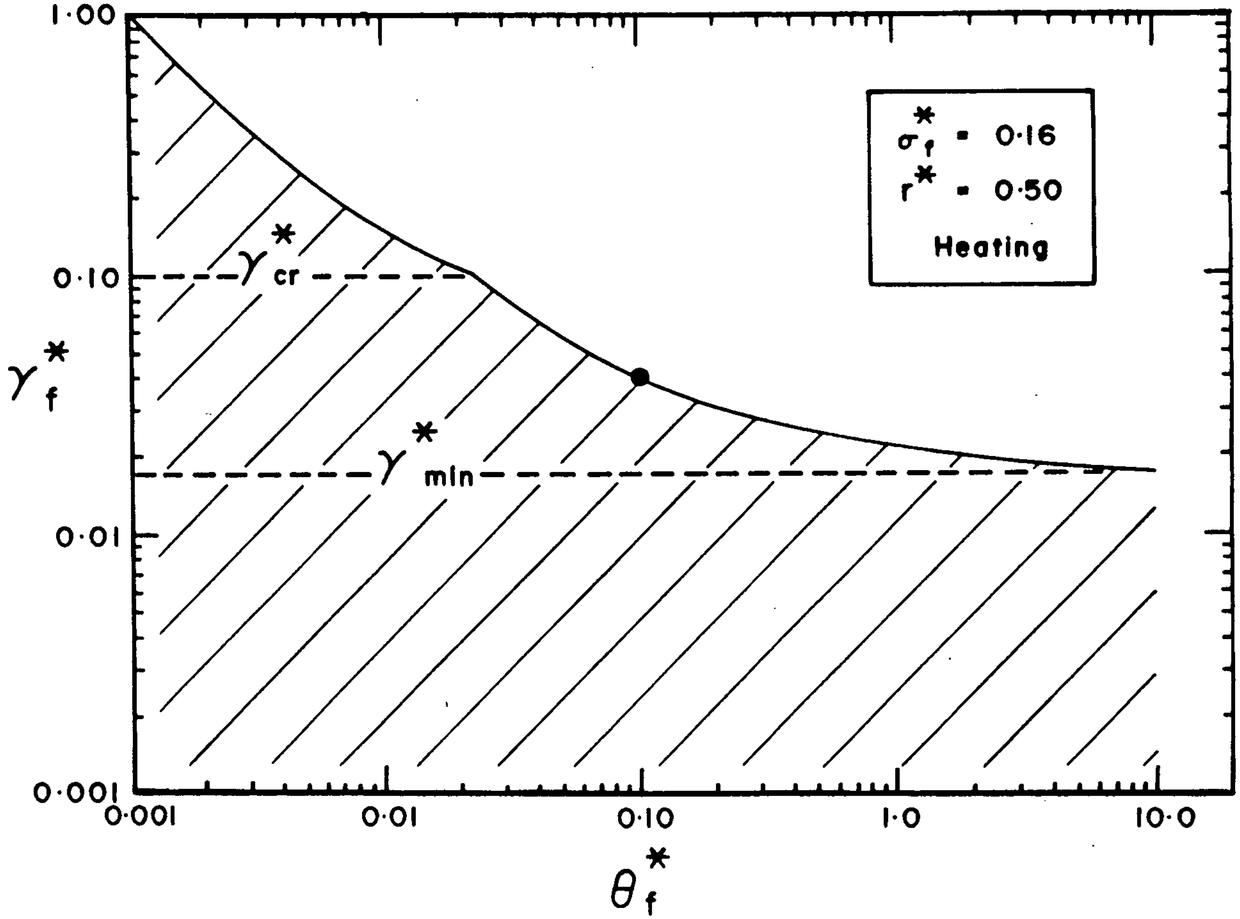

Figure 5.18 Dimensionless thermal load at fracture versus Fourier modulus at fracture. (σ_f^*=0.16, r^*=0.50, heating)

Table XX, illustrates all the typical features of fracture initiation loci. The inverse relationship possesses two characteristic values of dimensionless thermal load; γ^*_{min}, the minimum value required to produce fracture, and γ^*_{cr}, the value located at the point of abrupt change in curvature at which a transition in component at fracture takes place. For the range $\gamma^*_{min}<\gamma^*<\gamma^*_{cr}$ the σ_y component causes fracture and, for the range $\gamma^*>\gamma^*_{cr}$ the σ_x component reaches the specified fracture strength first.

In addition to facilitating computation, the dimensionless graphical approach provides a means for a geometric interpretation of thermal shock fracture initiation. The $\gamma^*_f-\theta^*_f$ curve defines the practical limits of a particular problem by identifying all the combinations of variables which satisfy the fracture criterion $\sigma_M=\sigma_f$. It separates the safe operating regime, the cross-hatched area below the curve where $\sigma_M<\sigma_f$, from the region above which is practically inaccessible and one of academic interest only as $\sigma_M>\sigma_f$.

This approach is particularly suitable for the industrial lining problem as the dimensionless parameters σ^*_f and r^* can be viewed as constraints which, once set by the selection of a component, fix the position of the fracture initiation locus in the $\gamma^*_f-\theta^*_f$ space. Before final selection it is possible to evaluate the effect of changes in mechanical properties and geometry in terms of a repositioning of the fracture initiation curve, whereas the influence of thermal expansion coefficient and thermal diffusivity can be interpreted in terms of a movement along the γ_f^*-θ_f^* curve.

5.5.2 Location of Fracture

The location of fracture is an important parameter which can have a significant impact on the nature and extent of thermal shock damage. Chang[18] has suggested that the location of fracture is a function of heating rate because with an increase in heating rate the location of a particular value of stress moves closer to the hot face. This is an important point which requires clarification.

Figure 5.19 gives the center line distribution of σ_y in dimensionless form for three combination of γ^* and θ^*. Curve A corresponds to the case where the fracture stress of $\sigma_f^* = 0.16$ is just attained at time $\theta_f^* = 0.38$ and curve B for identical conditions except for a doubling of the heating rate. Curves A and B are in line with the observations of Chang who noted that the magnitude of stress is proportional to heating rate, while the location of the peak stress is independent of heating rate.

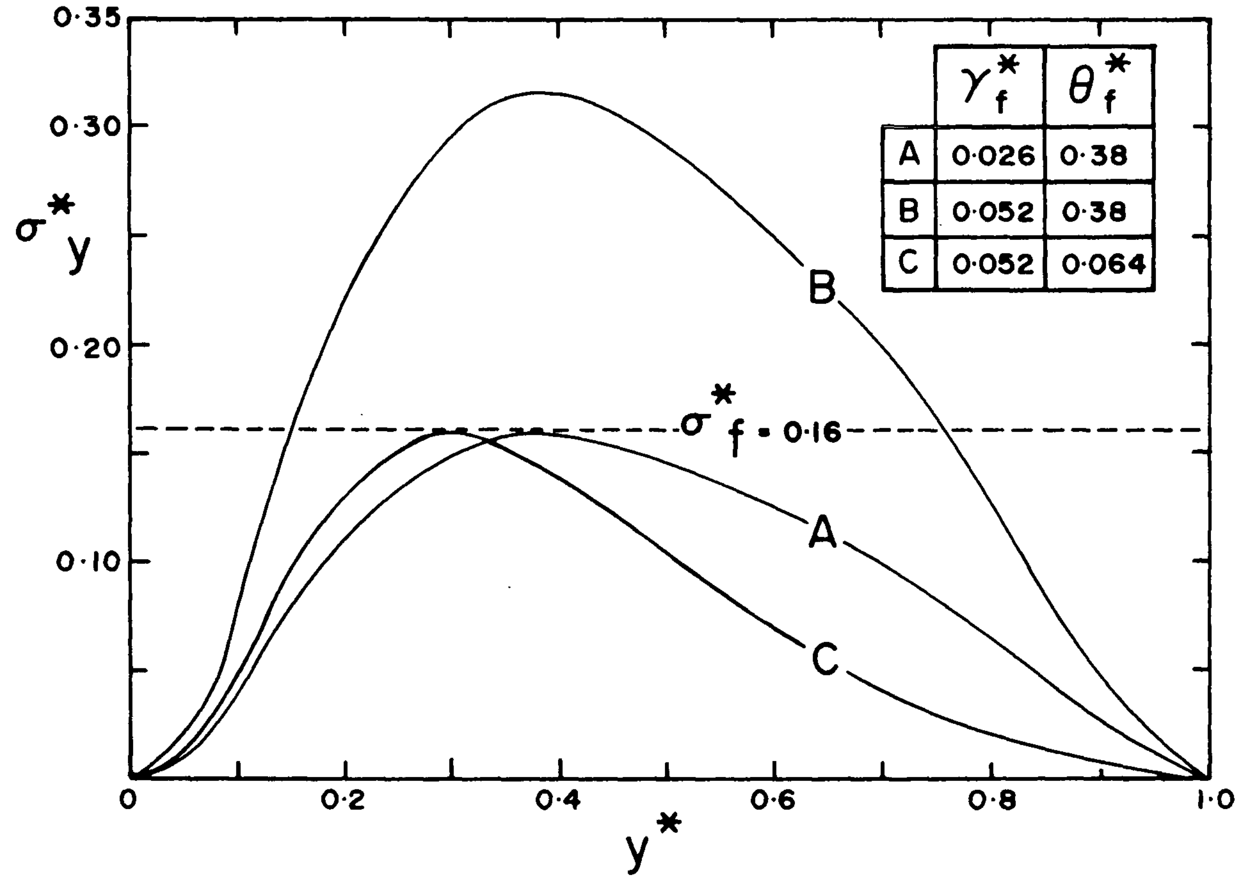

Figure 5.19 Dimensionless σ_y center line distribution for various dimensionless thermal load and Fourier modulus

That the position of any prescribed stress (for example $\sigma_f^*=0.16$) moves closer to the hot face with increasing heating rate is apparent from the relative positions of curve A and B. However, the implication of using this observation as an explanation for the dependence of location of fracture on heating rate is to suggest that the stress distribution at fracture is that given by curve B which is equivalent to stating that the material is capable of sustaining a stress double that of the fracture strength.

Curve C, the stress distribution at fracture for a heating rate double that of case A, illustrates that the location and time of fracture are both dependent on γ_f^* or heating rate. The effect of an increase in γ_f^* is to cause the stress field to develop more quickly in regions near the hot face with the consequence that the peak tensile stress reaches the fracture stress at an earlier time at a location nearer the hot face. In the limit as $\gamma_f^* \rightarrow \infty$, fracture tends to occur instantaneously at the hot face.

Figures 5.20 and 5.21 can be used to determine the location of fracture. Figure 5.20 gives the location along the center line of the maximum principal tensile stress on heating, $(y_M^c)^*$,as a function of

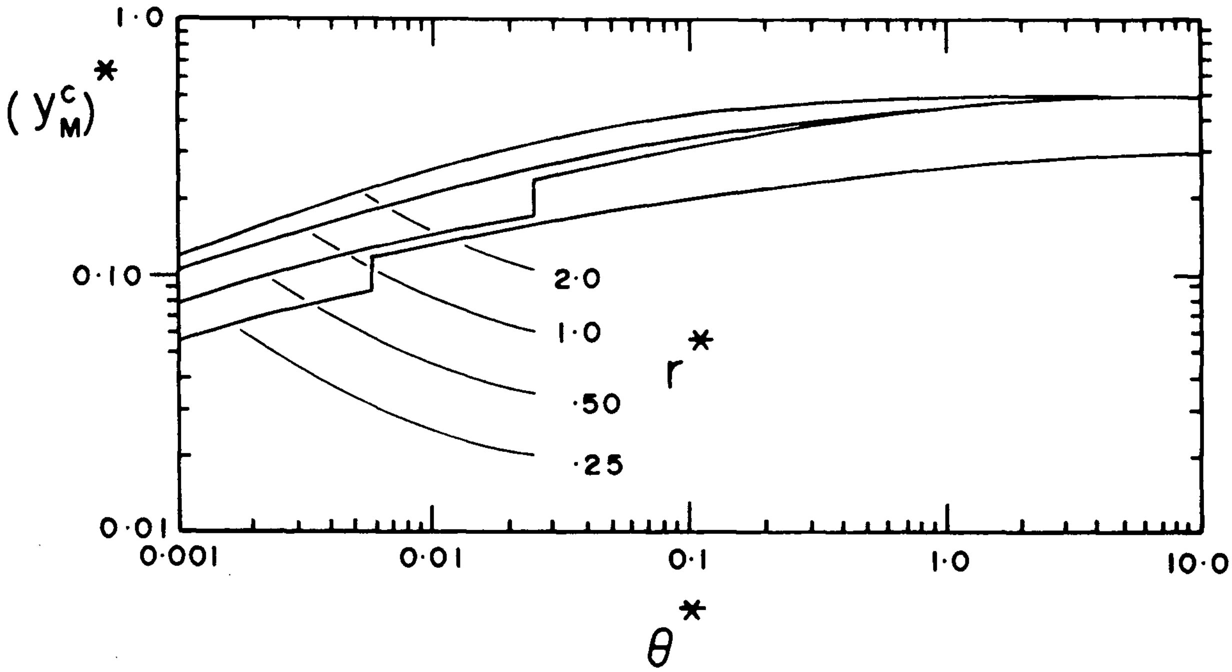

Figure 5.20 Dimensionless location of maximum principal tensile stress on heating versus Fourier modulus for various aspect ratio.

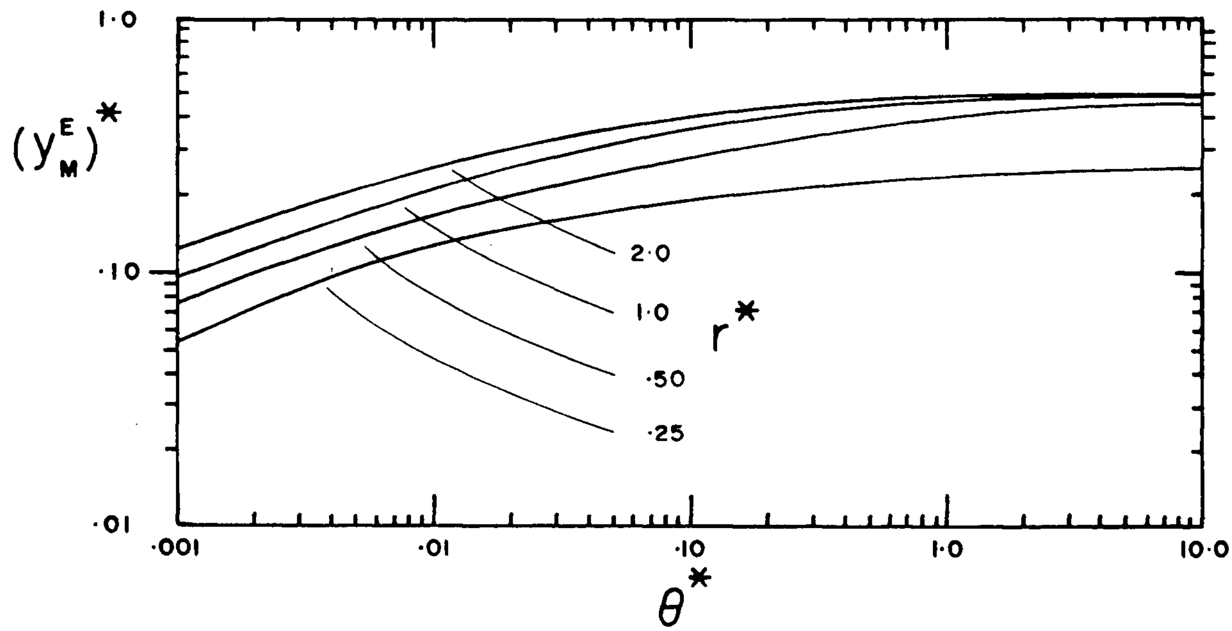

Figure 5.21 Dimensionless location of peak σ_y stress along the outside edge ($x=\pm w/2$) versus Fourier modulus for various aspect ratio.

Fourier modulus. The discontinuity in the curves of $r^* < 1.0$ coincides with the point at which the transition in σ_M occurs, with the σ_x component dominating to the left of the discontinuity and the σ_y component to the right. Figure 5.21 gives the location along the outside edge of the peak σ_y stress, $(y_M^E)^*$, as a function of θ^* for the cooling case.

5.5.3 Analysis of Fracture

All of the preliminary requirements for a thermoelastic analysis of the fracture behaviour of traction-free rectangular shapes subjected to a constant heating or cooling rate have now been presented. The dimensionless solutions for temperature, location and magnitude of maximum principal tensile stress, and total strain energy can be used to determine time of fracture, orientation and location of fracture stress, total strain energy at fracture, and a parameter of industrial importance, hot face temperature at fracture T_{hf}, which for the constant heating rate problem is given by

$$T_{hf} = \frac{(\theta_f^*)(\gamma_f^*)}{\alpha} . \tag{5.33}$$

The procedure for fracture analysis is outlined with reference to the example case of Table XXII. The values corresponding to the example case are given in brackets. The method is as follows:

(i) compute σ_f^* and r^* ($\sigma_f^*=0.16$ and $r^*=0.50$)

(ii) construct $\gamma_f^*-\theta_f^*$ curve using equation 5.32 and Table XVIII (see Figure 5.22)

(iii) construct $U_f^*-\theta_f^*$ curve using γ_f^* values, equation 5.25, and Table XXI, (see Figure 5.22)

(iv) compute γ_f^* for given problem, ($\gamma_f^*=0.04$)

(v) locate θ_f^* on $\gamma_f^*-\theta_f^*$ curve, ($\theta_f^*=0.11$)

(vi) locate U_f^* on $U_f^*-\theta_f^*$ curve, ($U_f^*=0.031\text{x}10^{-7}$)

(vii) locate y_f^* on $(y_M^c)^*-\theta^*$ in Figure 5.22, ($y_f^*=0.32$)

(viii) compute t_f using equation 5.29, (t_f=73 min)

(ix) compute U_f using equation 5.26, (U_f=0.11 Joules/cm)

Table XXII

Reference Case for Figures 5.23-5.27

Heating Rate (ϕ)	6 °C/min
Fracture Strength (σ_f)	12 MPa
Elastic Modulus (E)	60 GPa
Thermal Diffusivity (a)	0.01 cm^2s^{-1}
Thermal Expansion Coefficient (α)	$10x10^{-6}$ $°C^{-1}$
Poisson's Ratio (ν)	0.20
Width (w)	10 cm
Length (ℓ)	20 cm

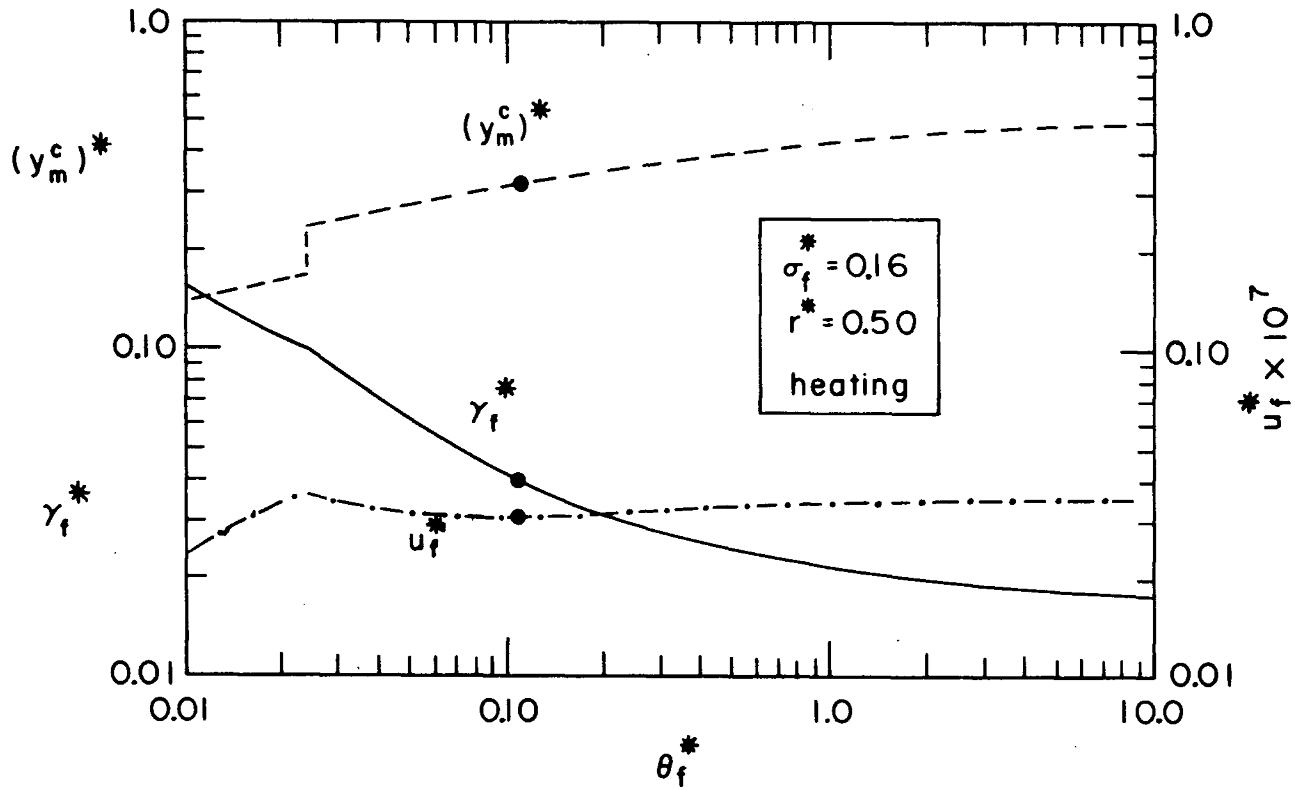

Figure 5.22 Dimensionless thermal load, total strain energy, and location versus Fourier modulus. (σ_f^*=0.16, r^*=0.50, heating)

(x) compute y_f using equation 5.5, (y_f=6.4 cm)

(xi) compute T_{hf} using equation 5.33, (T_{hf}=440 °C)

If desired the temperature profile at fracture can be estimated using the value of θ_f^* and Figure 5.2. The strain energy numerical computations are based on a unit thickness of 1 cm. The total strain energy at fracture for the example case is evaluated using equation 5.26 as follows:

$$U_f = (0.031\text{x}10^{-7})(60\text{x}10^9\frac{N}{m^2})(20\text{x}20\text{x}1\frac{cm^3}{cm})(\frac{cm^3}{10^6 cm^3})(\frac{1.2}{0.8})$$
$$= 0.11 \text{ Joules/cm thickness}$$

Thus, for the two-dimensional case, the ℓ^2 term in equation 5.26 essentially represents a volume per unit thickness. The example case is one of plane strain. The plane stress case is obtained using the same procedure but setting Poisson's ratio to zero.

5.5.4 Influence of the Individual variables

The procedure for fracture analysis described in the previous section has been used to construct the curves in Figures 5.23 to 5.25

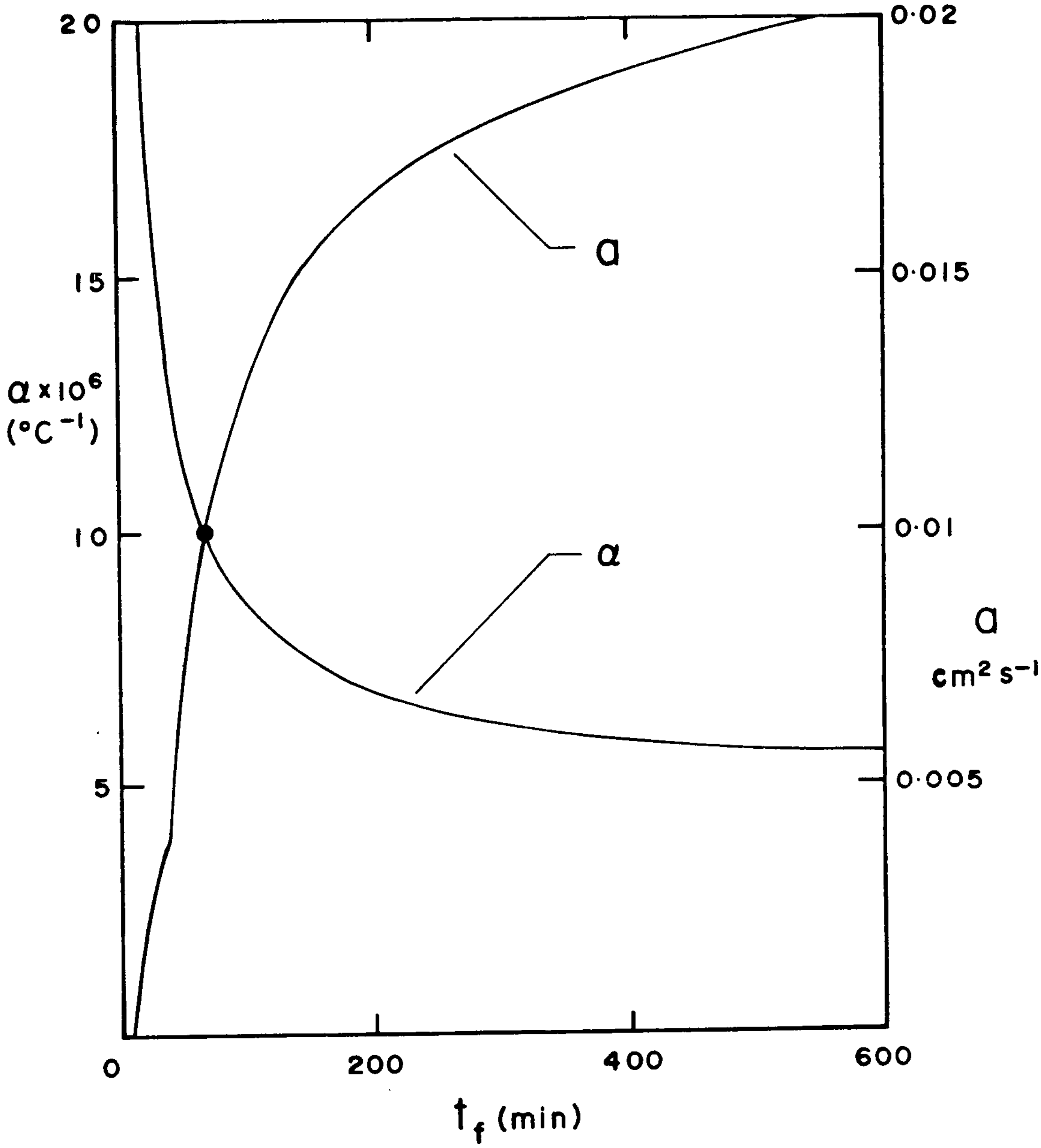

Figure 5.23 Coefficient of thermal expansion and thermal diffusivity versus time of fracture. Based on the example case of Table XXII.

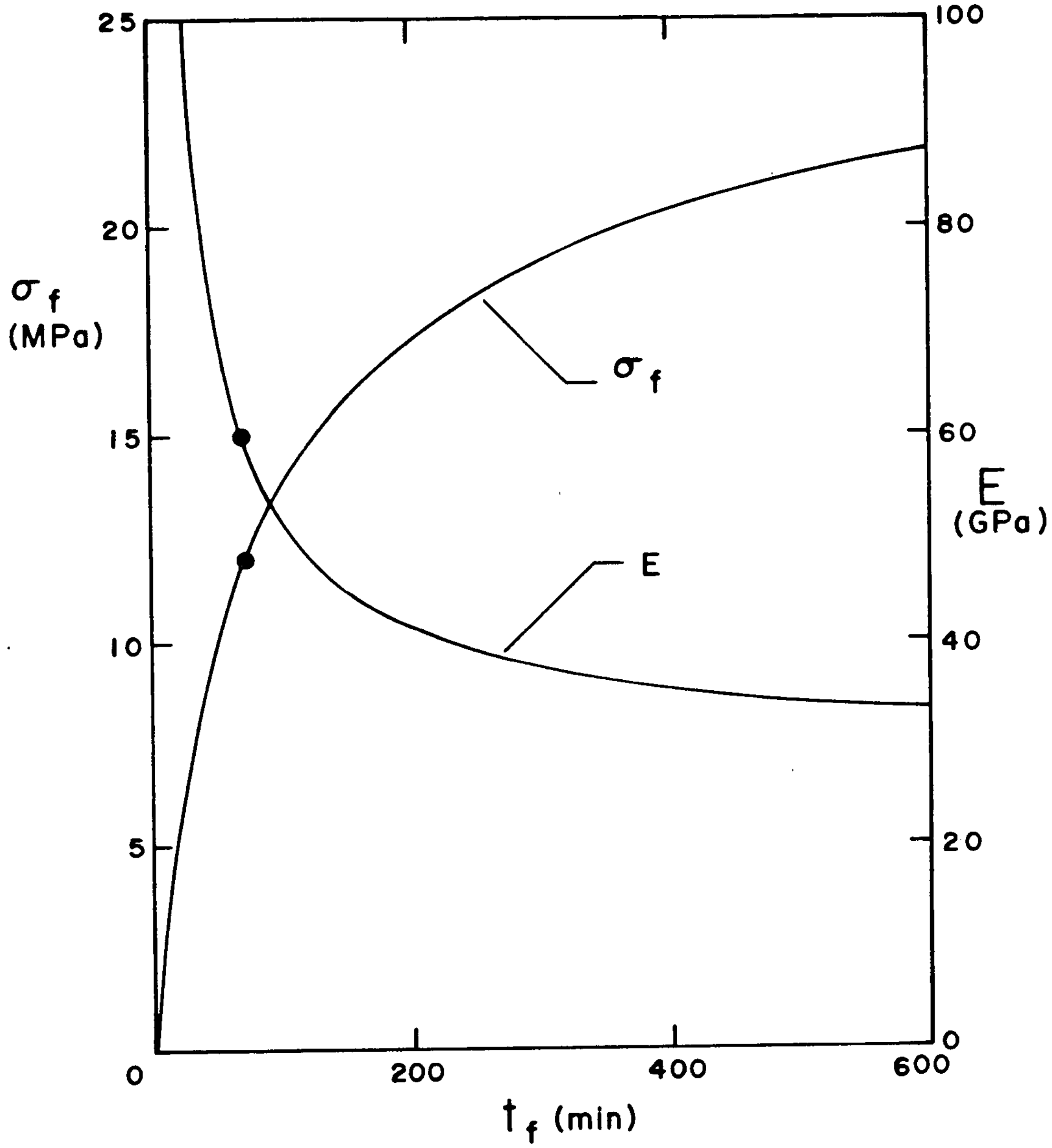

Figure 5.24 Fracture strength and elastic modulus versus time of fracture. Based on the example case of Table XXII.

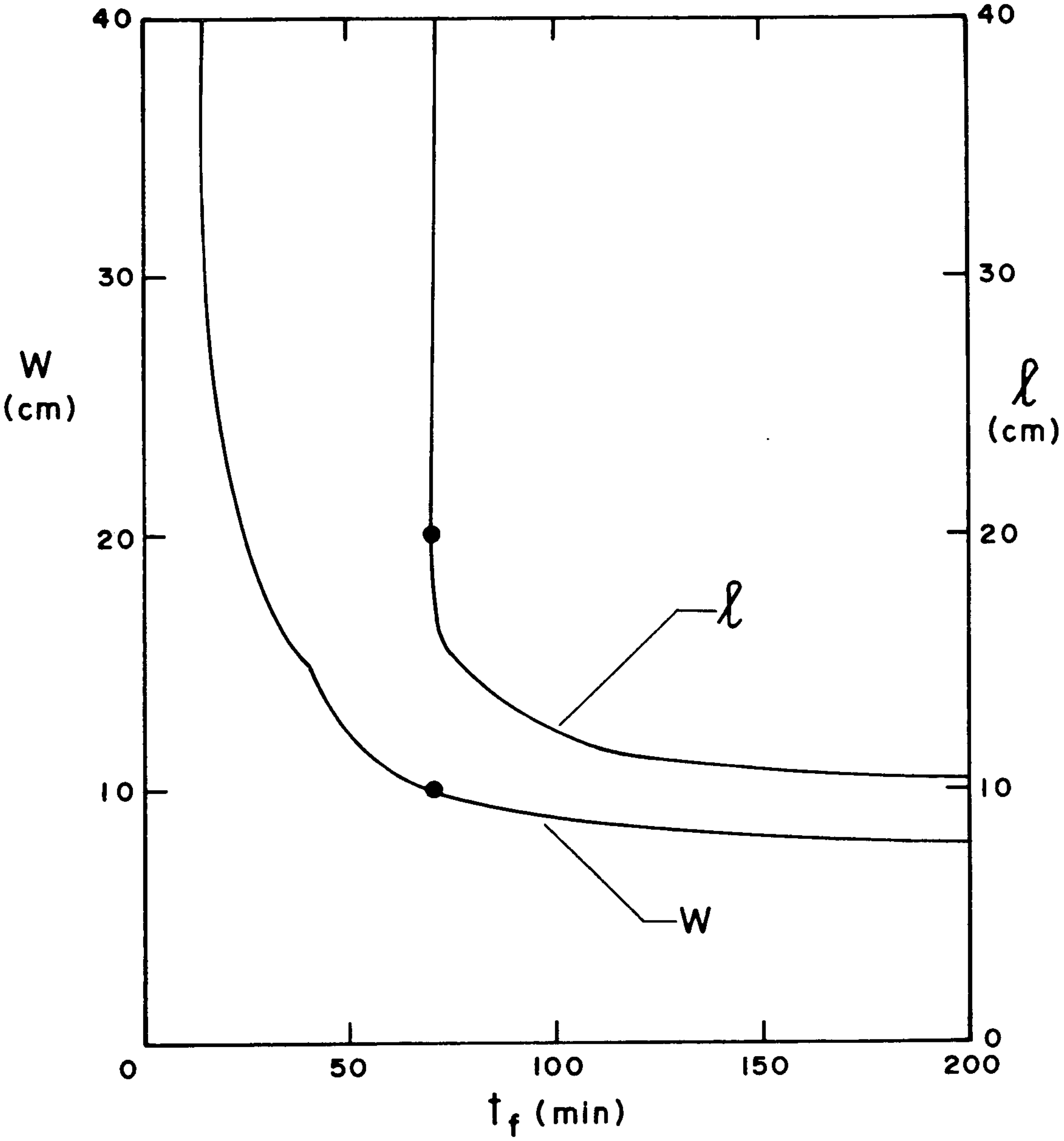

Figure 5.25 Width and length versus time of fracture. Based on the example case of Table XXII.

which highlight the influence of thermal and mechanical properties and geometry on time of fracture. The approach taken in constructing each curve was to vary the parameter of interest while holding all other variables fixed at the values of the example case of Table XXII. The position of the example case on each curve is indicated by a large dot.

The asymptotic nature of the variations is characteristic of the nature of the stress solution for the constant heating rate problem. With the exception of thermal diffusivity, the influence of the thermal and mechanical properties on time of fracture is qualitatively similar to that noted for the constant heat transfer coefficient case discussed in Chapter 4. In both cases the time of fracture varies directly with fracture strength and inversely with coefficient of thermal expansion and elastic modulus.

For the constant h case, time of fracture is directly proportional to the ratio of thermal conductivity to thermal diffusivity which suggests that t_f varies directly with the product of density and specific heat, but is independent of thermal conductivity. In the contrast to the constant h case, the variation in Figure 5.23 suggests that time of fracture varies directly with thermal diffusivity which, in turn, suggests that t_f varies directly with thermal conductivity and inversely with density and specific heat.

The effect of changes in the geometry of the example case on time of fracture is illustrated in Figure 5.25. The asymptotic inverse relationships indicate that: (i) for a fixed thermal shock (ϕ_f= 6°C/min for the example) there exists a critical minimum size which must be exeeded before fracture occurs; (ii) time to fracture rapidly decreases with increases in size above the critical value, and (iii) there exists an upper limit of size at which the time of fracture is independent of geometry. The trends in Figure 5.25 are generally in line with the size effect observed in the Semler and Nakayama experiments. Finally, it is apparent that the severe thermal shocks such as furnace heating and water quenching are not only convenient but necessary in laboratory thermal shock studies in order to cause fracture in the typically small specimens used in such invesitgations.

The consideration of thermal and mechanical properties and geometry is primarily of interest in the design and selection of refractory components. Once selection has been made for a particular application, the major concern involves the impact of thermal operating practice on the thermal shock fracture behavior of the refractory components. In the two-dimensional thermoelastic model operating practice is simulated by a constant heating or cooling rate.

The nature of damage is a significant consideration with regard to the rate of refractory wear of industrial linings. Bricks with cracks oriented perpendicular to the hot face are relatively stable in comparison to those with cracks running parallel to the hot face from the standpoint that, in the latter case, separation can result in the loss of a substantial portion of the lining. In such a case the amount of loss is dependent on the distance between the crack and the hot face. The interdependence of heating rate, location and time of fracture, strain energy at fracture, and hot face temperature at fracture is illustrated in Figures 5.26 and 5.27.

From Figure 5.26 the effect of increasing heating rate on the example case is to cause fracture to occur at an earlier time. The total strain energy at fracture is relatively constant in the range $\phi_f < 15$ °C/min where the σ_y component dominates. However, in the range $\phi_f > 15$°C/min U_f tends to zero with increasing ϕ_f. This trend indicates a correspondence between the infinite heating rate case and the case of an instantaneous change in surface temperature which was discussed in the previous chapter.

The influence of heating rate on location of fracture stress is shown by the dashed line in Figure 5.27. The inverse relationship suggests that unsuccessful attempts to avoid fracture by heating at a slower rate can theoretically result in a greater loss of brickwork as, in addition to delaying fracture and obtaining a higher hot face temperature, the effect of a lower heating rate is to cause the location

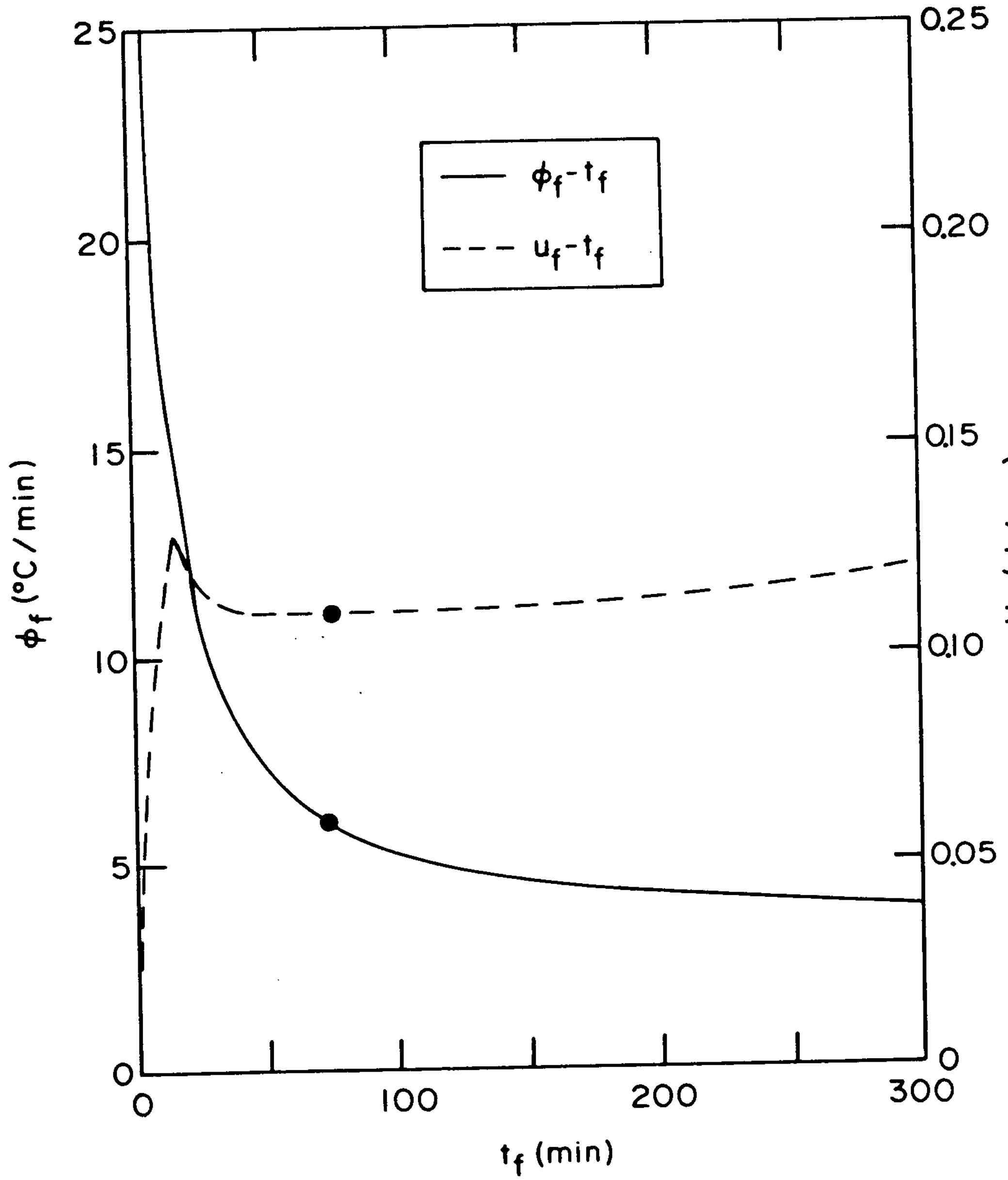

Figure 5.26 Heating rate and total strain energy at fracture versus time of fracture. Based on the example case of Table XXII.

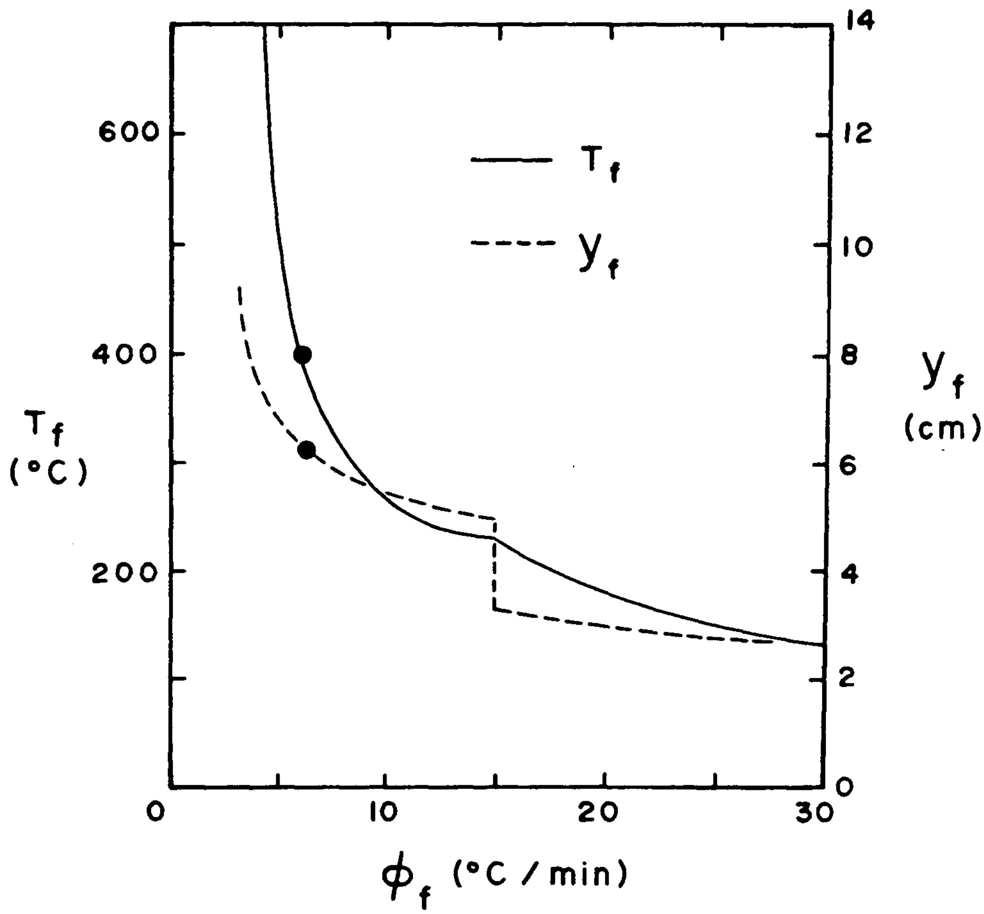

Figure 5.27 Temperature of the hot face at fracture and location at fracture versus time of fracture. Based on the example case of Table XXII.

of the fracture stress to move away from the hot face. An additional point regarding the location of the maximum principal tensile stress is that it reflects the extent of penetration of the stress and strain energy fields (see Appendix I). Thus, while the total strain energy appears to be relatively independent of heating rate over a wide range, the concentration of strain energy throughout the shape can vary significantly with ϕ.

Industrial processes, thermal shock tests, and labatory experiments all possess a characteristic range of temperature through which a component or specimen is heated or cooled. While the objective from the outset in much thermal shock experimental work is to cause fracture, the objective in industrial operations is generally to avoid fracture. It is clear from Figure 5.27 that if the example shape is to be used in an application for which $T_f \approx 400°C$, then the optimum heating rate is slightly less than 6°C/min.

If heated at a greater rate fracture will occur, and if at a lesser rate then longer heating times are required with consequence of higher heat losses and reduced furnace or vessel availability. The remainder of this work is concerned with the development of resistance to fracture initiation and damage parameters useful for the design and selection of refractory components which can be related to thermal operating practice.

5.6 Resistance to Fracture Initiation.

5.6.1 Safe Heating and Cooling Rate.

A theoretical parameter which reflects the industrial objective is safe rate ϕ_s which is defined as the maximum rate at which the hot face of a rectangular shape can be heated or cooled through a specified temperature range T_s to produce a maximum principal tensile stress just below the fracture strength. The ϕ_s dependence can be expressed in function notation as

$$\phi_s = f(\, T_s,\ \alpha,\ a,\ \sigma_f,\ E,\ \nu,\ w,\ \ell). \tag{5.34}$$

The dimensionless form of 5.34 is

$$\gamma_s^* = f(\, \varepsilon_s^*,\ \sigma_f^*,\ r^*) \tag{5.35}$$

where γ_s^* is the safe dimensionless thermal load corresponding to ϕ_s and the dimensionless temperature constraint ε_s^* is defined by

$$\varepsilon_s^* = \alpha\ T_s\ . \tag{5.36}$$

Each point on the locus of fracture initiation corresponds to a unique hot face temperature. The problem is to determine the particular combination of dimensionless thermal load and Fourier modulus on the curve that produces the specified fracture strength at the instant the hot face reaches the required temperature. The temperature constraint equation, expressed in dimensionless form as

$$\gamma^* = (\theta^*)^{-1}(\varepsilon_s^*), \tag{5.37}$$

gives all the combinations of γ^* and θ^* yielding a specified ε_s^* which, for known α, corresponds to a particular T_s. The safe dimensionless thermal load γ_s^* is located at the intersection of the locus of fracture initiation curve and temperature constraint curve.

Figure 5.28 illustrates the graphical technique for the determination of γ_s^* for the example case of Table XXII and $T_s = 1000°C$. The temperature constraint curve is easily plotted in the $\gamma^*-\theta^*$ space by noting that, in log-log form, the curve of equation (5.37) is a straight line of slope minus one which passes through the point (θ^*,γ^*) given by $(1.0,\varepsilon_s^*)$. Once γ_s^* is known the safe heating rate is found by substituting the appropriate value into the expression for γ^* (equation 5.13).

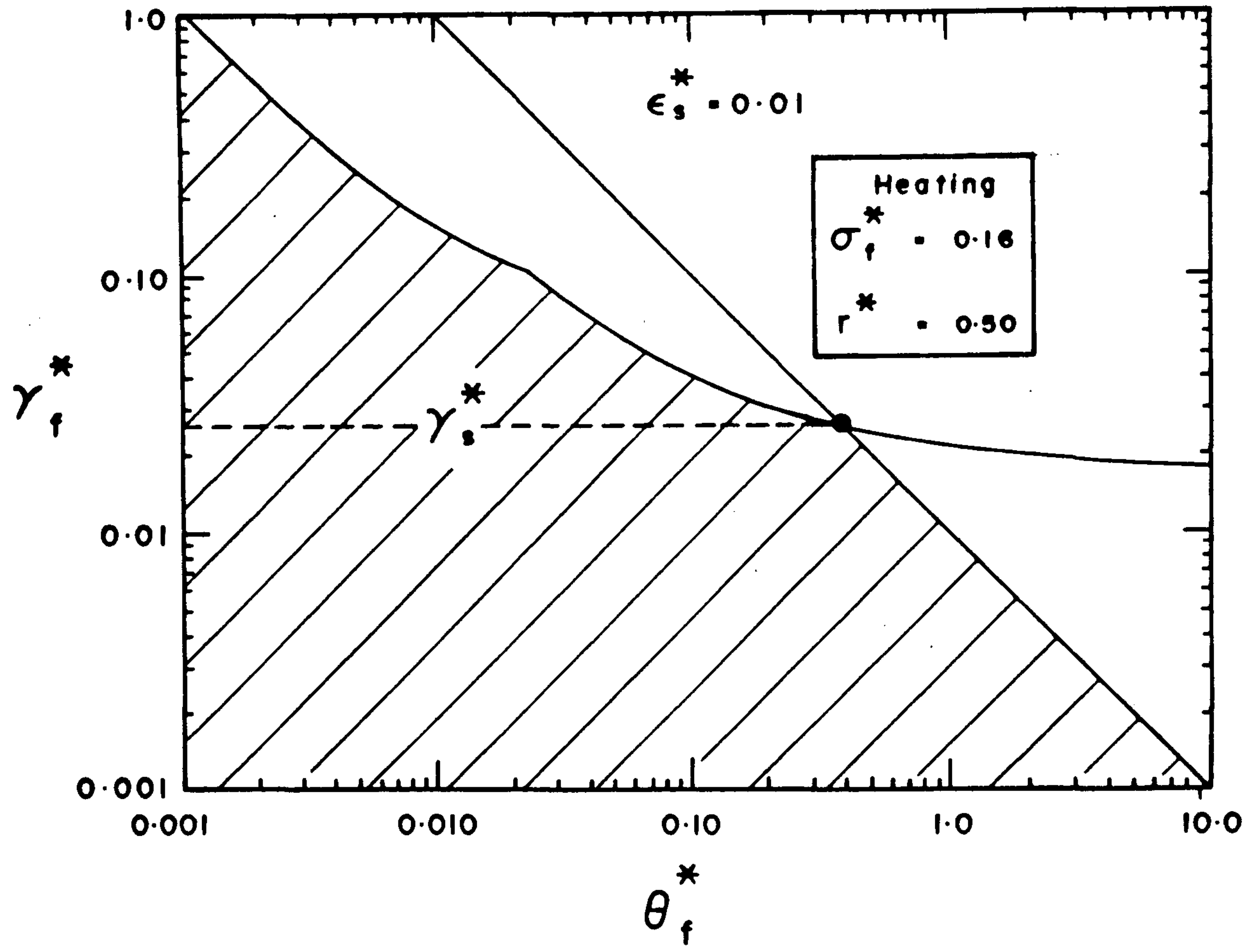

Figure 5.28 Locus of fracture initiation and temperature constraint curve (σ_f^*=0.16, r^*=0.50, heating)

The dimensionless graphical approach permits a geometric interpretation of the industrial problem. The upper portion of the locus of fracture initiation and the lower portion of the temperature constraint curve, which are joined at γ_s^*, form a boundary which delineates the safe operating operating zone (cross-hatched region under the curve). Along the boundary two outcomes are possible. For $\gamma^* > \gamma_s^*$, the fracture strength is attained before the desired hot face temperature is reached. For $\gamma^* < \gamma_s^*$, the component is safely heated to the required hot face temperature, the smaller the γ^* the longer the heating period. At all points within the safe operating zone the maximum principal tensile stress and the hot face temperature are less than the boundary values of σ_f and T_s.

5.6.2 Experimental Support.

While the constant heating or cooling rate problem has been considered for theoretical analyses on numerous occasions, only two investigations could be found in the literature which presented quantitative experimental results pertaining to this particular thermal boundary condition. Both studies involved commercial silica bricks.

Howie[95] conducted constant heating rate experiments on four types of silica brick. A series of specimens (4.5x3x3 in) of each brand were heated on the 3x3 in face up to a hot face temperature of 350°C at different rates using the apparatus in Figure 5.29. After cooling the location of fracture was noted (Figure 5.30) and subsequently correlated with heating rate. A comprehensive set of the Howie results are reproduced in Appendix 10.

The results of the Howie study shown in Figure 5.31 (dry specimens) and Figure 5.32 (wet specimens) are in general agreement with the theoretically predicted relationship in Figure 5.27. In both cases the location of fracture is observed to vary inversely with heating rate. The maximum safe rate of heating for normal dry hard-fired bricks was found to be 5-6°C/min; that of a softer-fired dry specimen about 8°C/min; and that of wet specimens about 3.5°C/min.

Clements[12] discussed the influence of geometry on the safe heating rate of commercial silica brick. He stated that test pieces in the form of rectangular prisms measuring 4.5x3x3 in. heated through a 3x3 in. end, can be heated without cracking at more than twice the rate that will crack a 6x4.5x3 in. piece of the same material heated through the 6x3 in. face. The maximum safe rate of heating for a 9x4.5x3 in. shape, heated through the 9x3 in face, is 1/4 to 1/5 that of the small

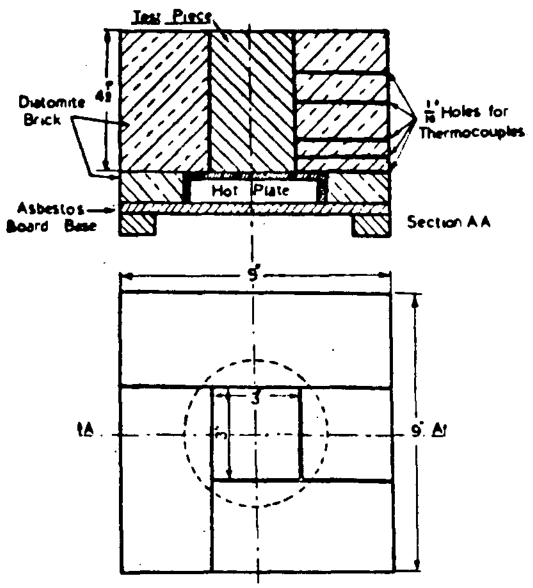

Figure 5.29 Diagrammatic sketch of apparatus for hot face spall tests (after reference 95)

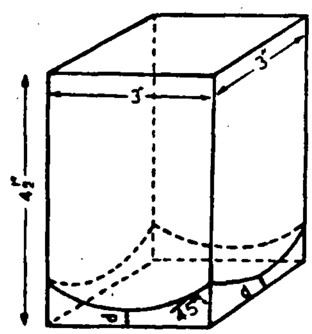

Figure 5.30 Diagram of spalled specimen showing distances measured (after reference 95)

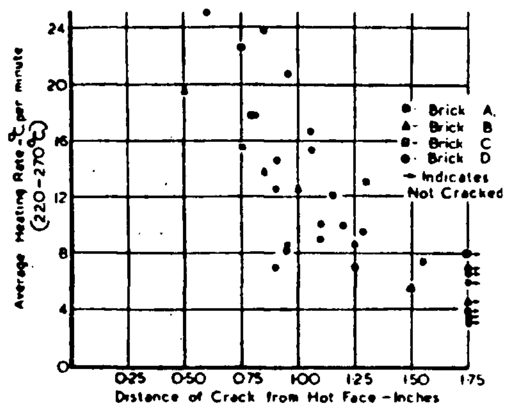

Figure 5.31 Relationship between heating rate and distance of crack from hot face - dry specimens (after reference 95)

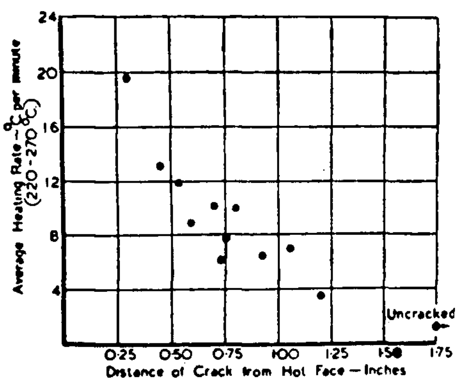

Figure 5.32 Relationship between heating rate and distance of crack from hot face - wet specimens (after reference 95)

prism. He reported the safe heating rates of the pieces having the 6x3 and 3x3-in. faces as 4°C/min and 10°C/min.,respectively.

Furthermore, he stated that the 4.5x3x3-in. pieces invariably crack parallel to the heated face, whereas both the larger sizes invariably crack normal to this face. Such fracture patterns are in line with thermoelastic predictions based on the use of a maximum principal tensile stress fracture criterion. However, it was also noted that peculiar fracture patterns were occasionally observed for shapes with aspect ratio of one (see Figure 4.38). The tabulated values of the maximum principal tensile stress (Table XVIII) suggest that the nature of the flaw distribution is likely to play a more dominant role in the fracture behaviour of such shapes as the difference in the magnitude of the σ_x and σ_y components is not so pronounced as it is for the extreme geometries.

In order to compute the safe heating rates for these cases it is necessary to estimate some of the material properties as Howie and Clements give little information about the specimens tested. Howie does give thermal expansion curves for the commercial bricks, from which a value of $\alpha \approx 30\times10^{-6}\,{}^{\circ}C^{-1}$ can be estimated and used in conjunction with an estimate of T_s of 300-350°C to obtain a dimensionless temperature constraint of $\varepsilon_s^* \approx 0.01$. An estimate of thermal diffusivity of silica brick of $a \approx 0.007$ cm^2/s is obtained using values of thermal conductivity, bulk density, and specific heat given in reference [21].

Literature values are also used to approximate dimensionless fracture strength σ_f^*. In a separate paper, Clements[96] gives values for critical strain ε_{cr}, defined as the modulus of rupture divided by the elastic modulus, for six brands of commercial bricks, the average being $\varepsilon_{cr} = 0.88\pm0.02$ millistrains. In the same paper it is noted that the critical strain data can be converted to a tensile form by using the result of Astbury[97] (see Figure 5.33) which shows the measured tensile strength to be approximately one-half that of the flexural strength. Substitution of one-half of ε_{cr} and a value of Poisson's ratio[98] of 0.14 into equation (5.3) gives $\sigma_f^* \approx 0.38$.

Table XXIII contains the safe heating rates of various sizes of commercial silica brick reported by Howie and Clements and the values computed using the procedure outlined in the previous sections. More important than the good agreement between the theoretically-predicted and experimentally-observed values is the fact that the thermoelastic model accounts for the general effect of size. While selection of other material properties would alter the magnitude of the safe heating rates, the relative values for the various geometries would not be significantly affected.

Table-XXIII

Safe Heating Rates For Various Sizes of Silica Brick

Size (in)	r^*	γ_s^*	Howie[95] (°C/min)	Clements[12] (°C/min)	Computed (°C/min)
3x4.5x3	0.67	0.058	5 - 8	10	9.4
6x4.5x3	1.33	0.020	-	4	3.2
9x4.5x3	2.0	0.014	-	2 - 2.5	2.3

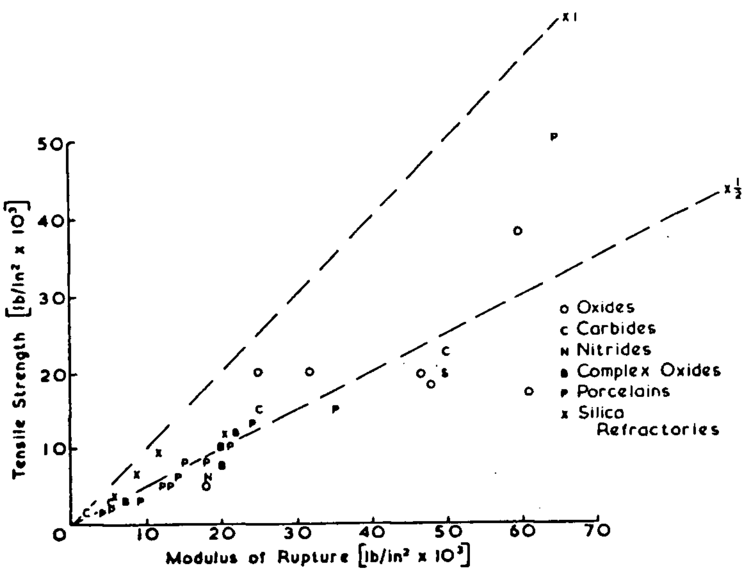

Figure 5.33 Tensile strength versus modulus of rupture of ceramics (after reference 97)

To summarize, a solution for the maximum principal tensile stress of the two-dimensional constant heating rate problem has been used to develop a resistance to fracture initiation parameter which accounts for the influence of material properties, geometry, and temperature range, and distinguishes between the heating and cooling cases. The parameter is determined using a graphical technique to solve a system of two simultaneous dimensionless equations consisting of the locus of fracture initiation and the temperature constraint curve. Theoretical predictions are in good agreement with safe heating rates reported for various sizes of commercial silica brick.

5.6.3 Design and Selection.

In this section the influence of the individual variables on the design and selection of refractory components is considered. The approach taken is to focus on the example heating case of Table XXII for a safe temperature range of 1000°C, and using it as a reference point (indicated by the large dot in Figures 5.34 - 5.36) consider each variable in turn. The data in Table XXII was chosen to represent an average material and does not correspond to any particular type of refractory. The following analysis is essentially an expansion of the solution to the multi-dimensional problem about a single point.

Geometry exerts a strong influence on resistance to fracture

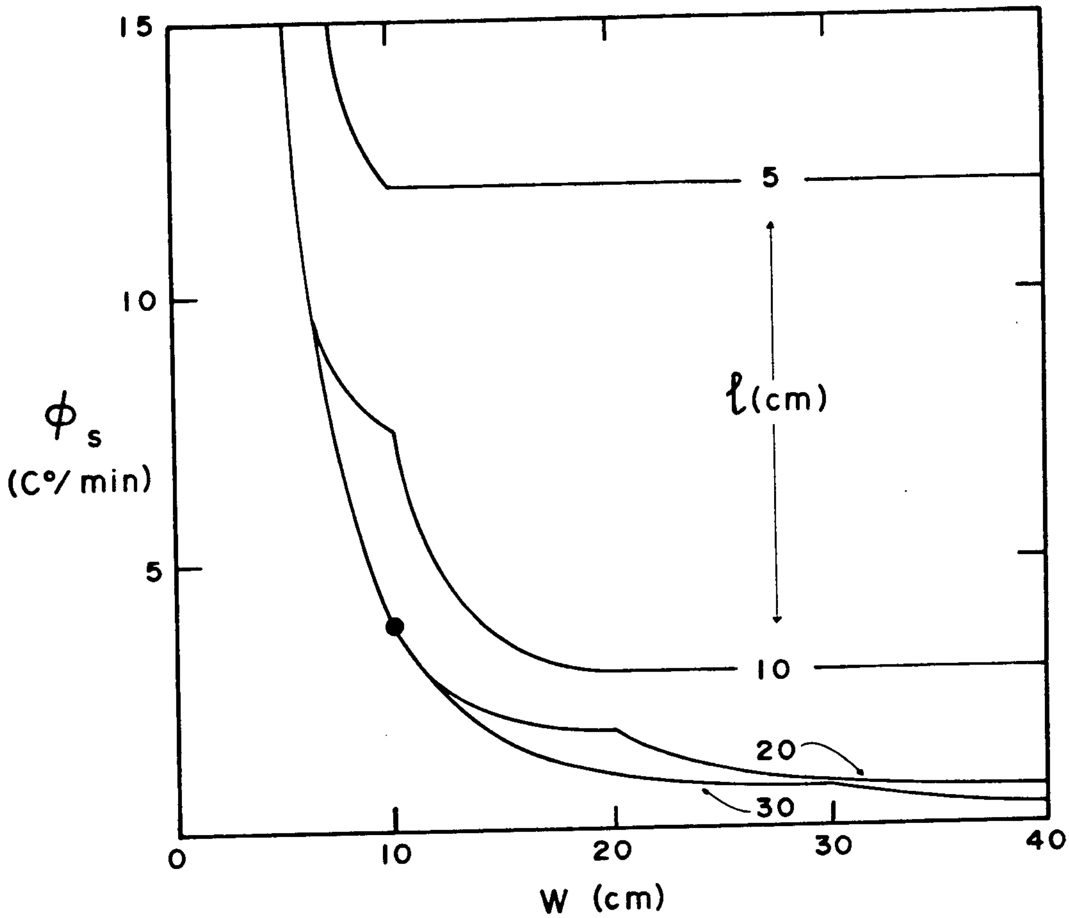

Figure 5.34 Safe heating rate versus width for various lengths. Based on the data of Table XXII and T_s=1000 °C.

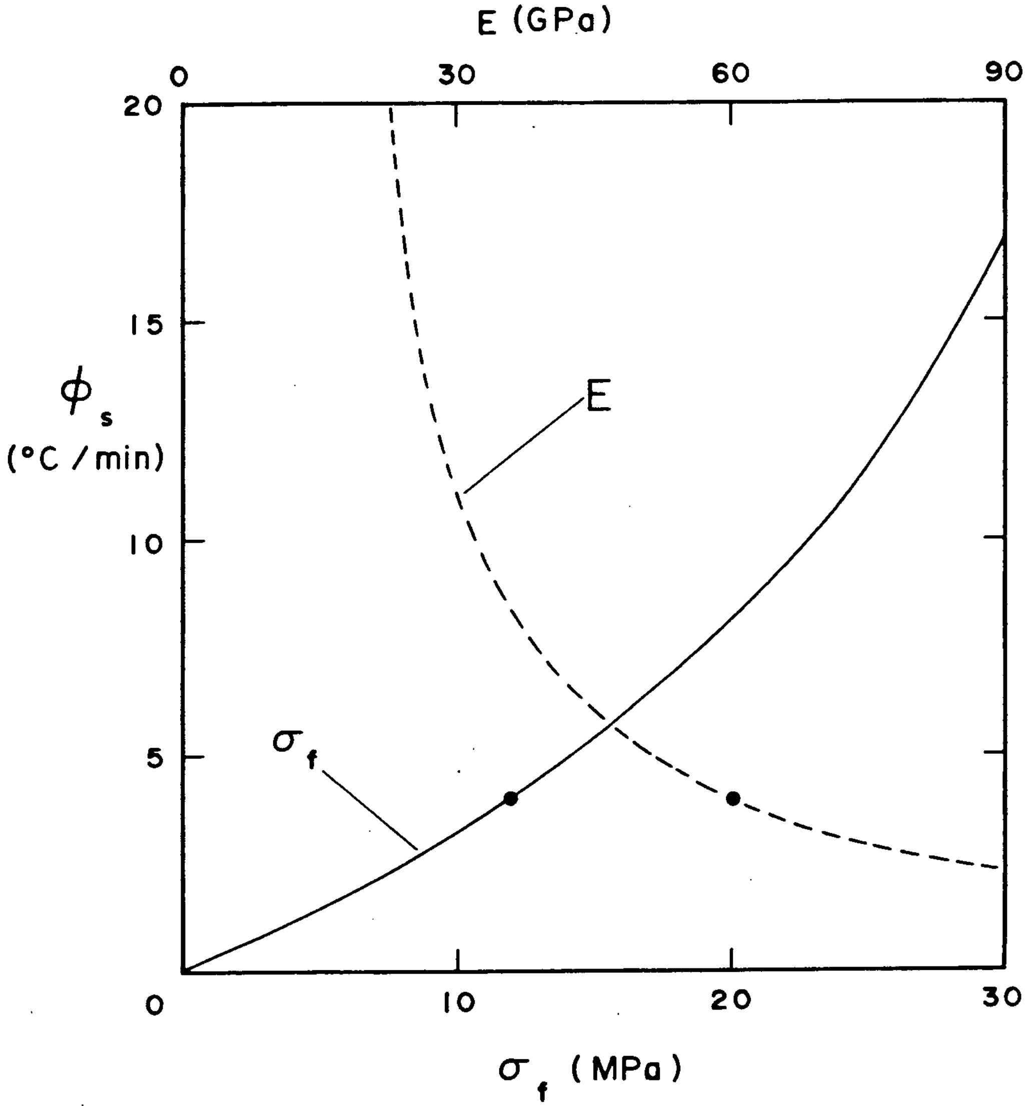

Figure 5.35 Safe heating rate versus fracture strength and elastic modulus. Based on the data of Table XXII and T_s=1000 °.

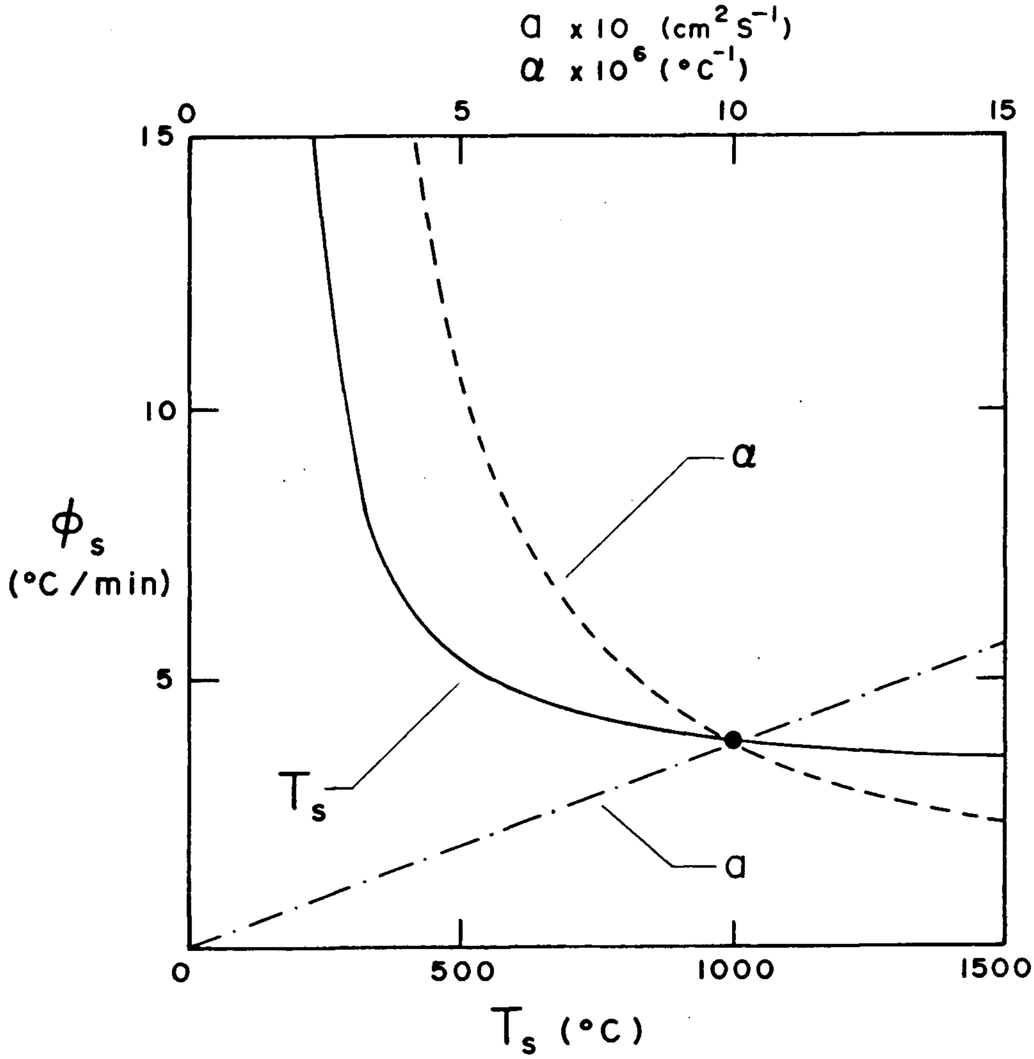

Figure 5.36 Safe heating rate versus temperature range, thermal diffusivity, and coefficient of thermal expansion. Based on data of Table XXII and T_s=1000°C.

initiation. Figure 5.34 shows the variation of ϕ_s with width for several values of length. The discontinuity in curvature in the ℓ=10, 20, and 30 cm curves indicates a transition in component at fracture. The σ_x component dominates along the portion of the curve to the right of the discontinuity and the σ_y to the left. The horizontal portions of the ℓ=5 and ℓ=10 cm curves correspond to the infinite slab case (width greater than twice length) for which the magnitude of the peak stress is independent of width.

With regard to optimum geometry, the curves indicate that maximum resistance to fracture initiation is associated with BOF-type geometries in which the width is much less than the length. In comparison, a semi-universal ladle brick shape (~ 18 x 18 cm) with the same material properties would possess poor thermal shock resistance. A brick of standard dimensions (~ 10 x 20 cm) has an intermediate value of safe heating rate.

It is also noteworthy that the geometry of a component continuously changes throughout the life of the lining due to corrosion-erosion and thermal stress fracture. Thus resistance to fracture initiation is a time-dependent property of lining components. The curves in Figure 5.34 suggest that the decrease in length that naturally occurs with service tends to increase thermal shock resistance. For example, with regard to the reference case, a decrease in ℓ from 20 to

5 cm is accompanied by a three-fold increase in safe heating rate.

The mechanical properties of refractory products are primarily determined at the production level by such factors as composition, particle size distribution, and nature of the raw material and thermal schedule during firing. Due to the nature of the product, significant scatter in fracture strengths is generally observed even when testing bricks from the same kiln batch. However, with regard to fracture initiation, it is important to note that it is not the absolute magnitude of the fracture strength or elastic modulus that is significant, but the ratio of these two properties (neglecting the effect of Poisson's ratio).

Figure 5.35 shows the effect of changes in σ_f and E on ϕ_s while holding all other variables fixed. The curves indicate that optimum resistance to fracture initiation is obtained with combinations of high σ_f and low E. In practice it is extremely difficult to alter these properties independently as both are sensitive to changes in texture. High fracture strength is invariably associated with high elastic modulus.

While geometry and mechanical properties can be influenced significantly at the production level, the thermal diffusivity and coefficient of thermal expansion are essentially fixed by composition.

Porosity has some effect on thermal properties but the range of porosity to be found in commercial products is not that substantial. The ϕ_s variations in Figure 5.36 indicate that desirable combinations of these two variables are low α and high a. These variables are more of a factor in the selection of commercial products. The $\phi_s - T_s$ relationship is in line with the observation of Ainsworth[10] who noted that the safe heating rate varies inversely with temperature.

In the selection of refractory structural components many factors must be weighed before choosing from a variety of commercial products of different material properties and geometry. In the following hypothetical case the objective is to select the most suitable structural component given the operating constraint of T_s = 1000°C. The criterion for selection is resistance to fracture initiation.

The properties of the four materials under consideration are given in Table XXIV. Materials A and D represent extreme cases of strength to elastic modulus ratio, with the beneficial aspect of high σ_f^* of A being offset by a high thermal expansion coefficient and relatively low thermal diffusivity and the negative features of D being compensated for by a high thermal diffusivity. Materials B and C are of intermediate σ_f^*, with B being characterized by the positive and negative

Table XXIV

Resistance to Fracture Initiation of Materials A, B, C, and D

Size: 10 x 20 cm

Material	$\sigma_f^* \times 10^3$	$\alpha \times 10^6$ ($°C^{-1}$)	a (cm^2s^{-1})	R" ($cm^2s^{-1}°C$)	ϕ_s (°C/min)
A	0.48	20	0.0067	0.16	4.7
B	0.24	5	0.0033	0.16	7.8
C	0.16	10	0.01	0.16	3.9
D	0.08	15	0.03	0.16	3.1

attributes of extremely low coefficient of thermal expansion and thermal diffusivity, respectively. Material C, the sample case of Table XXII, is representative of a material possessing average properties.

Table XXII also contains values of the Kingery parameter R" and ϕ_s, the latter for the 10x20 cm geometry and heating conditions of the example case. According to the Kingery parameter all of the materials possess equivalent resistance to fracture initiation, whereas the safe rate parameter indicates a substantial range in thermal shock resistance, with ϕ_s of material B more than double that of material D. That the safe rate parameter distinguishes between materials of identical R" indicates that the positive attributes of high σ_f^* and low α are more beneficial than that of high thermal diffusivity, a variable which varies directly with ϕ_s.

The results in the rows of Table XXV indicate the strong influence of geometry. For example, doubling the width of a 5 x 20 cm piece of material B, the most thermal shock resistant material, decreases the safe heating rate by a factor of four to a value significantly less than that of a 5 x 20 cm piece of material D, the least thermal shock resistant material. In general, larger sizes require lower heating rates. However, it is noteworthy that increasing the length in going from the 10 x 20 to 10 x 40 size to give a BOF-type

Table-XXV

Safe Heating Rates (°C/min) for Various Sizes of A, B, C, and D

Material	Dimensions (w×ℓ cm)				
	5x20	10x20	20x20	10x40	20x40
A	18	4.7	2.1	4.6	1.2
B	31	7.8	2.7	7.8	2.0
C	16	3.9	1.9	3.9	0.98
D	12	3.1	1.6	3.2	0.77

geometry has no effect on the safe heating rate.

The remaining consideration is heating versus cooling. The safe cooling rates in Table XXVI indicate that the ranking of the materials in terms of resistance to fracture initiation is similar (B-A-C-D), but that the magnitude of safe cooling rate is only one-quarter to one-half that of the safe heating rate. Thus the potential for fracture is much greater on cooling.

On the basis of resistance to fracture initiation, material B is clearly the best choice and the 5 x 20 cm shape is the best geometry. However, other constraints enter into the refractory selection problem. Joints between adjacent bricks are particularly susceptible to slag penetration and, consequently, enhanced wear due to corrosion-erosion. Also, if thermal expansion is not accounted for during heat-up, thermal stress fracture can occur at the hot face corners where neighbouring bricks impinge on each other. Another factor that can limit the size of ladle bricks is overhead crane capacity.

To summarize, the safe heating or cooling rate ϕ_s is a theoretical resistance to fracture initiation parameter which is applicable to the industrial lining problem. This parameter can be used to quantitatively assess the influence of thermal and mechanical

Table XXVI

Safe Cooling Rates (°C/min) for Various Sizes of A, B, C, and D

Material	Dimensions (wxℓ cm)				
	5x20	10x20	20x20	10x40	20x40
A	6.5	1.7	0.55	1.6	0.41
B	8.1	2.0	0.57	2.0	0.50
C	6.2	1.5	0.53	1.5	0.39
D	5.3	1.4	0.50	1.3	0.34

properties, geometry, heating, cooling, and temperature and thereby facilitate the design and selection of refractory structural components.

5.7 Resistance to Thermal Shock Damage

5.7.1 Resistance to Damage Parameter

The resistance to damage parameter R_d for the constant heat transfer coefficient case of Chapter 4 can be made applicable to the constant heating rate problem with a slight modification of the definition of available strain energy at fracture U_a. In the constant h problem only infinite slab geometries were considered. For such a problem the fracture stress is always a σ_x component which tends to propagate cracks along the center line (see Figure 5.12)

In the case of the two-dimensional problem the fracture stress can also be a σ_y component which tends to propagate cracks parallel to the hot face (see Figure 5.12). Furthermore, it is apparent from the contour maps in Appendix I that the development of the stress and strain energy density fields is time-dependent. Both the magnitude and extent of penetration of the fields into the shape are related to the transient behaviour of the thermal field. The portion of the shape under stress tends to increase with time and the extent of penetration in the direction of heat flow can be approximated as twice y_M, where y_M is the distance between the hot face and the peak value of principal tensile stress.

Thus, for the two-dimensional problem the available strain energy at fracture is defined as

$$U_a = \frac{U_T}{2\zeta} \tag{5.38}$$

where the parameter ζ is the appropriate dimension in the direction perpendicular to the expected line of crack propagation. If the fracture stress is a σ_x component, then $\zeta = w$. If the fracture stress is the σ_y component, then $\zeta = 2 \cdot y_M^y$, where y_M^y can be estimated using Figures 5.20 and 5.21. As with the infinite slab constant h case, the parameter U_a is meant to reflect the total strain energy associated with the tensile region of a 1 x 1 cm column spanning a specimen along the line of expected crack propagation.

5.7.2 Experimental Support

The most comprehensive study of thermal shock damage of refractory components subjected to the constant heating rate boundary

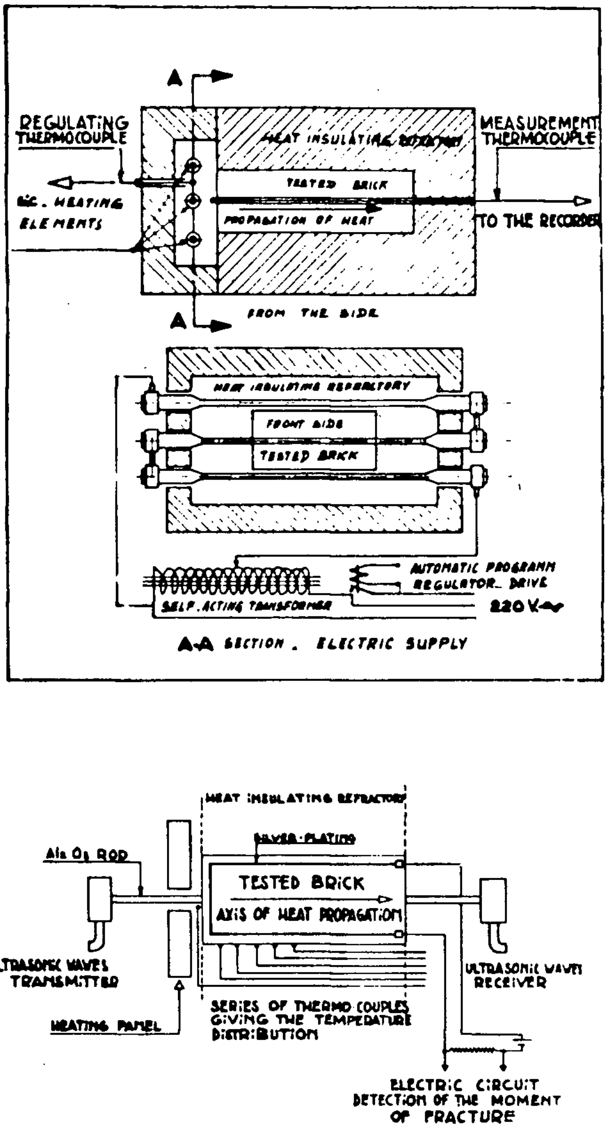

Figure 5.37 Test furnace and diagram of the lay-out of the apparatus (after reference 99)

condition was done by Kiehl and Valentin[99] who tested some sixty types of refractories using the test furnace and arrangement shown in Figure 5.37. The provision for detection of the moment of fracture is an important feature not provided in most experimental studies.

The test procedure consisted of heating standard bricks (230 x 115 x 65 mm) on the 115 x 65 mm face at a constant rate to a maximum of 1000°C. The extent of damage was determined as the ratio of after-shock modulus of rupture to before-shock modulus of rupture. General observations can be summarized as follows.

(i) In all cases a critical rate of heating was observed for which "total fracture" (total separation or separation > 90%) occurred. The critical rate ranged from 2-3°C/min to 100°C/min.

(ii) Fracture always occurred in a zone 6 to 8 cm behind the hot face with the crack essentially parallel to the hot face. As the heated face was always less than 1000 °C at the instant of fracture, it was concluded that this type of thermal shock is a low-temperature phenomenon.

(iii) A rapid decrease in modulus of rupture was often observed for specimens heated at rates well below the critical value. Sometimes internal cracks extending over bigger or smaller parts of the cross-section were found, though the bricks appeared all right from the outside.

As indicated in Figure 5.38, three types of behaviour were observed when the ratio P/P_o was plotted against heating rate. Groups A and B covered materials with known poor thermal shock resistance such as dense magnesia types and acid resisting refractories. Group C contained the vast majority of the aluminosilicate refractories and mullite and corundum types.

Figure 5.39 shows the results of the thermoelastic analysis of the thermal shock behaviour of standard-sized bricks of materials A, E, and F of the Nakayama study subjected to the Kiehl and Valentin constant heating rate test. The curves in Figure 5.39 begin at the safe heating rate of each material for T_s = 1000°C. As no data was given for the materials corresponding to the curves in Figure 5.38, it can only be stated that the trends of damage resistance parameter versus heating rate for the three Nakayama materials - high alumina, magnesia, and chamotte - indicate characteristic behaviour and appear to correlate reasonably well with the type of strength loss versus heating rate curves in Figure 5.38. The general observations of Kiehl and Valentin are all in line with the thermoelastic eleastic interpretation of fracture behaviour.

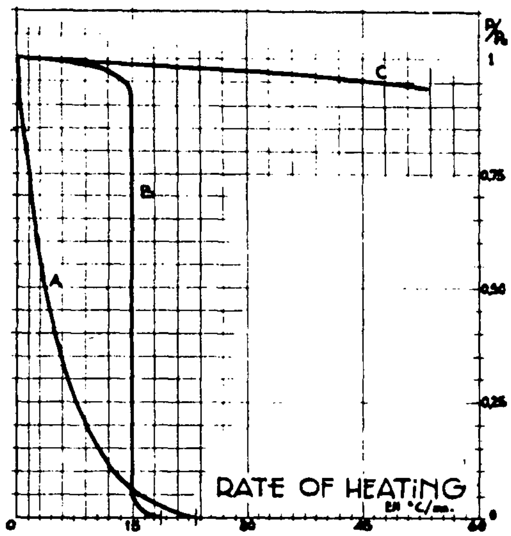

Figure 5.38 Rate of rise in temperature plotted against P/P_0. (after reference 99)

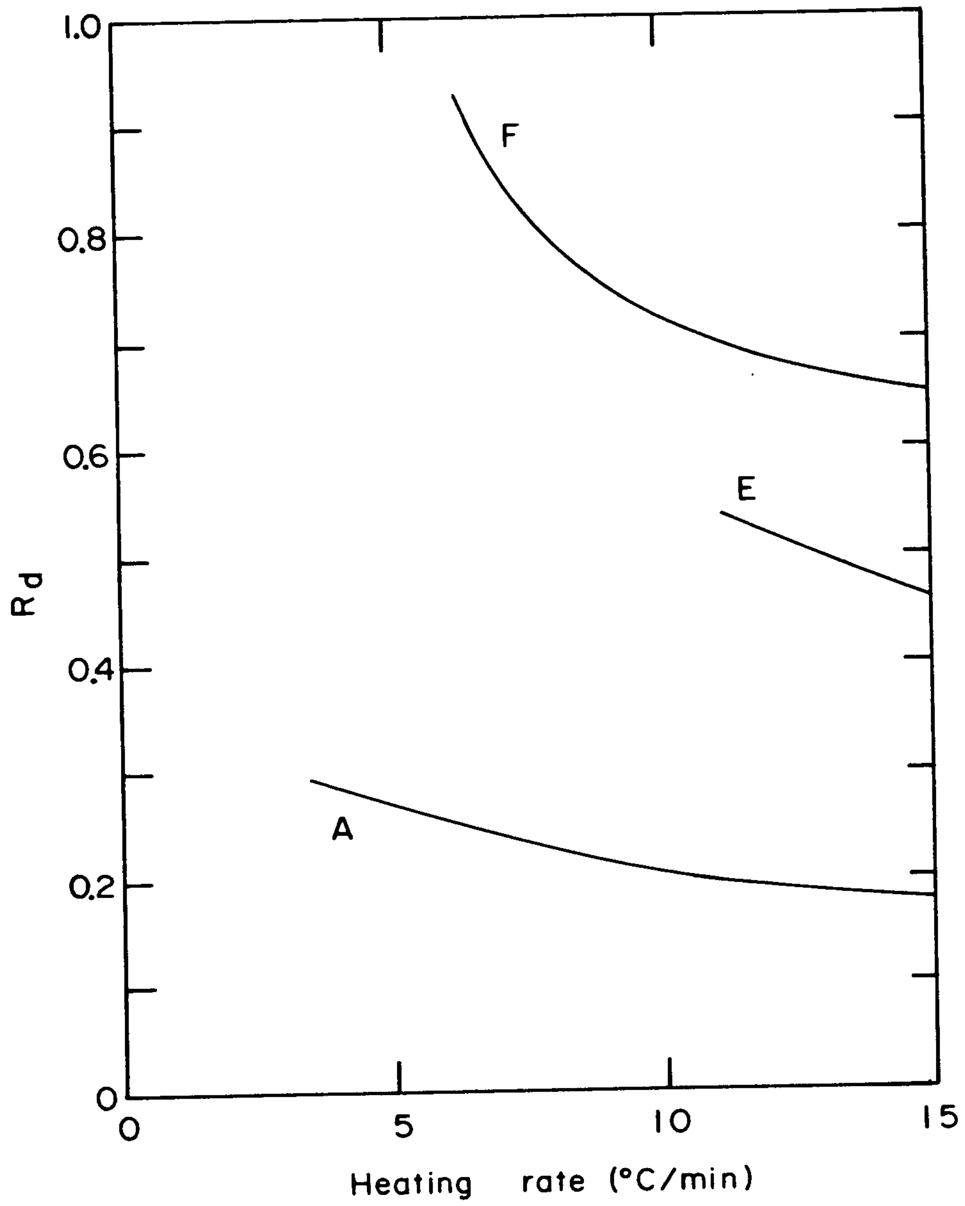

Figure 5.39 Thermoelastic damage resistance parameter versus heating rate for materials A, E, and F of Nakayama study.

5.7.3 Design and Selection

As the ultimate goal is to avoid fracture in lining components, design and selection should be based on the safe heating rate parameter ϕ_s. However, the potential for damage as reflected by the parameter R_d is of interest in many applications in which it is difficult to control the thermal conditions. Furthermore, the parameter R_d is a logical secondary criteria for design and selection in those cases in which the safe heating and cooling rates are similar.

In this section R_d is computed for several of the safe heating rate cases of section 5.6.3. The R_d curves in Figures 5.40 and 5.41 correspond to the ϕ_s variations in Figures 5.35 and 5.36. The variations reflect the impact of the individual variables on strain energy as the curves were constructed using a fixed surface energy of γ=50 J/m^2.

The curve in Figure 5.40 suggests that resistance to damage is essentially independent of coefficient of thermal expansion, thermal diffusivity, and temperature range. This is somewhat surprising as these variables have a strong influence on ϕ_s. Figure 5.36 indicates that safe heating rate varies directly with thermal diffusivity and inversely with coefficient of thermal expansion and temperature range.

From equation 5.26 it is apparent that the α, a, and T_s can

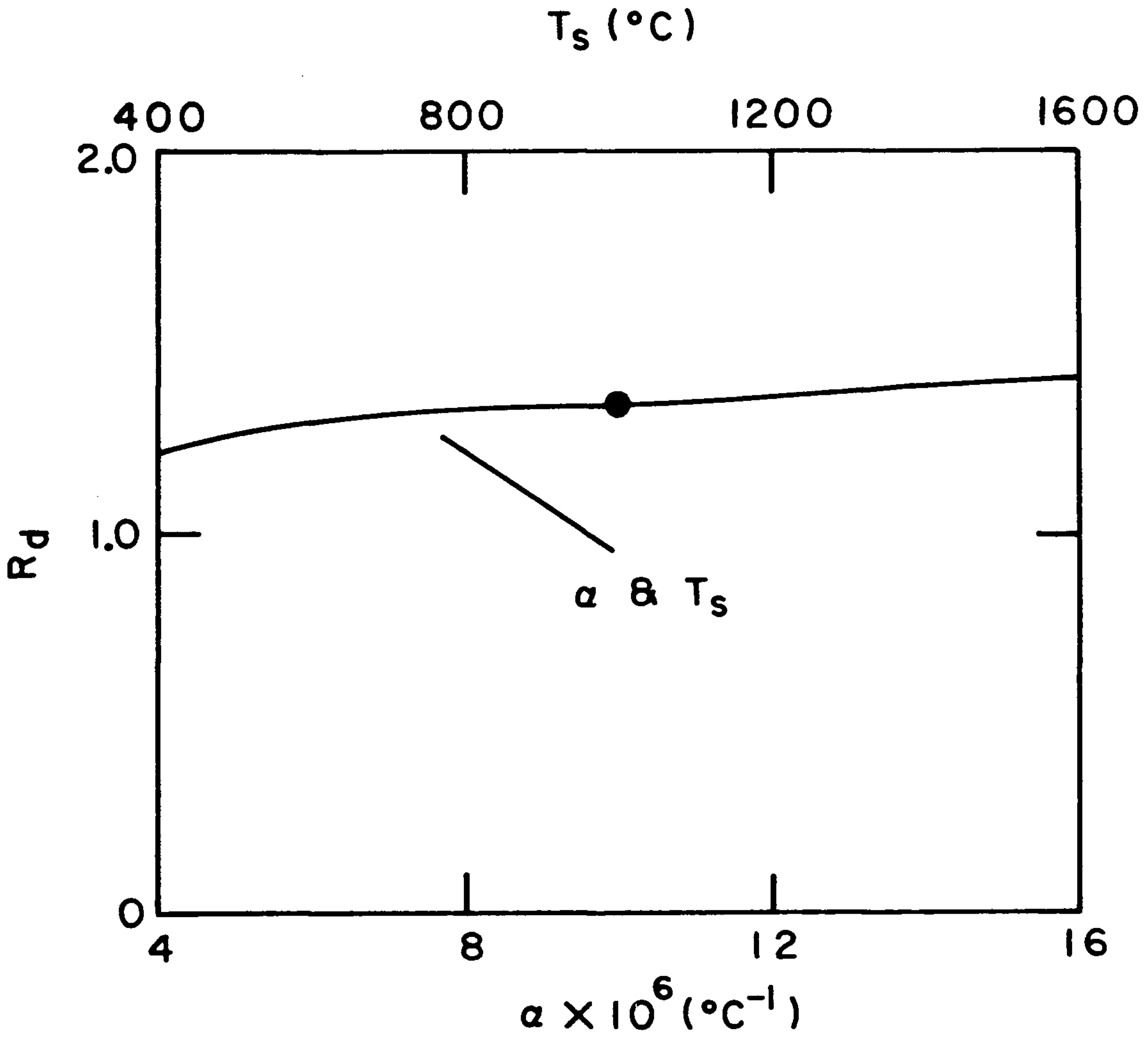

Figure 5.40 Thermoelastic damage resistance parameter versus coefficient of thermal expansion and safe temperature range.

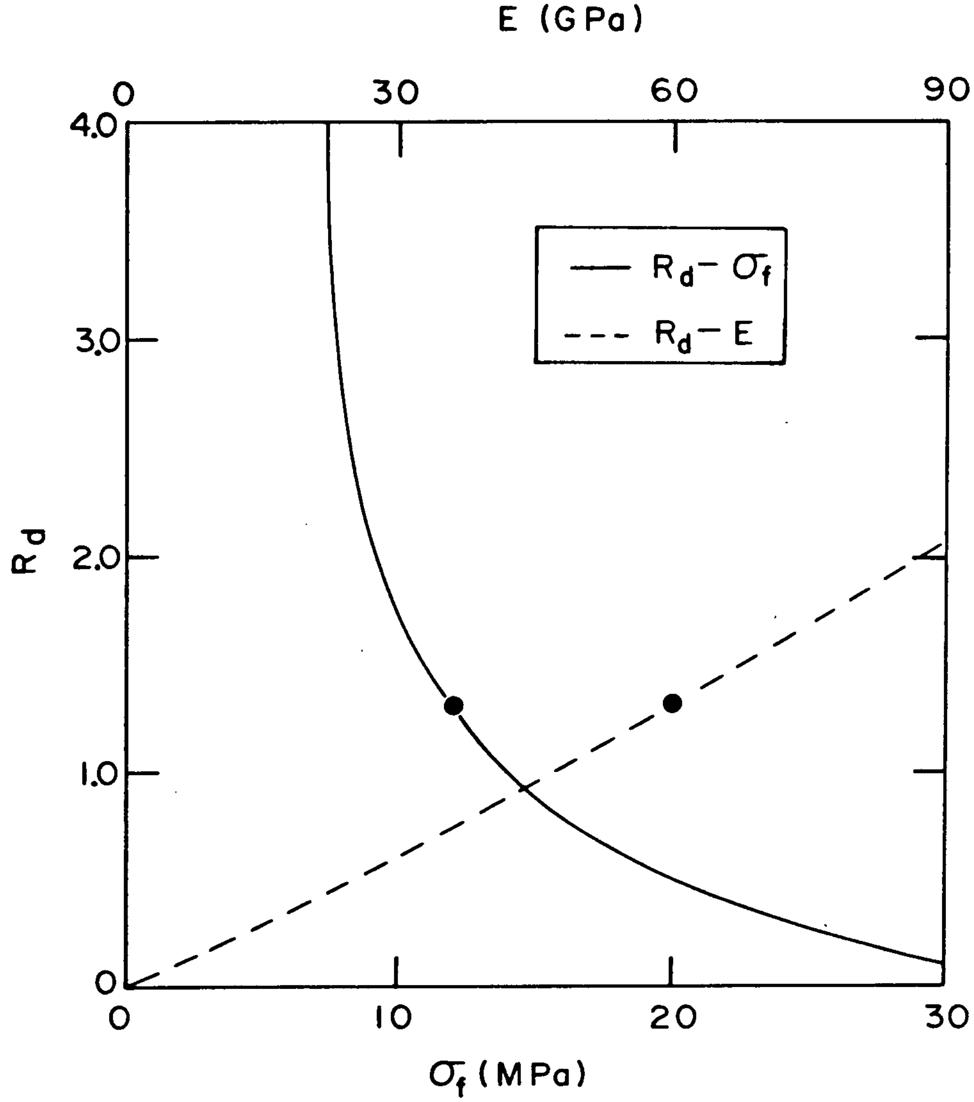

Figure 5.41 Thermoelastic damage resistance parameter versus elastic modulus and fracture strength.

influence total strain energy only by influencing U^* which, according to equation 5.23, is dependent on γ^*, θ^*, and r^*. From Figure 5.28 it is apparent that the magnitude of γ_s^* and corresponding θ^* for the example case are affected only by changes which shift the locus of fracture initiation curve or the temperature constraint curve.

A change in thermal diffusivity does not alter the location of either case. Changes in α and T_s shift the temperature constraint curve, but hardly affect the magnitude of γ_s^* as the example case is located on a relatively flat portion of the $\gamma_f^*-\theta_f^*$ curve. Thus, for the safe heating rate analysis, total strain energy at fracture is relatively independent of thermal expansion coefficient, temperature range, and thermal diffusivity.

Unlike the thermal properties, the mechanical properties exert a significant influence on resistance to damage. Changes in these variables alter σ_f^* which causes the $\gamma_f^*-\theta_f^*$ curve to shift vertically which, in turn, significantly alters γ_s^* and, consequently, U^*. With regard to the mechanical properties the curves in Figures 5.35 and 5.41 suggest that resistance to fracture initiation and resistance to damage are inversely related.

Table XXVII gives corresponding values of R_d for the various

Table XXVII

Damage Resistance of Various Sizes of A, B, C, and D

Material	Dimensions (wxℓ cm)				
	5x20	10x20	20x20	10x40	20x40
A	0.17	0.083	0.026	0.083	0.042
B	0.53	0.28	0.12	0.27	0.14
C	1.3	0.78	0.22	0.65	0.39
D	4.9	3.3	0.87	2.2	1.7

sizes of materials A, B, C, and D in Table XXV. The damage parameters were computed using fixed $\gamma = 50\ J/m^2$ and $E = 100$ GPa. A comparison of the values in the two tables suggests that, in general, both resistance to fracture initiation and resistance to damage are inversely related to width. As has been noted in previous sections the influence of length is more complex. In the case of fixed w=20 cm, increasing the length tends to decrease both resistance to initiation and to damage while, in the case of w=10 cm, increasing the length has negligible effect on either.

The relatively few cases considered in this work have been presented primarily for illustrating the scope of the fracture analysis procedure. While general trends are evident with regard to the influence of the individual variables on the thermal shock resistance parameters, it should be emphasized that both the stress and strain energy solutions for the two-dimensional model are highly nonlinear. Consequently, the trends noted for the example case may or may not reflect those of all other cases. However, the tabulated values and fracture analysis procedure can be used to obtain results for any case quickly without the requirement of computer evaluation.

Chapter 6

Summary

6.1 Conclusions

(1) This work is novel in that a two-dimensional constant heating rate thermoelastic model has been used to develop both resistance to fracture initiation and resistance to damage parameters which account for the influence of thermal and mechanical properties, geometry, and temperature range, while distinguishing between the heating and cooling cases.

(2) A fundamental requirement for the derivation of the thermal shock resistance parameters was the development of an invertible general solution for the maximum principal tensile stress (σ_M) as well as a general solution for total strain energy (U) in terms of time (t), heating rate (ϕ), thermal expansion coefficient (α), thermal diffusivity (a), elastic modulus (E), Poisson's ratio (ν), width (w), and length (ℓ).

(3) Contrary to the statement of Chang et al, the problem is amenable to dimensional analysis which has been applied to reduce the number of variables from nine to four. It has been demonstrated that for the constant heating rate problem dimensionless maximum principal tensile stress (σ_M^*) and dimensionless total strain energy (U^*) are functions of Fourier modulus (θ^*), aspect ratio (r^*), and dimensionless thermal load (γ^*).

(4) Characteristic properties of the constant heating rate problem, not previously reported, are that σ_M^* is directly proportional to γ^* and total strain energy U^* is directly proportional to the square of γ^* for conditions of fixed θ^* and r^*.

(5) Tables of σ_M^* and U^* for a wide range of Fourier modulus and aspect ratio and fixed $\gamma^*=0.01$ have been generated using a finite element numerical method. These tables, in conjunction with the relationships noted above, can be used to determine dimensionless maximum principal tensile stress and total strain energy for arbitrary conditions.

(6) A simple procedure has been described for inverting the stress solution to obtain loci of fracture initiation ($\gamma_f^*-\theta_f^*$) curves which give all the combinations of γ^* and θ^* that produce a specified dimensionless fracture strength for a shape of given aspect ratio.

(7) An important factor in the industrial problem not accounted for in previous theoretical derivations of thermal shock resistance parameters is the temperature range of heating or cooling. This aspect of the problem is handled by introducing a dimensionless temperature constraint equation which gives all the combinations of γ^* and θ^* producing a specified value of dimensionless temperature range ε_s^*. This parameter is defined as the product of thermal expansion coefficient and temperature range T_s.

(8) With the dimensionless approach the influence of the individual variables on fracture initiation behaviour of the two-dimensional model can be interpreted geometrically in terms of shifts in the $\gamma_f^*-\theta_f^*$ and temperature constraint curves. The safe dimensionless thermal load γ_s^*, located at the intersection of the two curves, together with the specified σ_f^* and r^* define a set of combinations of variables which satisfy both the fracture criterion and the temperature range constraint.

(9) A new resistance to fracture initiation parameter ϕ_s has been developed which is defined as the maximum rate at which a given rectangular shape can be heated or cooled through a specified temperature range T_s without attaining the fracture strength σ_f.

The parameter is computed using the appropriate γ_s^* value.

(10) A new resistance to damage parameter R_d has been developed which is defined as the ratio of surface energy per unit area γ to available strain energy at fracture U_a.

(11) It has been conclusively shown that the thermoelastic approach can be fruitfully applied to the analysis of thermal stress fracture behaviour of refractory materials without explicit consideration of the flaw distribution.

(12) Good agreement between thermoelastic predictions and published experimental results with regard to strength retained versus thermal shock relationships, location of fracture, and safe heating rates indicates that the maximum principal tensile stress fracture criterion is valid and that the premise that extent of crack propagation is related to available strain energy at fracture is reasonable for the cases considered.

6.2 Recommendations for Future Work

No previous experimental investigation has provided all of the information required for the computation of the thermal stress field at the instant of fracture in a given experiment. The minimum requirements for a thermoelastic analysis are knowledge of thermal and mechanical properties, size, temperature profile at fracture, and location of crack.

Thus a natural starting point for future work is the development of an experimental arrangement to provide the above information. Acoustic emission analysis is recommended for the determination of time of fracture. With a complete set of results for a given experiment, the study of other aspects of the thermal shock problem such as the prediction of crack patterns is possible.

References

1. F.H. Norton, "A General Theory of Spalling", J. Am. Ceram. Soc., 8 [1] 29-39, (1925).

2. F.H. Norton, "The Mechanism of Spalling", J. Am. Ceram. Soc., 9, 446-461, (1926).

3. F.H. Norton, "Refractories", 4th Ed., McGraw-Hill, 244-267, (1968).

4. F.W. Preston, "The Spalling of Brick", J. Am. Ceram. Soc., 9 [10] 654-658, (1926).

5. F.W. Preston, "Theory of Spalling", J. Am. Ceram. Soc., 16 [3] 131-133, (1933).

6. A. Winkelmann and O. Schott, "Uber thermische Widerstands-coefficienten verscheidener in ihrer Abhangegkeit von der chemischen Zusammensetzung", Ann. Physik. Chem., 51, 730, (1894).

7. W.D. Kingery, "Factors Affecting Thermal Stress Resistance of Ceramic Materials", J. Am. Ceram. Soc., 38 [1] 3-15, (1955).

8. V.S. Kienow, "Crack Formation in Fired Converter Brick", Ber. Dt. Keram. Ges., 47, 426-430, (1970).

9. R.L. Schultz, B. Brezny, and D. Hambrick, "The Effect of Gunning on the Thermal Shock Resistance of Steel Plant Ladles", Steelmaking Proceedings, Vol. 61, Chicago, 115-125, (1978).

10. J.H. Ainsworth, "Calculation of Safe Heat-Up Rates for Steel Plant Furnace Linings", Am. Ceram. Soc. Bull., 58 [7] 676-678, (1979).

11. B. Brezny, "Crack Formation in BOF Refractories During Gunning", Am. Ceram. Soc. Bull., 58 [7] 679-682, (1979).

12. J.F. Clements, "Thermal Shock in Furnace Structures", The A.T. Green Book, British Ceramic Research Association, Stoke-on-Trent, 18-29, (1959).

13. I.F. Guilliat and H.W. Chandler, "Stress Analysis in Carbon Cathode Beams During Electrolysis", Light Metals, Vol. 1, 437-451, (1977).

14. H.W. Chandler, "Thermal Stress in Ceramics", Trans. J. Brit. Ceram. Soc., Vol. 80, 191-195, (1981).

15. M. Kumagai, R. Uchimura, and H. Kishida, "Evaluation of Thermal Shock Resistance of Refractories by Using Acoustic Emission Technique", Kawasaki Steel Technical Report, No.1, Sept., 79-88, (1980).

16. J. Sweeney and M. Cross, "Analyzing the Stress Response of Commercial Refractory Structures in Service at High Temperatures I. A Simple Model of Viscoelastic Stress Response", Trans. J. Br. Ceram. Soc., 81, 21-24, (1982).

17. J. Sweeney and M. Cross, "Analyzing the Stress Response of Commerical Refractory Structures in Service at High Temperature II. A Thermal Stress Model for Refractory Structures", Trans. J. Br. Ceram. Soc., 81, 47-52, (1982).

18. W.S. Chang, C.E. Knight, D.P.H. Hasselman, and R.G. Mitchiner, "Analysis of Thermal Stress Failure of Thick-Walled Refractory Structures", J. Am. Ceram. Soc., 66 [10] 708-713, (1983).

19. J.F. Clements and J. Vyse, "Thermal Conductivity of Some Refractory Materials", Trans. Brit. Ceram. Soc., Vol. 56, 296-308, (1957).

20. E. Ruh and J.S. McDowell, "Thermal Conductivity of Refractory Brick", J. Am. Ceram. Soc., 45 [4] 189-195, (1962).

21. Modern Refractory Practice, 4th Ed., Harbison-Walker Refractories, Pennsylvania, (1961).

22. D. Woodhouse and G.C. Padgett, "Fundamental Aspects of the Mechanical Properties of Refractory Brick", IX International Ceramic Congress, Brussels, 315-327, (1964).

23. J.J. Uchno, "Grain Size Effects on the Thermal Shock Resistance Parameters of Magnesite Brick", Master of Science Thesis, Pennsylvania State University, December, (1973).

24. D.J. Landini, "Fracture of Dolomite Refractories", Master of Science Thesis, Pennsylvania State University, March, (1980).

25. C.A. Schumacher, "Fracture of Alumina Refractories", Master of Science Thesis, Pennsylvania State University, August, (1980).

26. G.R. Rigby, "The Strength of Basic Brick at Temperatures between 20°C and 1400°C with Special Reference to Direct Bonded Brick", Xth International Ceramic Congress, Stockholm, 317-327, (1966).

27. G.R. Rigby, "Mechanical Properties of Basic Brick I. A Survey of the Magnesia-Chrome System", Trans. J. Brit. Ceram. Soc., Vol. 69, 189-198, (1970).

28. G.R. Rigby, "Mechanical Properties of Basic Brick II. The Effect of Chrome Ore Sizing", Trans. J. Brit. Ceram. Soc., Vol. 70, 97-104, (1971).

29. G.R. Rigby, "Mechanical Properties of Basic Brick III. The Role of the Silicate Phases", Trans. J. Brit. Ceram. Soc., Vol. 70, 151-162, (1971).

30. J.A. Kuszyk, "Fracture and Thermal Shock Resistance Parameters of Direct-Bonded Magnesite-Chrome Refractories", Master of Science Thesis, Pennsylvania State University, August, (1974).

31. G.C. Padgett, J.A. Cox and J.F. Clements, "Stress/Strain Behaviour of Refractory Materials at High Temperatures", Trans. Brit. Ceram. Soc., Vol. 68, 63-73, (1969).

32. E.I. Greaves, "Stress Properties of High Alumina and Basic Refractories and Their Use in Arc Furnace Roofs", Refractories Journal, No. 3, 13-22, (1978).

33. G.C. Padgett and D.J. Brettany, "The Relaxation Behaviour of Refractories", Trans. Brit. Ceram. Soc., Vol. 73, 153-165, (1974).

34. J.A. Coath, B. Wilshire and D.R.F. Spencer, "A Comparison of the High Temperature Creep and Fracture Behaviour of Magnesia and Doloma", Trans. Brit. Ceram. Soc., Vol. 75, No. 5, 104-107, (1976).

35. A.J. Harbach and W.F. Ford, "Dimensional Changes Induced in Basic Refractories by Temperature and Atmosphere Cycling", Trans. Brit. Ceram. Soc., Vol. 63, 143-161, (1964).

36. R.C. Rossi, "Thermal Expansion of BeO-SiC Composites", J. Am. Ceram. Soc., 52 [5] 290-291, (1969).

37. R.J. Leonard and R.H. Herron, "Volume Expansion and Structural Damage in Periclase-Chrome Refractories", Ceramic Bulletin, 51, [12] 891-895, (1972).

38. B.K. Ganguly, K.R. McKinney and D.P.H. Hasselman, "Thermal Stress Analysis of Flat Plate with Temperature-Dependent Thermal Conductivity", J. Am. Ceram. Soc., 58 [9-10] 455-456, (1975).

39. D.P.H. Hasselman and G.E. Youngblood, "Enhanced Thermal Stress Resistance of Structural Ceramics with Thermal Conductivity Gradient", J. Am. Ceram. Soc., 61 [1-2] 49-52, (1978).

40. K. Satyamurthy, J.P. Singh, M.P. Kamat and D.P.H. Hasselman, "Effect of Spatially Varying Porosity on the Magnitude of Thermal Stress During Steady-State Heat Flow", J. Am. Ceram. Soc., 62 [7-8] 431-433, (1979).

41. P. Stanley and F.S. Chau, "The Effect of Temperature-Dependence of Properties on Thermal Stresses in Cylinders", Thermal Stresses in Severe Environments, Ed. by D.P.H. Hasselman and R.H. Heller, Plenum Press, New York, 61-80, (1980).

42. K. Satyamurthy, M.P. Kamat, J.P. Singh and D.P.H. Hasselman, "Effect of Spatially Varying Thermal Conductivity on Magnitude of Thermal Stress in Brittle Ceramics Subjected to Convective Heating", J. Am. Ceram. Soc., 63 [7-8] 363-367, (1980).

43. T. Ozyener, K. Satyamurthy, C.E. Knight, G. Ziegler, J.P. Singh and D.P.H. Hasselman, "Effect of ΔT- and Spatially Varying Heat Transfer Coefficient on Thermal Stress Resistance of Brittle Ceramics Measured by the Quenching Method", J. Am. Ceram. Soc., 66 [1] 53-58, (1983).

44. K. Satyamurthy, J.P. Singh, M.P. Kamat and D.P.H. Hasselman, "Transient Thermal Stresses in Cylinders with Square Cross Section Under Conditions of Convective Heat Transfer", J. Am. Ceram. Soc., 63 [11-12] 694-698, (1980).

45. D.P.H. Hasselman, "Elastic Energy at Fracture and Surface Energy as Design Criteria for Thermal Shock", J. Am. Ceram. Soc., 46 [11] 535-540, (1963).

46. J. Nakayama, "Direct Measurement of Fracture Energies of Brittle Heterogeneous Materials", J. Am. Ceram. Soc., 48 [11] 583-587, (1965).

47. J. Nakayama and M. Ishizuka, "Experimental Evidence for Thermal Shock Damage Resistance", Ceramic Bulletin, 45 [7] 666-669, (1966).

48. F.J.P. Clarke, H.G. Tattersall and G. Tappin, "Toughness of Ceramics and their Work of Fracture", Proceedings of Brit. Ceram. Soc., No.6, June, 163-172, (1966).

49. R.W. Davidge and G. Tappin, "Thermal Shock and Fracture in Ceramics", Trans. Brit. Ceram. Soc., Vol. 66, (8), 405-422, (1967).

50. J.H. Ainsworth and R.E. Moore, "Fracture Behaviour of Thermally Shocked Aluminum Oxide", J. Am. Ceram. Soc., [52] 628-629, (1969).

51. D.P.H. Hasselman, "Unified Theory of Thermal Shock Fracture Initiation and Crack Propagation in Brittle Ceramics", J. Am. Ceram. Soc., 52 [11] 601-604, (1969).

52. D.P.H. Hasselman, "Thermal Stress Crack Stability and Propagation in Severe Thermal Environments", Ceramics in Severe Environments, Eds. W.W. Kriegel and H. Palmour III, Plenum Press, New York, 89-103, (1971).

53. J.B. Berry, "Some Kinetic Considerations of the Griffith Criterion for Fracture - I. Equations of Motion at Constant Force", J. Mech. Phys. Solids, Vol. 8, 194-206, (1960).

54. J.B. Berry, "Some Kinetic Considerations of the Griffith Criterion for Fracture - II. Equations of Motion at Constant Deformation", J. Mech. Phys. Solids, Vol. 8, 207-216, (1960).

55. J.N. Goodier, "Thermal Stress and Deformation", Journal of Applied Mechanics, September, 467-474, (1957).

56. R.A. Sack, "Extension of Griffiths Theory of Rupture to Three Dimensions", Proc. Phys. Soc. (London), 58A, 729-736, (1946).

57. J.B. Walsh, "The Effect of Cracks on the Compressibility of Rock", Journal of Geophysical Research, 70 [2] 381-389, (1965).

58. A.A. Griffith, "The Phenomena of Rupture and Flow in Solids", Philosophical Transactions of the Royal Society, 221A, 163-198, (1920).

59. D.P.H. Hasselman, "Thermal Stress Resistance Parameters for Brittle Refractory Ceramics: A Compendium", Ceramic Bulletin, 49 [12] 1033-1037, (1970).

60. D.P.H. Hasselman, "Strength Behaviour of Polycrystalline Alumina Subjected to Thermal Shock", J. Am. Ceram. Soc., 53 [9] 490-495, (1970).

61. T.K. Gupta, "Strength Degradation and Crack Propagation in Thermally Shocked Al_2O_3", J. Am. Ceram. Soc., 55 [5] 249-253, (1972).

62. J. Gebauer, D.A. Krohn and D.P.H. Hasselman, "Thermal-Stress Fracture of a Thermomechanically Strengthened Aluminosilicate Ceramic", J. Am. Ceram. Soc., 55 [4] 198-201, (1972).

63. J.A. Coppola and R.C. Bradt, "Thermal-Shock Damage in SiC", J. Am. Ceram. Soc., 56 [4] 214-218, (1973).

64. K. Anzai and H. Hashimoto, "Thermal Shock Resistance of Silicon Carbide", Journal of Material Science, Letters, 12, 2351-2353, (1977).

65. J.H. Ainsworth and R.H. Herron, "Thermal Shock Damage Resistance of Refractories", Ceramic Bulletin, 53 [7] 533-538, (1974).

66. A.L. Treusch Jr. and R.C. Bradt, 'Panel Spalling Weight Loss and R'''' of Fireclay Refractories", Ceramic Bulletin, 59 [7] 748, (1980).

67. S. Persson, "A New Method for Characterizing the Sensitivity to Thermal Shock of Refractories at High Temperature Levels", Third Nordic High Temperature Symposium, Ris Denmark, Vol. 1 37-55, (1972).

68. S. Persson, "Thermal Shock Resistance of Refractories: Correlation Between Relative Loss of Strength and the Thermal Stress Resistance Parameter R_{st}", 3rd Technologies, Rimini, May, 3-6, (1976).

69. M. Kumagai, R. Uchimura and H. Kishidaka, "Studies of Fracture Behaviour of Refractories Under Thermal Shock Conditions Using an Acoustic Emission Technique", Advances in Acoustic Emission, Dunhert, U.S.A., 233-248, (1981).

70. T. Shirawa, Y. Sakamoto, H. Yamaguchi, T. Suzuki, K. Fujisawa and T. Arabori, "Acoustic Emission Characteristics of Firebricks", ibid 213-232.

71. C.E. Semler, T.H. Hawisher and R.C. Bradt, "Thermal Shock of Alumina Refractories: Damage-Resistance Parameters and the Ribbon Test", Ceramic Bulletin, 60 [7] 724-729, (1981).

72. E. Glenny and M.G. Royston, "Transient Thermal Stress Promoted by Rapid Heating and Cooling of Brittle Circular Cylinders", Trans. Brit. Ceram. Soc., 57 [10] 645-677, (1958).

73. T.K. Gupta, "Effects of Specimen Size on the Strength Degradation of Al_2O_3 Subjected to Thermal Shock", J. Am. Ceram. Soc., 58 [3-4] 158-159, (1975).

74. P.F. Becher, D. Lewis III, K.R. Carman and A.C. Gonzalez, "Thermal Shock Resistance of Ceramics: Size and Geometry Effects in Quench Tests", Ceramic Bulletin, 59 [5] 542-548, (1980).

75. A.G. Evans, "Thermal Fracture in Ceramic Materials", Proc. Brit. Ceram. Soc., No. 25, 217-237, (1975).

76. A.G. Evans and E.A. Charles, "Structural Integrity in Severe Thermal Environments", J. Am. Ceram. Soc., 60, [1-2] 22-28, (1970).

77. W. Weibull, "A Statistical Distribution Function of Wide Applicability", J. Applied Mechanics, September, 293-297, (1951).

78. D.G.S. Davies, "The Statistical Approach to Engineering Design in Ceramics", Proc. Brit. Ceram. Soc., No. 22, June, 429-452, (1973).

79. P. Stanley, H. Fessler and A.D. Swill, "An Engineer's Approach to the Prediction of Failure Probability of Brittle Components", ibid, 453-487.

80. N. Williams, J. Easley, S. Rolfe, "Strength of Materials", McGraw-Hill Book Co., 316, (1981).

81. M.G. Stout and J.J. Petrivic, "Multiaxial Loading Fracture of Al_2O_3 Tubes: I. Experiments", J. Am. Ceram. Soc., 67, [1] 14-18, (1984).

82. C.E. Semler and T.H. Hawisher, "Evaluation of the Thermal Shock Resistance of Refractories Using the Ribbon Test Method", Ceramic Bulletin, 59, [7] 732-738, (1980).

83. C.E. Semler, "Modified Prism Spalling Test Evaluates Thermal Shock Resistance", Refractories Journal, 1, 12-17, (1981).

84. J.H. Chesters, "Refractories Production and Properties", The Iron and Steel Institute, London, 511, (1973).

85. J.F. Clements, "The Role of Temperature Cycling in Thermal Shock Testing", Refractories Journal, July, 4-9, (1972).

86. J. Nakayama, "Thermal Shock Resistance of Ceramic Materials", Fracture Mechanics of Ceramics, Vol. II, Microstructure, Materials, and Applications. Ed. R.C. Bradt, D.P.H. Hasselman, F.F. Lange, Plenum Press, New York, 759-777, (1974).

87. W.F. Brown and J.E. Srawley, ASTM Special Technical Publication No. 410, 13-14, (1966).

88. D.R. Larson and D.P.H. Hasselman, "Comparative Spalling Behaviour of High-Alumina Refractories subjected to Sudden Heating and Cooling", Trans. Brit. Ceram. Soc., 74 (2), 59-64, (1975).

89. D.R. Larson, J.A. Coppola, D.P.H. Hasselman and R.C. Bradt, "Fracture Toughness and Spalling Behaviour of High-Al_2O_3 Refractories", J. Am. Ceram. Soc., 57 (10), 417-421, (1974).

90. H.S. Carslaw and J.C. Jaeger, 'Conduction of Heat in Solids', Oxford University Press, London, 122, (1959).

91. F. Kreith, 'Principles of Heat Transfer', Dun-Donnelley Publisher, New York, 497, (1976).

92. ibid, p 523.

93. B.A. Boley and J.H. Weiner, 'Theory of Thermal Stresses', John Wiley and Sons, New York, (1960), p. 284.

94. H.S. Carslaw and J.C. Jaeger, 'Conduction of Heat in Solids', Oxford University Press, London, 104, (1959).

95. T.W. Howie, "Spalling of Silica Brick", Trans. of the Brit. Ceram. Soc., 45 (2), 45-69, (1946).

96. J.F. Clements, "Fracture Strains of Technical Refractories", Proc. Brit. Ceram. Soc., No. 6, June, 137-147, (1966).

97. N.F. Astbury, "Advances in Materials Research in the NATO Countries", Pergamon Press, London, 369, (1963).

98. W.R. Davis, "Measurement of the Elastic Constants of Ceramics by Resonant Frequency Methods", Trans. of the Brit. Ceram. Soc., 67, 515-541, (1968).

99. J.P. Kiehl and G. Valentin, "Dependence of the Mechanical Properties of Dense Porous Refractories on Thermal Cycling, Science of Ceramics, 4, 3-23, (1968).

Appendix I

Background Information for Thermoelastic Analysis

Appendix 1

Background

1. Thermoelastic Analysis

The pertinent equations for the various one- and two-dimensional cases considered are summarized in this section[1]. The two-dimensional thermoelastic problem consists of the determination of displacements (u,v), strains (ε_x, ε_y, γ_{xy}), and stresses (σ_x, σ_y, τ_{xy}) in solid bodies under prescribed temperature distributions. Unless otherwise stated, one-dimensional temperature profiles of the form

$$T = T(y) \tag{I-1}$$

are considered with geometry, direction of heat flow, and the stress convention indicated in Figure I-1.

For the case of no body forces, the eight unknowns satisfy the following eight equations:

$$\frac{\partial \sigma_x}{\partial x} + \frac{\partial \tau_{xy}}{\partial y} = 0 \tag{I-2}$$

$$\frac{\partial \tau_{xy}}{\partial x} + \frac{\partial \sigma_y}{\partial y} = 0 \qquad \text{(I-3)}$$

$$\varepsilon_x = \frac{1}{E} (\sigma_x - \nu \, \sigma_y) + \alpha T \qquad \text{(I-4)}$$

$$\varepsilon_y = \frac{1}{E} (\sigma_y - \nu \, \sigma_x) + \alpha T \qquad \text{(I-5)}$$

$$\gamma_{xy} = G \, \tau_{xy} \qquad \text{(I-6)}$$

$$\varepsilon_x = \frac{\partial u}{\partial x} \qquad \text{(I-7)}$$

$$\varepsilon_y = \frac{\partial v}{\partial y} \qquad \text{(I-8)}$$

$$\gamma_{xy} = (\frac{\partial u}{\partial y} + \frac{\partial v}{\partial x}) \qquad \text{(I-9)}$$

where (I-2) - (I-9) consist of two equilibrium equations, three stress-strain relations, and three strain-displacement relations. Linear stress-strain behaviour is assumed and elastic modulus E, shear modulus G and Poissons ratio ν are related by

$$G = \frac{E}{2(1+\nu)} \qquad \text{(I-10)}$$

There are two types of two-dimensional thermoelastic problems: plane strain and plane stress. A state of plane strain is defined by the set of equations

$$u = u(x,y) \tag{I-11}$$

$$v = v(x,y) \tag{I-12}$$

$$w = 0 \tag{I-13}$$

where w is the displacement in the z-direction. Plane stress is defined by the equations

$$\sigma_z = \tau_{xz} = \tau_{yz} = 0 \tag{I-14}$$

The concept of plane strain is usually applied to long prismatic bodies and that of plane stress to thin bodies.

Both the plane strain and plane stress cases satisfy equations (I-2) - (I-9) provided that for the plane strain formulation the constants E, ν and α are replaced by E_1, ν_1, and α_1 respectively, where

$$E_1 = \frac{E}{1 - \nu^2} \tag{I-15}$$

$$\nu_1 = \frac{\nu}{1 - \nu} \tag{I-16}$$

and

$$\alpha_1 = \alpha \, (1 + \nu) \tag{I-17}$$

The plane strain case has the additional out-of-plane σ_z component where

$$\sigma_z = \nu \, (\sigma_x + \sigma_y) + \alpha E T \tag{I-18}$$

and, for plane stress, the additional strain component given by

$$\varepsilon_z = \frac{\nu}{E} \, (\sigma_x + \sigma_y) + \alpha T \tag{I-19}$$

Two one-dimensional problems commonly considered are the rectangular beam and infinite slab cases. With respect to Figure I-1, the rectangular beam geometry is such that the thickness in the z-direction is negligible (plane stress condition) and the width w is much greater than length ℓ. For this problem the only non-zero stress component is the centerline σ_x component which, after the coordinate transformation

$$y' = y - h \tag{I-20}$$

where h is the half-length $\ell/2$, is given by

$$\sigma_x = \alpha E \left\{ - T + \frac{1}{2h} \int_{-h}^{+h} T dy' + \frac{3y'}{2h^3} \int_{-h}^{+h} T y' dy' \right\} \tag{I-21}$$

The geometry of the infinite slab case is such that the dimensions in the x and out-of-plane z directions extend indefinitely. The only non-zero stress components for this case are located along the center line and, with respect to the same coordinate transformation, are given by

$$\sigma_x = \sigma_z = \frac{\alpha E}{1 - \nu} \left\{ -T + \frac{1}{2h} \int_{-h}^{+h} T dy' + \frac{3y'}{2h^3} \int_{-h}^{+h} T y' dy' \right\} \tag{I-22}$$

For infinite slab geometries the strain energy density along the center line is given by

$$U_0 = \frac{1}{2} (\varepsilon_x - \alpha T) \sigma_x \tag{I-23}$$

and the strain along the center line by

$$\varepsilon_x = \alpha T_{ave} \tag{I-24}$$

where the average temperature is given by

$$T_{ave} = \frac{1}{2h} \int_{-h}^{+h} T \, dy' \tag{I-25}$$

Substituting (I-24) into (I-23) gives

$$U_0 = \frac{1}{2} \sigma_x \alpha (T_{ave} - T) \tag{I-26}$$

Total strain energy U for the two-dimensional cases considered is determined as the integral of the strain energy density U_0 over the area of the shape where

$$U_o = \frac{1}{2E} (\sigma_x{}^2 + \sigma_y{}^2 + \sigma_z{}^2) + \frac{\nu}{E} (\sigma_x \sigma_y + \sigma_y \sigma_z + \sigma_z \sigma_x) + \frac{1 + \nu}{E} (\tau_{xy}^2) \tag{I-27}$$

2. Nature of the Thermal Stress Field

The characteristic features of the two-dimensional thermal stress field in rectangular shapes for the heating case are illustrated in Figure I-2. On heating, the σ_x component is tensile in the central region, compressive in the hot (y=0) and cold (y=ℓ) face regions, and zero along the outer edges (x=±w/2). The maximum tensile and compressive values - designated $(\sigma_x^c)_M$ and (σ_x^0), respectively - are located along the center line x=0 (Figure I-2A). The shape of σ_x

distribution along other lines of x = constant is similar to that of the center line distribution. Along lines of y = constant the absolute value of the σ_x component decreases from a maximum value at the center line to zero at the outer edge in a similar manner to that of the variation in Figure I-2B.

On heating, the σ_y component is tensile in the central regions, compresive along the outside edges, and zero along the hot and cold faces. The maximum tensile value $(\sigma_y^c)_M$ is located along the center line (Figure I-2B) and the maximum compressive value $(\sigma_y^E)_M$ along the outside edge (Figure I-2C).

The shear stress τ_{xy} is zero along the center line (symmetry) and along the external edges (boundary condition). Figure I-2D gives the τ_{xy} distribution along all other lines of x=constant. On heating the maximum value $(\tau_{xy})_M$ occurs in the general region of the hot face corners.

If all parameter are held fixed the effect of cooling is simply to reverse the sign of the stresses. On heating the maximum principal tensile stress is the greater of $(\sigma_x^c)_M$ and $(\sigma_y^c)_M$ and on cooling it is the greater of σ_x^0 and $(\sigma_y^E)_M$.

The stress and strain energy density fields are strongly dependent on time and geometry. The transient behaviour of both is related to that of temperature. Figure I-3 shows the dimensionless temperature distribution for values of Fourier modulus of 0.01, 0.10, and 1.0.

The transient behaviour of thermal stress is illustrated in Figures I-4, I-5, and I-6 which show the stress contour maps of the σ_x, σ_y, and τ_{xy} components for the values of θ^*=0.01, 0.10, and 1.0 and fixed r^*=0.50 and γ^*=0.05. Both the magnitude of the field and the extent of penetration into the shape increase with increasing Fourier modulus.

The influence of geometry on the σ_x, σ_y, and τ_{xy} fields is illustrated in Figures I-7, I-8, and I-9, respectively. These plots give the stress contours for each component for aspect ratio of 0.25, 1.0, 2.0, and 4.0 for conditions of fixed θ^*=0.10 and γ^*=0.05. As in the case of transient behaviour, the magnitude of the field and extent of penetration into the shape increase with increasing aspect ratio.

Figures I-10 and I-11 illustrate the influence of time and geometry on the strain energy density field. Figure I-10 gives the contours for the Fourier moduli of Figure I-3 of 0.01, 0.10, and 1.0 and fixed $r^*=0.50$ and $\gamma^*=0.05$. Figure I-11 gives the U_0 contours for aspect ratio of 0.25, 1.0, and 2.0 and fixed conditions of $\theta^*=0.10$ and $\gamma^*=0.05$. The transient and geometric effects are similar to those noted in the case of the stress field.

References

1. B. Boley and J. Weiner, Theory of Thermal Stress, John Wiley and Sons, New York, Chapter 8, 1960.

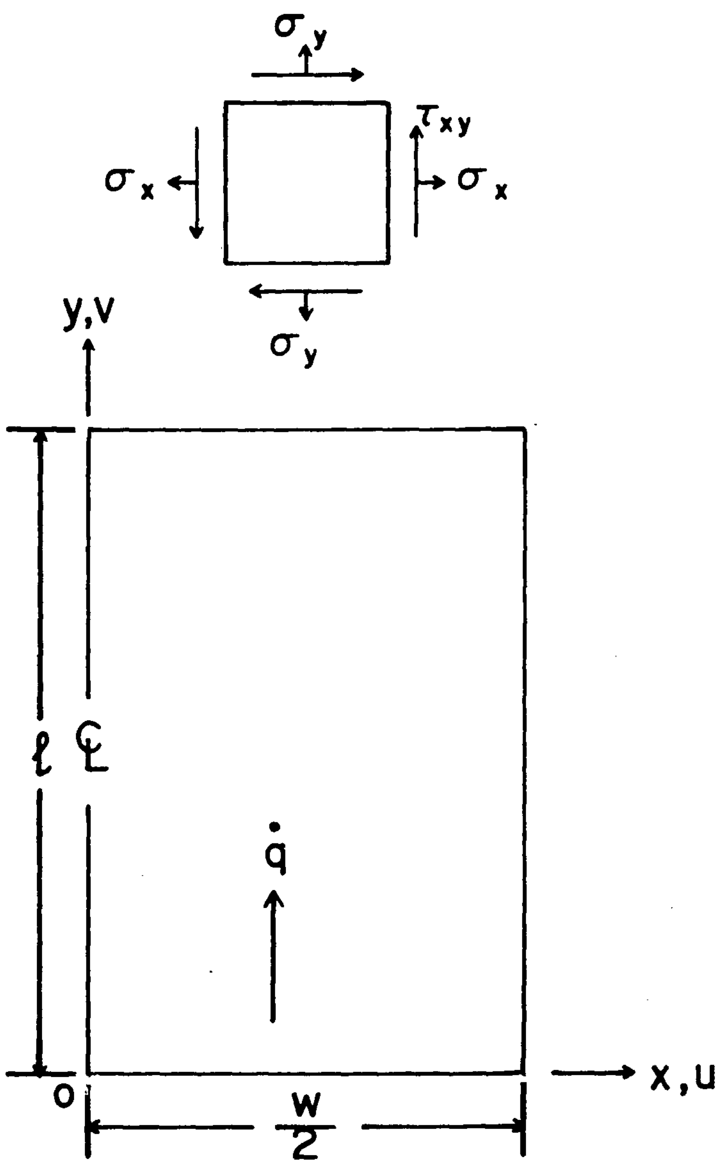

Figure I-1. Geometry, direction of heat flow, and stress convention for two-dimensional thermoelastic model.

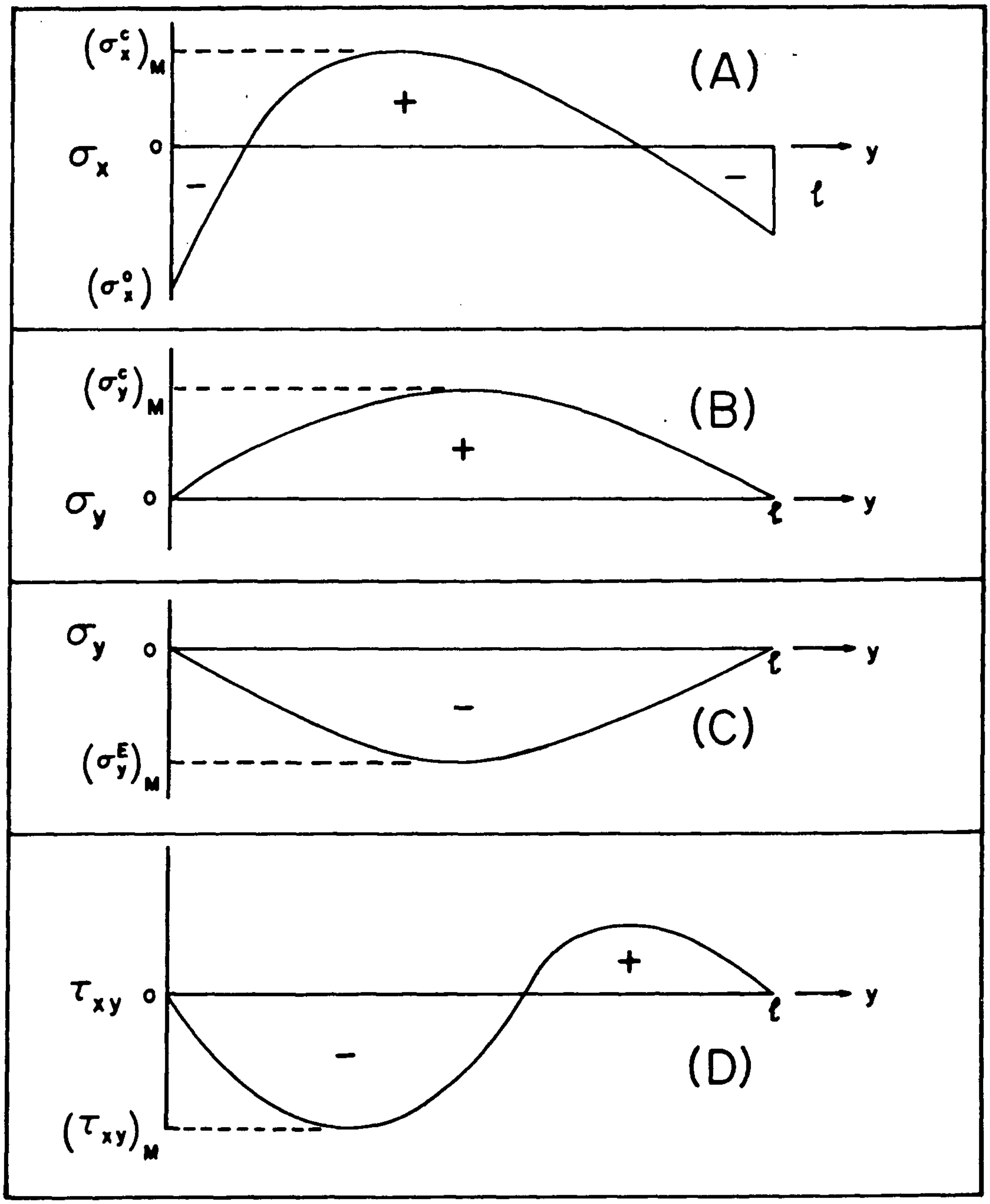

Figure I-2. Characteristic features of the two-dimensional thermal stress field.

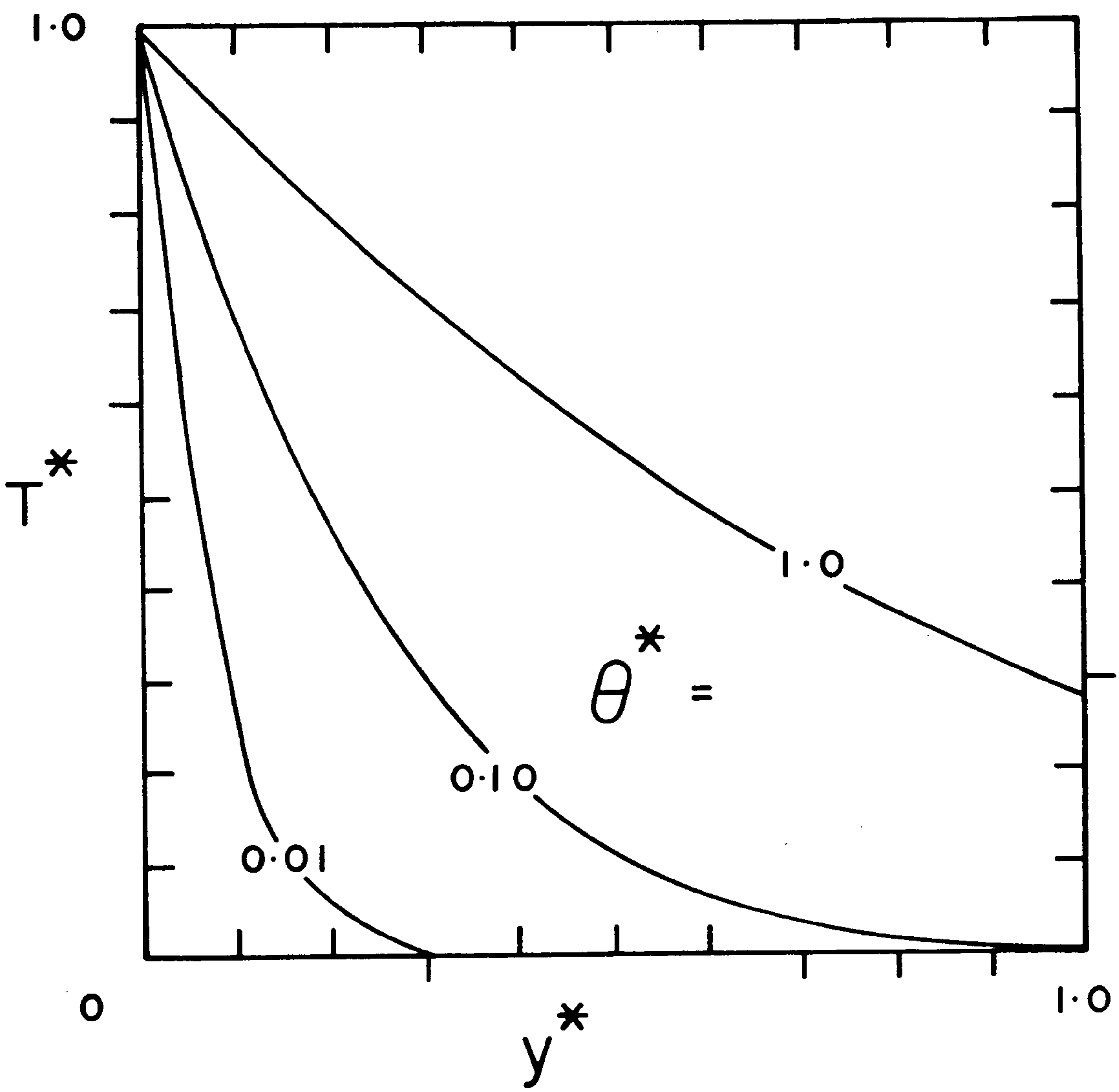

Figure I-3. Dimensionless temperature profiles for Fourier modulus of 0.01, 0.10, and 1.0.

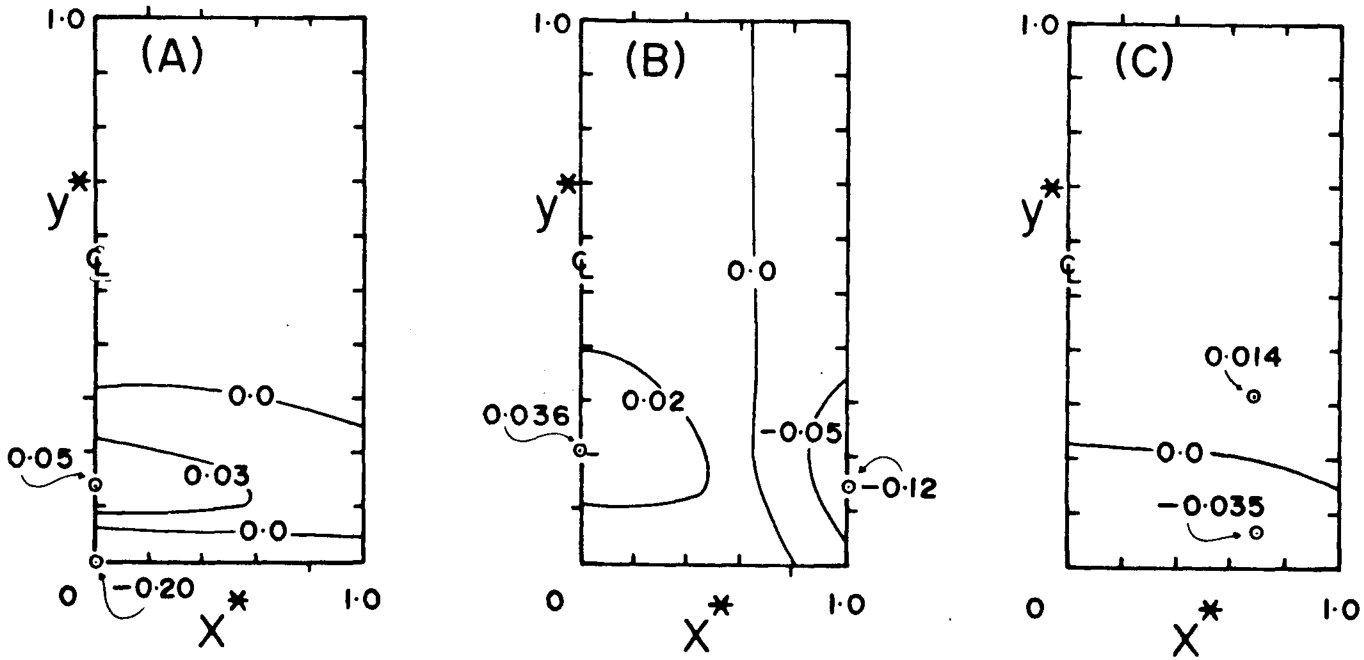

Figure I-4. Stress field for Fourier modulus of 0.01: (A) σ_x^*, (B) σ_y^*, and (C) τ_{xy}^* (r^*=0.50 and γ^*=0.05).

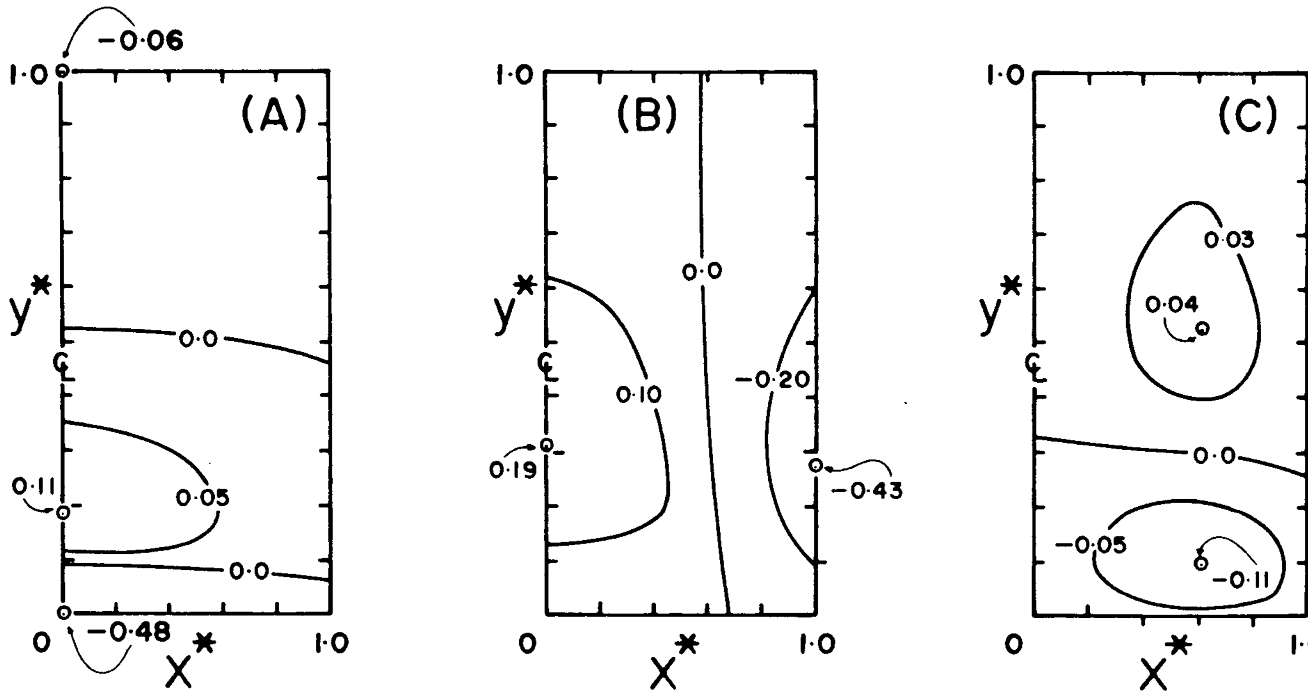

Figure I-5. Stress field for Fourier modulus of 0.10: (A) σ_x^*, (B) σ_y^*, and (C) τ_{xy}^* (r^*=0.50 and γ^*=0.05).

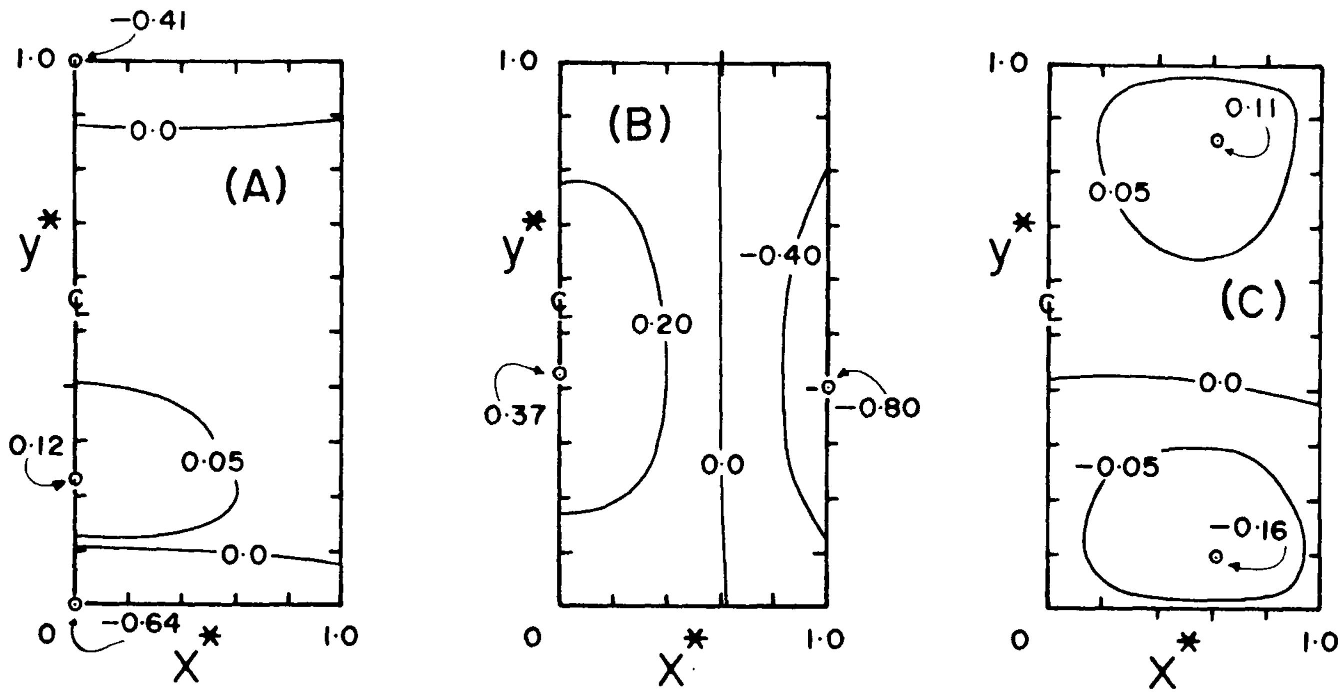

Figure I-6. Stress field for Fourier modulus of 1.0: (A) σ_x^*, (B) σ_y^*, and (C) τ_{xy}^* (r^*=0.50 and γ^*=0.05).

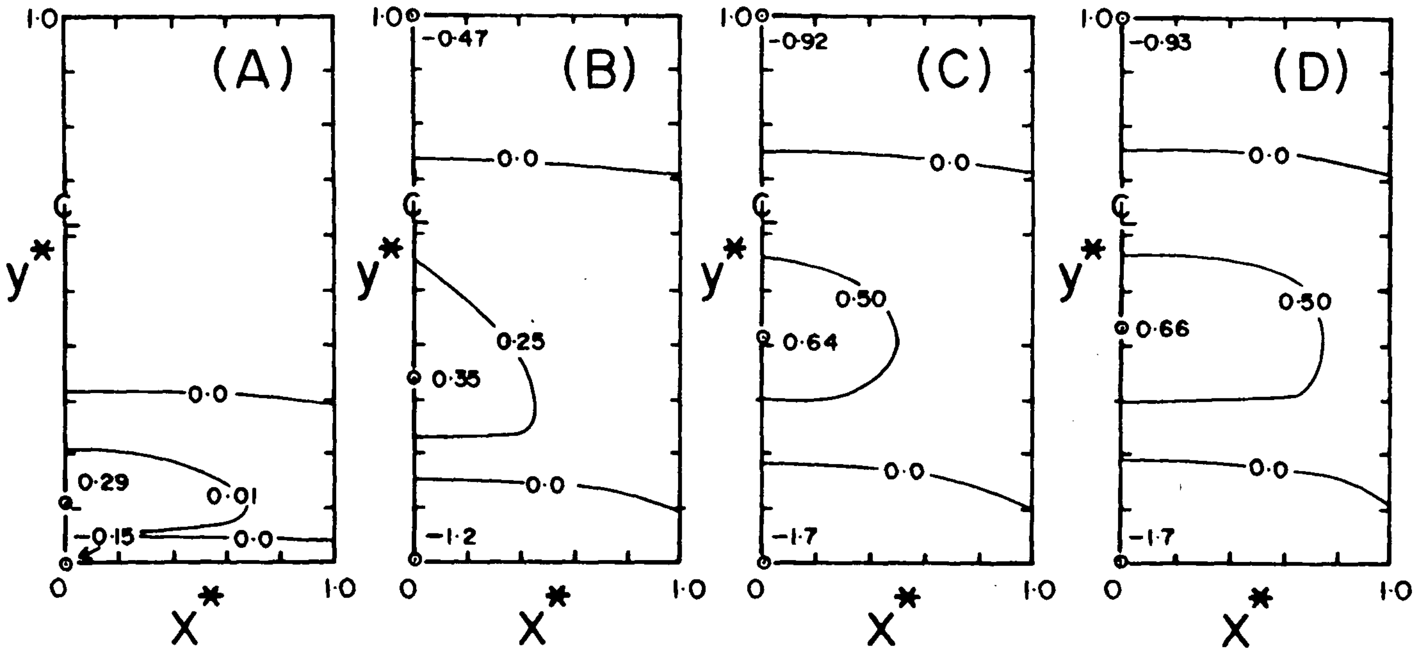

Figure I-7. σ_x field for various aspect ratio. (A) 0.25, (B) 1.0, (C) 2.0, and (D) 4.0. (θ^*=0.10 and γ^*=0.05)

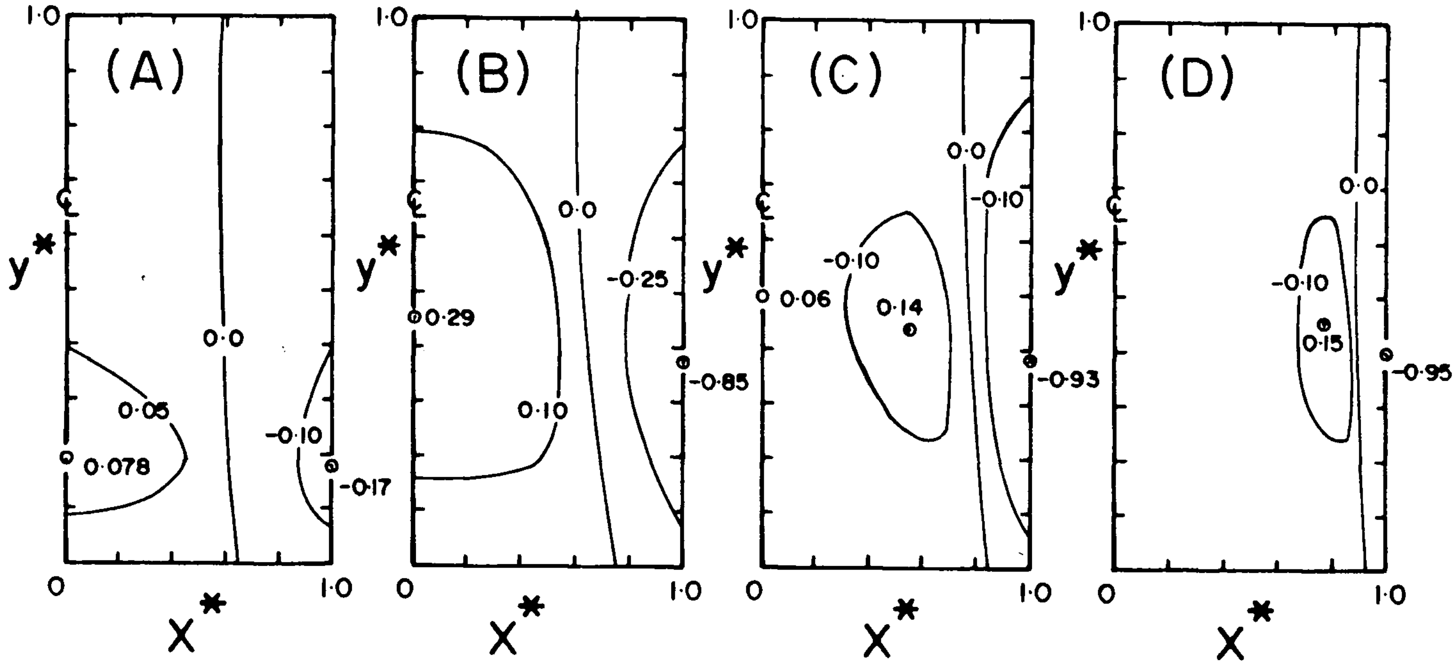

Figure I-8. σ_y field for various aspect ratio. (A) 0.25, (B) 1.0, (C) 2.0, and (D) 4.0. (θ^*=0.10 and γ^*=0.05)

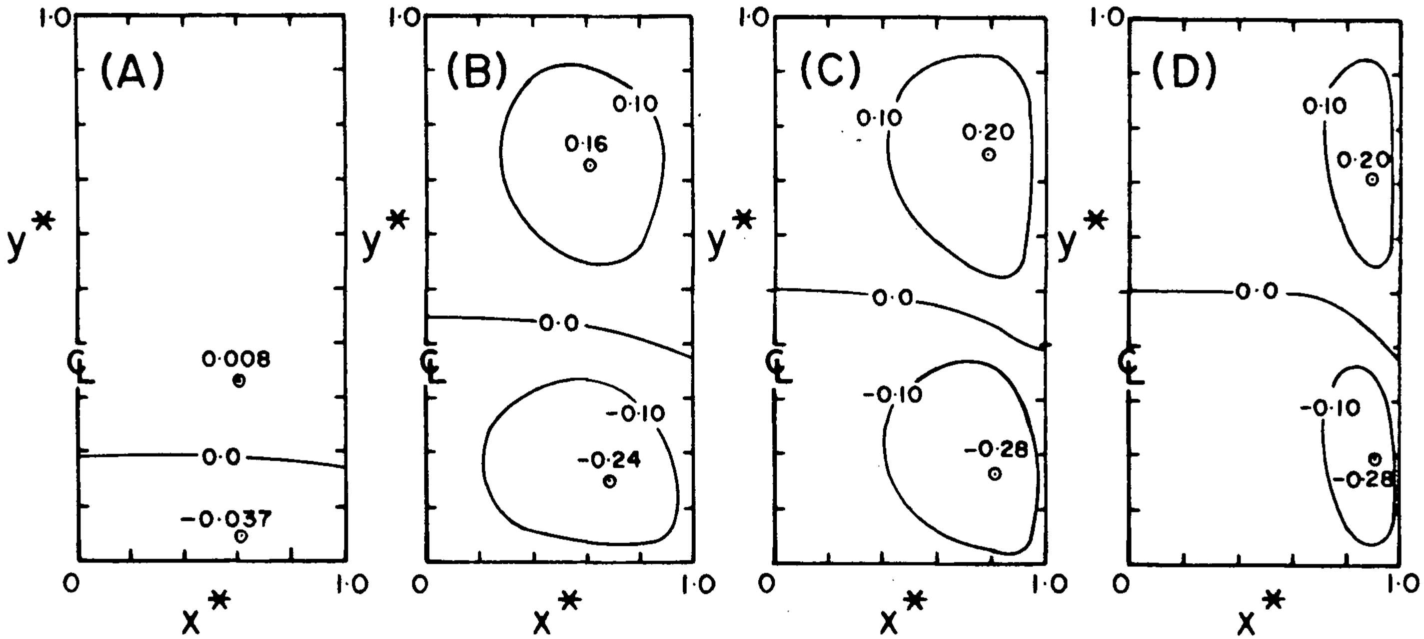

Figure I-9. τ_{xy} field for various aspect ratio. (A) 0.25, (B) 1.0, (C) 2.0, and (D) 4.0. (θ^*=0.10 and γ^*=0.05)

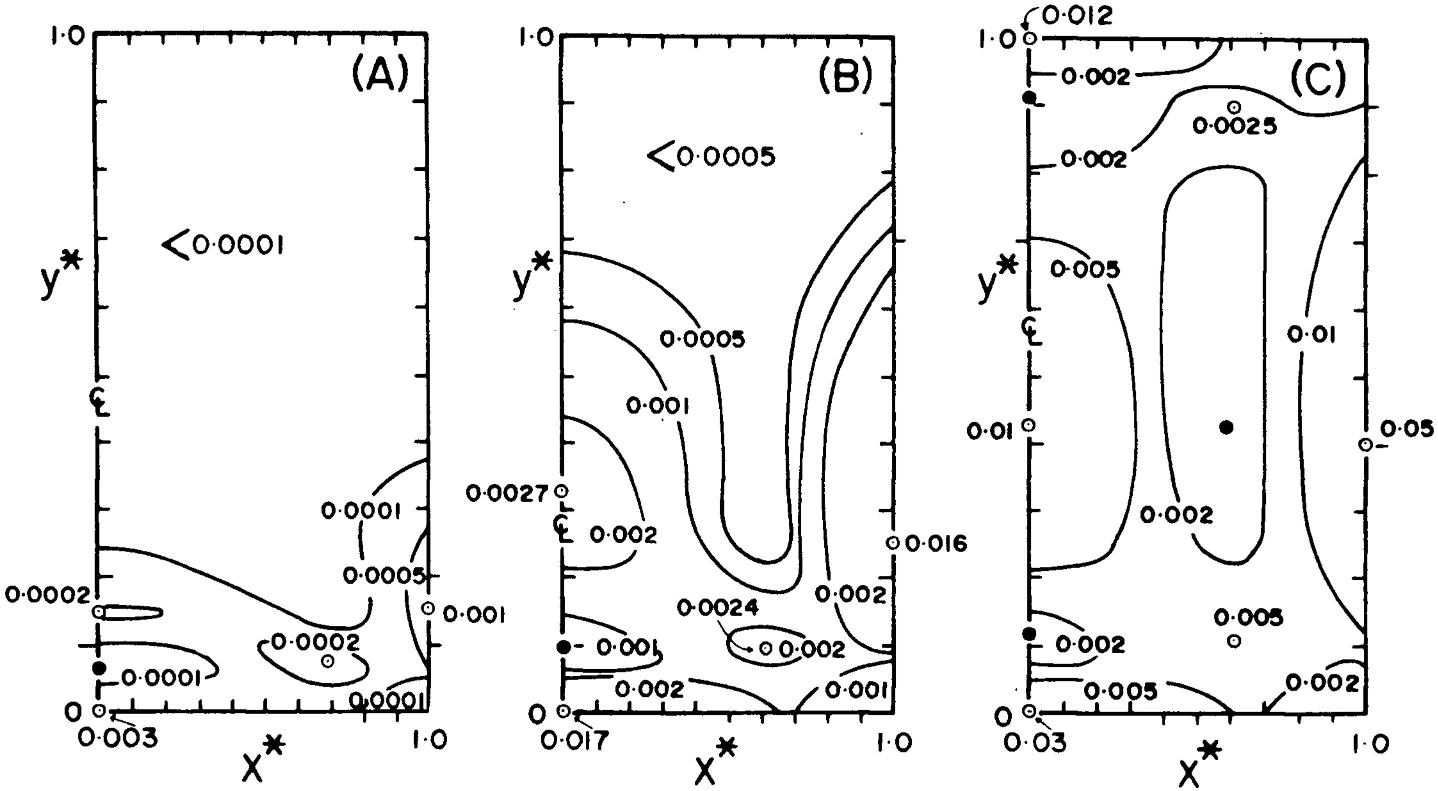

Figure I-10. Strain energy density fields for various Fourier modulus (A) 0.01, (B) 0.10, and (C) 1.0. (r^*=0.50 and γ^*=0.05)

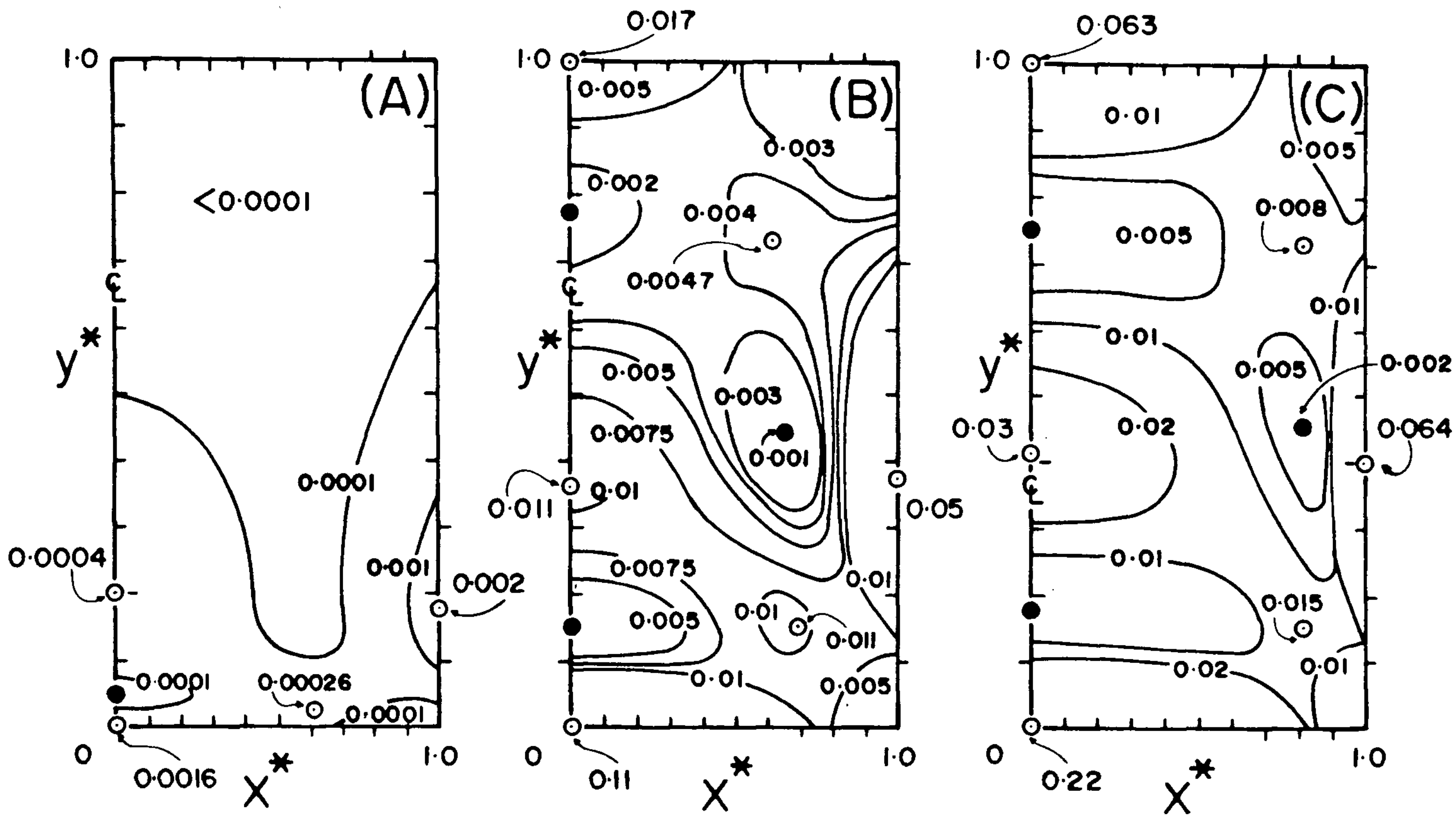

Figure I-11. Strain energy density fields for various aspect ratio.
(A) 0.25, (B) 1.0, and (C) 2.0. (β^*=0.10 and γ^*=0.05)

Appendix II

Numerical Method

Appendix II

Numerical Method

The thermal stress fields and total strain energy of the various cases considered have been computed using a two-dimensional finite element model. Isoparametric 8-noded quadrilaterial elements and Gauss quadrature numerical integration were used. The computer program was constructed in such a way as to handle both the plane strain and plane stress cases. The local and global coordinate systems, node numbering, and interpolation functions for the isoparametric formulation can be found in [1] along with the sampling points and weights used for the third order Gauss quadrature.

Three of the stresses of interest - $(\sigma_x^c)_M$, $(\sigma_y^c)_M$, $(\sigma_y^E)_M$, were determined by first evaluating the stress at the Gauss points nearest the centerline and outside edge and then selecting the appropriate maximum value. The component $(\sigma_x^0)_M$ was determined as the value at the node at the midpoint of the hot face. Strain energy was computed element by element using numerical integration and the total was arrived at by summing over all elements.

The results of a convergence test on a typical size of rectangular shape considered for the constant heating rate problem are given in Tabler II-1. The dimensional variables are defined and the thermal conditions stated in Appendix VIII. The variables NX, NY, and NE refer to the number of elements along the width, the length, and the total number, respectively. The values in brackets indicate the percentage change with respect to the next coarser mesh.

It is apparent from a comparison of results for the coarse and fine meshes that even relatiely coarse grids produce reasonable results. As little change is observed when the mesh is increased from 200 to 400 elements, most computations were performed using 200 element grids.

Verification of results consisted of a number of indirect checks in addition to reproducing the results of Chang[2] et al for the two-dimensional constant heating rate case. Hollow cylinder and infinite slab one-dimensional solutions were approximated by suitable modification of the boundary conditions and geometry. An additional check was the comparison of theoretical and computed values of the rato of plane stress and plane strain of various parameters. For the traction-free thermal stress problem, the theoretical ratios for dispalcements, strains, stresses, and strain energy are:

$$\frac{(\text{displacements and strains})_{\text{plane strain}}}{(\text{displacements and strains})_{\text{plane stress}}} = 1+\nu \qquad \text{(II-1}$$

$$\frac{(\text{stress})_{\text{plane strain}}}{(\text{stress})_{\text{plane stress}}} = \frac{1}{1-\nu} \qquad \text{(II-2)}$$

$$\frac{(\text{strain energy})_{\text{plane strain}}}{(\text{strain energy})_{\text{plane stress}}} = \frac{1+v}{1-v} \qquad \text{(II-3)}$$

As solutions for the total strain energy of two-dimensiopnal thermoelastic problems could not be found, several elementary cases were considered for verification of the numerical results. The numerical method yielded the zero strain energy state of the traction-free rectangular shape with constant or linear temperature profile. The numerical technique also reproduced the plane stress and plane strain values of strain energy density U_o for the case of the plate subjected to a uniform temperature rise while displacements are fixed on the bounding surface.

References

1. R. D. Cook, "Concepts and Applications of Finite Element Analysis", John Wiley and Sons, New York (1981)

2. W. C. Chang, C. E. Knight, D. P. H. Hasselman, and R. G. Mitchiner, " Analysis of Thermal Stress Failure of Segmented Thick-walled Refractory Structures", J. Am. Ceram. Soc., 66 [10] 708-713 (1983)

Table II-1

CONVERGENCE TEST RESULTS FOR 20x20 cm SHAPE

(dimensionless stress given in millistrains)

(θ^*=.10, r^*=1.0, γ^*=0.05)

	MESH			
	1	2	3	4
NX NY NE	5 10 50	10 10 100	10 20 200	20 20 400
$(\sigma_x^c)_M^*$	.3498	.3474 (-.69)	.3463 (-.32)	.3460 (-.09)
$(\sigma_y^c)_M^*$	.2775	.2770 (-.18)	.2719 (-1.8)	.2716 (-.11)
$(\sigma_x^0)^*$	1.247	1.239 (-.64)	1.228 (-.89)	1.225 (-.24)
$(\sigma_y^E)_M^*$	.8812	.8756 (-.64)	.8528 (-2.6)	.8522 (-.07)
U^*	.51995	.51979(-.03)	.51904(-.14)	.51899(-.01)

Appendix III

Dimensional Analysis of the Convective Heat Transfer Thermoelastic Problem

Appendix III

Dimensional Analysis of the Convective Heat Transfer Thermoelastic Problem

Dimensional analysis is used to obtain the dimensionless functional forms of thermal stress σ and total strain energy u for the two-dimensional constant convective heat transfer thermoelastic problem. The dimensional forms are

$$\sigma = f\ (x,\ y,\ t,\ E,\ v,\ \alpha,\ a,\ k,\ h,\ T_\infty,\ w,\ \ell) \tag{III-1}$$

and

$$U = f\ (t,\ E,\ v,\ \alpha,\ a,\ k,\ h,\ T_\infty,\ w,\ \ell) \tag{III-2}$$

The Buckingham Π theorem states that the number of dimensionless parameters needed to correlate the variables in a given process is equal to n-m, where n is the number of variables involved and m is the number of fundamental dimensions. Thus the thermal stress dependence can be expressed in terms of nine dimensionless parameters and the total strain energy in terms of seven. Rayleigh's method of indices is used to obtain the dimensionless groupings.

The thermal stress relationship is considered first. Equation (III-1) can be rewritten as

$$\sigma = (x)^a \ (y)^b \ (t)^c \ (E)^d \ (v)^e \ (\alpha)^f \ (a)^g \ (k)^h \ (h)^i \ (T_\infty)^j \ (w)^k \ (\ell)^\ell \qquad \text{(III-3)}$$

and the fundamental units of each substituted to give

$$\left[\frac{M}{LT^2}\right]^1 = [L]^a [L]^b [T]^c \left[\frac{M}{LT^2}\right]^d [\quad]^e \left[\frac{1}{\Theta}\right]^f \left[\frac{L^2}{T}\right]^g \left[\frac{ML}{T^3\Theta}\right]^h \left[\frac{M}{T^3\Theta}\right]^i [\Theta]^j [L]^k [L]^\ell \qquad \text{(III-4)}$$

Balancing each fundamental dimension gives

$$M : \quad 1 = d + h + i \qquad \text{(III-5)}$$

$$L : \ -1 = a + b - d + 2g + h + k + \ell \qquad \text{(III-6)}$$

$$T : \ -2 = c - 2d - g - 3h - 3i \qquad \text{(III-7)}$$

$$\Theta : \quad 0 = -f - h - i + j \qquad \text{(III-8)}$$

and expressing four of the exponents in terms of the remainder yields

$$d = 1 - h - i \qquad \text{(III-9)}$$

$$g = c - h - i \qquad \text{(III-10)}$$

$$j = f + h + i \qquad \text{(III-11)}$$

$$\ell = -a - b - 2c + i - k \qquad \text{(III-12)}$$

Substituting the above into (III-4) and separating exponents lead to

$$\left(\frac{\sigma}{E}\right) = \left(\frac{x}{\ell}\right)^a \left(\frac{y}{\ell}\right)^b \left(\frac{at}{\ell^2}\right)^c (\nu)^e (\alpha T_\infty)^f \left(\frac{kT_\infty}{Ea}\right)^h \left(\frac{hT_\infty}{Ea}\right)^i \left(\frac{w}{\ell}\right)^k \quad \text{(III-13)}$$

The right-hand side of (III-13) can be manipulated to give the following nine dimensionless combinations:

$$\frac{\sigma}{E} = f\left(\frac{x}{w}, \frac{y}{\ell}, \frac{at}{\ell^2}, \nu, \alpha T_\infty, \frac{h\ell}{k}, \frac{kT_\infty}{Ea}, \frac{w}{\ell}\right) \qquad \text{(III-14)}$$

For the simple linear thermoelastic problems being considered the factor (σ/E) is directly proportional to (αT_∞) and inversely proportional to ($1-\nu$). Also the combination (kT_∞/Ea) can be ignored as the elastic modulus is assumed to be independent of temperature. Thus equation (III-14) reduced to

$$\frac{\sigma\,(1-\nu)}{E\alpha T_\infty} = f\left(\frac{x}{w}, \frac{y}{\ell}, \frac{at}{\ell^2}, \frac{h\ell}{k}, \frac{w}{\ell}\right) \qquad \text{(III-15)}$$

A similar analysis would show that the seven dimensionless parameters of the total strain energy dependence can be expressed in the following form

$$\frac{U}{E\ell^2} = \left(\frac{at}{\ell^2}, \frac{h\ell}{k}, \frac{w}{\ell}, \alpha\, T_\infty, \nu, \frac{kT_\infty}{Ea}\right. \qquad \text{(III-16)}$$

As with the stress analyais ν can be combined with the dependent parameter and the factor (kT_∞/Ea) may be ignored.

Thus the dimensionles forms of (III-1) and (III-2) are

$$\sigma_h^* = f\ (x^*,\ y^*,\ \Theta^*,\ \beta^*,\ r^*) \tag{III-17}$$

and

$$U_h^* = f\ (\Theta^*,\ \beta^*,\ T_\infty^*,\ r^*) \tag{III-18}$$

where

$$\sigma_h^* = \frac{\sigma\ (1-\nu)}{E\ \alpha\ T_\infty} \tag{III-19}$$

$$U_h^* = \frac{U\ (1-\nu)}{E\ell^2\ (1+\nu)} \tag{III-20}$$

$$x^* = \frac{x}{w} \tag{III-21}$$

$$y^* = \frac{y}{\ell} \tag{III-22}$$

$$\theta^* = \frac{at}{\ell^2} \tag{III-23}$$

$$\beta^* = \frac{h\ell}{k} \tag{III-24}$$

$$T_{\infty}^{*} = \alpha T_{\infty} \tag{III-25}$$

$$r^{*} = \frac{w}{\ell} \, . \tag{III-26}$$

For applications in which particular members of the thermal stress field are of interest - for example the maximum principal tensile stress - the dimensionless location (x^{*}, y^{*}) is a dependent parameter and equation (III-17) reduces to

$$\sigma_{h}^{*} = f\ (\Theta^{*}, \beta^{*}, r^{*}) \tag{III-27}$$

For the one-dimensional infinite slab problem, stress is independent of aspect ratio r^{*} and (III-18) reduces to

$$\sigma_{h}^{*} = f\ (\Theta^{*}, \beta^{*}) \tag{III-28}$$

where dimensionless stress is only dependent on Fourier modulus θ^{*} and Biot modulus β^{*}.

APPENDIX IV

Tabulated Values of the Dimensionless Maximum Principal Tensile Stress for the Symmetric Heating and Cooling and Nonsymmetric Heating Infinite Slab Thermoelastic Problems

TABLE IV-1

<u>Dimensionless Maximum Principal Tensile Stress for Various Fourier and Biot Modulus for the Symetric Cooling Infinite Slab Case</u>

θ^*	β^*						
	.10	.15	.20	.30	.50	.70	1.0
.0001	-	-	-	-	.00614	.00858	.0122
.0002	-	-	-	-	.00849	.0119	.0169
.0004	-	-	-	-	.0116	.0162	.0231
.0007	-	-	-	-	.0150	.0209	.0296
.001	.00356	.00534	.00711	.0106	.0176	.0245	.0347
.002	.00491	.00735	.00978	.0146	.0242	.0335	.0474
.004	.00676	.0101	.0134	.0201	.0331	.0458	.0643
.01	.0103	.0154	.0203	.0302	.0495	.0681	.0947
.02	.0138	.0206	.0273	.0404	.0657	.0898	.124
.04	.0183	.0272	.0359	.0529	.0851	.115	.156
.1	.0250	.0370	.0486	.0708	.112	.148	.196
.2	.0293	.0431	.0562	.0809	.125	.162	.209
.4	.0310	.0450	.0582	.0821	.122	.154	.190
1.0	.0295	.0418	.0525	.0704	.0954	.111	.122

TABLE IV-1 (cont'd)

Dimensionless Maximum Principal Tensile Stress for Various Fourier and Biot Modulus for the Symmetric Cooling Infinite Slab Case

θ^*	β^*					
	1.5	2.0	3.0	5.0	7.0	10.0
.0001	.0183	.0242	.0360	-	-	
.0002	.0251	.0333	.0494	-	-	
.0004	.0343	.0453	.0668	-	-	
.0007	.0439	.0579	.0848	-	-	
.001	.0514	.0676	.0987	.156	.208	.276
.002	.0697	.0911	.132	.204	.267	.346
.004	.0939	.112	.174	.262	.335	.423
.010	.136	.175	.242	.350	.431	.520
.020	.175	.221	.299	.414	.493	.572
.040	.217	.269	.351	.462	.531	.594
.100	.262	.313	.388	.474	.519	.557
.200	.267	.309	.364	.418	.443	.462
.400	.230	.254	.281	.300	.306	.308
1.00	.128	.127	.120	.107	.0981	.0905

TABLE IV-2

Dimensionless Maximum Principal Tensile Stress for Various Fourier Modulus and Biot Modulus for the Symmetric Heating Infinite Slab Case

θ^*	β^*						
	0.10	0.15	0.20	0.30	0.50	0.70	1.0
.001	.000100	.000150	.000200	.000300	.0005	.000692	.000982
.002	.000200	.000300	.000400	.000597	.00099	.00138	.00195
.004	.000400	.000599	.000800	.00119	.00196	.00272	.00384
.010	.00101	.00153	.00200	.00298	.00490	.00675	.00942
.020	.00199	.00299	.00393	.00582	.00953	.0131	.0181
.040	.00395	.00590	.00778	.0115	.0186	.0253	.0347
.10	.00902	.0134	.0176	.0258	.0411	.0550	.0737
.20	.0134	.0197	.0258	.0373	.0581	.0762	.0992
.40	.0154	.0224	.0290	.0411	.0618	.0784	.0976
1.0	.0148	.0210	.0265	.0357	.0487	.0569	.0636

TABLE IV-2 (cont'd)

Dimensionless Maximum Principal Tensile Stress for Various Fourier Modulus and Biot Modulus for the Symmetric Heating Infinite Slab Case

θ^*	β^*					
	1.5	2.0	3.0	5.0	7.0	10.0
.001	.00146	.00192	.00281	.00449	.00602	.00808
.002	.00287	.00377	.00547	.00859	.0113	.0149
.004	.00563	.00734	.0105	.0162	.0209	.0269
.010	.0137	.0177	.0248	.0368	.0461	.0568
.020	.0259	.0330	.0453	.0645	.0786	.0936
.040	.0489	.0612	.0817	.111	.131	.151
.10	.100	.122	.155	.196	.221	.243
.20	.129	.152	.183	.216	.233	.247
.40	.120	.134	.151	.164	.169	.171
1.0	.0675	.0676	.0646	.0584	.0542	.0505

TABLE IV-3

Dimensionless Maximum Principal Tensile Stress for Various Fourier Modulus and Biot Modulus for the Nonsymmetric Heating Infinite Slab Case

θ^*	β^*								
	1.0	1.5	2.0	3.0	5.0	7.0	10.0	15.0	20.0
.001	.00307	.00455	.00599	.00878	.0140	.0188	.0252	.0343	.0418
.002	.00546	.00806	.0106	.0153	.0240	.0317	.0417	.0550	.0653
.004	.00937	.0137	.0178	.0256	.0392	.0507	.0648	.0825	.0952
.01	.0172	.0249	.0320	.0449	.0660	.0818	.100	.121	.134
.02	.0246	.0350	.0443	.0603	.0845	.101	.119	.137	.147
.04	.0303	.0422	.0523	.0686	.0907	.105	.118	.129	.135
.10	.0306	.0405	.0482	.0591	.0710	.0770	.081	-	-

APPENDIX V

Results of the Thermoelastic Analysis of the Nakayama Experiments

TABLE IV-1

REFRACTORY A

T	h $\frac{cal}{scm^2 °C}$	$(\sigma_f^*)_h$	β_f^*	Θ_f^*	t_f (s)	U_f (J/cm)	$(\sigma_f)_{FE}$ (MPa)	% Diff
950	0.00322	0.0177	0.46	0.0425	3.00	0.100	26.3	+ 2.0
1000	0.00362	0.0168	0.52	0.0350	2.50	0.111	26.0	+ 0.8
1100	0.00445	0.0153	0.64	0.0260	1.86	0.139	26.0	+ 0.8
1200	0.00540	0.1140	0.77	0.0200	1.43	0.170	26.2	+ 1.6
1300	0.00643	0.0130	0.92	0.0155	1.11	0.202	26.3	+ 1.9
1400	0.00765	0.0120	1.10	0.0120	0.86	0.234	26.0	+ 0.8
1500	0.00900	0.0112	1.28	0.00960	0.69	0.272	26.2	+ 1.6

TABLE IV-2

REFRACTORY B

T	h $\frac{cal}{scm^2 °C}$	$(\sigma_f^*)_h$	β_f^*	Θ_f^*	t_f (s)	U_f (J/cm)	$(\sigma_f)_{FE}$ (MPa)	% Diff
1050	.00405	0.0731	1.35	0.0730	12.2	0.0513	20.4	+ 2.0
1100	.00445	0.0699	1.48	0.0620	10.3	0.0562	20.1	+ 0.5
1200	.00540	0.0641	1.80	0.0465	7.75	0.0690	20.1	+ 0.5
1300	.00643	0.0592	2.14	0.0355	5.92	0.0810	19.7	- 1.5
1400	.00765	0.055	2.55	0.0280	4.67	0.0959	19.6	- 2.0
1500	.00900	0.0513	3.00	0.0227	3.78	0.112	19.7	- 1.5

TABLE IV-3

REFRACTORY C

T	h $\frac{cal}{scm^2 °C}$	$(\sigma_f^*)_h$	β_f^*	Θ_f^*	t_f (s)	U_f (J/cm)	$(\sigma_f)_{FE}$ (MPa)	% Diff
850	0.00258	0.0254	0.86	0.0327	5.45	0.0803	14.1	- 0.7
1000	0.00362	0.0215	1.20	0.0198	3.30	0.112	14.0	0.0
1100	0.00445	0.0196	1.48	0.0147	2.45	0.136	14.0	0.0
1200	0.00540	0.0180	1.80	0.0113	1.88	0.165	14.0	0.0
1300	0.00643	0.0166	2.14	0.00876	1.46	0.191	14.0	+ 0.7
1400	0.00765	0.0154	2.55	0.00690	1.15	0.223	14.1	+ 0.7
1500	0.00900	0.0144	3.08	0.00558	0.93	0.259	14.2	+ 1.4

TABLE IV-4

REFRACTORY D

T	h $\frac{cal}{scm^2 °C}$	$(\sigma_f^*)_h$	β_f^*	Θ_f^*	t_f (s)	U_f (J/cm)	$(\sigma_f)_{FE}$ (MPa)	% Diff
1050	.00405	0.0686	1.35	0.0682	11.4	0.0414	16.5	+ 3.1
1100	.00445	0.0655	1.48	0.0570	9.50	0.0447	16.1	+ 0.6
1200	.00540	0.0600	1.80	0.043	7.17	0.0548	16.0	0.0
1300	.00643	0.0554	2.14	0.0337	5.62	0.0658	16.1	+ 0.6
1400	.00765	0.0514	2.55	0.0263	4.38	0.0769	15.9	- 0.6
1500	.00900	0.0480	3.00	0.0210	3.50	0.0888	15.7	- 1.9

TABLE IV-5

REFRACTORY E

T	h $\frac{cal}{scm^2 °C}$	$(\sigma_f^*)_h$	β_f^*	Θ_f^*	t_f (s)	U_f (J/cm)	$(\sigma_f)_{FE}$ (MPa)	% Diff
1100	0.00445	0.0131	0.202	0.068	1.55	0.0397	21.9	- 0.5
1200	0.00540	0.0120	0.245	0.0508	1.15	0.0491	21.9	- 0.5
1300	0.00643	0.011	0.292	0.0390	0.89	0.0596	21.9	- 0.5
1400	0.00765	0.0103	0.348	0.0305	0.69	0.0707	21.7	- 1.4
1500	0.00900	0.00958	0.409	0.0243	0.55	0.0840	21.8	- 0.9

TABLE IV-6

REFRACTORY F (2x7 cm)

T	h $\frac{cal}{scm^2 °C}$	$(\sigma_f^*)_h$	β_f^*	Θ_f^*	t_f (s)	U_f (J/cm)	$(\sigma_f)_{FE}$ (MPa)	% Diff
950	0.00322	0.0428	1.28	0.0390	7.80	0.0237	4.72	- 2.7
1000	0.00362	0.0407	1.45	0.0330	6.60	0.0266	4.69	- 3.3
1100	0.00445	0.0370	1.78	0.0246	4.92	0.0328	4.69	- 3.3
1200	0.00540	0.0339	2.16	0.0190	3.80	0.0401	4.74	- 2.3
1300	0.00643	0.0313	2.57	0.0148	2.96	0.0469	4.71	- 2.9
1400	0.00765	0.0291	3.06	0.0117	2.34	0.0549	4.70	- 3.1
1500	0.00900	0.0271	3.60	0.00955	1.91	0.0642	4.80	- 1.0

TABLE IV-7

REFRACTORY F (4x10 cm)

T	h $\frac{cal}{scm^2 °C}$	$(\sigma_f^*)_h$	β_f^*	θ_f^*	t_f (s)	U_f (J/cm)	$(\sigma_f)_{FE}$ (MPa)	% Diff
650	0.00154	0.0626	1.23	0.0650	52.00	.0438	4.85	0.0
700	0.00176	0.0582	1.41	0.0540	43.2	.0529	4.97	2.5
900	0.00289	0.0452	2.31	0.0246	19.6	.0862	4.71	- 2.9
1100	0.00445	0.0370	3.56	0.0135	10.8	.132	4.76	- 1.9
1300	0.00643	0.0313	5.14	0.00795	6.36	.178	4.66	- 3.9
1500	0.00900	0.0271	7.20	0.00510	4.08	.237	4.67	- 3.7

APPENDIX VI

Results of the Thermoelastic Analysis of the Larson Heating and Cooling Experiments

TABLE VI-1A

Refractory 2 - Heating

T (°C)	h ($\frac{cal}{scm^2 °C}$)	$(\frac{\sigma_f^*}{h})$	β^*	Θ_f^*	t_f (s)	U (J/cm)	σ_f (MPa)
800	.00230	.0242	.230	0.130	6.50	.0333	14.0
900	.00282	.216	.282	0.0850	4.25	.0437	14.4
1000	.00362	.0194	.362	0.058	2.90	.0556	14.3
1100	.00445	.0176	.445	0.0418	2.09	.0684	14.0
1200	.00540	.0161	.540	0.0322	1.61	.0856	14.3
1300	.00643	.0149	.643	0.0248	1.24	.101	14.1
1400	.00765	.0138	.765	0.0195	.98	.120	14.2

TABLE VI-1B

Refractory 2 - Cooling

ΔT (°C)	h ($\frac{cal}{scm^2 °C}$)	$(\frac{\sigma_f^*}{h})$	β_f^*	Θ_f^*	t_f (s)	U (J/cm)	σ_f (MPa)
200	.00525	.0968	.525	.049	2.45	.00367	14.0
300	.00475	.0645	.475	.021	1.05	.00248	14.1
400	.00460	.0484	.460	.0115	.58	.00191	14.3
600	.00485	.0323	.485	.00400	.20	.00111	14.2
800	.00550	.0242	.550	.0016	.080	.000695	14.2
1000	.00670	.0194	.670	.000657	.0329	.000459	14.6
1180	.00800	.0164	.800	.000300	.015	.000326	14.6

TABLE VI-2A

Refractory 6 - Heating

T (°C)	h ($\frac{cal}{scm^2 °C}$)	$\frac{(\sigma_f^*)}{h}$	β^*	Θ_f^*	t_f (s)	U (J/cm)	σ_f (MPa)
1000	.00362	.0319	.517	.0695	4.96	.0893	18.2
1100	.00445	.0290	.636	.0500	3.57	.111	18.7
1150	.00492	.2077	.703	.0440	3.14	.125	18.9
1200	.00540	.0266	.771	.0385	2.75	.139	19.0
1300	.00643	.0245	.919	.0297	2.12	.165	18.8
1400	.00765	.0228	1.09	.0230	1.64	.192	18.6

TABLE VI-2B

Refractory 6 - Cooling

ΔT (°C)	h ($\frac{cal}{scm^2 °C}$)	$\frac{(\sigma_f^*)}{h}$	β_f^*	Θ_f^*	t_f (s)	U (J/cm)	σ_f (MPa)
200	.00525	.159	.75	.125	8.93	.00111	19.4
300	.00475	.106	.679	.0448	3.20	.00819	20.7
400	.00460	.0797	.657	.0172	1.23	.00434	19.0
600	.00485	.0531	.693	.00580	.414	.00255	19.1
800	.00550	.0398	.786	.00222	.159	.00153	18.9
1000	.00670	.0319	.957	.00089	.0636	.000970	19.1
1180	.00800	.0270	1.14	.00041	.0293	.000670	19.2

TABLE VI-3A

Refractory 8 - Heating

T (°C)	h ($\frac{cal}{scm^2\,°C}$)	$\frac{(\sigma_f^*)}{h}$	β^*	Θ_f^*	t_f (s)	U (J/cm)	σ_f (MPa)
800	.00230	.0268	.383	.0778	6.48	0.0388	13.5
900	.00282	.0238	.470	.0553	4.61	.0518	13.9
1000	.00362	.0214	.603	.0385	3.21	.0649	13.5
1100	.00445	.0195	.742	.0285	2.38	.0802	13.6
1200	.00540	.0178	.900	.0213	1.78	.0954	13.4
1300	.00643	.0165	1.07	.0170	1.42	.116	13.7
1400	.00765	.0153	1.28	.0130	1.08	.130	13.3

TABLE VI-3B

Refractory 8 - Cooling

ΔT (°C)	h ($\frac{cal}{scm^2\,°C}$)	$\frac{(\sigma_f^*)}{h}$	β_f^*	Θ_f^*	t_f (s)	U (J/cm)	σ_f (MPa)
200	.00525	.107	.875	.0185	1.54	.00211	13.6
300	.00475	.0714	.792	.00840	0.700	.00142	13.6
400	.00460	.0535	.767	.00460	.383	.00105	13.6
600	.00485	.0357	.808	.00165	.138	.000629	13.7
800	.00550	.0268	.917	.00066	.0550	.000402	13.9
1000	.00670	.0214	1.12	.000265	.0220	.000280	14.1
1180	.00800	.0181	1.33	.000125	.0104	.000249	14.2

TABLE VI-4A

Refractory 15 - Heating

T (°C)	h $\left(\frac{cal}{scm^2 °C}\right)$	$\frac{(\sigma_f^*)}{h}$	β^*	Θ_f^*	t_f (s)	U (J/cm)	σ_f (MPa)
800	.00230	.0426	.460	.117	11.7	0.0375	11.1
900	.00282	.0379	.574	.0763	7.6	.0480	11.1
1000	.00362	.0341	.724	.051	5.1	.0592	10.7
1100	.00445	.0310	.890	.0385	3.85	.0757	10.9
1200	.00540	.0284	1.08	.0295	2.95	.0932	11.0
1300	.00643	.0262	1.29	.0228	2.28	.109	10.9
1400	.00765	.0244	1.53	.0188	1.88	.136	11.4

TABLE VI-4B

Refractory 15 - Cooling

ΔT (°C)	h $\left(\frac{cal}{scm^2 °C}\right)$	$\frac{(\sigma_f^*)}{h}$	β_f^*	Θ_f^*	t_f (s)	U (J/cm)	σ_f (MPa)
200	.00525	.171	1.05	.051	5.10	.00447	11.5
300	.00475	.114	.95	.0185	1.85	.00266	11.3
400	.00460	.0853	.92	.0092	.92	.00182	11.1
600	.00485	.0568	.97	.0032	.320	.00108	11.2
800	.00550	.0426	1.10	.00125	.125	.000660	11.2
1000	.00670	.0341	1.34	.00048	.048	.000406	11.2
1180	.00800	.0289	1.60	.00021	.021	.000295	11.0

TABLE VI-5A

Refractory 19 - Heating

T (°C)	h $(\frac{cal}{scm^2 °C})$	$(\frac{\sigma_f^*}{h})$	β^*	Θ_f^*	t_f (s)	U (J/cm)	σ_f (MPa)
800	.00230	.0617	.575	.17	21.3	.0491	11.4
900	.00282	.0548	.705	.10	12.5	.0618	11.5
1000	.00362	.0493	.905	.0654	8.18	.0796	11.4
1100	.00445	.0448	1.11	.0475	5.94	.0985	11.3
1150	.00492	.0429	1.23	.0400	5.00	.106	11.0
1200	.00540	.0411	1.35	.0345	4.31	.115	10.8
1300	.00643	.0379	1.61	.0274	3.43	.140	11.0
1400	.00765	.0352	1.91	.0220	2.75	.168	11.2

TABLE VI-5B

Refractory 19 - Cooling

ΔT (°C)	h $(\frac{cal}{scm^2 °C})$	$(\frac{\sigma_f^*}{h})$	β_f^*	Θ_f^*	t_f (s)	U (J/cm)	σ_f (MPa)
200	.00525	.247	1.31	.0835	10.4	.00705	10.7
300	.00475	.164	1.19	.0295	3.69	.00487	11.4
400	.00460	.123	1.15	.0140	1.75	.00335	11.3
600	.00485	.0822	1.21	.00460	.575	.00193	11.4
800	.00550	.0617	1.38	.00180	.225	.00120	11.4
1000	.00670	.0493	1.68	.00070	.0875	.000740	11.5
1180	.00800	.0418	2.0	.00033	.0413	.000547	11.7

TABLE VI-6A

Refractory 21 - Heating

T (°C)	h $(\frac{cal}{scm^2 °C})$	$(\frac{\sigma_f^*}{h})$	β^*	Θ_f^*	t_f (s)	U (J/cm)	σ_f (MPa)
800	.00230	.0513	.575	.118	14.75	.0273	7.07
900	.00282	.0456	.705	.0760	9.50	.0337	6.92
1000	.00362	.0410	.905	.0517	6.46	.0434	6.87
1100	.00445	.0373	1.11	.0390	4.88	.0553	6.99
1200	.00540	.0342	1.35	.0286	3.58	.0646	6.75
1300	.00643	.0315	1.61	.0230	2.88	.0793	6.94

TABLE VI-6B

Refractory 21 - Cooling

ΔT (°C)	h $(\frac{cal}{scm^2 °C})$	$(\frac{\sigma_f^*}{h})$	β_f^*	Θ_f^*	t_f (s)	U (J/cm)	σ_f (MPa)
200	.00525	.205	1.31	.0485	6.06	.00303	7.05
300	.00475	.137	1.19	.0170	2.125	.00176	6.97
400	.00460	.103	1.15	.00800	1.10	.00128	7.00
600	.00485	.0684	1.21	.00303	.379	.000757	7.05
800	.00550	.0513	1.38	.00120	.150	.000472	7.10
1000	.00670	.0410	1.68	.00047	.0588	.000300	7.19
1180	.00800	.0348	2.0	.00022	.0275	.000236	7.29

TABLE VI-7A

<u>Refractory 23 - Heating</u>

T (°C)	h $(\frac{cal}{scm^2 °C})$	$\frac{(\sigma_f^*)}{h}$	β^*	Θ_f^*	t_f (s)	U (J/cm)	σ_f (MPa)
900	.00282	.0446	.718	.0720	9.0	0.1343	27.4
1000	.00362	.0401	.905	.0508	6.35	0.174	27.6
1100	.00445	.0365	1.11	.0372	4.65	0.2146	27.2
1200	.00540	.0335	1.35	.0285	3.56	0.262	27.4
1300	.00643	.0309	1.61	.0225	2.81	0.314	27.7
1400	.00765	.0287	1.91	.0175	2.19	0.364	27.4
1400	.00765	.0138	.765	0.0195	.98	.120	14.2

TABLE VI-7B

<u>Refractory 23 - Cooling</u>

ΔT (°C)	h $(\frac{cal}{scm^2 °C})$	$\frac{(\sigma_f^*)}{h}$	β_f^*	Θ_f^*	t_f (s)	U (J/cm)	σ_f (MPa)
200	.00525	.201	1.31	.043	5.38	.0108	27.8
300	.00475	.134	1.19	.0155	1.94	.00639	27.4
400	.00460	.100	1.15	.00820	1.03	.00477	27.8
600	.00485	.0669	1.21	.00290	3.63	.00291	28.2
800	.00550	.0502	1.38	.00115	1.44	.00182	28.4
1000	.00670	.0401	1.68	.00044	.0550	.00112	28.5
1180	.00800	.0340	2.0	.00021	.0263	.000915	29.1

TABLE VI-8A

Refractory 27 - Heating

T (°C)	h ($\frac{cal}{scm^2 °C}$)	($\frac{\sigma_f^*}{h}$)	β^*	Θ_f^*	t_f (s)	U (J/cm)	σ_f (MPa)
1000	.00362	.0540	1.21	.0553	9.22	.153	23.0
1100	.00445	.0491	1.48	.0400	6.67	.186	22.5
1200	.00540	.0450	1.80	.0305	5.08	.226	22.5
1300	.00643	.0416	2.14	.0237	3.95	.266	22.3
1400	.00765	.0386	2.55	.0187	3.12	.311	22.3

TABLE VI-8B

Refractory 27 - Cooling

ΔT (°C)	h ($\frac{cal}{scm^2 °C}$)	($\frac{\sigma_f^*}{h}$)	β_f^*	Θ_f^*	t_f (s)	U (J/cm)	σ_f (MPa)
200	.00525	.270	1.75	.0605	10.1	.0117	22.7
300	.00475	.180	1.58	.0190	3.17	.00675	22.9
400	.00460	.135	1.53	.0098	1.63	.00503	23.4
600	.00485	.0900	1.62	.00305	.508	.00268	22.9
800	.00550	.0675	1.83	.00118	.197	.00164	23.0
1000	.00670	.0540	2.23	.00045	.0750	.00101	23.1
1180	.00800	.0458	2.67	.000218	.0360	.000827	23.7

TABLE VI-9A

Refractory 28 - Heating

T (°C)	h ($\frac{cal}{scm^2 °C}$)	$\frac{(\sigma_f^*)}{h}$	β^*	Θ_f^*	t_f (s)	U (J/cm)	σ_f (MPa)
800	.00230	.0617	.767	.113	18.8	.0737	16.9
900	.00282	.0557	.957	.071	11.8	.0912	16.4
1000	.00362	.0502	1.21	.0505	8.42	.119	16.6
1100	.00445	.0456	1.48	.0365	6.08	.143	16.2
1150	.00492	.0436	1.64	.0315	5.25	.157	16.1
1200	.00540	.0418	1.80	.028	4.67	.175	16.2
1300	.00643	.0386	2.14	.022	3.67	.208	16.3
1400	.00765	.0358	2.55	.0174	2.90	.244	16.3

TABLE VI-9B

Refractory 28 - Cooling

ΔT (°C)	h ($\frac{cal}{scm^2 °C}$)	$\frac{(\sigma_f^*)}{h}$	β_f^*	Θ_f^*	t_f (s)	U (J/cm)	σ_f (MPa)
200	.00525	.249	1.75	.0430	7.17	.00724	16.4
300	.00475	.166	1.58	.0150	2.50	.00432	16.5
400	.00460	.125	1.53	.008	1.33	.00329	16.8
600	.00485	.0831	1.62	.00260	.43	.00181	16.7
800	.00550	.0623	1.83	.001	.167	.00111	16.7
1000	.00670	.0498	2.23	.00039	.065	.000716	16.9
1180	.00800	.0422	2.67	.000184	.0307	.000592	17.2

TABLE VI-10A

Refractory 31 - Heating

T (°C)	h ($\frac{cal}{s cm^2 °C}$)	$\frac{(\sigma_f^*)}{h}$	β^*	Θ_f^*	t_f (s)	U (J/cm)	σ_f (MPa)
800	.00230	.0350	.767	.0480	9.0	.0177	4.19
900	.00282	.0311	.940	.0368	6.13	.0211	3.97
1000	.00362	.0280	1.21	.0263	4.38	.0273	4.00
1100	.00445	.0255	1.48	.0197	3.28	.0336	4.02
1200	.00540	.0234	1.80	.0150	2.50	.0401	4.03
1300	.00643	.0216	2.14	.0117	1.95	.0469	4.05

TABLE VI-10B

Refractory 31 - Cooling

ΔT (°C)	h ($\frac{cal}{s cm^2 °C}$)	$\frac{(\sigma_f^*)}{h}$	β_f^*	Θ_f^*	t_f (s)	U (J/cm)	σ_f (MPa)
200	.00525	.140	1.75	.0074	1.23	.000440	4.03
300	.00475	.0934	1.58	.0036	.60	.000320	4.13
400	.00460	.0701	1.53	.002	.333	.000240	4.16
600	.00485	.0467	1.62	.00068	.113	.000134	4.13
800	.00550	.0350	1.83	.00026	.0433	.0000895	4.14
1000	.00670	.0280	2.23	.00011	.0183	.0000835	4.29
1180	.00800	.0238	2.67	.000056	.00093	.000852	4.07

TABLE VI-11A

Refractory 34 - Heating

T (°C)	h ($\frac{cal}{scm^2 °C}$)	$\frac{(\sigma_f^*)}{h}$	β^*	Θ_f^*	t_f (s)	U (J/cm)	σ_f (MPa)
800	.00230	.0593	.767	0.103	17.2	.0501	10.3
900	.00282	.0527	.940	0.068	11.3	.0619	10.0
1000	.00362	.0474	1.21	0.0475	7.92	.0810	10.1
1100	.00445	.0431	1.48	0.0338	5.63	.0959	9.69
1200	.00540	.0395	1.80	0.0263	4.38	.119	9.86
1300	.00643	.0365	2.14	0.0210	3.50	.143	10.1

TABLE VI-11B

Refractory 34 - Cooling

ΔT (°C)	h ($\frac{cal}{scm^2 °C}$)	$\frac{(\sigma_f^*)}{h}$	β_f^*	Θ_f^*	t_f (s)	U (J/cm)	σ_f (MPa)
200	.00525	.237	1.75	.036	6.00	.00440	10.1
300	.00475	.158	1.58	.0135	2.25	.00276	10.2
400	.00460	.1191	1.53	.007	1.17	.00202	10.3
600	.00485	.0790	1.62	.00225	.375	.00109	10.1
800	.00550	.0593	1.83	.00084	.140	.000601	10.0
1000	.00670	.0474	2.23	.000338	.0563	.000435	10.3
1180	.00800	.0402	2.67	.000160	.0267	.000372	10.4

APPENDIX VII

Results of the Thermoelastic Analysis of the Semler Experiments

TABLE VII-1

Results for Splits (ℓ = 11.43cm)

No.	$(\sigma_f^*)_h$	Θ_{1000}^*	β_f^*	h $\left(\frac{cal}{scm^2 °C}\right)$	Θ_f^*	t_f (s)	U_f (J/cm)	σ_f (MPa)	y_f (cm)
S1	.0408	.0321	9.1	.00557	.00212	19.8	1.216	19.9	2.0
S2	.0396	.0276	9.81	.00515	.00188	20.5	2.840	45.3	1.8
S3	.0401	.0184	12	.00420	.00153	25.0	1.341	27.2	1.6
S4	.0412	.0184	12	.00420	.00161	26.3	.910	14.2	1.6
S5	.0409	.0184	12	.00420	.00160	26.1	.705	11.2	1.6
S6	.0502	.0184	12	.00420	.00213	34.8	.761	13.7	2.0
S7	.0562	.0184	12	.00420	.00257	42.0	1.038	17.3	2.1
S8	.0974	.0184	12	.00420	.00735	120.	.720	9.71	2.9
S9	.0696	.0184	12	.00420	.00370	60.4	.704	9.78	2.3
S10	.0471	.0138	13.8	.00362	.00170	37.0	1.47	22.7	1.7
S11	.0565	.00919	17	.00297	.00185	60.4	2.216	34.1	1.8
S12	.0477	.00919	17	.00297	.00140	45.7	1.964	31.6	1.5

TABLE VII-2

Results for Quarters (ℓ = 5.72cm)

No.	$(\sigma_f^*)_h$	Θ^*_{1000}	β_f^*	h $\left(\frac{cal}{scm^2\,°C}\right)$	Θ_f^*	t_f (s)	U_f (J/cm)	σ_f (MPa)	y_f (cm)
S1	.0408	.128	4.6	.00563	.00472	11.0	.553	19.8	1.3
S2	.0396	.110	4.92	.00516	.00410	11.2	1.26	44.9	1.2
S3	.0401	.0734	6.1	.00427	.00320	13.1	.596	26.8	1.1
S4	.0412	.0734	6.1	.00427	.00343	14.0	.412	14.2	1.1
S5	.0409	.0734	6.1	.00427	.00340	13.9	.391	11.2	1.1
S6	.0502	.0734	6.1	.00427	.00465	19.0	.355	13.8	1.3
S7	.0562	.0734	6.1	.00427	.00565	23.1	.488	17.3	1.3
S8	.0974	.0734	6.1	.00427	.023	94.1	.370	9.83	2.1
S9	.0696	.0734	6.1	.00427	.00850	34.8	.342	9.84	1.6
S10	.0471	.0550	7.0	.00367	.00352	19.2	.658	22.5	1.1
S11	.0565	.0367	8.5	.00297	.00375	30.7	.991	33.4	1.2
S12	.0477	.0367	8.5	.00297	.00300	24.5	.911	32.1	1.1

TABLE VII-3

Results for Bars (ℓ = 2.54cm)

No.	$(\sigma_f^*)_h$	θ_{1000}^*	β_f^*	h $(\frac{cal}{scm^2 \circ C})$	θ_f^*	t_f (s)	U_f (J/cm)	σ_f (MPa)	y_f (cm)
S1	.0408	.651	1.78	.00491	.021	9.68	.214	20.4	.86
S2	.0396	.558	2.0	.00472	.0154	8.28	.486	46.1	.81
S3	.0401	.372	2.58	.00406	.0103	8.31	.230	27.6	.71
S4	.0412	.372	2.58	.00406	.0110	8.87	.157	14.5	.72
S5	.0409	.372	2.58	.00406	.0108	8.71	.121	11.3	.72
S6	.0502	.372	2.58	.00406	.0170	13.7	.141	14.2	.82
S7	.0562	.372	2.58	.00406	.0216	17.4	.188	17.3	.87
S8	.0974	.372	2.58	.00406	No fract	300	.022	3.35	
S9	.0696	.372	2.58	.00406	No fract	300	.034	4.74	
S10	.0471	.279	3.05	.00360	.0112	12.0	.263	23.4	.72
S11	.0565	.186	3.76	.00296	.0113	18.2	.392	34.3	.72
S12	.0477	.186	3.76	.00296	.0081	13.1	.337	31.9	.67

Appendix VIII

Dimensional Analysis of the Stress Dependence of the Constant Heating Rate Thermoelastic Problem

APPENDIX VIII

DIMENSIONAL ANALYSIS OF CONSTANT HEATING RATE THERMOELASTIC PROBLEM

The number of variables in the thermal stress dependence of equation (1) can be reduced using dimensional analysis.

$$\sigma = f(\ x,\ y,\ t,\ \phi,\ a,\ E,\ \alpha,\ \nu,\ \ell,\ w\ ) \qquad (1)$$

The fundamental dimensions of mass [M], length [L], time [T], and temperature [Θ] of each variable are listed in Table 1. The Buckingham π theorem states that the number of dimensionless parameters needed to correlate the variables in a given process is equal to n-m, where n is the number of variables involved and m is the number of fundamental dimensions included in the variables. Rayleigh's method of indices is used to determine the dimensionless groupings.

The number of dimensionless parameters is 7 as n=11 and m=4. Equation (1) can be rewritten as

$$(\sigma)^{1} = (x)^{a}(y)^{b}(t)^{c}(\phi)^{d}(a)^{e}(E)^{f}(\alpha)^{g}(l)^{h}(w)^{i}(\nu)^{j} \qquad (2)$$

and the fundamental units of each variable substituted to give

$$[\frac{M}{LT^2}]^1 = [L]^a[L]^b[T]^c[\frac{\theta}{T}]^d[\frac{L^2}{T}]^e[\frac{M}{LT^2}]^f[\frac{1}{\theta}]^g[L]^h[L]^i[\ ]^j. \quad (3)$$

Balancing each fundamental dimension, expressing four of the exponents in terms of the remainder, substituting into (2), and separating exponents leads to (4).

$$(\frac{\sigma}{E}) = (\frac{x}{\ell})^a (\frac{y}{\ell})^b (\frac{at}{\ell^2})^e (\phi\alpha t)^g (\frac{w}{\ell})^i (\nu)^j \quad (4)$$

It is desirable to have x associated with w and to have only one time dependent dimensionless parameter. This is accomplished by multiplying and dividing the right hand side of (4) by $(\frac{w}{\ell})^a$ and $(\frac{at}{\ell^2})^g$ to yield

$$(\frac{\sigma}{E}) = (\frac{x}{w})^a (\frac{y}{\ell})^b (\frac{at}{\ell^2})^{e+g} (\frac{\phi\alpha\ell^2}{a})^g (\frac{w}{\ell})^{i+a} (\nu)^j \quad (5)$$

The number of dimensionless parameters is reduced by one by combining ν with σ and E.

Thus the dimensionless form of equation (1) is

$$\sigma^* = f\ (x^*,\ y^*,\ \theta^*,\ r^*,\ \gamma^*) \tag{6}$$

where

$$\sigma^* = \frac{\sigma(1-\nu)}{E} \tag{7}$$

$$x^* = \frac{x}{w} \tag{8}$$

$$y^* = \frac{y}{\ell} \tag{9}$$

$$\theta^* = \frac{at}{\ell^2} \tag{10}$$

$$r^* = \frac{w}{\ell} \tag{11}$$

$$\gamma^* = \frac{\phi\alpha\ell^2}{a} \tag{12}$$

Appendix IX

Dimensional Analysis of the Strain Energy Dependence of the Constant Heating Rate Thermoelastic Problem

Appendix IX

Dimensional Analysis of the Strain energy Dependence

The fundamental dimensions of mass [M], length [L], time [T], and temperature [Θ] of each variable in total strain energy dependence of equation (1) are listed in Table 1.

$$U = f(\ t,\phi,a,E,\alpha,w,\ell,\nu) \tag{1}$$

The Buckingham π theorem states that the number of dimensionless parameters needed to correlate the variables in a given process is equal to n-m, where n is the number of variables involved and m is the number of fundamental dimensions included in the variables. The number of dimensionless parameters is 5 as n=9 and m=4. Equation (1) can be rewritten as

$$(U)^{1} = (t)^{a}(\phi)^{b}(a)^{c}(E)^{d}(\alpha)^{e}(\ell)^{f}(w)^{g}(\nu)^{h} \tag{2}$$

and the fundamental units of each variable substituted to give

$$\left[\frac{ML}{T^2}\right]^{1} = [T]^{a}\left[\frac{\Theta}{T}\right]^{b}\left[\frac{L^2}{T}\right]^{c}\left[\frac{M}{LT^2}\right]^{d}\left[\frac{1}{\Theta}\right]^{e}[L]^{f}[L]^{g}[\ \ ]^{h}. \tag{3}$$

Balancing each fundamental dimension, expressing four of the exponents in terms of the remainder, substituting into (2), separating exponents, and manipulating to give only one time-dependent parameter leads to

$$\left(\frac{U}{E\ell^2}\right) = \left(\frac{at}{\ell^2}\right)^{c+e} \left(\frac{\phi\alpha\ell^2}{a}\right)^{e} \left(\frac{w}{\ell}\right)^{g} (\nu)^{h} \qquad (4)$$

A further simplification is possible by using the plane strain relationship to combine ν with U and E to give

$$\left(\frac{U(1-\nu)}{E\ell^2(1+\nu)}\right) = f\left(\frac{at}{\ell^2}, \frac{\phi\alpha\ell^2}{a}, \frac{w}{\ell} \right) \qquad (5)$$

Thus the dimensionless form of equation (1) is

$$U^* = f\ (\theta^*, \gamma^*, r^*) \qquad (6)$$

where

$$U^* = \frac{U(1-\nu)}{E\ell^2(1+\nu)} \qquad (7)$$

$$\theta^* = \frac{at}{\ell^2} \qquad (8)$$

$$\gamma^* = \frac{\phi\alpha\ell^2}{a} \tag{9}$$

$$r^* = \frac{w}{\ell} \tag{10}$$

Table IX-1

VARIABLES FOR DIMENSIONAL ANALYSIS

Variable	Symbol	Fundamental Units
strain energy/unit thickness	U	ML/T^2
time	t	T
heating or cooling rate	ϕ	Θ/T
thermal diffusivity	a	L^2/T
elastic modulus	E	$M/(LT^2)$
thermal expansion coefficient	α	$1/\Theta$
Poisson's ratio	ν	
length	l	L
width	w	L

APPENDIX X

Results of Howie Experiments

TABLE I.—SPALL TESTS ON SILICA BRICKS "A"—DRY.

Test No.	Heating Rate on Hot Face (220–270° C.) ° C. per min.	Distance of Crack from Hot Face, inches	Porosity (per cent.).	Bulk Density (g./c.c.).	Specific Gravity (By Porosity).
1	0·7	Uncracked			
2	2·9	do.	30·1	1·63	2·33
3	4·0	do.	28·3	1·67	2·33
4	4·8	do.	30·4	1·62	2·32
5	5·0	1·10 (Slight crack—not typical.)	30·1	1·63	2·33
6	6·7	Uncracked	29·3	1·64	2·33
7	6·95	do.	30·4	1·62	2·33
8	7·0	0·90	29·8	1·63	2·33
9	7·1	1·25	30·6	1·62	2·33
10	9·1	1·10	28·8	1·66	2·33
11	9·6	1·27			
12	10·0	1·20	28·9	1·65	2·32
13	14·7	0·92			
14	15·4	1·07	30·4	1·62	2·33
15	17·85	0·825			
16	17·85	0·80			
17	23·8	0·85	29·1	1·65	2·32
18	25·0	0·60	29·1	1·65	2·33

TABLE II.—SPALL TESTS ON SILICA BRICKS "B"—DRY.

Test No.	Heating Rate on Hot Face (220–270° C.) ° C. per min.	Distance of Crack from Hot Face, inches.	Porosity (per cent.).	Bulk Density (g./c.c.).	Specific Gravity (By Porosity).
19	3·3	Uncracked	27·9	1·69	2·34
20	5·7	1·50	29·3	1·65	2·34
21	8·2	0·95	25·6	1·73	2·33
22	10·1	1·10	27·7	1·69	2·34
23	12·5	0·90	26·9	1·69	2·32
24	16·7	1·05	27·6	1·69	2·33
25	20·8	0·95	28·8	1·67	2·34

TABLE III.—SPALL TESTS ON SILICA BRICKS "C"—DRY.

Test No.	*Heating Rate on Hot Face (220–270° C.) °C. per min.*	*Distance of Crack from Hot Face, inches.*	*Porosity (per cent.).*	*Bulk Density (g./c.c.).*	*Specific Gravity (By Porosity).*
26	3·8	Uncracked	28·1	1·67	2·33
27	7·5	1·55	26·1	1·74	2·35
28	8·6	0·95	27·5	1·68	2·32
29	12·2	1·15	28·9	1·67	2·35
30	13·2	1·30	27·1	1·71	2·35
31	15·6	0·75	27·4	1·69	2·33
32	22·7	0·75	26·0	1·74	2·35

TABLE IV.—SPALL TESTS ON SILICA BRICKS "D"—DRY.

Test No.	*Heating Rate on Hot Face (220–270° C.) °C. per min.*	*Distance of Crack from Hot Face, inches.*	*Porosity (per cent.).*	*Bulk Density (g./c.c.).*	*Specific Gravity (By Porosity).*
33	4·6	Uncracked	29·0	1·69	2·39
34	5·0	do.	29·8	1·67	2·38
35	7·9	do.	30·3	1·65	2·37
36	8·7	1·20 (Very slight cracks.)	30·2	1·65	2·37
37	12·5	1·00	29·9	1·67	2·38
38	13·9	0·80	29·1	1·69	2·39
39	19·6	0·55	29·9	1·65	2·37
40	19·6	0·45	29·7	1·68	2·39

TABLE VI.—SPALLING TESTS ON BRICKS "A" SOAKED IN WATER

Test No.	*Heating Rate on Hot Face (220–270° C.) °C. per min.*	*Distance of Crack from Hot Face, inches.*	*Porosity (per cent.).*	*Bulk Density (g./c.c.).*	*Specific Gravity (By Porosity).*
47	1·2	Uncracked	29·7	1·63	2·33
48	3·5	1·20	30·4	1·62	2·33
49	5·5	0·91			
50	6·25	0·70			
51	7·0	1·05	29·8	1·63	2·32
52	7·7	0·75	28·8	1·66	2·33
53	8·8	0·60			
54	10·0	0·80	28·1	1·68	2·33
55	11·1	0·70	30·1	1·63	2·33
56	11·9	0·53	31·0	1·61	2·33
57	13·2	0·45	30·2	1·62	2·32
58	19·6	0·30	29·0	1·65	2·33